Magnetoelastic properties of iron-based amorphous wires

Atalay, Selcuk

Award date:
1992

Awarding institution:
University of Bath

Magnetoelastic Properties of Iron-Based Amorphous Wires

Submitted by Selçuk Atalay

for the degree of PhD

of the University of Bath

1992

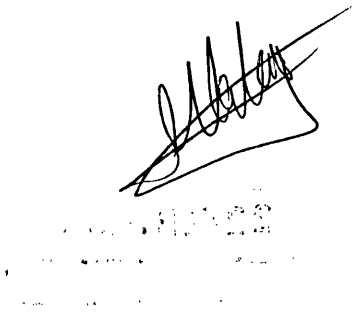

ProQuest LLC
789 East Eisenhower Parkway
P.O. Box 1346
Ann Arbor, MI 48106-1346

PREFACE

Part of this study have been presented at following conferences and published or are to be published in the following papers:

S. Atalay and P.T. Squire, "Field-Dependent Shear Modulus and Internal friction in Annealed Iron-Based Amorphous Wires", *J. Magn. Magn. Mat.*, **101** (1991) 47.

S. Atalay and P.T. Squire, "Comprative Measurements of the Field Dependence of Young's Modulus and Shear Modulus in Fe-Based Amorphous Wire", *J. Appl. Phys.*, **70** (1991) 6516.

S. Atalay and P.T. Squire, "Torsional Pendulum System for Measuring the Shear Modulus and Internal Friction of Magnetoelastic Amorphous Wires", *Meas. Sci. Technol.*, **3** (1992) 735.

S. Atalay and P.T. Squire, "Magnetoelastic Properties of Cold-Drawn FeSiB Amorphous Wires", *IEEE Trans.on Magn.*, **28(5)**, (1992), 3144.

S. Atalay and P.T. Squire, "Magnetomechanical Damping in Amorphous Wires", IOP Meeting on Current Research in Magnetism, London 1992.

S. Atalay and P.T. Squire, "Magnetomechanical Damping in FeSiB Amorphous Wires", accepted for publication in *J. Appl. Phys.*

D. Atkinson, P.T. Squire, M. R. J. Gibbs, S. Atalay and D. G. Lord, " The Effect of Annealing and Crystallisation on the Magnetoelastic Properties of Fe-Si-B Amorphous Wire", submitted to *J. Appl. Phys.*

D. Atkinson, P.T. Squire, M. R. J. Gibbs, S. Atalay and D.G. Lord, "Control of Magnetoelastic Properties of Fe-Si-B Amorphous Wire", IEEE Meeting on Current Topics in Applied Magnetism, Keele 1992.

I would like to thank my supervisor, Mr P.T. Squire, for his guidance and encouragement. I am also grateful to Dr M.R.J Gibbs for useful discussions. Additional thanks are due to Dr A.P. Thomas, Miss T. Lafford, Mr M. Maylin, Dr D. Atkinson, Dr C.F. Kilby, Mr M. Tatar and to Mr R. Draper.

I also would like to express my special thanks to Mr I. Adiguzel, Mr I. Ozdemir and Dr B. Cevik for forwarding money from Turkey during my study.

This project was funded by Inonu University, Malatya, Turkey.

Abstract

In this project, the magnetomechanical properties of amorphous wires were investigated. The Young's modulus and magnetostriction as a function of applied magnetic field were measured. To measure the shear modulus and magnetomechanical damping as a function of applied field, tensile stress and torsional strain an inverted torsional pendulum system was designed.

Published data on the magnetic and magnetoelastic properties of amorphous wires are reviewed. The theoretical models concerning the magnetoelastic properties of the ferromagnetic materials are also reviewed.

The saturation magnetostriction of the Fe-based amorphous wire was derived from the engineering magnetostriction. Magnetoelastic properties of the wires were improved by furnace and current annealing. Changes in both Young's modulus and shear modulus of up to 80% in a magnetic field were obtained. The effect of the annealing temperature and time on the field dependence of the Young's modulus and shear modulus is explained using the Squire model. From the magnetostriction and modulus measurements as functions of applied field, the average angle of the magnetic moments with respect to the wire axis at H=0 is estimated. It was observed that annealing first reduces the internal stress; further annealing leads to surface crystallisation, which favours a circumferential domain structure in the Fe-based wires.

The magnetomechanical damping behaviour of the amorphous wires is explained using the Smith-Birchak [1969] and Degauque-Astie [1980] models. The internal stress values were estimated using the Smith-Birchak model. It was found that the internal stress is reduced from the initial value of >200 MPa to as low as 2.3 MPa.

LIST OF SYMBOLS

A	Area
A_n	Oscillation Amplitude
B_r	Remanent Flux Density
B_m	Maximum Flux Density
C	Capacitance
D	Diameter
D_n	Spring Constant
d	Magnetomechanical Coupling
e_p	Matteucci Voltage
E	Young's Moduli
E_o	Young's Moduli at zero applied field
E_s	Young's Moduli at saturation
E_{min}	Minimum Value of Young's Modulus
f	Frequency
G	Shear Moduli
G_o	Shear Moduli at zero applied field
G_s	Shear Moduli at saturation
G_{min}	Minimum Value of Shear Moduli
G_{max}	Maximum Value of Shear Moduli
H	Field
H_c	Coercivity
H_d	Demagnetising Field
H_i	Internal Field
H_k	Anisotropy Field
H_{max}	Maximum Applied Field
I	Current / Moment of Inertia
K	Anisotropy Constant / Magnetomechanical Hysteresis Loop Constant
K_u	Induced Anisotropy Constant
K_n	Spring Constant
K_s	Shape Anisotropy Constant
k	Magnetomechanical Coupling Factor / Damping Constant
l	Length
m	Mass
M	Magnetisation
M_s	Saturation Magnetisation
M_r	Remanence Magnetisation
n	Number of Turns / Oscillation Mode
N_d	Demagnetising Factor
N_x	Demagnetising Factor
N_y	Demagnetising Factor
P	Power
Q^{-1}	Damping

Q^{-1}_{max}	Peak Value of Damping
r	Radius
R	Resistance
R_o	Resistance at Room Temperature
S_n	Spring Constant
t	Poisson's Ratio / Time
T	Temperature / Period
T_c	Curie Temperature
T_x	Crystallisation Temperature
T_g	Glass Transition Temperature
U	Amplitude of Magneto Elastic Wave / Total Energy
U_h	Hysteresis Energy Loss
U_k	Anisotropy Energy
U_{ms}	Magnetoelastic Energy
U_{ex}	Exchange Energy
U_s	Shape Anisotropy Energy
U_o	Initial Amplitude of Magneto Elastic Wave
V	Voltage / Velocity
x	Distance
W_n	Strain Energy
Δ	Change in ...
λ	Magnetostriction
λ_s	Saturation Magnetostriction
λ_e	Engineering Magnetostriction
χ	Susceptibility
υ	Magnetic Hysteresis Loop Constant
μ_o	Permeability of Free Space
α	Direction Cosines / Thermal Resistance Coefficient
θ	Angle
θ_i	Initial Angle
θ_f	Final Angle
σ	Tensile Stress
ϕ	Easy Axis Angles / Phase
β	Thermal Resistance Coefficient
ρ	Density / Resistivity
ε	Strain
ω_o	Angular Frequency

Table of Contents

1 Introduction

1.1 Aim of Study

The aims of this project are to investigate the magnetic field dependence of Young's modulus, E, and magnetostriction, λ, and the magnetic field, tensile stress and torsional strain,ε, dependence of the shear modulus, G, and the magnetomechanical damping, Q^{-1}. The work reported here was carried out on $Fe_{77.5}Si_{7.5}B_{15}$ amorphous wires with various diameters from 50μm to 140μm. The wires were produced by the in-rotating-water spinning method. To reduce the diameter, wires were cold-drawn. The field dependence of λ, E, G and Q^{-1} is important in understanding magnetomechanical properties and the domain structure of materials.

This project reports the effects of furnace, current and magnetic field annealing on the magnetic and magnetoelastic properties of Fe-based amorphous wires.

The magnetic field dependence of λ and Young's modulus was explained semi quantitatively using the model proposed by Squire [1990] which assumes that amorphous ribbon is field annealed at an oblique angle to the ribbon axis. This induces an easy axis in the annealing field direction leading to a domain structure which consists of regions separated by 180° domain walls. Magnetisation occurs both by moment rotation and by domain wall motion.

The Degauqe and Astie [1980] model was used to explain the torsional strain and field dependence of magnetomechanical damping. The model assumes that the maximum value of the damping (the damping peak) is proportional to the number of 90° domain

walls which perform irreversible jumps. The magnetic field plays two important roles. Small magnetic fields increase the peak value of the damping and higher fields lead to a decrease in the damping peak.

In this chapter, the magnetic and magnetomechanical parameters used in this study are defined and a brief introduction to amorphous alloys is given.

1.2 Basic Magnetic Parameters

M-H loop: The most outstanding characteristic of a magnetic material is its hysteresis loop, also called its M-H loop. A typical M-H loop is shown in figure 1.1 where H_c is coercivity, M_r is remanent magnetisation, M_s is saturation magnetisation and U_h is energy loss. The loop can be divided into three parts. The first part is the low field region where the shape of the loop often follows Rayleigh's relation:

$$M = \chi_o H + 2\upsilon H^2 \qquad (1.1)$$

where χ_o is the initial susceptibility and υ is a constant. The second part of the curve is between the first part and the knee. In this part, magnetisation increases rapidly with increasing applied magnetic field, H. The third part lies between the knee and the saturation magnetisation, M_s. At saturation all the magnetic moments align in the direction of H, so that further increase in H does not change the magnetisation.

When the magnetic field is reduced to zero from any magnetised state of the sample, the remaining magnetisation is called the remanent magnetisation.

Coercivity and coercive field: The coercive field can be defined as the reverse applied field required to reduce the magnetisation to zero from any value. The coercivity is the field necessary to reduce the magnetisation to zero from saturation.

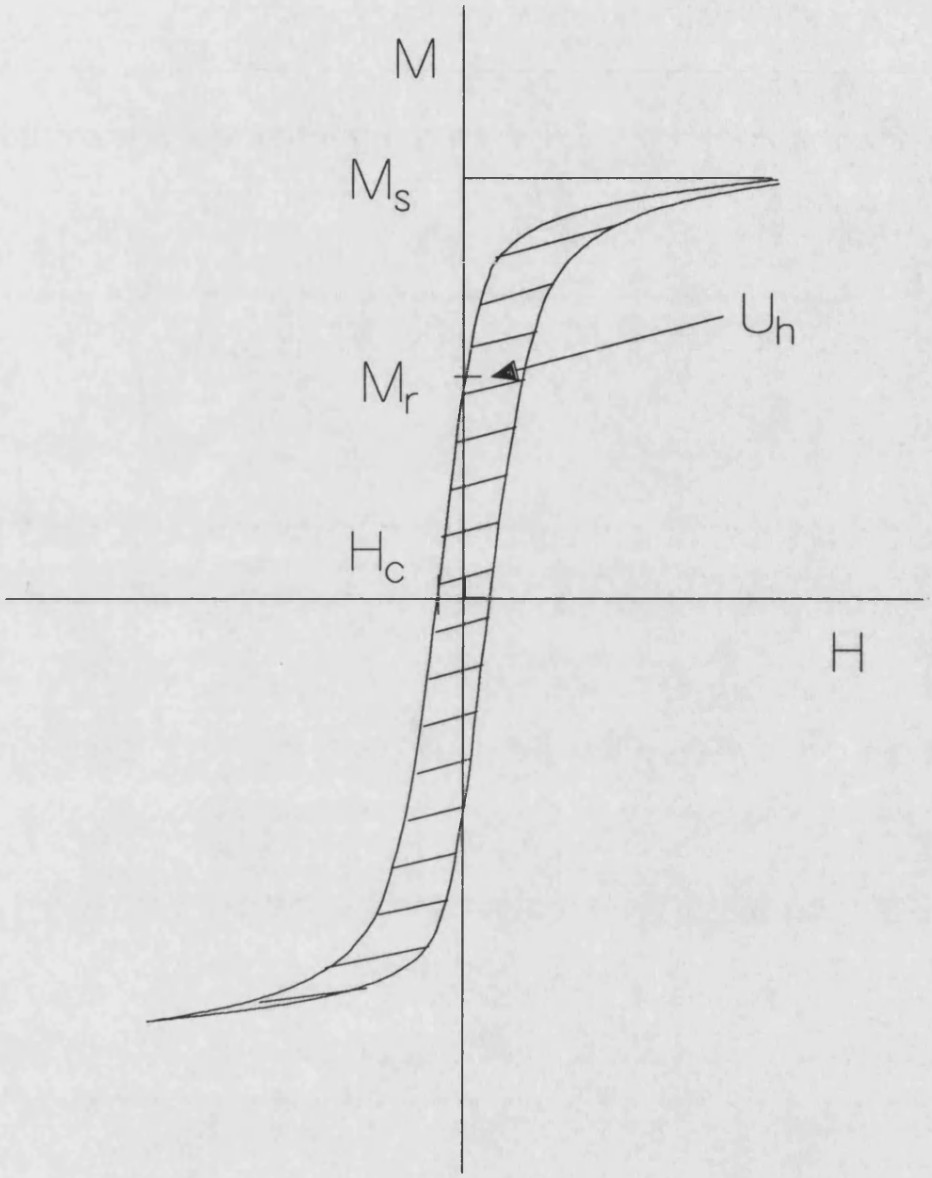

Figure 1.1: Variation of the magnetisation of a typical magnetic material with applied field (M-H loop).

Susceptibility: For many magnetic materials, magnetisation, M, is proportional to the applied field, H, according to the relation:

$$M = \chi H \tag{1.2}$$

where χ is the susceptibility. Since the M and H have the same dimensions χ is dimensionless. However in practise, magnetic materials do not always have a constant susceptibility. So, the rate of change of M with H (dM/dH) is sometimes used as χ, which is then called the differential susceptibility. The initial susceptibility, χ_o, is the susceptibility at low fields ($\chi_o = (dM/dH)_{H \to 0}$).

Hysteresis loss: When a ferromagnetic material is made to go through one complete M-H cycle, the total work done on the sample is called the hysteresis loss, U_h, which is equal to the area enclosed by the M-H loop as shown in figure 1.1. Energy loss in materials is caused by eddy currents and irreversible motion of the domain walls.

Anisotropy energy: This is the energy per unit volume necessary to rotate the magnetisation into the direction of the applied field. The anisotropy energy is given by the area shown in the figure 1.2. This area represents the average of the total local anisotropies in the sample, and is given by:

$$U_k = \mu_o \int_0^{M_s} H dM \tag{1.3}$$

The anisotropy energy can be separated into the contributing anisotropy energies which are magnetocrystalline, shape, stress and induced anisotropy.

1) Magnetocrystalline anisotropy: This is due to the spin-orbit interaction between the atomic magnetic moments. There is also orbit-lattice coupling in the crystal structure. When an external field is applied to the sample, the field tries to orient the spin of the electron into the direction of the field. The orbit of the electron also tends to be oriented.

But electron orbits are strongly coupled to the lattice and resist rotating into the field direction; the energy required to overcome this coupling is called the crystal anisotropy energy. When the magnetisation is rotated by the magnetic field, the stored energy is given by:

$$U = K_o + K_1(\alpha_1^2\alpha_2^2 + \alpha_2^2\alpha_3^2 + \alpha_3^2\alpha_1^2) + K_3(\alpha_1^2\alpha_2^2\alpha_3^2 + ...) \qquad (1.4)$$

where α_1, α_2 and α_3 are direction cosines between the magnetisation direction and the crystal axes and K_o, K_1 and K_3 are anisotropy constants. K_o is usually ignored, because it is the angular dependence in anisotropy energy which is of interest. K_1 is about the order of 10^4 for a typical crystalline magnetic material (Cullity [1972] Jiles [1991] and Heck [1967]).

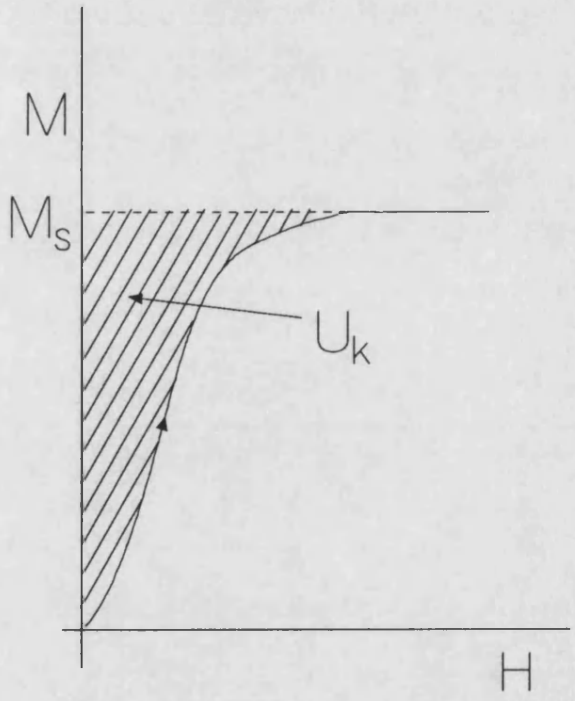

Figure 1.2: Definition of the anisotropy energy (shadowed area).

In amorphous magnetic alloys, there is no macroscopic crystal anisotropy, because amorphous alloys have only short range order (typically 1 nm). So there will be only local crystal anisotropy. On the macroscopic scale, if these local anisotropies are averaged out, the total crystal anisotropy will be zero (Luborsky [1983]).

2) Shape anisotropy: In a magnetic field, magnetic poles are produced at free surfaces of a material, so there will be a magnetic field (H_d, demagnetising field) inside the specimen. This field is oriented in the direction opposite to that of the external applied field. The demagnetising field is:

$$H_d = N_d M \tag{1.5}$$

where N_d is the demagnetising factor, which depends on the shape of the sample (Hence, the shape of the sample can be a source of the anisotropy). H_d along the short axis of the sample is stronger than along the long axis of the sample.

For a rod, the magnetostatic energy is given by:

$$U_{ms} = \mu_o\left(\frac{1}{2}M^2N_y + \frac{1}{2}(N_y - N_x)M^2\sin^2\theta\right), \tag{1.6}$$

where θ is the angle between easy axis and rod direction, and N_x and N_y are the demagnetising constants along the rod axis and the radial direction, respectively. The anisotropy constant, K_s, is:

$$K_s = \frac{1}{2}\mu_o(N_y - N_x)M^2 \tag{1.7}$$

For a rod-shaped sample, the easy axis is in the direction of the rod axis but magnetisation is very difficult in the radial direction. Shape anisotropy depends on y/x (where x is the half length of the rod and y is the radius of the rod) ratio which determines N_y-N_x. For example, for a material which has $M_s = 1.3 \times 10^6$ A/m and y/x=3.5, K_s is about 3.9×10^5 Jm^{-3} (Cullity [1972]).

3) Stress anisotropy: In magnetic materials in their as-prepared states, the internal stresses are not always zero, because in the production process, the quenching of the materials is not uniform. These internal stresses produce local anisotropies which can be reduced by stress-relief heat treatments. Stress anisotropy energy (i.e. magnetoelastic energy) can be written as:

$$U_{me} = K_\sigma \sin^2\theta \qquad (1.8)$$

where $K_\sigma = (3/2)\lambda_s\sigma_i$, σ_i is internal stress and λ_s is saturation magnetostriction (Cullity [1972]).

In the case of amorphous alloys, the anisotropy due to the internal stress in the as-cast sample can be reduced by annealing. The anisotropy energy can be reduced as low as 38 Jm^{-3} in iron-based metallic glasses (Hodson [1986]).

4) Anisotropy induced by annealing: Magnetic field annealing of materials induces an anisotropy in the direction of the field. This anisotropy is not very strong, typically of the order of a few hundred Jm^{-3} (Luborsky [1975] and [1977]).

When a current is applied to a material, a magnetic field will be created in the circumferential direction inside and around the sample. This field induces a helical anisotropy in wire-shaped materials and transverse anisotropy in ribbon materials. The induced anisotropy due to the current annealing in a typical amorphous alloy is also a few hundred Jm^{-3} (Vazquez [1986]).

Domains and domain wall motion: A ferromagnetic material prefers to be subdivided into domains rather than be uniformly magnetised, because a material always wants to be in a state in which its total energy is a minimum. A domain is a region where the

magnetisation is uniform and equal to M_s, but different domains are magnetised in different directions. Therefore, the average magnetisation of a sample could be less than M_s, and could even be zero at H=0.

The boundary between domains is called a domain wall where the direction of the magnetic moments change gradually from site to site from one direction to another. Therefore, a domain wall has a thickness to accommodate the gradual change in the magnetic moment direction.

When a magnetic field is applied to a material, the magnetisation changes. Magnetisation occurs by either magnetic moment rotation or domain wall motion. Domain wall motion can be reversible or irreversible. In crystalline materials, the domain wall moves reversibly in very small applied fields. In other words, the walls are displaced by small amounts when the magnetic field is applied, but if the field is removed they return to the their original positions. At larger fields, the domain wall motion becomes irreversible. In this case, the domain walls do not return to their original positions when the field is removed. The main reason for irreversible domain wall movement is that the domain wall energy is not constant. It varies in an irregular manner because of the variation in the local internal stresses. (Jakubovics [1987]).

Curie Temperature: The spontaneous magnetisation depends on temperature. It decreases with increasing temperature and becomes zero at a characteristic temperature T_c called the Curie temperature.

1.3 Magnetoelastic Properties

1.3.1 Magnetostriction

Magnetostriction can be defined as the change in the material dimensions accompanying a change in the magnetic field. Two kinds of magnetostriction occur in magnetic materials: volume and linear magnetostriction.

The linear magnetostriction, λ, is a function of the magnetisation state of the sample. It reaches a maximum at magnetic saturation. λ is the result of moment rotation and 90° domain wall motions.

The saturation magnetostriction, λ_s, is the fractional change in the length between the demagnetised state of the material and its magnetically saturated state. Typical values of λ_s for amorphous alloys vary between -10×10^6 and 40×10^6 (Hernando *et al* [1988]).

The engineering magnetostriction, λ_e, is the strain difference before and after the application of a field. λ_e is defined as

$$\lambda_e = \frac{3}{2}\lambda_s(\cos^2\theta_f - \cos^2\theta_i) \qquad (1.9)$$

where θ_f is the final angle between the moments and H, and θ_i is the initial angle.

1.3.2 Damping

For an oscillating material, the damping can be defined as the ratio of the energy loss per oscillation, ΔU, to the energy at maximum amplitude during one oscillation. It is denoted by Q^{-1}, so

$$Q^{-1} = \frac{\Delta U}{U}, \tag{1.10}$$

where $U=\sigma^2/2E$, σ is the applied stress and E is Young's modulus.

Magnetic damping can be explained by the superposition of three mechanisms: macroeddy currents, microeddy currents and magnetomechanical hysteresis. Eddy current losses are a function of the oscillation frequency and are independent of the oscillation amplitude. Therefore, eddy current losses are high at high frequencies. Magnetomechanical hysteresis loss is independent of the oscillation frequency and depends on the oscillation amplitude. Magnetomechanical hysteresis is basically due to the irreversible motion of 90° domain walls (Bozorth [1951]).

1.3.3 ΔE and ΔG Effects

Magnetic moment rotation and elastic deformation can be coupled by magnetostriction to produce magnetomechanical effects such as the ΔE or ΔG effects (where E is Young's modulus and G is the shear modulus). The ΔE and ΔG effects are related, because E is related to G by

$$E = 2(1+t)G \tag{1.11}$$

where t is Poisson's ratio. The ΔE effect is the magnetic field dependence of the Young's modulus due to the magnetostriction. E is defined as the ratio of the stress to the strain. The ΔE effect is a ramification of the property that a change of stress in a material occurs when it is magnetised. When a stress is applied to a magnetic material, two kinds of strain are produced: magnetoelastic strain, ε_H, and mechanical elastic strain, ε_s. The modulus is given by:

$$E = \frac{\sigma}{\varepsilon_s + \varepsilon_H} \tag{1.12}$$

For a saturated sample, the magnetoelastic strain is zero, because no moment rotation can occur, so:

$$E_s = \frac{\sigma}{\varepsilon_s} \tag{1.13}$$

From equations 1.12 and 1.13, the magnitude of the ΔE effect is defined by:

$$\frac{\Delta E}{E} = \frac{E_s - E}{E} = \frac{\varepsilon_H}{\varepsilon_s} \tag{1.14}$$

where E_s is the modulus at saturation. The ΔE effect in amorphous alloys is much greater than that in crystalline materials due to the lack of crystalline anisotropy in amorphous alloys.

The magnetic field annealing has a large effect on the ΔE effect. Figure 1.3 shows the effect of the annealing angle on the field dependence of Young's modulus.

The magnetoelastic coupling constant, k, is a factor which is determined by the fractional conversion of the elastic energy into magnetic energy (O'Dell [1982]). It is given as a function of Young's modulus:

$$k^2 = 1 - \frac{E}{E_s} \tag{1.15}$$

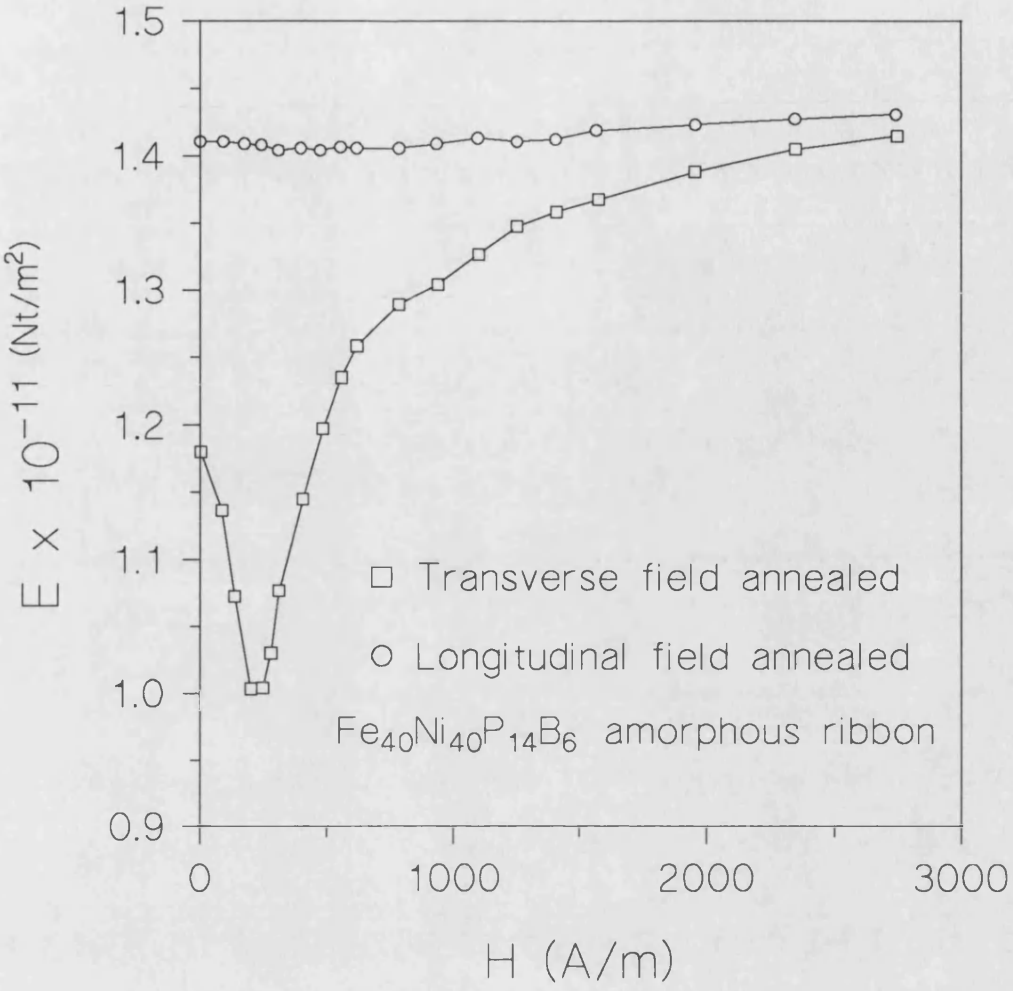

Figure 1.3: Young's modulus of field annealed amorphous $Fe_{40}Ni_{40}P_{14}B_6$ ribbons as a function of applied field (after Moorjani [1984]).

1.4 Amorphous Alloys

Amorphous alloys, also called metallic glasses, were first produced in 1960 by Duwez. Different methods were developed to produce amorphous alloys, such as vacuum evaporation, ion implantation, cathode sputtering and melt-spinning. It has been found that the properties of the amorphous alloys are greatly influenced by the conditions and methods of production. The most commonly used production method is melt-spinning.

In this technique, a jet of molten metal is ejected onto the outer surface of a wheel to form amorphous alloy in a ribbon shape (Bigot 1985). The ribbons produced are usually 1-100 mm wide and 25-50 μm thick, with lengths from a few metres up to several kilometres in a single run of the system (Overshott [1987]).

Amorphous alloys are produced by quenching liquid alloys at rates of 10^5-10^6 K/s so as to pass crystallisation and retain the supercooled liquid in the solid state. This structure can be simply characterised by lack of the atomic periodicity beyond a few atomic distances (O'Handley [1987]). The lack of the atomic periodicity in long range was also confirmed by X-ray diffraction studies (Grazyk [1978]).

Amorphous alloys in wire form became available in 1981. Wires were first produced by Masumoto *et al* [1981] using the in-rotating-water melt spinning method.

Amorphous alloys are generally composed of about 80% transition metals Fe, Co or Ni and 20% metalloid elements like C, B, P or Si. This gives a large number of alloys with different compositions, leading to various values of M_s, λ_s, K_u, Curie and crystallisation temperatures and resistivity (Hernando *et al* [1988]).

As a result of their amorphous structure, metallic glasses have low coercivity, and magnetic losses, high susceptibility and low anisotropy. The coercivity can be as low as a few A/m, the maximum susceptibility is of the order of 10^5 and a typical saturation induction is about 1 Tesla. Amorphous alloys are very strong materials. At room temperature the typical elongation reaches up to 2% under the stress. They show high fracture toughness (Anantharaman [1985]).

As-cast amorphous alloys have a large casting stress induced during the quenching process. The properties desired for these materials can be obtained by relieving the

casting stress by different heat treatments such as furnace and current annealing.

1.5 Applications

The applications of amorphous alloys are based on inductance changes in a coil having an amorphous alloy as the core. In other words, the effect of the magnetic fields or applied stresses in determining the susceptibility of the amorphous alloys makes them useful materials for sensor applications. Such effects are directly related to the amorphous structure, magnetostriction and atomic mobility. These allow magnetic anisotropy to be induced by thermal treatments under the effect of applied field or stress to obtain the desired magnetomechanical properties (Luborsky *et al* [1975]).

Amorphous alloys sensors can be classified into two groups: a) sensors using low magnetostrictive alloys, such as magnetic field, displacement and current sensors, b) sensors using high magnetostrictive materials, such as transducers, force, tension, stress, torsion and pressure sensors. A wide range of force, field, pressure etc. sensors and application areas have been given by Hernando *et al* [1988], Mohri [1984a] and Gibbs and Squire [1989]. For example, Squire and Gibbs [1987] and Kilby and Squire [1992] used the ΔE effect to relate the magnetic field to the velocity of shear waves in Fe-based amorphous ribbons. The typical properties and application areas for amorphous alloys are given in table 1.1.

Effect	Explanation	Technical Use
Magnetostriction	Change in the shape of the material with magnetisation	In combination with piezo-electric elements for magnetometers and potentiometers
ΔE Effect	Change in Young's modulus with magnetisation	Acoustic delay line components for magnetic field measurements
Magnetoresistance	Change in resistance with magnetisation	Magnetoresistive sensors
Wiedemann effect	A torsion is produced in a current carrying rod when subjected to a longitudinal field	Torque and force measurements
Matteucci effect	Torsion of rod in a longitudinal field changes magnetisation	Magnetoelastic sensors
Sixtus-Tonks effect (Domain wall propagation)	Pulse magnetisation by large Barkhausen effect	Pulse sensors

Table 1.1: Magnetic effects for sensor applications (after Boll [1989]).

2 An Introduction to Amorphous Wires

2.1 Introduction

Amorphous wires of various alloy compositions produced to date have been reported to exhibit high mechanical strengths (Hagiwara *et al* [1982a]) and high resistance (Inoue *et al* [1982]) which are at the same levels as those for the ribbon material. Additionally, amorphous wires have been found to show some unique magnetic properties, which are different from the ribbon materials, owing to a different domain structure caused by a different solidification process and speed (Chen *et al* [1984]).

This chapter will give a brief history of amorphous wires. Some of the magnetic and mechanical properties and the effect of stress and heat treatments on the properties of the wires will be discussed. Also, some of applications for the wires will be given very briefly.

2.2 Production of Amorphous Wires

Amorphous alloys were first produced in ribbon form by the melt-spinning method in 1960 (Duwez [1967]). In 1980, Masumoto *et al* [1981] succeeded for the first time in producing amorphous wires by the "in-rotating-water melt spinning technique". In this technique, cooling rates of $5 \times 10^5 - 1 \times 10^6$ K/s are obtained for Fe-Si-B wire (Hagiwara *et al* [1982b]). Figure 2.1 shows a schematic illustration of the production system. In the production process, the alloy is first melted in an electric furnace before being ejected, by high argon pressure through a ruby nozzle, which is at the end of the quartz tube. The melted alloy is rapidly solidified by cooling water which is rotating at high speed, and

a continuous wire is formed. This wire is collected by centrifugal force in the inner side of the drum. Typically, the amount of alloy melted in one run is about 1g. The maximum length of wire fabricated in one ejection operation can be as long as several kilometres. Additionally, by changing the inner diameter of the ruby nozzle, wires are produced with various diameters in the range 80 to 250μm (Masumoto *et al* [1981] and Ogasawara *et al* [1990]). The variation in the wire diameter is about 10% for wire approximately 150μm in diameter and tends to decrease with decreasing diameter (Inoue *et al* [1982]). Therefore, wire produced by this technique possesses a good uniformity of shape. The maximum diameter for the formation of the amorphous wire depends on the composition of the wire. Inoue *et al* [1982] showed that the maximum diameter for Fe-P-C amorphous wire is about 230μm and the probability of forming amorphous structure tends to decrease with increasing or decreasing phosphorus and carbon contents, because the change in the carbon or phosphorus content causes a remarkable increase in the viscosity of the molten alloy.

Inoue *et al* [1982] and [1987] have reported that during the production process of wires, some quenching parameters affect formation of the wire. The typical quenching parameters are: a) the distance from the surface of the water to the end of the quartz tube, b) the nozzle size, c) the ejection pressure, d) the temperature of the molten alloy, e) the temperature of the cooling water, f) the ratio of the water velocity to the drum velocity.

The diameter of a wire can be reduced by cold-drawing or warm-drawing. With cold-drawing, the diameter of the wire can be reduced from 150μm to 50μm after multiple drawing process. Hagiwara *et al* [1982a] and Chen *et al* [1984] have found that the application of cold-drawing to wires results in an increase in the homogeneity of the wire shape, the tensile fracture strength and the fracture elongation. Wires are so ductile that no cracks have been observed on the surface of cold-drawn wires. However,

cold-drawing has been found to decrease the Young's modulus (Chen *et al* [1984]). The process also leads to changes in the magnetic properties of the wire due to the internal stress induced during drawing.

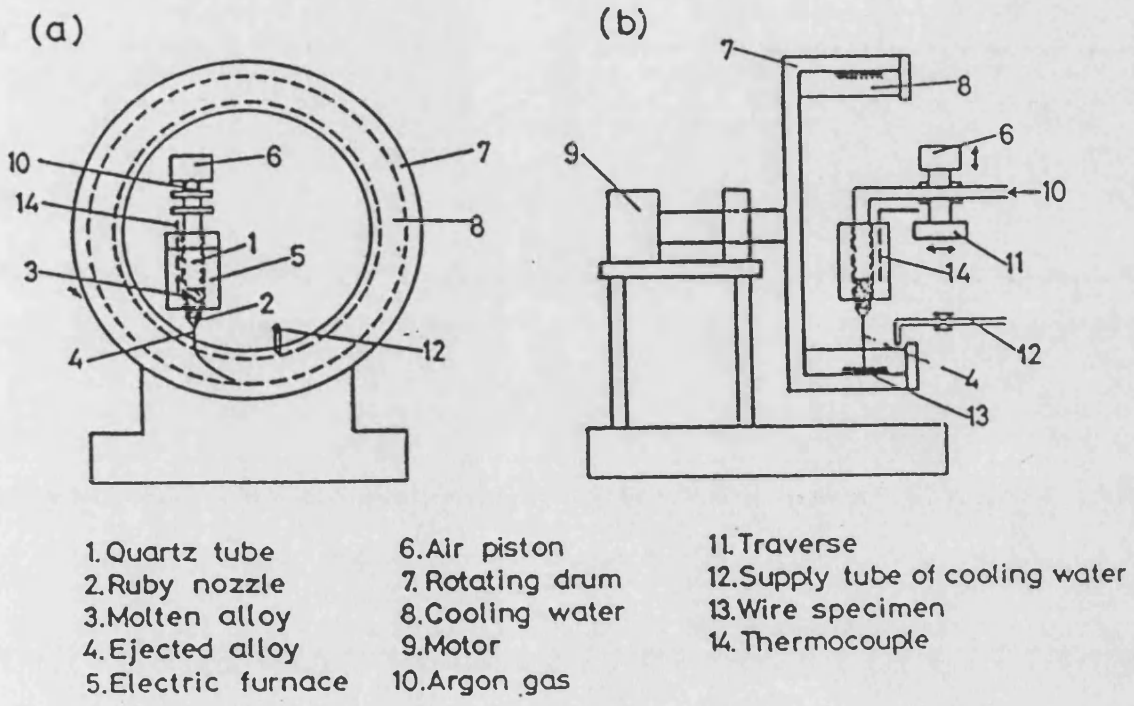

1. Quartz tube
2. Ruby nozzle
3. Molten alloy
4. Ejected alloy
5. Electric furnace
6. Air piston
7. Rotating drum
8. Cooling water
9. Motor
10. Argon gas
11. Traverse
12. Supply tube of cooling water
13. Wire specimen
14. Thermocouple

Figure 2.1: The quenching apparatus for the production of amorphous wire, a) front view, b) side view (reproduced from Masumoto *et al* [1981]).

The disadvantages caused by the cold-drawing can be reduced by warm-drawing. Figure 2.2 shows the apparatus and the method for the warm-drawing of the amorphous wires. In this method, the wires can be drawn at various temperatures and then immediately cooled by water (Inoue *et al* [1986]). The drawing velocity is about 0.25m s^{-1}. Wires can be drawn so that the cross-section of the area is reduced about 40%. Warm-drawing is

always performed well below the crystallisation temperature; drawing just below the crystallisation temperature leads to fractures in the wire caused by the partial crystallisation.

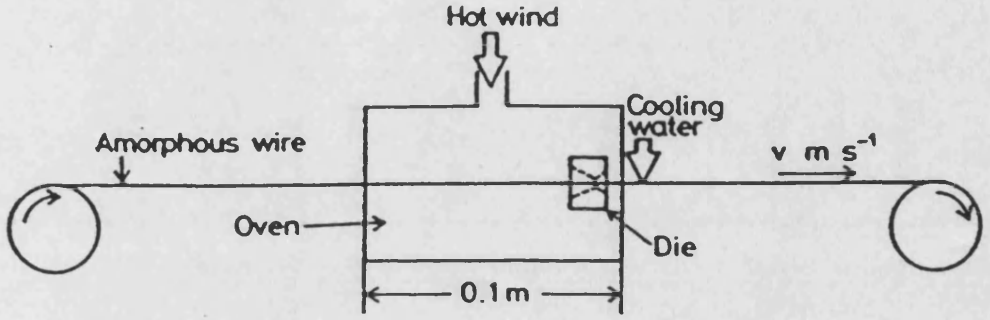

Figure 2.2: Schematic representation of warm-drawing equipment (reproduced from Inoue *et al* [1986]).

2.3 Mechanical Properties

Amorphous wires exhibit high strength and good bending quality. The typical mechanical properties for amorphous wires are shown in table 2.1. Both tensile strength and elongation first increase with cold-drawing; further cold-drawing leads to a decrease in tensile strength and elongation (Hagiwara *et al* [1982b]). The maximum tensile strength value for $Co_{77.5}Si_{12.5}B_{10}$ wire is about 3580MPa which is comparable with the best hard drawn piano wires.

Alloy Composition	σ (MPa)	ε_f (%)	E (GPa)
$Co_{77.5}Si_{12.5}B_{10}$	3580	3.0	-
$Co_{72.5}Si_{12.5}B_{15}$	3450	3.0	123
$Fe_{75}Si_{10}B_{15}$	3410	2.8	119
$Fe_{77.5}P_{12.5}C_{10}$	2790	2.7	104
$(Ni_{0.75}Si_{0.08}B_{0.17})_{99}Al_1$	1730	2.9	115

Table 2.1: The tensile strength, σ, the fracture elongation, ε_f, and Young's modulus of un-drawn amorphous wires (after Hagiwara *et al* [1982b] and Inoue *et al* [1987]).

Chen *et al* [1984] reported that with increasing Fe-Si-B wire diameter from 80μm to 210μm, Young's modulus at saturation, E_s, increases from 165GPa to 175GPa and also that Young's modulus at zero applied field, E_o, increases. However, the ΔE effect ($\Delta E=(E_s-E_o)/E_o$) decreases from 6% to 1%. Chen suggested that the increment in E_s is due to an increase in the degree of structural ordering as a result of a slower cooling rate. The decrease in the ΔE effect is due to the reduction in the areas of 90° magnetic domain walls and maze type domains. Cold-drawing leads to a monotonic decrease in the E_s value of Fe-Si-B wire from 175GPa to 165GPa. The decrease in E_s is due to the increase in structural disorder.

2.4 Internal Stress and Anisotropy Distributions in As-cast Amorphous Wires

The different magnetic behaviours of the as-cast amorphous ribbon and of the wire with

the same composition can be explained by their different internal stress distributions induced during the solidification processes. For ribbons produced by melt spinning, there will be a temperature gradient from the wheel surface to the outer surface of the ribbon. Therefore, the internal stresses are distributed randomly in the transverse and longitudinal directions of the ribbon. In the case of amorphous wires produced by the in-rotating-water melt spinning technique, when the molten alloy hits the water first the outer shell solidifies, then the inner core solidifies and shrinks. Figure 2.3 shows a schematic view of the wire during quenching. As a result of this cooling process, a radial tension is created in the outer shell and an axial tensile stress is created in the inner core. Mitra and Vazquez [1990a] suggested that the internal axial stress induced by the temperature gradient in the inner core is very small. The main cause of the internal stress in the axial direction in the inner core is due to the shrinking in this volume of the wire. The proposed internal stress distributions for Fe-based and Co-based amorphous wires are given in figure 2.4.

As a result of these stress distributions, an axial anisotropy is created at the inner core of the positively magnetostrictive wire and an azimuthal anisotropy is created in a negatively magnetostrictive wire [Mitra and Vazquez [1990a]). Also, the radial tensile stress creates a strong radial anisotropy in the outer shell of the wire with positive magnetostriction and a circumferential anisotropy distribution for a negative magnetostrictive wire.

The internal stress distribution in as-cast wires has been studied by Liu *et al* [1990], Madurga and Hernando [1990] and Velazquez *et al* [1991]. Madurga and Hernando suggested that the solidification process occurs according to the following conditions:

1) During solidification, the cylindrical shape of the molten alloy is conserved.

2) The heat transfer from the molten alloy to the water is along the radial direction.

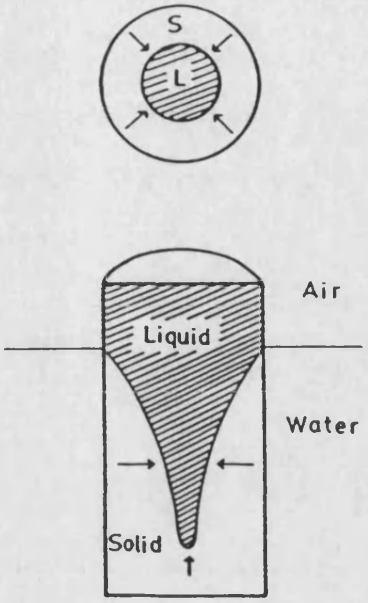

Figure 2.3: Schematic view of the lateral and transverse cross-section of the amorphous wire during solidification (reproduced from Mitra and Vazquez [1990a]).

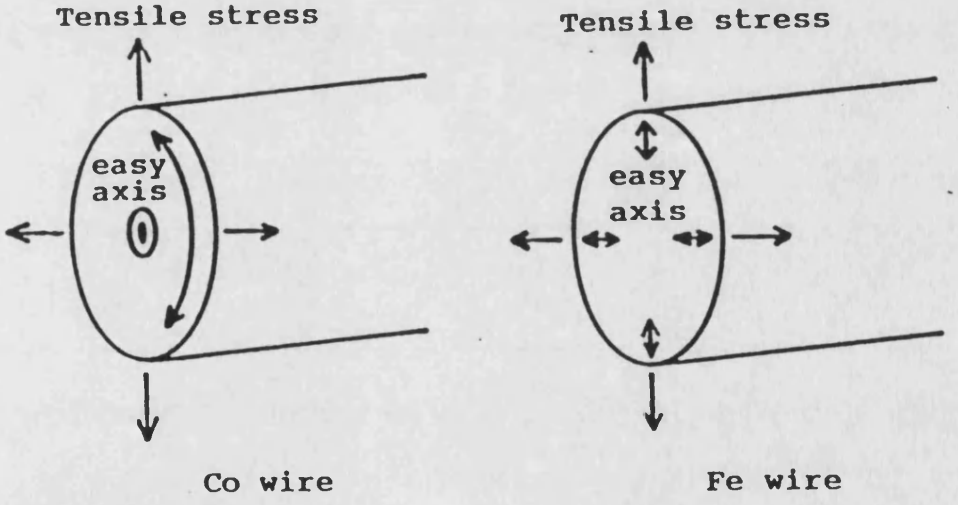

Figure 2.4: Internal stress distribution and easy axis of magnetisation of Fe-based and Co-based wires (reproduced from Yamasaki [1990]).

3) The outer shell solidifies first and solidification propagates with cylindrical symmetry towards to the inner core.

4) The source of the internal stress is the non-simultaneous solidification of the different shells.

Their mathematical model showed that the tensile stress distribution along the radial direction of the wire has a peak around 0.7R (where R is the radius of the wire). This can be related to the magnetic remanence, M_r, in the wire, which is around $(0.7)^2 M_s$.

Velazquez *et al* [1991] used the classical theory of elasticity to explain the internal stress, and therefore the anisotropy distribution in as-cast wire. They calculated different stress components by considering the wire as a series of thin tubular shells with solidification starting at the outer shell and propagating towards the inner core. The expressions for the induced internal stresses are:

$$\sigma_r(x,\varepsilon) = \left(\frac{kE}{1-t}\right)\left(\frac{1}{x^2}\right)$$

$$\left\{\left(\frac{x^2-\varepsilon^2}{1-\varepsilon^2}\right)\int_\varepsilon^1 xT(x)dx - \int_\varepsilon^x xT(x)dx\right\} \qquad (2.1)$$

$$\sigma_\phi(x,\varepsilon) = \left(\frac{kE}{1-t}\right)\left(\frac{1}{x^2}\right)$$

$$\left\{\left(\frac{x^2+\varepsilon^2}{1-\varepsilon^2}\right)\int_\varepsilon^1 xT(x)dx + \int_\varepsilon^x xT(x)dx - x^2T(x)\right\} \qquad (2.2)$$

$$\sigma_z(x,\varepsilon) = \left(\frac{kE}{1-t}\right)\left\{\left(\frac{2}{1-\varepsilon^2}\right)\int_\varepsilon^1 xT(x)dx - T(x)\right\} \qquad (2.3)$$

where σ_r is the stress in the radial direction, σ_ϕ is the azimuthal stress, σ_z is the axial stress, T(x) is the temperature of the point x (x=r/R, where R is the radius of the wire

and r is the cylindrical coordinate), ε is the reduced radius, E is the Young's modulus, k is the dilation coefficient and t is the Poisson's ratio. They also assumed that the temperature along the radial direction varies according to:

$$T(x) = T_2 + ((T_1 - T_2)(\log x / \log \varepsilon)) \qquad (2.4)$$

Integration of the equations 2.1, 2.2 and 2.3 gives the stresses in the radial, azimuthal and axial directions.

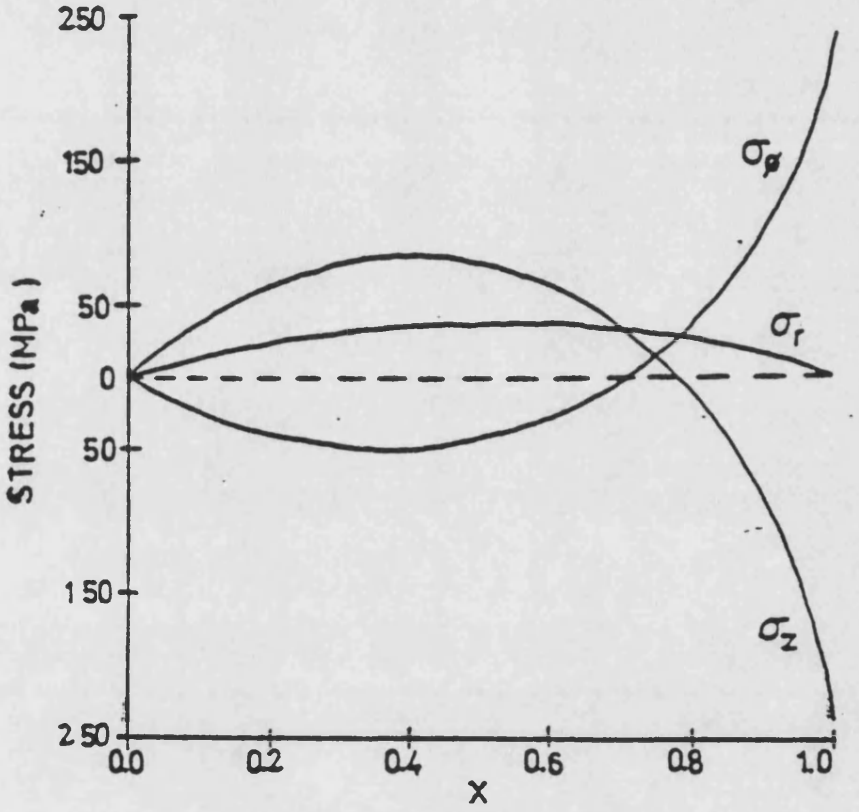

Figure 2.5: Radial, azimuthal and axial stress distributions (reproduced from Velazquez *et al* [1991]).

Figure 2.5 shows the internal stress distributions obtained from equations 2.1, 2.2 and 2.3. Typical values for amorphous wire are T_1=1400K, T_2=300K, E=100GPa, t=0.33

and $k=4\times10^{-8}$ K^{-1}. The magnitude of the internal stress is determined by $kE/(1-t)$ multiplied by the average temperature during the solidification process. This gives us an order of magnitude of 100MPa as a maximum stress. Yamasaki [1990] model only gives the internal stress direction. Velazquez *et al* [1991] is very simple model and the model cannot explain the existence of inner core and outer shell in as-cast wire. But this model give the approximately internal stress values and stress distributions in different directions.

2.5 Magnetic Properties

2.5.1 Large Barkhausen Jump

The most striking difference in the magnetic behaviour of the amorphous wires from that of ribbons is observed at low magnetic field. An unmagnetised magnetostrictive amorphous wire is magnetised only when the applied field exceeds a critical field, H_n, and magnetisation occurs through the Large Barkhausen Jump (LBJ) (Mitra *et al* [1992]). The LBJ occurs due to the movement of a single domain wall throughout the inner core of the wire so that the direction of magnetisation is reversed in the inner core (Yamasaki *et al* [1988]). The typical hysteresis loops are shown in figure 2.6.

The critical field is determined by the domain wall energy and H_n is given by:

$$H_n \propto \sqrt{\lambda_s/M_s} \qquad (2.5)$$

Amorphous wires with zero magnetostriction or with very small magnetostriction ($\lambda_s \leq 5\times10^{-6}$) do not show the LBJ. This behaviour is considered to be associated with the decrease in the wall energy due to the decrease in λ_s (equation 2.5), giving rise to a decrease in the magnetic field, H_n, forming the reverse magnetic domains (Yamasaki *et al* [1985]). H_n can be controlled by heat treatments, twisting (Kawamura [1988]) and

etching. Mohri *et al* [1984] reduced the diameter of the $Fe_{81}Si_4B_{14}C_1$ amorphous wires from 128μm to 120μm by etching. At this diameter, H_n slightly decreased. The LBJ disappeared when the diameter was smaller than 100μm. This shows that the stress distribution in the outer shell of the wire applies a stress to the magnetically soft inner core. Additionally, annealing of the amorphous wires leads to disappearance of the LBJ due to the relief of the internal stresses.

The length of the wire also plays an important role. When the length of a 125μm-diameter Fe-Si-B wire is smaller than 6cm, the LBJ does not occur because of the demagnetisation effect. This length limitation can be overcome by cold-drawing the wire. But the cold-drawn wires do not initially exhibit the LBJ. Therefore, the cold-drawn wires are usually annealed under the effect of tensile stress and an axial magnetic field to create the inner core. After annealing treatments, the cold-drawn Fe-based wire with a diameter of 50μm and 2cm length shows the typical square M-H loop and exhibits the LBJ.

Domain wall propagation in the inner core of the wire has been studied by Mohri *et al* [1984], Kawamura *et al* [1988], Gibbs *et al* [1992], Malmhall *et al* [1987] and many others. The domain wall propagation systems are based on the classic Sixtus and Tonks method. In this method, the wire is usually placed inside a fine glass tube and two pick-up coils are wound around the wire. A large coil is provided to apply a driving magnetic field along the entire length of the wire. Additionally, an exciting coil is placed at one end of the wire to nucleate the domain wall. When a domain wall is nucleated, it propagates along the length of the wire. This leads to voltage pulses in each pick-up coil. From the separation, x, of the coils and the time of flight, t, the velocity of the wall can be calculated using the basic equation "V_w=x.t". Figure 2.7 shows the domain wall

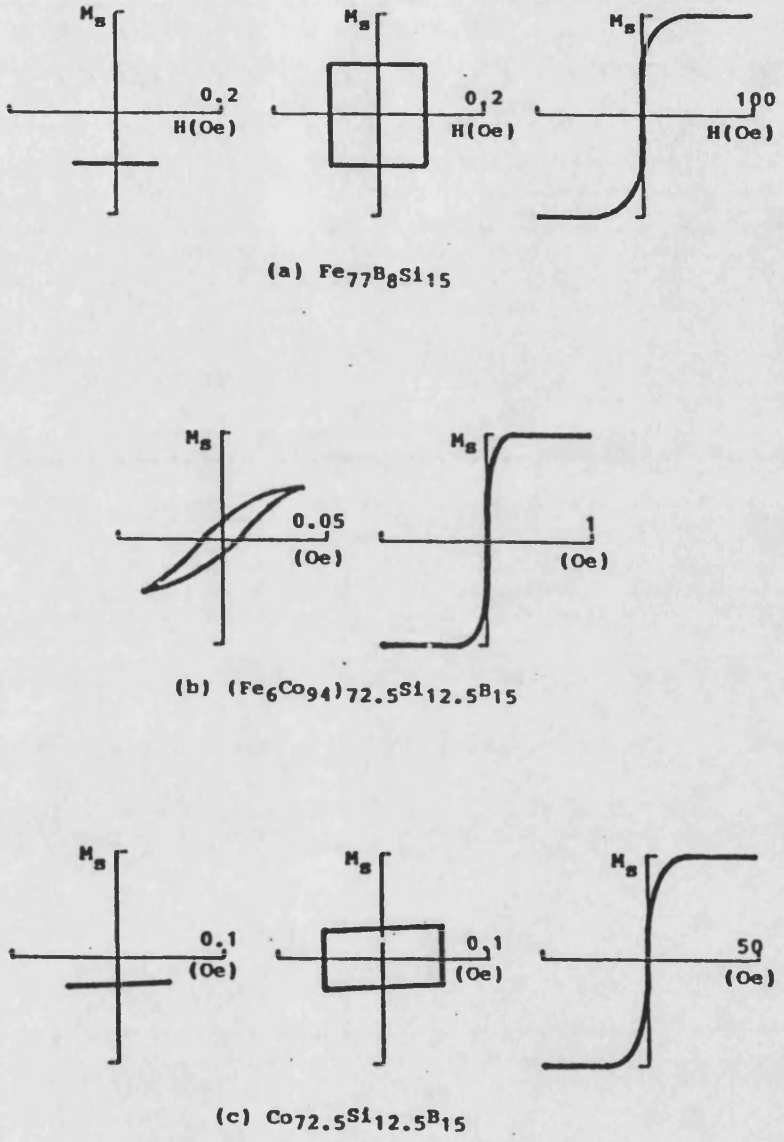

Figure 2.6: Hysteresis loops of amorphous wires measured at 60Hz a) $Fe_{77}B_8Si_{15}$ wire with positive magnetostriction b) $(Fe_6Co_{94})_{72.5}Si_{12.5}B_{15}$ wire with zero magnetostriction c) $Co_{72.5}Si_{12.5}B_{15}$ with negative magnetostriction (reproduced from Yamasaki *et al* [1988]).

propagation velocity as a function of driving field. The domain wall velocity increases linearly with increasing driving field and is given by:

$$V_w = 2M_s(H - H_n)/\beta \qquad (2.6)$$

where β is the eddy current damping coefficient. Also, Mohri [1990] proposed that the peak value of the voltage induced into the pick-up coil is proportional to the domain wall velocity, the number of turns on the pick-up coil and the cross-sectional area of the inner core of the wire.

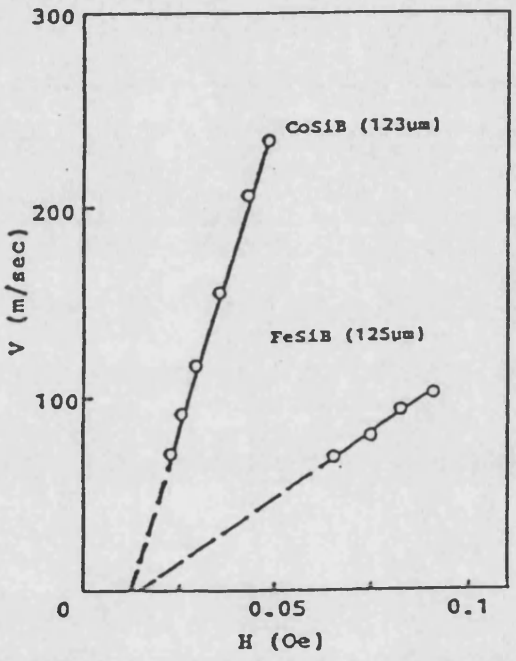

Figure 2.7: Domain wall propagation velocity as a function of driving field for Fe-based and Co-based wires (reproduced from Humphrey [1990]).

2.5.2 Matteucci Effect

The Matteucci effect has been known since 1847. When an AC magnetic field is applied to a ferromagnetic wire in a direction parallel to the wire axis, a pulse voltage will be

generated between the ends of the wire. This voltage is defined as a Matteucci voltage, e_p, and is expressed in the following equation as:

$$e_p = c\frac{d\phi}{dt} \qquad (2.7)$$

where ϕ is a circular flux in the sample and is the result of $\nabla \mathbf{E} = -\partial \mathbf{B}/\partial t$. Therefore, any change in the magnetisation leads to a Matteucci voltage (Kimura *et al* [1991]). One of the advantages of the Matteucci effect is that a magnetic device can be set up without any pick-up coils (Mohri [1990]).

Figure 2.8 shows a pulse generation element using Co-based amorphous wire to which an AC voltage is applied. A sharp voltage pulse is obtained through a high pass filter which eliminates a sinusoidal voltage component due to the resistance of the wire.

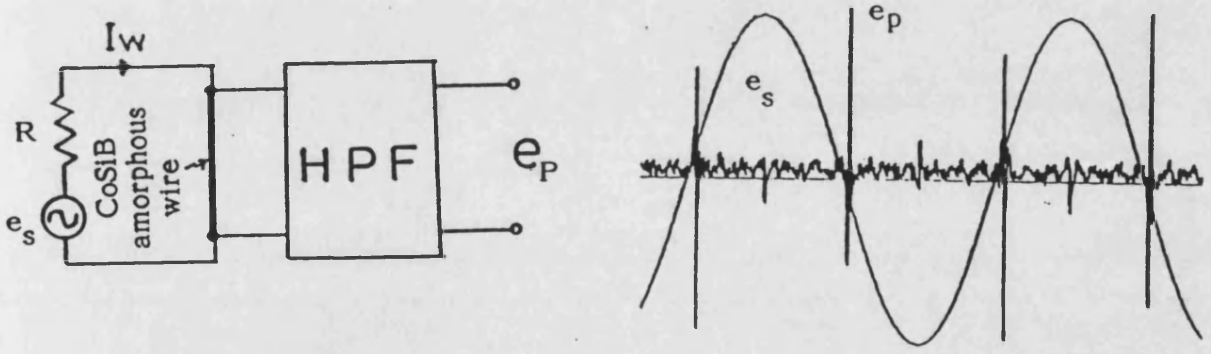

Figure 2.8: Matteucci effect in Co-based wire (reproduced from Mohri [1990]).

The Matteucci voltage is a result of the helical magnetisation component in the wire. Kinoshita [1990] proposed that the magnetic moments in the inner core of an amorphous wire do not really align in the wire axis direction. According to Kinoshita, the easy axis

direction in the inner core of the wire is between 40° and 60° to the wire axis direction. Mohri [1985] showed that e_p is a function of the AC field frequency and of twisting. When the wire is twisted e_p is greatly changed, e.g. for $Fe_{77.5}Si_{7.5}B_{15}$ amorphous wire with a diameter of 125μm, e_p is increased from 2mV to 40mV by twisting the wire 0.1 turn/cm. This improvement is due to the increase of the easy axis angle of magnetisation with respect to the wire axis in the inner core of the wire.

2.5.3 Domain Studies

Domain observations of amorphous wires have been performed by Mohri *et al* [1985], Wun-Fogle *et al* [1989a] and Makino *et al* [1989] by the Bitter method. The domain pictures only give information about domains on the surface of the wires. Co-based wires have bamboo-like straight walls and Fe-based wires have maze domain configurations. Therefore, it was postulated that Co-based wires have magnetisation components in the circumferential direction in the outer shell. From the maze domain configuration on the surface of Fe-based wires, it was suggested that the magnetisation components are perpendicular to the wire surface in the outer shell. Mohri *et al* [1985] observed that neither wire change their surface domain configuration before and after LBJ, so the wires must have a magnetisation component in the wire axis direction in the inner core. As a result, a core-sheath domain model was proposed as shown in figure 2.9.

Mohri *et al* [1985] also observed that all the zigzag maze domains do not align transversely to the wire axis; in fact some of them align in angles ±40°-70° with respect to wire axis. This shows that as-cast wire is not uniform along the length and that random twisting stresses exist which are induced during the solidification process.

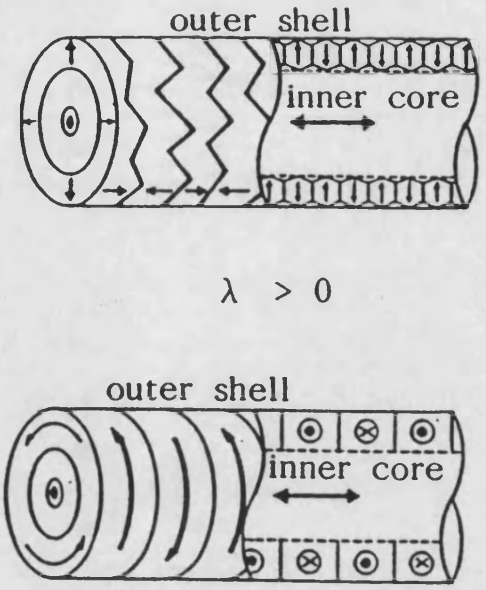

Figure 2.9: Suggested domain structure for Fe-based wire ($\lambda>0$) and Co-based wire ($\lambda<0$) (reproduced from Mohri [1990]).

The suggested domain structures in figure 2.9 for as-cast wire do not show any helical component, but the observed Matteucci effect indicates that there must be a helical magnetisation component in the wire. Although the proposed domain model can explain the LBJ and observed domain pictures, it is far from explaining fully the magnetic properties of as-cast wires.

The inner core diameter was calculated by Madurga *et al* [1990a] by assuming that the ratio of the remanent magnetisation to the saturation magnetisation is equal to the ratio of the cross-sectional area of the inner core to the total cross-sectional area. For as-cast $Fe_{77.5}Si_{7.5}B_{15}$ wire this ratio is 0.5, which gives the radius of the inner core ~0.7 times the wire radius.

Wun-Fogle *et al* [1989a] and Letcher *et al* [1991] studied the domain structure of transversely field annealed $Fe_{77.5}Si_{7.5}B_{15}$ wire. The wire was annealed at 475°C in a magnetic field of 624 kA/m directed normal to the wire axis. Straight lines perpendicular to the wire axis were observed on the polished surface of the annealed wire. The typical spacing between the lines is ~7-10μm. Also, some maze domains were observed and the M-H loops of field annealed wires show Barkhausen Jumps at low field. This indicates that there are still residual stresses and that the anisotropy induced by field annealing is not high enough to create an easy axis in radial direction. From the domain pictures and observed Barkhausen Jump, Savage [1990] proposed a domain structure for field annealed wire (figure 2.10). According to this domain structure, the outer shell has transverse domains and the inner core has longitudinal domains.

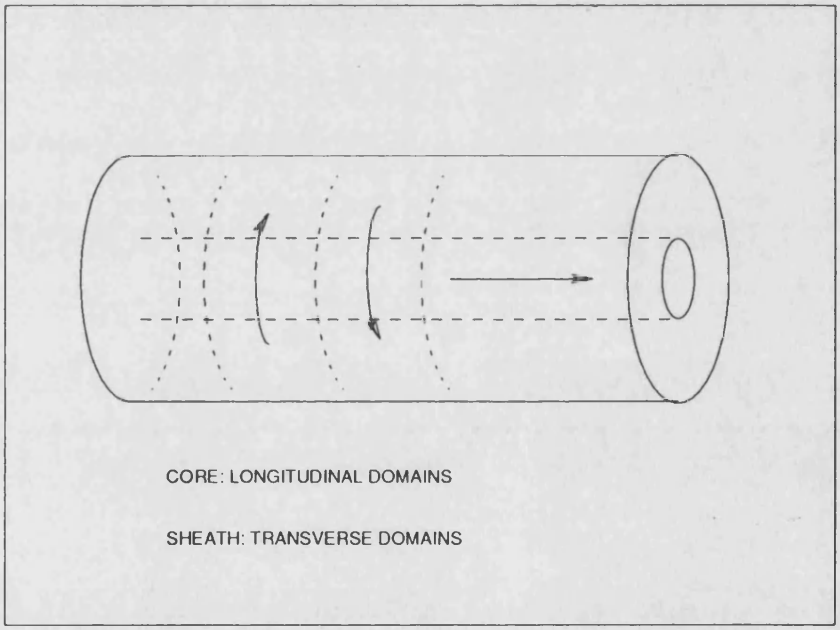

Figure 2.10: Model for domain structure in transverse field annealed Fe-based amorphous wire (after Savage [1990]).

2.5.4 Some Other Magnetic Properties

One of the main advantages of amorphous wires is that the magnetic properties vary considerably and smoothly with the composition and the annealing history of the wire. Therefore, it is possible to tailor the magnetic behaviour to that required for a particular application. Table 2.2 gives some of the magnetic parameters for as-cast amorphous wires.

Composition	M_s (T)	M_r/M_s	K (Jm^{-3})	λ_s ($\times 10^{-6}$	σ_i (MPa)
$Fe_{72.5}Si_{12.5}B_{15}$	1.30	0.498	2200	25	60
$(Fe_{0.60}Co_{0.40})_{72.5}Si_{12.5}B_{15}$	1.18	0.476	1700	16	73
$(Fe_{0.20}Co_{0.80})_{72.5}Si_{12.5}B_{15}$	0.79	0.496	580	5	80
$Co_{72.5}Si_{12.5}B_{15}$	0.64	0.313	240	-3	54
$Fe_{78}Si_9B_{13}$	1.45	0.456	3100	35	60
$Fe_{77}Cr_1Si_9B_{13}$	1.51	0.448	2000	32	43
$Fe_{88}Cr_{10}Si_9B_{13}$	0.82	0.469	720	8	61
$Fe_{75}Si_{10}B_{15}$	1.43	0.431	3700	32	78
$(Fe_{0.98}Ni_{0.02})_{75}Si_{10}B_{15}$	1.42	0.455	4000	30	91
$(Fe_{0.88}Ni_{0.12})_{75}Si_{10}B_{15}$	1.17	0.450	2300	24	65

Table 2.2: Magnetic properties of amorphous as-cast wires (reproduced from Mohri [1990]).

The M-H loops of Fe-based wires vary greatly with applied magnetic field and sample length. As the length of the wire decreases below 6cm, inverse domains form at the ends of the wire leading to variation in the domain structure and H_c with the sample length. H_c reaches a stable state after a critical length (Ogasawara [1987]). Cold-drawing leads to huge increases in H_c and anisotropy constant, K, values, because cold-drawing introduces a considerable irregular internal stresses (Manabe *et al* [1988]). Mitra *et al* [1992] found that the behaviour of H_c is mainly determined by the relative influence of the internal and external stresses. At low external stresses, H_c is determined by internal stress but, when the external stress becomes much bigger than internal stress, H_c increases linearly with increasing external stress. It has also been reported that twisting of the wire causes an increase in the H_c value for Fe-based wires (Sushita *et al* [1985]).

Kinoshita *et al* [1986] and Malmhall *et al* [1987] studied the effect of the external stresses on the M_r/M_s. They found that with applied tensile stress, the M_r value of $Fe_{77.5}Si_{7.5}B_{15}$ wire increases and reaches M_s after a critical tensile stress value of ~400MPa. At zero applied stress M_r/M_s is about 0.5, M_r decreases with applied compressive stress, becoming zero when the applied compressive stress is about 60MPa.

Susceptibility measurements on amorphous wires were reported by Mitra *et al* [1990a]. The effect of tensile stress on the normalised inverse AC susceptibility, χ_r/χ_σ, (where χ_σ is the susceptibility at remanence at applied stress, σ, and χ_r is the susceptibility at remanence at zero stress) was studied. χ_r/χ_σ decreases at lower stress values. When the applied stress is about 275-300MPa, χ_r/χ_σ starts to increase rapidly for Fe-Si-B and Fe-Co-Cr-Si-B wires. The sudden increase in susceptibility is due to the increase in the axial anisotropy and the reduction of the perpendicular anisotropy. After a critical stress value the remanent magnetisation reaches the saturation magnetisation value and then the susceptibility starts to decrease with increasing applied stress. In the case of non-magnetostrictive Fe-Co-Nb-Si-B wire, χ_r/χ_σ decreases with increasing stress.

Heat treatments on the amorphous wires are found to be effective above 350°C. Below this temperature, the internal structural relaxation has almost no influence on the magnetic properties. Even after six months annealing at 200°C no change was observed in the magnetic properties (Ogasawara [1987]). Konno and Mohri [1989] studied the effect of annealing on the induced anisotropy, K_u, by stress for $Fe_{77.5}Si_{7.5}B_{15}$ wire. They reported that annealing leads to a large variation in the K_u value. When the wire is annealed at 400°C, the K_u value firstly starts to decrease from 3000 Jm^{-3} and it reaches a minimum of 1000 Jm^{-3} after annealing for 5 hours at this temperature. Further annealing increases the K_u due to partial crystallisation.

The current annealing dependence of magnetic parameters such as H_c and M_r has been studied by Gonzalez et al [1991]. Current annealing first gives rise to a gradual relaxation of the internal stress, as can be deduced from the decrease in H_c and increase in M_r. When a magnetic material is current annealed a helical anisotropy is induced into the material, depending on the current intensity and material properties. Gonzalez proposed that a very short current anneal does not induce any helical anisotropy into $Fe_{77.5}Si_{7.5}B_{15}$ as-cast wire. When the wire was pre-annealed, it was observed that a helical anisotropy was induced from the beginning of the current annealing. Annealing of 125μm diameter $Fe_{77.5}Si_{7.5}B_{15}$ wire with a 550mA current for 1 minute leads to complete stress relief. Further annealing induces a helical anisotropy of ~50 Jm^{-3}. Moreover, for a longer annealing time the helical anisotropy is found to saturate. This temperature behaviour of the induced helical anisotropy can be related to the internal stress in the wire. According to Gonzalez, once the internal stress is relieved the helical anisotropy can be induced easily.

2.6 Magnetostriction

The induced anisotropy of amorphous alloys is mainly magnetoelastic in origin. As a result, the magnetic properties depend very much on the magnetostriction constant. So accurate determination of the magnetostriction constant is important in order to understand magnetic materials. Magnetostriction of ribbon materials has been studied comprehensively. But, because of the shape of the wire it is very difficult to perform the direct measurement of its magnetostriction. The saturation magnetostriction of wires has been measured by Madurga *et al* [1990b], Yamasaki *et al* [1990b] and Mitra and Vazquez [1990b] using small angle magnetisation rotation method (SAMR). In this method, the rotation of the small angle of magnetisation is obtained by application of a small amplitude AC field, H_y, and a high bias field, H_z, perpendicular and parallel to the wire axis, respectively. The bias field must be high enough to saturate the sample. The induced voltage due to the change in the magnetisation is detected by a pick-up coil wound around the wire. The second harmonic of the voltage is given by:

$$V_{2f}^2 = C\frac{H_{ymax}}{H_z + H_k} \tag{2.8}$$

where $H_k = (3\lambda_s\sigma)/(\mu_o M_s)$ is the stress induced anisotropy field, H_{ymax} is the amplitude of the AC field, H_y, and σ is the applied tensile stress. The variation of σ leads to a change in the pick-up coil voltage, V_{ef}, due to the change in H_k. In order to keep V_{ef} constant as a function of σ, H_z is modified. The modified value of H_z directly gives the anisotropy field H_k. Measuring H_k at different tensile stresses, λ_s is obtained from the following equation:

$$\lambda_s = \frac{1}{3}\mu_o M_s\left(\frac{\Delta H_k}{\Delta\sigma}\right) \tag{2.9}$$

Mitra and Vazquez [1990b] measured λ_s for low magnetostriction wire of nominal composition $(Fe_{6.3}Co_{90.7}Nb_1)_{77.5}Si_{7.5}B_{15}$. It is about 2.1×10^{-7} for the as-cast state. The wire was then annealed at 450°C. It was found that λ_s increases with annealing time and reaches a maximum of $8x10^{-7}$ after 30 minutes annealing. With further annealing at this temperature, λ_s decreases. They assumed that the decrease in λ_s is due to the development of microcrystalline structure inside the wire.

Yamasaki *et al* [1990b] measured the compositional variation of λ_s of Fe-Co based amorphous as-cast wires using the SAMR method. λ_s of 32.9×10^{-6} and -2.6×10^{-6} were measured for $Fe_{75}Si_{10}B_{15}$ and $Co_{72.5}Si_{12.5}B_{15}$ wires, respectively. The composition variation of λ_s for $(Fe_{1-x}Co_{1-x})_{75}Si_{10}B_{15}$ was also measured and it was found that λ_s decreases with increasing Co content and becomes zero around x=0.95.

Clark and Wun-Fogle [1989] measured the field dependence of magnetostriction, λ_e, for transverse field annealed $Fe_{77.5}Si_{7.5}B_{15}$ wire. A magnetic field of 624 kA/m was applied during the annealing. λ_e at saturation for the wire field annealed at 450°C is 23×10^{-6} and λ_e for the wire field annealed at 475°C is 28×10^{-6}. Assuming the transverse field annealing was successful and $\lambda_s=(3/2)\lambda_e$, They obtained the $\lambda_s=15 \times 10^{-6}$ and 19×10^{-6} for 450°C and 475°C field annealed wires, respectively, which are considerably lower than the values usually reported.

Konno and Mohri [1989] and Konno *et al* [1990] measured the anisotropy constant and λ_s. A high compressive stress ~40MPa was applied to induce an easy axis in the radial direction of the wire (figure 2.11). As a result, magnetisation occurs only by moment rotation with the applied field parallel to the wire axis.

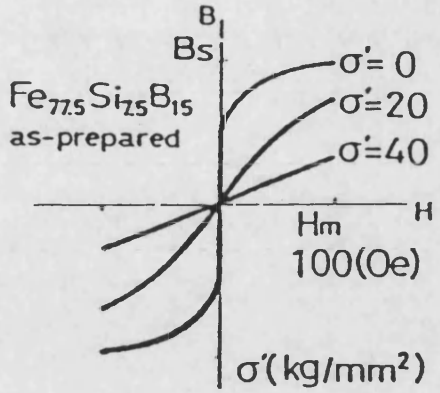

Figure 2.11: Compressive stress dependence of 60Hz hysteresis loops for as-cast $Fe_{77.5}Si_{7.5}B_{15}$ wire (reproduced from Konno and Mohri [1989]).

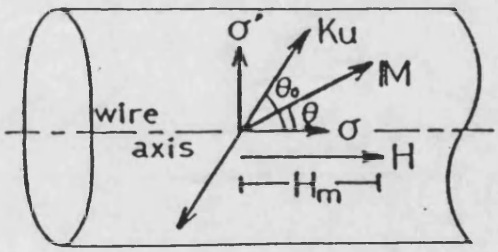

Figure 2.12: Magnetisation rotation model for Fe based amorphous wire under the effect of compressive stress (reproduced from Konno and Mohri [1989]).

Figure 2.12 shows the proposed moment rotation model where M is the magnetisation vector, θ is the angle between the magnetisation and the wire axis, θ_o is the angle between the wire axis and the induced easy axis, σ is the tensile stress and σ' is the compressive stress. θ and θ_o are given by:

$$\theta = \cos^{-1}(B_m/B_s)$$

$$\theta_o = \cos^{-1}(B_r/B_s) \qquad (2.10)$$

at $\sigma=\sigma'=0$. B_r is the remanent flux density, B_s is the saturation flux density and B_m is the maximum flux density in the magnetic field with amplitude H_m. K_u and λ_s are obtained from the minimisation of the total energy. The anisotropy energy is $-K_u\cos^2(\theta_o-\theta)$, the magnetoelastic energy is $-(3/2)\lambda_s\sigma\cos^2\theta$ and $-(3/2)\lambda_s\sigma'\sin^2\theta$ and the magnetisation energy is $-M_sH_m\cos\theta$. K_u is given by:

$$K_u = \frac{M_sH_m\sin\theta}{\sin 2(\theta_o-\theta)} \qquad (2.11)$$

at $\sigma=\sigma'=0$. For negatively magnetostrictive wire,

$$\lambda_s = \frac{K_u\sin 2(\theta_o-\theta) - M_sH_m\sin\theta}{(3/2)\sigma\sin 2\theta} \qquad (2.12)$$

at $\sigma'=0$. For a positively magnetostrictive wire,

$$\lambda_s = \frac{K_u\sin 2(\theta_o-\theta) - M_sH_m\sin\theta}{-(3/2)\sigma'\sin 2\theta} \qquad (2.13)$$

θ and θ_o were calculated from the B_r and B_m values which were obtained from the hysteresis loop. By using equations 2.10, 2.11 and 2.12, λ_s was calculated.

Figure 2.13 shows the calculated λ_s values as a function of annealing time. During the annealing treatments, the annealing temperature was kept at 400°C or 450°C while the annealing time was varied from 1 hour to 6 hours. λ_s was measured to be $\sim 35\times10^{-6}$ for as-cast $Fe_{77.5}Si_{7.5}B_{15}$ wire. It was observed that λ_s increases with annealing time and

reaches a maximum of 41.2×10^{-6} for a wire annealed at 400°C for 3 hours. λ_s starts to decrease with further annealing. The change in λ_s as a function of annealing temperature is about 15% which is very large change in λ_s. Our measurements showed that the total change in λ_s as a function of annealing time is not bigger than 2% (see chapter 5). Therefore, magnetostriction measurement method used by Konno is not a good way to measure λ_s. We assume the largest error in their measurement is due to the friction between wire and glass tube.

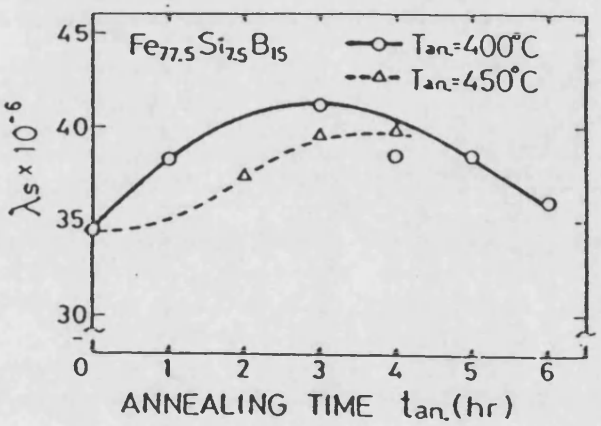

Figure 2.13: Magnetostriction of $Fe_{77.5}Si_{7.5}B_{15}$ amorphous wire as a function of annealing time (reproduced from Konno and Mohri [1989]).

2.7 Magnetoelastic Wave Propagation and Magnetoelastic Properties

Magnetoelastic wave (MEW) generation and propagation in $Fe_{77.5}Si_{7.5}B_{15}$ amorphous wires was studied by Kakuno *et al* [1987],[1989] and [1990]. The MEW was generated by a driving magnetic field which was created by passing a tone-burst current pulse

through a driving coil. The generated MEW is propagated up to a detection coil. The amplitude of a propagated wave is given as a function of distance by:

$$U = U_o \exp(-\alpha x) \qquad (2.14)$$

where U_o is the initial amplitude at the beginning, α is the attenuation coefficient and x is the propagation distance. Comparison of the results obtained for the as-cast ribbon with a similar composition with wire showed that the attenuation coefficient for the wire is much lower at higher field. α is about 6.7 m^{-1} at H=0 and 1.5m^{-1} at H=11 kA/m. The MEW propagation velocity is 4700 m/s at H=0.

Kokuno observed in as-cast wire that the main wave under investigation was followed by anomalous waves which greatly deteriorate the frequency characteristic of the main wave. It was suggested that scattering centres are the sources of the anomalous waves. These scattering centers are induced during the production process and exist throughout the wire volume. Cold-drawing was found to be very effective in removing scattering centers. Although the anomalous waves vanish after cold-drawing, the generation of MEW was then found to be very difficult. This problem was solved by partial annealing. A small region of the cold-drawn wire was annealed and a region highly sensitive to the driving magnetic field was obtained. As a result, this small region serves as an excellent source for generating the MEW.

The change in the MEW propagation velocity, V, as a function of applied magnetic field is shown in figure 2.14 (Kawamura *et al* [1989]). The change in V ,V_{min}/V_{sat} (V_{min} is the minimum value of velocity and V_{sat} is the velocity at saturation) is very small for as-cast $Fe_{77.5}Si_{7.5}B_{15}$ amorphous wire with a diameter of 125μm. When the as-cast wire is torsion annealed the change becomes slightly bigger. V_{min}/V_{sat} is largest (~0.88) when the wire is torsion annealed after cold-drawing. The variation in the velocity of the propagated MEW is due to the ΔE effect, because the V is function of Young's modulus: $V = \sqrt{E/\rho}$.

Wun-Fogle *et al* [1989b] measured the magnetomechanical coupling factor, k_{33}, as a function of applied field for the transverse field annealed $Fe_{77.5}Si_{7.5}B_{15}$ amorphous wire. The maximum value of k_{33} (~0.92) is almost as high as in ribbon material.

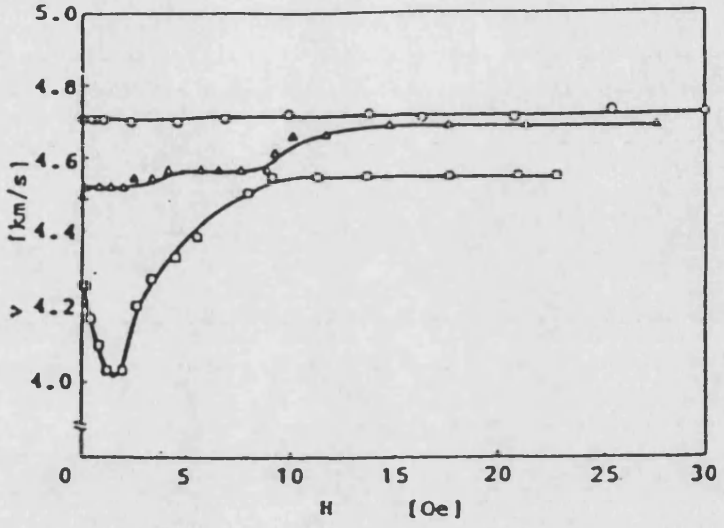

Figure 2.14: MEW propagation velocity for $Fe_{77.5}Si_{7.5}B_{15}$ amorphous wire as a function of applied field, circle is as-cast wire, triangle is torsion annealed un-drawn wire, square is torsion annealed after cold-drawing (diameter is 50μm) (reproduced from Kawamura *et al* [1989]).

2.8 Applications

Since the magnetic properties of amorphous wires are different from any other materials, for example large Barkhausen jump, Matteucci effect and domain wall propagation, the wire are useful in many applications. Table 2.3 shows some properties and application areas of amorphous wires.

The advantages of amorphous wires as sensor materials are as follows,

1) High tensile strength (3580 MPa which is as high as the best hard drawn piano wire). This makes it possible to introduce the high stress in the wire without breaking (Hagiwara *et al* [1982b]).

2) High electric resistivity (130 μohm-cm) which is useful in quick response sensors (Hagiwara *et al* [1982a]).

3) High magnetostrictive properties which makes them useful as in stress sensor and transducer applications.

Property	Application
Domain wall propagation	Distance sensor Signal wave generator
Pulse generation	Rotation speed sensor Magnetic card reader
High harmonics generation	Security sensor Transponder
Bistable flux reversal	Magnetic field sensor Magnetic switch
Matteucci effect	Digitiser

Table 2.3: Properties and application of amorphous wires (after Mohri [1990]).

3 Theory

3.1 Temperature Dependence of Some Magnetoelastic Parameters

Amorphous alloys, usually obtained at high quenching rate (~10^6 K/s), possess a large frozen-in structural disorder. Amorphous alloys are in a metastable state. Therefore, when they are annealed below their crystallization temperature they relax towards a more stable structure. The rate of the changes in the structure of the amorphous alloys at low temperatures is slow enough to be observed experimentally. Annealing of amorphous alloys around and above the crystallization temperature leads to irreversible changes in all properties.

In this section the relaxation of non-magnetic properties of amorphous alloys, such as peak value of damping and shear modulus (and therefore Young's modulus) will be discussed.

At the atomic level the local elastic constants vary from site to site. Therefore local compliances are also not homogeneous and non-linear effects become important. The shear modulus measurements by Egami [1984] showed that there are two types of temperature dependence of shear modulus. At low temperatures, G depends upon temperature only weakly, whereas, at high temperatures G values depend more strongly upon the temperature, as given by:

$$G(T) = G(0)\,(1 - T/T_g') \qquad (3.1)$$

where G(0) is the shear modulus at 0K and T_g' is the upper glass transition temperature (figure 3.1). The extrapolation of the theoretical curve to high temperature indicates that G=0 at around T_g' (~1500°C). Also, the extrapolation to low temperatures gives a value of G about 25% higher than the room temperature value. Each amorphous alloy has a

certain crystallization temperature ,T_x; when the annealing temperature reaches T_x, the modulus value increases. Therefore, the behaviour of G above T_x does not obey equation 3.1. The increase in G with crystallisation is due to the increase in density in the crystalline state. In an ideal crystalline material, under the effect of shear stress, the displacements of the atoms are forced in distinct crystallographic directions. In amorphous alloys, shifts along all directions are allowed, which means that atoms can be easily displaced against each other.

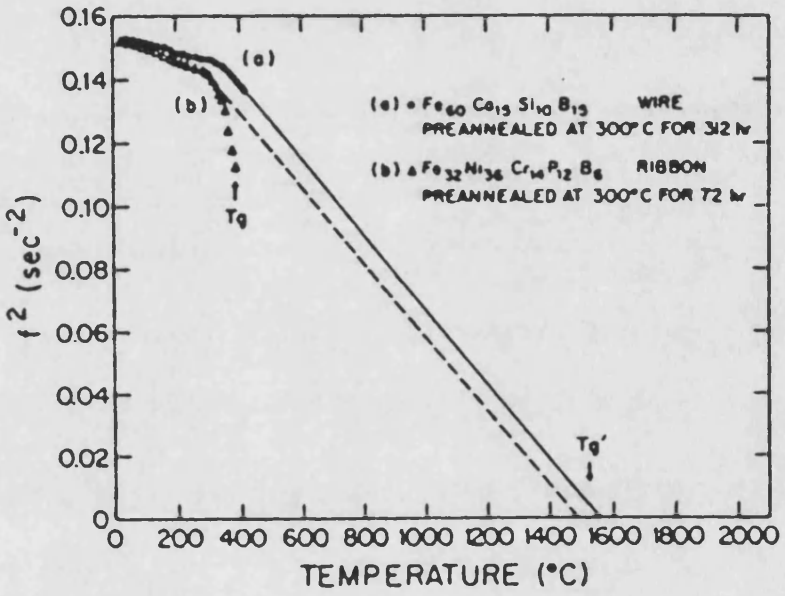

Figure 3.1: Temperature dependence of f^2 (f is frequency of the torsional oscillation and is proportional to G with the relationship; $G=cf^2$, where c is constant). The high temperature extrapolation shows that G=0 near T_g'(reproduced from Morito and Egami [1984a]).

Damping (or internal friction) properties of amorphous alloys have been studied by Morito [1983], Morito and Egami [1984a] and [1984b], Lu *et al* [1990] and others. Morito and Egami [1984a] and [1984b] showed that Q^{-1} is a relatively weak function of

temperature. Annealing first increased Q^{-1}, which then saturated to a finite value. Further annealing reduced Q^{-1} due to the partial crystallisation. The change in Q^{-1} was attributed by Morito and Egami to the atomic rearrangement in local units.

3.2 Magnetoelastic Properties

Magnetoelastic phenomena were known and studied in crystalline materials more than a hundred years ago, long before the amorphous alloys were discovered. The simple explanation of these phenomena can be given in terms of an interaction between stress and the configurational arrangement of magnetostrictively deformed domains and magnetic moments. In this section we will discuss magnetostriction, damping, ΔE, ΔG, pole effects and very briefly magnetoelastic coupling factor.

3.2.1 Damping

There is a loss of energy associated with the elastic vibration of any material. The ratio of this energy loss per cycle, ΔU, to the energy at maximum amplitude during a cycle, $U=\sigma^2/2E$, is defined as damping (equation 3.2).

$$Q^{-1} = \frac{\text{Energy Loss per Cycle}}{\text{Total Vibrational Energy}} = \frac{\Delta U}{U} \qquad (3.2)$$

It has been shown that the damping of ferromagnetic materials is considerably higher than that of non-magnetic materials because of the additional losses associated with irreversible domain wall movements (Cochardt [1959]).

There are many ways of taking measurements of damping. One of the fundamental ways is to determine the change of oscillation amplitude as the oscillation of the system dies out. This method is usually used in the torsional vibration system, the vibrating reed

system and the pulse echo system. The details of damping measurements for torsional vibration are given in chapter 4. In the vibrating reed system the amplitude is detected by an amplitude discriminator and a pulse counter (Kobelev [1987]). Damping can also be determined by resonance and antiresonance method and it is given by the following equations:

$$Q^{-1} = \frac{\Delta f_w}{f} \tag{3.3}$$

or,

$$Q^{-1} = \frac{1}{\sqrt{3}} \frac{\Delta f_A}{f} \tag{3.4}$$

where Δf_w is the frequency band width at 0.7 of resonance frequency peak amplitude, f, and f_A is the frequency band width at half maximum of the f peak amplitude (Bozorth [1951]).

Magnetic damping can be expressed by a superposition of the following three mechanisms: macroscopic eddy currents, Q^{-1}_{ME}; microscopic eddy currents, Q^{-1}_{m}; and magnetomechanical hysteresis, Q^{-1}_{h} (Kobelev *et al* [1987], Bozorth [1951] and Nowick and Berry [1972]), according to the relation:

$$Q_T^{-1} = Q_{ME}^{-1} + Q_m^{-1} + Q_h^{-1} \tag{3.5}$$

where Q^{-1}_{T} is the total magnetic damping.

3.2.1.1 Macroeddy and Microeddy Current Losses

Kersten [1934] was the first to suggest that an important part of the damping in ferromagnetic materials is due to the eddy currents caused by the alternating magnetisation. For a typical sample magnetised to an induction B_o and subjected to a small stress σ, the total change in the induction will be:

$$B = B_o + \alpha\sigma, \quad \alpha = dB/d\sigma \tag{3.6}$$

If σ is changed periodically with time, there will be a periodic change in flux which will induce eddy currents opposing the change in flux and leading to an energy loss. The macroeddy current loss was given as a function of H by Kobelev and Soifer [1986]:

$$Q^{-1} = \pi\Delta_{ME}(H)\frac{\omega\tau_{ME}(H)}{1+(\omega\tau_{ME}(H))^2} \tag{3.7}$$

where ω is the angular frequency of the oscillation, Δ_{ME} is the degree of the relaxation dependent on the magnetic field and $\tau_{ME} = Aa^2/D$. $D = \rho/4\pi\mu_o\mu_r$; A is a coefficient of the order of unity dependent on the shape of the sample and the nature of the vibration; a is the characteristic size of the sample (e.g. ribbon thickness); ρ is the electrical resistivity of the material; μ_r is the magnetic permeability.

The microeddy current loss is due to induced currents on a local scale. It is also given by equation 3.7, but in this case $\tau_m = Al^2/D$, where l is the characteristic size of the magnetic domain. Microeddy current depends on the domain structure of the material because the local change in magnetisation is not identical to the macroscopic change in magnetisation of the whole sample.

According to equation 3.7 both microeddy and macroeddy currents are functions of frequency. Therefore, at low frequencies the effect of eddy current losses is very small. Also, both are independent of the stress amplitude (Bozorth [1951]).

3.2.1.2 Magnetomechanical Hysteresis

Magnetomechanical hysteresis damping (hereafter MHD) depends on the amplitude of the oscillation and is independent of the oscillation frequency. MHD is basically due to the irreversible motion of 90° domain walls. MHD was discovered by Becker and

Kornetzki [1934]). They showed that under the influence of an external mechanical stress, domain walls move as they do under external magnetic field. The energy lost during a stress-strain cycle is called magnetomechanical hysteresis loss. Bozorth [1951], Cochardt [1953] and [1954], Smith and Birchak [1968], [1969], [1970] and [1972], Degauque and Astie [1980] and Motogi [1982] have attempted theoretically to explain MHD on the basis of shape of the magnetomechanical hysteresis loop (figure 3.2) and irreversible motion of 90° domain walls. The area of the stress-strain loop is equal to the energy loss per unit volume during a complete cycle. It was shown that this loop follows a type of mechanical Rayleigh's law at small stresses since the energy loss increases with the third power of the stress,

$$\Delta U = D\sigma^3 \tag{3.8}$$

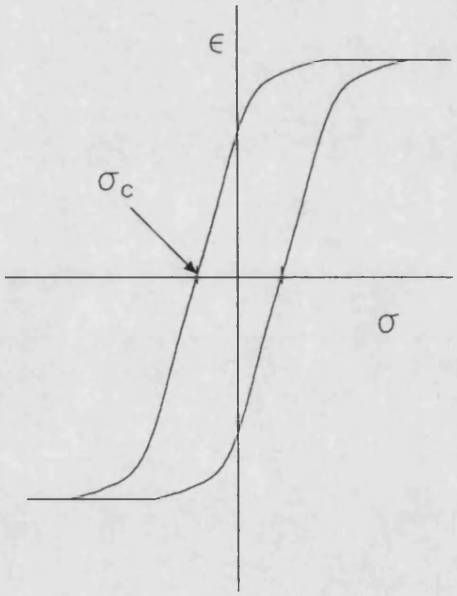

Figure 3.2: An example for a typical magnetomechanical hysteresis loop (after Nowick and Berry [1972]).

Kornetzki [1943] tried to obtain magnetomechanical damping as a function of torsional strain by relating the area of the mechanical hysteresis loop to the area of the magnetic hysteresis loop. The magnetic Rayleigh's law connects the magnetic field, H, and magnetisation, M, with the following equation:

$$M = \chi_o H + 2\upsilon H^2 \tag{3.9}$$

χ_o is the initial susceptibility and υ is the magnetic hysteresis constant. For small fields ΔU is given by:

$$\Delta U = \frac{8}{3}\upsilon H^3$$

or by,

$$\Delta U = \frac{8}{3}\upsilon \frac{M^3}{\chi_o^3} \tag{3.10}$$

It was assumed that the magnetisation changes as a function of stress according to the relation:

$$M = \frac{9}{8}\frac{\lambda_s \chi_o}{M_s}\sigma \tag{3.11}$$

The energy loss can be obtain by replacing M in equation 3.10 by the expression in equation 3.11. This gives:

$$\Delta U = \frac{243}{64}\frac{\upsilon \lambda_s^3}{M_s^3}\sigma^3 \tag{3.12}$$

From the definition of damping (equation 3.2) and $\sigma = E\varepsilon$, Q^{-1} can be obtained:

$$Q^{-1} = \frac{486}{64}\frac{\upsilon \lambda_s^3 E^2}{M_s^3}\varepsilon \tag{3.13}$$

Equation 3.13 shows that damping should increase linearly with increasing torsional strain, ε at lower values ε. This has been observed for all the ferromagnetic materials.

At higher ε values, the proportionality between Q^{-1} and ε as given by equation 3.13 must be expected to break down for the reason that ΔU no longer obeys equation 3.10 (Cochardt [1959]). If the material is strong enough and the magnetomechanical coercive force small enough to realize saturation, ΔU reaches a maximum value at this point and becomes independent of ε and ΔU should subsequently decrease as the inverse square of ε (Nowick and Berry [1972]). This has been observed for various ferromagnetic materials (Sumner and Entwistle [1959] and Frank and Ferman [1965]).

MHD behaviour has been explained by Cochardt [1953] in terms of critical stress, σ_c. He assumed that the larger the area of the mechanical hysteresis loop the higher the damping peak. The energy loss for small stress is given by equation 3.8. For stresses larger than the critical stress, the area of the hysteresis loop remains the same. For this case ΔU is equal to a constant and is expressed by:

$$\Delta U = K\lambda_s\sigma_c \tag{3.14}$$

where K is a constant which depends on the shape of the mechanical hysteresis loop. The definition of the damping leads to the equation:

$$Q^{-1} = 2GK\lambda_s\frac{\tau_c}{\tau}\left(1-\frac{3}{5}\frac{\tau_c^2}{\tau^2}\right) \quad \tau_c < \tau \tag{3.15}$$

τ_c is the critical torsional stress and τ is the torsional stress. This inverse square inverse decrement given by Cochardt is not, however, generally well obeyed. For iron-based materials, Smith and Birchak [1968], [1969] have shown that a more linear decrease exists. They explained the magnetomechanical damping behaviour in terms of the local average internal stress, σ_{loc}, distribution according to the expression:

$$N(\sigma_{loc}) = C\sigma_{loc}\exp(-a\sigma_{loc}^n) \tag{3.16}$$

where C and a are constants. Smith and Birchak considered the cases for n=1 and n=2. They also assumed that the energy loss, ΔU, depends on the average internal stress, σ_i, which opposes the domain wall motion and that the $N(\sigma_{loc})$ and ΔU functions have to

satisfy three conditions:

1) $N(\sigma_{loc})$ should satisfy:

$$\int_0^{\infty} N(\sigma_{loc})d\sigma_{loc} = 1 \tag{3.17}$$

2) For small stresses, the energy loss must satisfy mechanical Rayleigh's law:

$$\int_0^{\sigma} \Delta U_{loc} N(\sigma_{loc})d\sigma_{loc} \propto \sigma^3 \tag{3.18}$$

3) At larger stresses, the energy loss must saturate:

$$\Delta U = \int_0^{\infty} \Delta U_{loc} N(\sigma_{loc})d\sigma_{loc} = K\lambda\sigma_i \tag{3.19}$$

Where K is a dimensionless constant that depends on the shape of the stress-strain loop. Equations 3.17 and 3.19 yield values for C and a in equation 3.16. $N(\sigma_{loc})$ can then be written as:

$$N(\sigma_{loc}) = \frac{4}{\sigma_i^2}\sigma_{loc}\exp(-2\sigma_{loc}/\sigma_i) \tag{3.20}$$

To explain the effects of the magnetic field or applied tensile stress, Smith and Birchak substituted $(\sigma_i^2 + \sigma^2)^{1/2}$ for σ_i in equation 3.20, where σ is the applied tensile stress or equivalent for H. By renormalizing $N(\sigma_{loc})$ and inserting it into equation 3.19, ΔU can be calculated. From the definition of the damping (equation 3.2):

$$Q^{-1} = \frac{2K\lambda_s E_s}{\sigma_i}\frac{1}{1+W^2}\{(1-\exp(-2y)(1+2y+2y^2))/y^2\} \tag{3.21}$$

where

$$y = \frac{x}{\{1+(\sigma/\sigma_i)^2\}^{1/2}}, \quad W = \frac{\sigma}{\sigma_i}, \quad x = \frac{\varepsilon}{\varepsilon_i}$$

Figure 3.3 shows typical curves as a function of ε for different σ values.

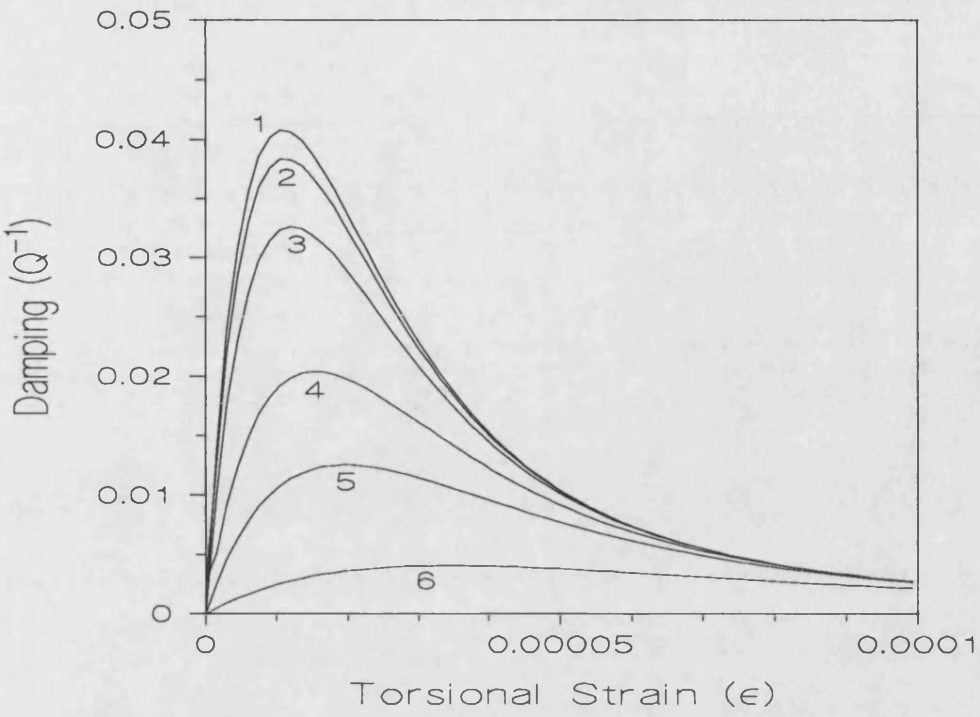

Figure 3.3: Smith and Birchak model curves for the influence of different values of σ on the damping: Curve (1) 0MPa, (2) 0.5MPa, (3) 1MPa, (4) 2MPa, (5) 3MPa, (6) 6MPa. For E_s=160GPa, λ_s=30ppm, K=0.02 and σ_i=2MPa (after Smith and Birchak [1969]).

Setting $dQ^{-1}/dx = 0$, to find position of maximum damping, leads to a relationship to fit the theory to experimental data:

$$x(Q^{-1}_{max}) = 0.7256(1 + W^2)^{1/2} \tag{3.22}$$

and

$$Q^{-1}_{max} = 0.34\frac{2K\lambda_s E_s}{\sigma_i}\frac{1}{(1 + W^2)}. \tag{3.23}$$

To see the effect of the applied magnetic field, Smith and Birchak assumed that σ can be replaced by $2\mu_o HM_s/3\lambda_s$.

The behaviour of the damping peak of magnetic materials as a function of magnetic field or tensile stress cannot be fully explained by the Smith and Birchak model, because the effect of field and stress on domain walls is represented as a random function. The model does not consider either domain structure or the angle between easy axis and H or σ_{eff}. As a result the Smith and Birchak model can only give the lowering of maximum damping value with increasing H or σ_{eff}.

The theoretical model for damping of Degauque and Astie (DA) [1980] assumes that, for a twisted ferromagnetic wire Q^{-1} is proportional to the ratio of the remanent torsional strain, ε_r, to ε.

$$Q^{-1} = \frac{\Delta U}{U} = \frac{\varepsilon_r}{\varepsilon} \tag{3.24}$$

ε_r is proportional to the number, S, of the 90° domain walls which perform irreversible jumps per unit volume. S is determined by the domain wall energies and positions. DA also proposed that the maximum and minimum levels of restoring force, dW/dx (where W is domain wall energy and x is domain wall position) are given by the following two equations:

$$N(\gamma) = \frac{4}{\bar{\gamma}^2}\gamma \exp\left(2\frac{\gamma}{\bar{\gamma}}\right),$$

$$N(\gamma) = \frac{1}{\bar{\gamma}^2}\beta \exp\left(\frac{\beta}{\bar{\gamma}}\right) \tag{3.25}$$

where,

$$\left|\left(\frac{dW}{dx}\right)_{max}\right| = \gamma$$

$$\left|\left(\frac{dW}{dx}\right)_{max} - \left(\frac{dW}{dx}\right)_{min}\right| = \beta$$

with the mean values:

$$\left|\overline{\left(\frac{dW}{dx}\right)_{max}}\right| = \bar{\gamma} = \frac{\bar{\beta}}{2}$$

By coupling the two function of equation 3.25, they obtained the maximum and minimum distribution function of dW/dx

$$N(\gamma, \beta) = N(\gamma)N(\beta) \tag{3.26}$$

The equilibrium position of the domain wall is determined by the condition:

$$\frac{dW}{dx} = \mp(Y + Z) \tag{3.27}$$

where Y+Z represents the external force which acts on the domain wall. Y is proportional to the applied field,

$$Y = \sqrt{2}\mu_o M_s H \cos\alpha \tag{3.28}$$

where α is the angle between H and the easy axis of magnetisation. Z is proportional to the torsional strain,

$$Z = \frac{3}{2}\lambda_s G\varepsilon \cos^2\theta \tag{3.29}$$

where θ is the angle between the mechanical stress and the easy axis.

The occurrence of the irreversible jumps is closely connected with the extreme values of the stress and the field. For simplicity, we consider a 90° domain wall located at 0 at equilibrium in the absence of any external forces (figure 3.4). The effect of the field and torsional strain (or stress) on the domain wall can be demonstrated by the following steps:

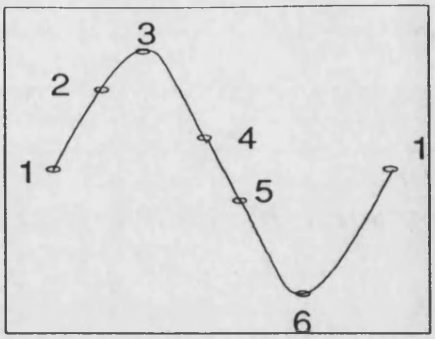

(a)

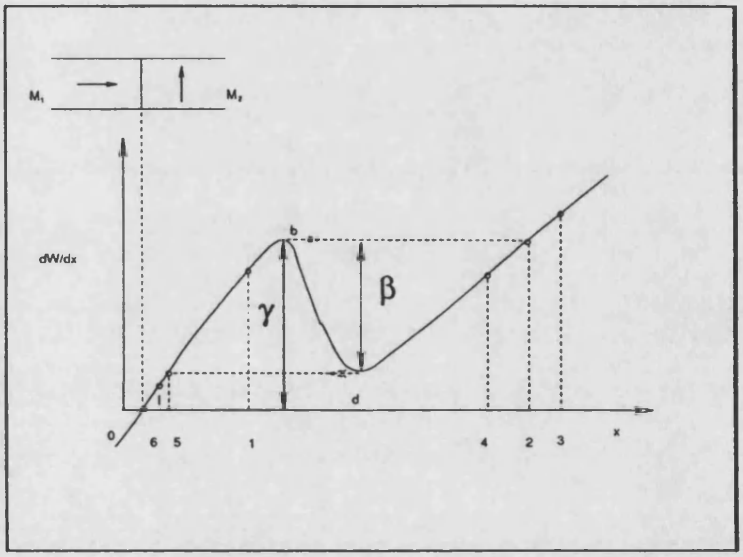

(b)

Figure 3.4: (a) Representation of a typical complete cycle of a torsional oscillation. (b) Domain wall movement under the influence of torsional strain and magnetic field (after Degauque and Astie [1980]).

a) With applied field the wall moves from position 0 to position 1,

b) In the first half of the cycle the domain wall performs an irreversible jump (b) to position 2. Then it goes to the position 3 with further increase in the amplitude of the oscillation (therefore ε)

c) In the second half of the cycle, the wall relaxes to position 4 and later an opposite

jump (d) takes place. The wall goes to position 5 and then 6 with further decrease in the amplitude of the oscillation.

d) When a whole cycle is completed the domain wall comes back to position 1 again.

All these steps take place if:

$$Y < \gamma < Y + Z$$

$$\gamma - Y < \beta < \gamma - Y + Z$$

The remanent torsional strain is given by:

$$\varepsilon_r = CS = \frac{1}{2}\int_Y^{Y+Z} d\gamma \int_{\gamma-Y}^{\gamma-Y+Z} N(\gamma,\beta)d\beta \qquad (3.30)$$

where C is the correction factor (C~1/Z) which takes into account that after the first movement some walls reach positions from which irreversible jumps cannot be performed during subsequent cycles. From equations 3.24 and 3.30, Degauque and Astie obtained an expression for the function $\psi_1 = \bar{\gamma}Q^{-1}$. When this is plotted against Z_1 ($Z_1 = Z/\bar{\gamma}$) the damping goes to negative values at small levels of Z_1, which is incorrect. We therefore re-derived the damping equation using the same conditions as used by Degauque and Astie. ψ_1 was obtained as:

$$\Psi_1 = \frac{1}{27Z_1^2}\exp(-2Y_1)\{-4\exp(-Z_1)(3Y_1(3Z_1+4)+3Z_1+5)$$

$$-4\exp(-3Z_1)(3Y_1(3Z_1+4)+9Z_1^2+15Z_1+5)$$

$$+4\exp(-4Z_1)(6Y_1(3Z_1+2)+18Z_1^2+18Z_1+5)+4(12Y_1+5)\} \qquad (3.31)$$

where $Y_1 = Y/\bar{\gamma}$.

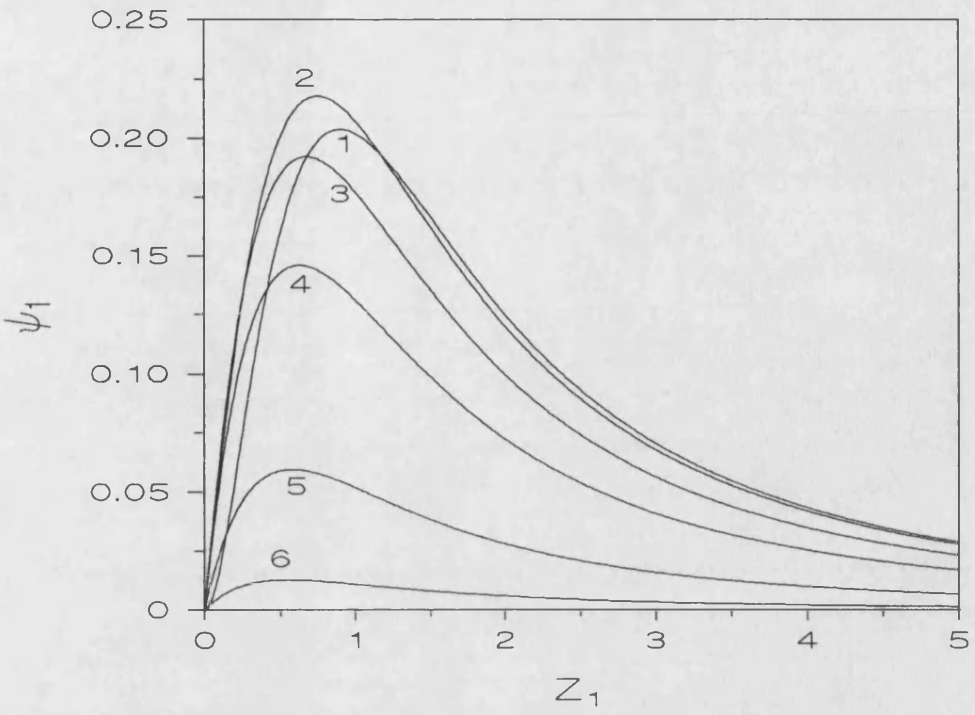

Figure 3.5 Theoretical variations of ψ_1 for different Y_1 (curves were obtained from equation 3.32): curve (1) Y_1=0, (2) 0.25, (3) 0.5, (4) 0.8, (5) 1.5, (6) 2.5.

Figure 3.5 shows ψ_1 against ε for some values of Y_1. According to figure 3.5, external forces play two important roles: 1) For a given amplitude of oscillation, ε can trigger a certain number of wall movements at H=0. Once the field is present, ε can trigger an even greater number of irreversible jumps. 2) Gradually, the field itself becomes capable of triggering more irreversible jumps. In this case, torsional strain can only provoke reversible movements of domain walls and therefore the peak value of the damping will be less.

3.2.2 Magnetostriction and Elastic Moduli

When a magnetic field is applied to a magnetic material, the body of the material elongates or contracts. This phenomenon is known as magnetostriction. It is given by:

$$\lambda = \frac{\Delta l}{l} \tag{3.32}$$

Δl is the total change in the length of the sample and l is length of the sample in the demagnetised state.

The field dependent magnetostrictive strain, sometimes called the engineering magnetostriction, λ_e, is related to λ_s by:

$$\lambda_e = \frac{3\lambda_s}{2}(\cos^2\theta_f - \cos^2\theta_i) \tag{3.33}$$

where θ_f is the final angle between the magnetic moment and H and θ_i is the initial angle. Field dependence of λ_e is shown in figure 3.6 for various anneal angles.

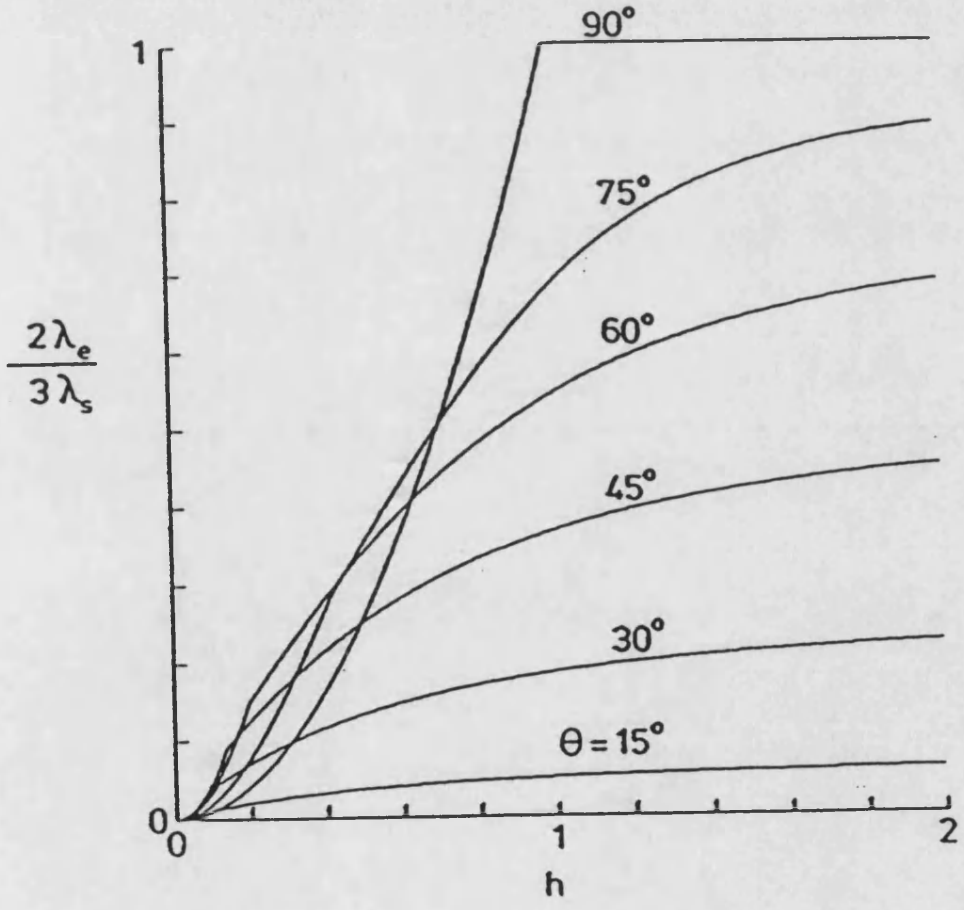

Figure 3.6: Normalised engineering magnetostriction against reduced field h for various annealing angles (reproduced from Squire [1990]).

The change in magnetostrictive strain with magnetisation leads to a change in both Young's modulus and shear modulus. When a stress is applied to a material two kinds of strain take place in the material: a) Magnetoelastic strain ε_H, due to moment rotation, and b) elastic strain. When a magnetic material is saturated the change in magnetoelastic strain is zero, because the moments do not rotate further. The modulus as a function of the stress is given by:

$$E = \frac{\sigma}{\varepsilon_s + \varepsilon_H} \tag{3.34}$$

and at saturation:

$$E_s = \frac{\sigma}{\varepsilon_s} \tag{3.35}$$

From equations 3.34 and 3.35:

$$\frac{\Delta E}{E} = \frac{E_s - E}{E} = \frac{\varepsilon_H}{\varepsilon_s} \tag{3.36}$$

This is known as the ΔE effect. ΔE effect in amorphous alloys is much bigger than that in crystalline materials. The maximum change in modulus observed in crystalline materials is a few percent(~10 percent). Due to the lack of crystal anisotropy in amorphous alloys, the change in the modulus as a function of field is much bigger (~80 percent). The ΔE effect also depends on the composition of the material (Table 3.1).

Magnetic annealing can produce a striking effect on the field dependence of Young's modulus, E(H). Thomas [1991] studied the effect of field annealing on E(H) and magnetostriction on $Fe_{40}Ni_{40}B_{20}$ amorphous ribbons. The annealing field direction was varied from 0° to 90° with respect to the ribbon length. As a result, an easy axis in the desired direction was obtained. Figure 3.7 shows the effect of the annealing angle, θ, on E(H). Thomas showed that the magnitude of the ΔE effect changes as a function of the

x	E_s (GPa)	E/E_s (%)	10^6 λ_s
0	160	50	42
2	179	42	38
4	160	15	49
6	155	16	52
8	165	28	43
10	147	19	28

Table 3.1: Magnetoelastic parameters of the series $(Fe_{0.79}Co_{0.21})_{75+x}Si_{15-1.4x}B_{10+0.4x}$ (reproduced from Gutierrez *et al* [1989]).

angle and that larger angles lead to larger changes in E(H). He also showed that the magnitude of the engineering magnetostriction, λ_e (field dependence of λ) is independent of the magnetic anisotropy constant, K_u, and λ_e is only a function of θ.

For 0° annealed sample the magnetic moments align parallel to the ribbon length. When a magnetic field is applied in the ribbon length direction, the magnetisation occurs due to the motion of 180° domain walls which does not induce any strain into the material. Therefore, E of the 0° annealed sample does not show any field dependence (figure 3.8.a). For transversely annealed samples all the magnetic moments align perpendicular to H (figure 3.8.b). In this case the magnetisation occurs by moment rotation which induces maximum magnetostrictive strain into the material, leading to the maximum ΔE effect (Moorjani and Coey [1984]).

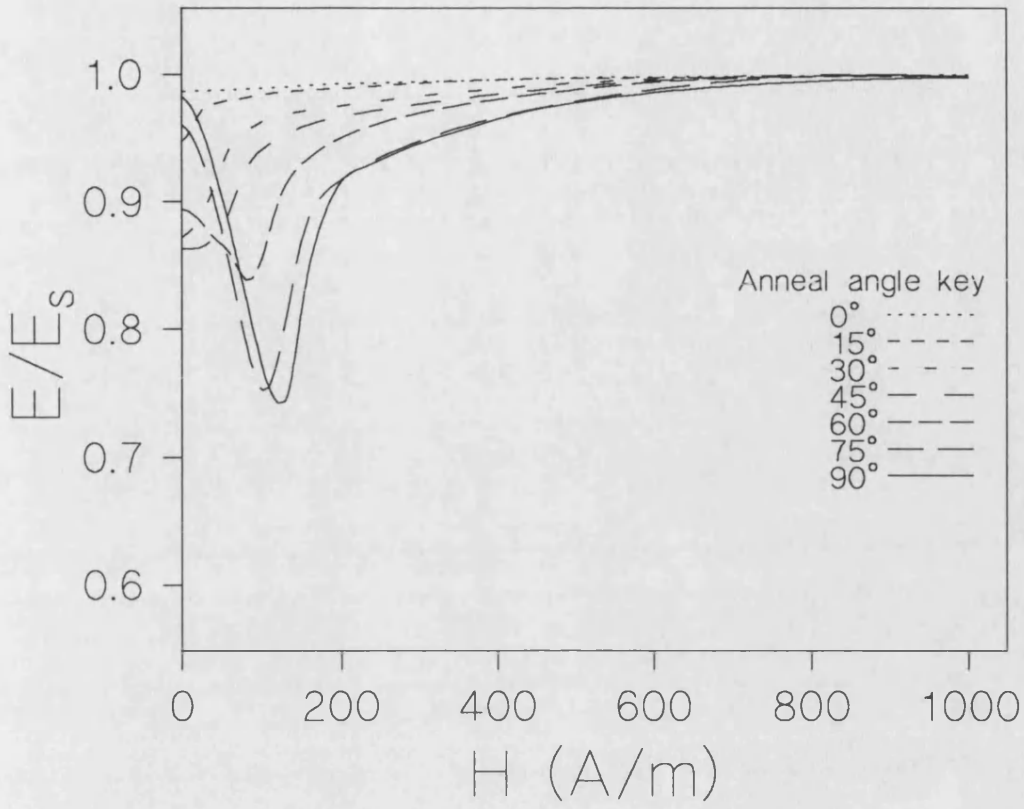

Figure 3.7: E/E_s curves for $Fe_{40}Ni_{40}B_{20}$ sample as a function of applied field for different values of θ (reproduced from Thomas [1991]).

The field dependence of E has been studied by many researchers including Berry and Pritchet [1976], Spano *et al* [1982], Livingston [1982] Squire [1990]. Berry and Pritchet tried to explain the E(H) behaviour in a way very similar to the model for damping. The ΔE effect was discussed by Livingston [1982] who proposed a simple model of the rotation of the magnetic moments. The model considers an amorphous ribbon which is annealed in a magnetic field parallel to the ribbon width to produce a magnetic easy axis in this direction. In the model, H and stress are applied in the ribbon plane perpendicular to the ribbon width. A longitudinal field will rotate the magnetic moments from the width direction towards the longitudinal direction. The field induces an energy density of

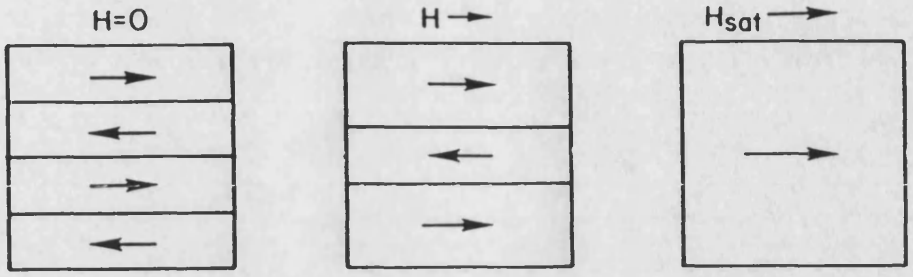

(a)

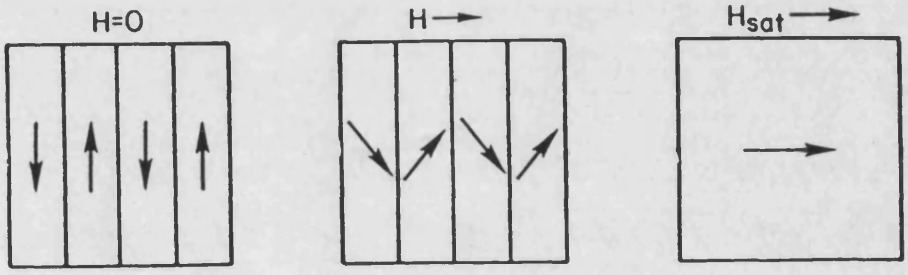

(b)

Figure 3.8: Schematic illustration of magnetisation with applied field, (a) H is parallel to an induced easy-axis, (b) H is perpendicular to an induced easy-axis (after Berry [1976]).

$-\mu_o M_s H\cos\theta$. θ can be found from the minimum energy condition. The total energy of the system is:

$$U = K_u \cos^2\theta - \mu_o M_s H \cos\theta \qquad (3.37)$$

From $(dU/d\theta)=0$,

$$\cos\theta = \frac{H}{H_k} \qquad (3.38)$$

where H_k ($=2K_u/\mu_o M_s$) is the anisotropy field. For a magnetostrictive material the strain changes from $-\lambda_s/2$ to λ_s (relative to the material in demagnetised state), the total change being $3\lambda_s/2$. The following equation gives the change of strain as a function of θ:

$$\varepsilon = \frac{3\lambda_s}{2}\left(\cos^2\theta - \frac{1}{3}\right) = \frac{3\lambda_s}{2}\left(\frac{H^2}{H_k^2} - \frac{1}{3}\right) \tag{3.39}$$

Hence,

$$d = \left(\frac{\partial \varepsilon}{\partial H}\right)_\sigma = \frac{3\lambda_s H}{H_k^2} \tag{3.40}$$

where d is the magnetomechanical coupling which reaches a maximum at $H=H_k$. If a longitudinal stress σ is applied, an energy density of $(-3/2)\lambda_s\sigma\cos^2\theta$ will be induced and H_k will be replaced by the reduced anisotropy field $H_{k\sigma}$, which is given by:

$$H_{k\sigma} = \frac{2K_u - 3\lambda_s\sigma}{\mu_o M_s}, \quad \sigma < \sigma_c \tag{3.41}$$

The model assumes that the magnetic easy axis does not change as long as $\sigma<\sigma_c=2K_u/3\lambda_s$. In equation 3.39, there will be additional Hooke's law term σ/E_s; if we make all these changes, the equation 3.39 becomes:

$$\varepsilon = \frac{\sigma}{E_s} + \frac{3\lambda_s}{2}\left(\frac{H^2}{H_{k\sigma}^2} - \frac{1}{3}\right) \tag{3.42}$$

The field and stress dependence of E is given by the following equation:

$$\frac{\Delta E}{E} = \frac{9\lambda_s^2 E_s H^2}{\mu_o M_s H_{k\sigma}^3} \tag{3.43}$$

One of the important parameters for comparing materials is the magnetomechanical coupling factor, k, which can be defined as the fractional energy transferred between magnetic and mechanical energies:

$$k = \left(1 + \frac{\mu_0 M_s H_{k\sigma}^3}{9\lambda_s E_s H^2}\right)^{1/2} \leq 1 \tag{3.44}$$

According to the Livingston model , the desired properties, such as large ΔE and high k, can be obtained with high λ_s and M_s and low K_u. All these quantities vary with the alloy composition. In particular, K_u is also very sensitive to annealing temperature and time. One of the important problems with Livingston model is that it considers the amorphous alloy to be fully stress relieved and with an ideal domain structure as shown in figure 3.8b. It is well known that amorphous alloys have a very large casting stress which cannot be fully relieved. Therefore, on a local scale, a sample will have a local internal stress distribution leading to a local anisotropy distribution. This leads to moment spread around the easy axis in each domain. The exchange anisotropy energy which is due to spin-spin coupling is also another cause for moment spread around the easy axis.

The Squire model [1990] is a more expanded form of the Livingston model. The model assumes that the amorphous ribbon is field annealed at different angles to the ribbon axis. This induces an easy axis in a direction, θ, to the direction of the magnetisation leading to a suggested domain structure shown in figure 3.9.

The domain structure consists of regions which are separated by 180° domain walls. The width of each region is taken as equal to d. The total free energy of the system is given by:

$$U = U_a + U_m + U_{ms} + U_w \qquad (3.45)$$

where U_a is the uniaxial anisotropy energy, U_m is the magnetostatic energy, U_{ms} is magnetoelastic energy and U_w is the domain wall energy. The equilibrium condition gives ϕ_1 and ϕ_2 in terms of the applied field and material parameters (anisotropy constant, λ_s, M_s etc).

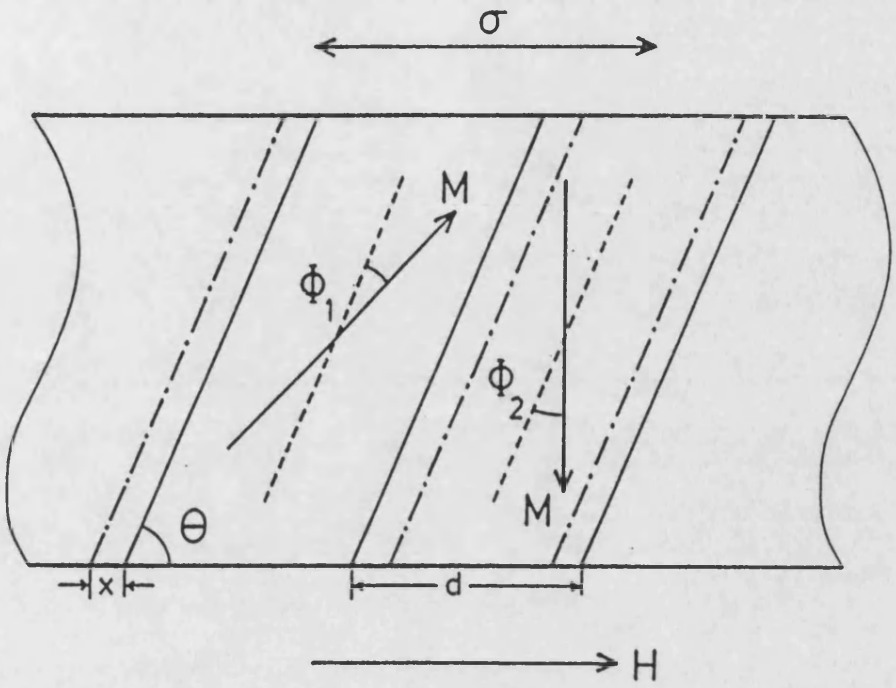

Figure 3.9: Schematic illustration of the domain structure suggested by Squire [1990].

The field dependence of E was obtained in a similar way to the Livingston model, defining the E by:

$$\frac{1}{E} = \frac{\partial \varepsilon}{\partial \sigma} \tag{3.46}$$

From the equation 3.46, an expression for the ΔE effect was obtained:

$$\frac{\Delta E}{E} = \frac{9}{8}\frac{\lambda_s^2 E_s}{K} F(h,\theta,\gamma) \qquad (3.47)$$

where,

$$F(h,\theta,\gamma) = \frac{\sin^2 2(\theta-\phi_1)}{\cos 2\phi_1 + h\cos(\theta-\phi_1) + 2\gamma\cos 2(\theta-\phi_1)}$$

where h (=H/H_a) is the reduced field and γ (=$3\lambda_s\sigma/4K_u$) is function of applied stress. The typical curves obtained from equation 3.47 are shown in figure 3.10 for various anneal angles.

The model considers that H plays two rôles in the magnetisation process of the sample 1) H rotates the magnetic moments from the easy axis direction by an angle ϕ_1 and ϕ_2 towards the applied field direction in each region, 2) H also moves domain walls. The relative effect of these two processes depends on θ. The wall motion is more effective at lower values of θ; moment rotation becomes more effective at larger θ. The knee on the curves shows the end of the wall motion. The model also suggests a second way to end domain wall motion. After a critical value of h the magnetic moments, initially opposed to H, suddenly flip and make the material a single domain. The flipping occurs only at larger values of θ, because at smaller values of θ the domain walls disappear before the flipping occurs. After flipping magnetisation occurs only by moment rotation. The sudden flipping of the moments leads to discontinuities in the E-H curves. Such discontinuities have not been observed for any material. The later work of Thomas [1991] showed that flipping cannot be observed, and that the magnetic moments rotate the same amount in each region ($\phi_1 \sim \phi_2$). However, several features of the model are not affected by these discrepancies.

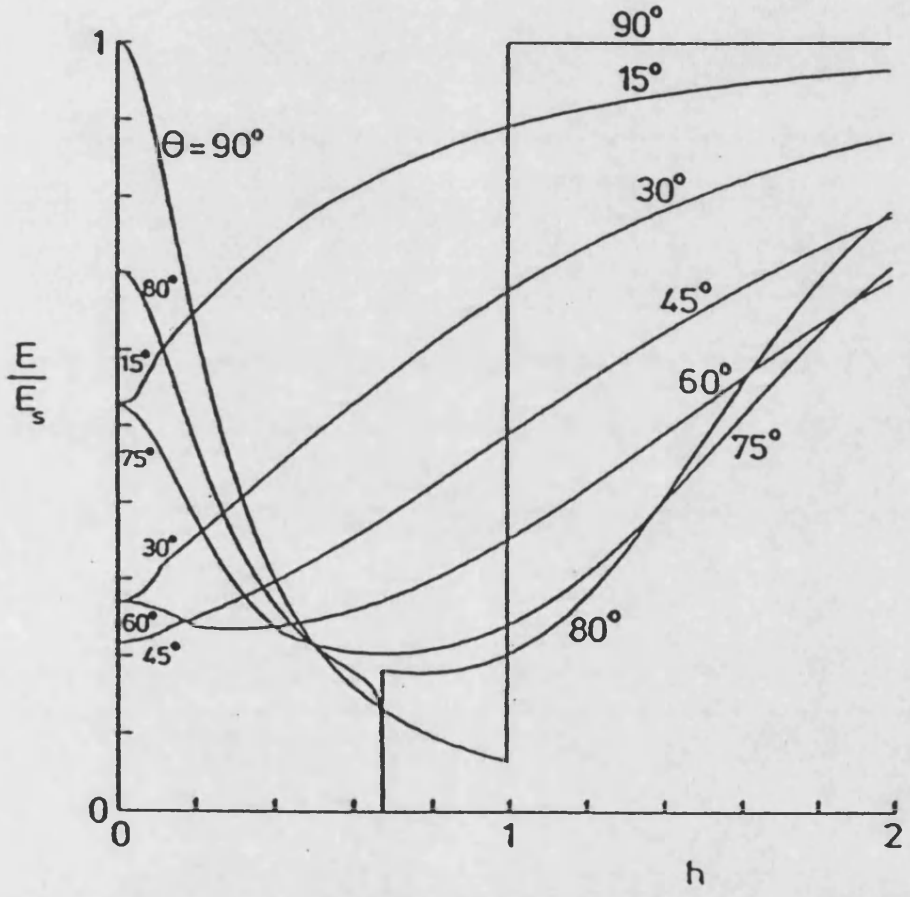

Figure 3.10:Normalised elastic modulus, E/E_s, against the reduced field h for various annealing angles. For γ=0, K=100 Jm^{-3}, λ_s=40ppm (reproduced from Squire [1990]).

One of the important results of the Squire model is that the average initial angle of the magnetic moments can be estimated from the Young's modulus value at H=0, E_o. If E_o is equal to E_s which shows that the moments align in a direction perpendicular to H. Figure 3.11 shows E_o obtained from equation 3.47 as a function of anneal angle.

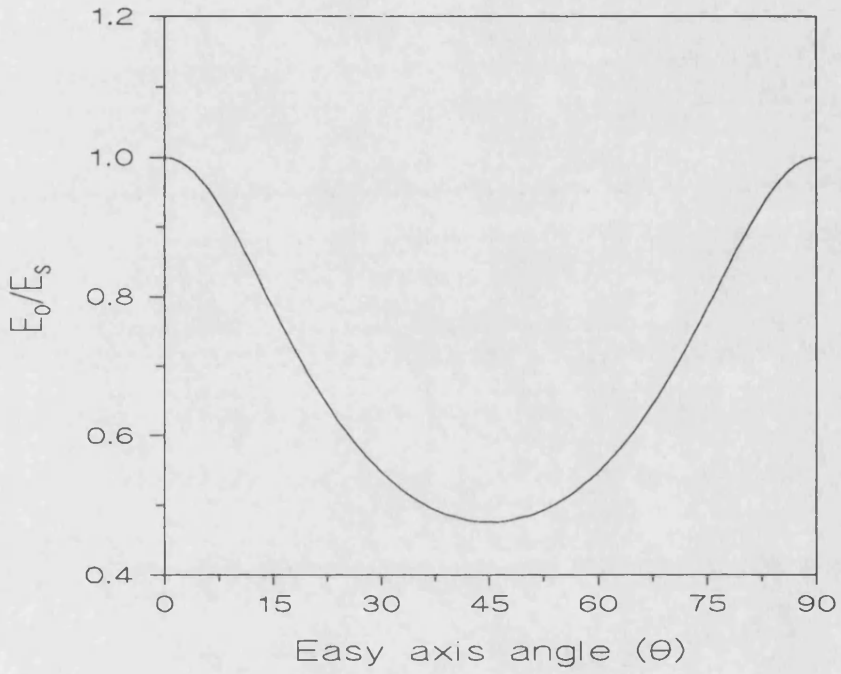

Figure 3.11: Young's modulus at H=0 as a function of annealing angle. The curve was obtained from equation 3.47 for K=200 Jm^{-3}, λ_s=35ppm, E_s=160GPa, h=0 and γ=0.

Although the detailed dependence of the shear modulus on applied field and stress is different from that of Young's modulus, the general features are expected to be similar. In particular, the magnitude of the ΔG effect is given by an expression of the form:

$$\frac{\Delta G}{G} = \frac{9}{8}\frac{\lambda_s^2 G_s}{K} D(h, \theta, \gamma) \qquad (3.48)$$

where D is a function similar to F in equation 3.47.

3.3 Partial Crystallisation

In the some recent studies it has been shown that for some applications the completely amorphous state is not always advantageous and that partial crystallisation might be better to improve some of the properties such as λ_e (Thomas [1991]).

Annealing at higher temperatures leads to the nucleation and growth of small crystallites rapidly. For a particular heat treatment range, flat and linear magnetisation curves were observed. This has been associated with the formation of a thin crystalline surface layer of α-Fe in Fe-based amorphous alloys (Ok and Morrish [1981]). There is a number of reasons to expect preferred crystallisation at surface: 1) During rapid solidification as well as during heat treatments surfaces are expected to accelerate nucleation as the crystalline phase replaces a portion of the original surface, thus reducing the total surface energy required for the nucleation. 2) Stresses building up during crystallisation due to the change in the volume can be more easily relieved at surface. 3) Surface crystallisation can also be accelerated by faster atomic transport on a free surface. 4) If the annealing treatments are not in a vacuum, the oxygen content near the surface may stabilize a number of crystalline phases. This leads to an increasing driving force for crystallisation at surface.

The surface crystallisation also has been confirmed with X-ray and Mössbauer studies of Ok and Morrish [1981] and Herzer and Hilzinger [1986]. The density measurements showed that a completely crystallised sample has a higher density than an amorphous sample. It follows that a crystallized layer at the surface of a ribbon contracts, causing a compressive stress on the internal amorphous portion of the ribbon and tensile stress in the crystallised region themselves. This stress distribution induces anisotropy easy axis perpendicular to surface in the amorphous bulk and parallel to surface in the

crystallised layer in Fe-based materials. Herzer and Hilzinger also showed that 1) Coercivity, H_c, increases quadratically with layer thickness for thin layers. For a thicker crystalline surface layer coercivity mechanism changes and H_c is determined by pinning of domain walls at the crystalline layer. 2) The remanent magnetisation of the material is a result of the crystallized surface, because of the in-plane anisotropy in this region.

Thomas [1991] studied the effect of the partial crystallisation on the engineering magnetostriction. He showed that the partial crystallisation increases λ_e. Therefore the measurement of λ_e could be another method to determine the induction of the perpendicular anisotropy in partly crystallised amorphous alloys.

4 Experimental Methods

4.1 Introduction

The majority of the work reported here was carried out on $Fe_{77.5}Si_{7.5}B_{15}$ amorphous wires with various diameters from 50μm to 140μm. The un-drawn and cold-drawn wires were supplied by Unitika Corporation, Japan and Dr A.O. Olafinjana, Department of Engineering Materials, Sheffield University, England. Relevant parameters on these wires are given in Table 1. This chapter will describe sample preparation, heat treatments and magnetisation, magnetostriction, ΔE, ΔG and damping measurements systems. X-ray diffraction and differential scanning calorimeter (DSC) systems will also be described briefly.

Alloy Type	Composition	Dia-meter (μm)	B_s (T)	T_c (°C)	T_x (°C)	E (MPa)	Supp. by
As-cast (AF-10)	$Fe_{77.5}Si_{7.5}B_{15}$	125	1.6	422	553	16.2	Unitika
As-drawn (DF-10)	$Fe_{77.5}Si_{7.5}B_{15}$	100	1.6	422	553	15.8	Unitika
As-cast	$Fe_{77.5}Si_{7.5}B_{15}$	140	1.6	422	553	16.5	Sheffield
As-cast	$Fe_{77.5}Si_{7.5}B_{15}$	95	1.6	422	553	15.8	Sheffield
As-cast	$Fe_{67}Si_{10}B_{15}Cr_8$	135	1.03	-	587	-	Sheffield

Table 4.1: List of the data on the wires used in this study.

4.2 Sample Preparation and Heat Treatments

As-cast amorphous wires can be heat treated in different ways to remove the large internal stress induced during the production process (Malmhall *et al* [1990] and Yamasaki [1990]) and to improve certain aspects of their behaviour. The easiest and most commonly used method is a heat treatment usually performed between just below the Curie temperature and just below the crystallisation temperature, sometimes in an external applied magnetic field. In this study, heat treatments were carried out in a furnace and by current annealing.

In furnace heat treatments, samples were cut with scissors to 7cm long for ΔE and magnetostriction measurements and to 22cm long for ΔG and damping measurements. Before annealing all the samples were cleaned with acetone to remove grease and dirt. A non-inductively wound tube furnace controlled by an Eurotherm temperature controller was used as in the annealing facilities. An aluminium plate was placed inside the tube furnace and allowed to equilibrate at the required temperature. The temperature of the plate was measured using a chromel-alumel thermocouple and the temperature was read on a Digitron meter.

The as-cast wire is received wound onto a reel. When the wire is removed from the reel, it has curled shape which is not suitable for use in the ΔE and ΔG measurement systems. To make the wire straight, before each anneal, the wire was inserted into a fine glass tube which was placed on the aluminium plate inside the furnace. When the annealing process was finished, the aluminium plate with the sample was taken out of the furnace and the glass tube was dropped onto a large cold aluminium plate. By this method a very rapid cooling rate of ~200°C/sec was obtained. The tube furnace, however, was found to have a temperature gradient along its length. The temperature is high in the

middle, decreases gradually around the middle part, then rapidly near the ends of the tube. For a 22cm long sample, this temperature gradient (~20°C difference between the ends of the wire at 450°C) causes some differences in the magnetic properties between the middle part and end sections of the sample (figure 4.1). To avoid this kind of problem, we inserted inside the tube furnace an aluminium thermal mass with an inner diameter of ~0.4cm. With the new thermal mass, the wire was inserted into a fine glass tube, then inserted into thermal mass. One end of the glass tube was kept outside the furnace. As soon as the anneal was finished, the glass tube was taken out and dropped onto a large aluminium plate.

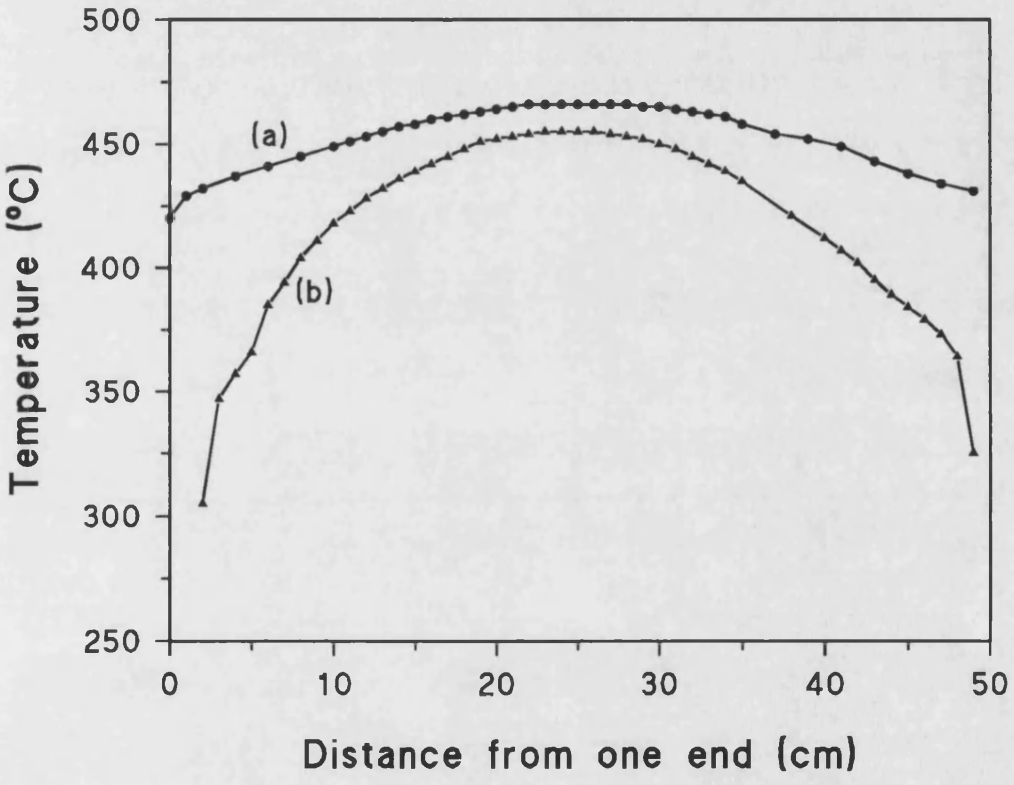

Figure 4.1: Temperature profile of tube furnace a) with big thermal mass, b) with small thermal mass.

Another method of relieving internal stress in the wires is current annealing. Wires were cut to 43cm lengths then inserted into fine glass tubes. Then each end of the wire was clamped and a dc current was applied along the wire. In order to measure the temperature of the wire, the change in the wire resistance was first measured as a function of temperature. This was done by putting the wire inside the furnace and increasing the temperature slowly (~5°C/min). During this process the resistance of the wire was measured using a multimeter. As can be seen from figure 4.2, the resistance increases approximately linearly with increasing temperature, up to T_x. When the temperature approaches the crystallisation temperature (~530°C) the wire resistance starts to decrease. Below ~480°C the wire resistance as a function of the temperature was fitted by the function;

$$\frac{R}{R_o} = (1 + \alpha(T - T_o)) \tag{4.1}$$

where R is resistance, R_o is resistance at room temperature, T is temperature, T_o is room temperature and α is the thermal resistance coefficient (~2.11×10^{-4} $°C^{-1}$) which is of the same order of previously reported values for amorphous alloys (Balanzat *et al* [1985]).

The change in R was then measured as a function of dc current. The data in figure 4.3 show that R varies approximately linearly with the square of current. The data were therefore fitted by the function;

$$\frac{R}{R_o} = (1 + \beta I^2) \tag{4.2}$$

where I is current. When the environment of the sample was changed a different β value was obtained, due to the change in heat absorption. Therefore each time the annealing condition changed the β value was re-calibrated. Typical β value is of the order of ~$0.15A^{-2}$. The current annealing temperature was derived from equation 4.3 which was obtained from equations 4.1 and 4.2:

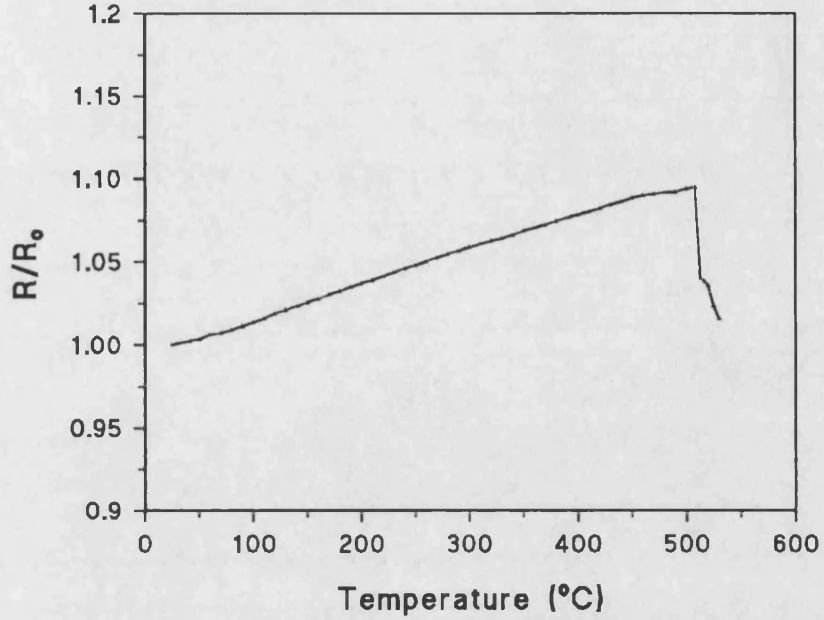

Figure 4.2: Temperature dependence of normalised resistance of FeSiB amorphous wire.

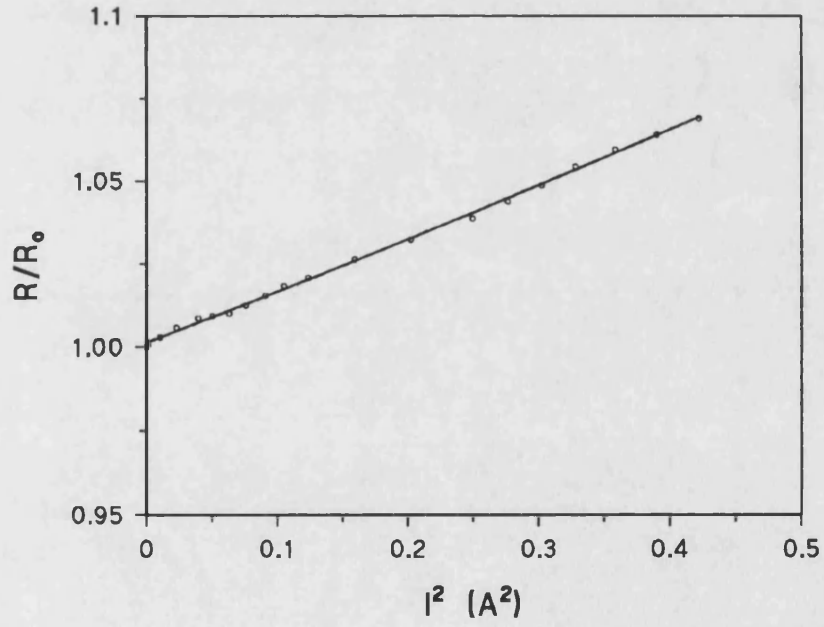

Figure 4.3: The change in the normalised resistance of FeSiB amorphous wire as a function of applied dc current.

$$T = \frac{\beta I^2}{\alpha} + T_o \qquad (4.3)$$

Transverse field annealing was carried out using a large water-cooled electromagnet with iron cores and a high temperature hot air blower (figure 4.4). The outlet of the blower was connected to a pyrex tube which was placed between the pole-pieces of the magnet. The wire was placed between two aluminium plates which were positioned horizontally in the pyrex tube directly between the centre of the pole pieces. Temperature was measured by means of a thermocouple attached to one of the aluminium plates. The maximum field produced using rectangular pole pieces is about 150 kA/m with a 5.5cm pole piece separation and is not enough to overcome the demagnetisation effect in the wire in the radial direction. Therefore the pole-piece shape was re-designed to be capable of producing a field of 875 kA/m with a 0.5cm pole piece gap. The field between the magnets is shown as a function of distance from the centre in figure 4.5. To obtain maximum field, the gap between the magnets was kept very small (~0.5cm). The sample was heated up by applying dc current. The wire temperature was found by the method explained above and the β value was re-calibrated.

4.3 Magnetic Measurements

The magnetic parameters of the amorphous wires were obtained from M-H (magnetic hysteresis) loops which give values of coercivity, remanent magnetisation, susceptibility and anisotropy constant. The system used (described by Squire *et al* [1988]), consists of a solenoid 1.5m long and of 7.5cm internal diameter. The solenoid was driven by a Kepco ±20A,±20V bipolar power supply such that a field of up to 15kA/m could be produced along axis of the solenoid. Two search coils, 8.2cm in length with 20000 turns were placed symmetrically inside the big solenoid, 47cm apart, on an aluminium frame.

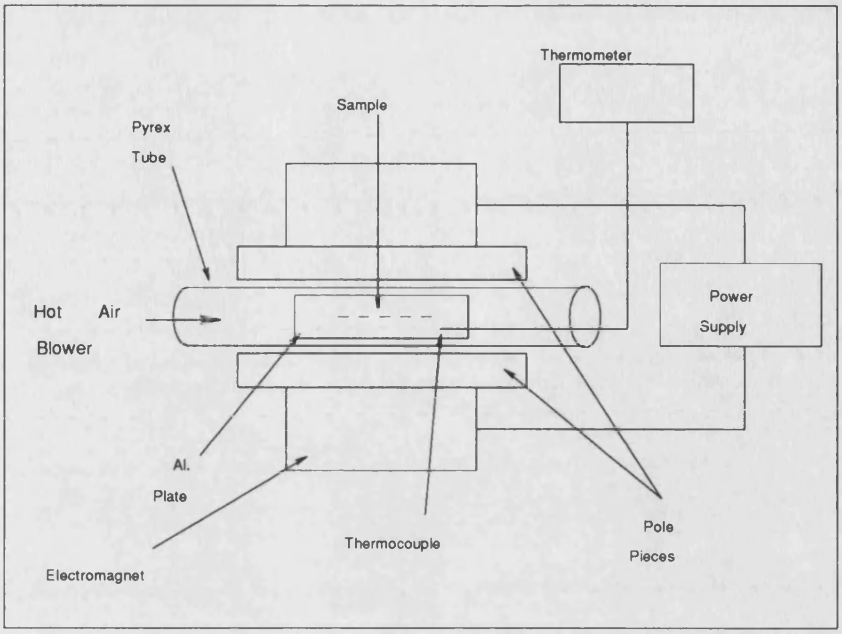

Figure 4.4: Block diagram of field annealing system.

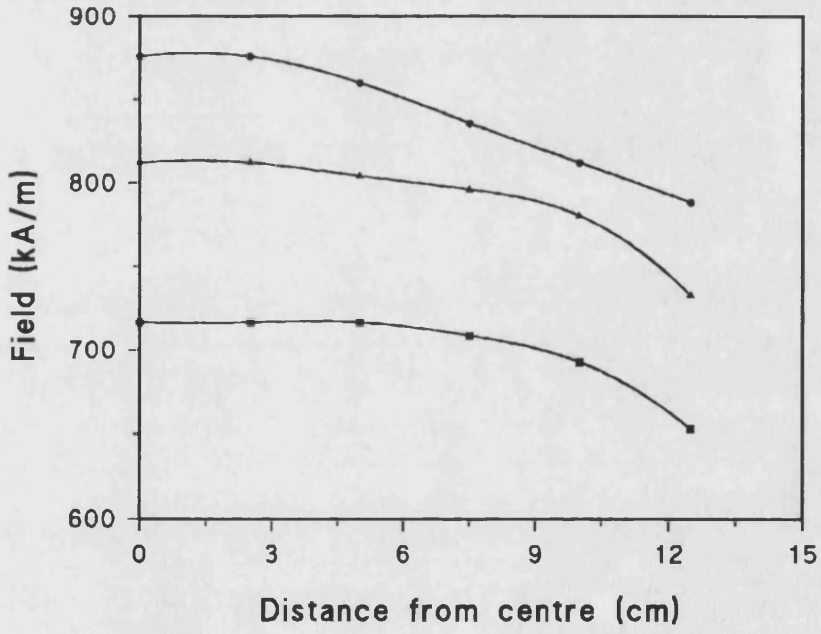

Figure 4.5: Measured field profiles between the pole pieces with driving currents 10, 20 and 25 Amps.

The search coils are arranged in a bridge circuit such that, in the absence of any sample when the field is applied, the total output is zero. When a ferromagnetic material is placed into one of the search coils and subjected to a magnetic field, the voltage ,V_1, induced in the search coil is given by Faraday's law:

$$V_1 = n\mu_o \frac{d}{dt}(A_c H + A_s M) \tag{4.4}$$

where μ_o is the permeability of free space, M is the magnetisation, A_c is the cross-sectional area of the search coil and A_s is the cross-sectional area of sample and n is the number of turns on the search coil. In the absence of any sample, the induced voltage, V_2, is:

$$V_2 = n\mu_o \frac{d}{dt}(A_c H) \tag{4.5}$$

The total output, V_o is the difference between equation 4.4 and equation 4.5, i.e:

$$V_o = n\mu_o \frac{d}{dt}(A_s M) \tag{4.6}$$

The time integral of the resulting output is proportional to the change in the magnetisation of the material.

The magnetisation of the sample was obtained by assuming that the sample was saturated at large magnetic fields (~8kA/m). Then the vertical axis was scaled by normalising measured magnetisation value at maximum applied field to the manufacturer's value of saturation magnetisation, M_s.

The cycling of the current through the solenoid (and of hence applied field) was controlled by computer. The power supply was operated in voltage mode. The required maximum field was set by adjusting a potentiometer across the power amplifier input. H was

determined from the measured potentiometer voltage and the number of turns on the solenoid. In soft magnetic materials such as amorphous wires, much of the M-H information could easily missed, if the applied field was stepped at a constant rate with time, because a very large change in magnetisation takes place in a small range of applied field. Therefore, the applied field was controlled by a shape function in order to get large steps in field around the maximum H, H_{max}, and small steps in field around H=0A/m. The function defined in the computer program is:

$$\frac{H}{H_{max}} = \frac{\tan(2b\pi t/T)}{\tan(b\pi/2)} \quad (0 < b < 1) \tag{4.7}$$

where t is current step number, T is the total number of steps and b is an adjustable shape factor. Small values of b lead to an almost linear change in H and larger values give a sharply peaked function. b can be adjusted to larger values to obtain more information in the low field region and to low values to get more information about the saturation of the sample.

One of the important problems in obtaining a closed loop with dc magnetisation measurement systems is drift. It was found that the total drift is almost linear with time, so drift correction was made by sharing the total drift at the end of the cycle equally among the individual points. Due to the geometry of the search coils, which were designed for ribbons, M-H loops of the amorphous wires were usually noisy. We reduced the noise level by cycling M-H measurements 3-4 times and taking the mean M values.

4.3.1 Calculation of Magnetisation Parameters

4.3.1.1 Coercivity

The M-H program includes a procedure to calculate coercivity. The program calculates H_c firstly by taking only 3 points on each side of the M-H data around M=0, and fitting

straight regression lines to these data sets. These lines are used to calculate the H values at zero magnetisation and H_c is taken as half the difference between these values. Then H_c is recalculated using 5 points around M=0 and the two values of coercivity are compared. If these values are not in agreement within a given tolerance (typically~0.01% the same process is repeated with two more points in each regression line, up to a maximum of 11 points. If there is still a big difference in H_c values, the same process was repeated with a greater tolerance value. In amorphous wires, due to a Large Barkhausen Jump at very low field, an accurate calculation of coercivity is difficult, because there is often no point around M=0. Therefore, some of the H_c calculations were performed manually. The M-H loop was taken from the plotter and half of the distance between M-H lines around M=0 was measured with a ruler. The distance to the maximum field (known) was also measured. By comparing these measurements, the first was converted to a value of H_c.

4.3.1.2 Internal Field

The internal field inside the sample, H_i, is always smaller than the applied field, H_a, due to the demagnetisation field. Poles are induced at the end of the sample leading to an internal field in the opposite direction to the applied field. Therefore, all the magnetic parameters have to be corrected. The internal field is reduced by the demagnetisation field, H_d.

$$H_i = H_a - H_d \tag{4.8}$$

where $H_d = N_d.M$ and N_d is the demagnetisation factor, which depends on the shape of the sample. H_i as a function of true susceptibility, χ, is given by:

$$H_i = \frac{H_a}{1 + N_d\chi} \tag{4.9}$$

In this study, data for M-H, ΔE, ΔG and damping measurements are given as a functions of applied field.

4.3.1.3 Anisotropy Constant

Anisotropy energy was determined from the area between the M-H loop and the M axis. This is given by:

$$U_k = \int_0^{M_s} \mu_o H dM \tag{4.10}$$

The area was calculated from M-H data by a computer program. This area is strictly the magnetisation energy which is taken to be a measure of anisotropy constant, K.

Another method to calculate anisotropy constant was given by Livingston [1982] who assumed that magnetisation occurs due only to moment rotation and that magnetisation is proportional to H until M reaches the saturation value M_s. This model can be used for transverse field annealed samples. Susceptibility and anisotropy energy for transversely annealed samples are given by:

$$\chi = \frac{M_s}{H_k}, \quad U_k = \frac{\mu_o H_k M_s}{2} \tag{4.11}$$

where H_k is the anisotropy field (the field at which magnetisation reaches the saturation value). The anisotropy energy in terms of the anisotropy constant can be written as:

$$U_k = -K_u \sin^2\theta \tag{4.12}$$

where θ is the angle between the applied field and the magnetisation. For a transverse field annealed sample θ is 90° and from equations 4.11 and 4.12,

$$K_u = \frac{\mu_o M_s^2}{2\chi} \qquad (4.13)$$

According to equation 4.13 K_u can be calculated from the true susceptibility.

4.4 Fibre Optic Dilatometer

The fibre optic dilatometer system measures the small changes in the length of a sample associated with magnetostriction. The full details of the system were given by Squire and Gibbs [1987] and Thomas [1991]. Figure 4.6 shows the basic principles of the system. One end of the sample was clamped and the other end was placed across the centre of the light beam. When the sample lengthens, it reduces the amount of light detected by a photo detector behind the sample. If it is assumed that the light (beam) power is distributed uniformly across the fibre and that the total change in the length of the sample is smaller than the diameter of the light beam, D, the variation of transmitted power, P, as a function of l is given by,

$$\frac{dP}{dl} = \frac{4P_o}{\pi D} = \text{Constant} \quad (dl \ll D) \qquad (4.14)$$

where P_o is the transmitted power without any sample in the system.

The block diagram of the fibre optic dilatometer is shown in figure 4.7. The fibre optic emitter is driven by a 10 kHz power supply and output of the emitter is split into two channels. One of the signals is coupled to the sample by an optical fibre. The transmitted optical power is detected as shown in figure 4.7. The transmitted power carried by an optical fibre is input to a signal detector. It is then combined with the second output from the splitter such that the total output from the combiner is zero when the sample is halfway across the fibre. Then the total signal output is fed into the lock-in amplifier with the AC emitter supply voltage. The dc output of the lock-in which is directly proportional

to change in the length of the sample, is connected to a computer. The change in the length of the sample (magnetostriction) is obtained as a function of applied field by means of a computer program.

The magnetic field is supplied by a pair of Helmholtz coils having a diameter of 400mm. These allow samples up to 130mm long to be in a magnetic field uniform to within 1%. Driven by a Kepco ±12A,±36V bipolar power supply, the Helmholtz coils are capable of producing magnetic fields of up to 8kA/m. The magnetic field is stepped in a way similar to that in the M-H system.

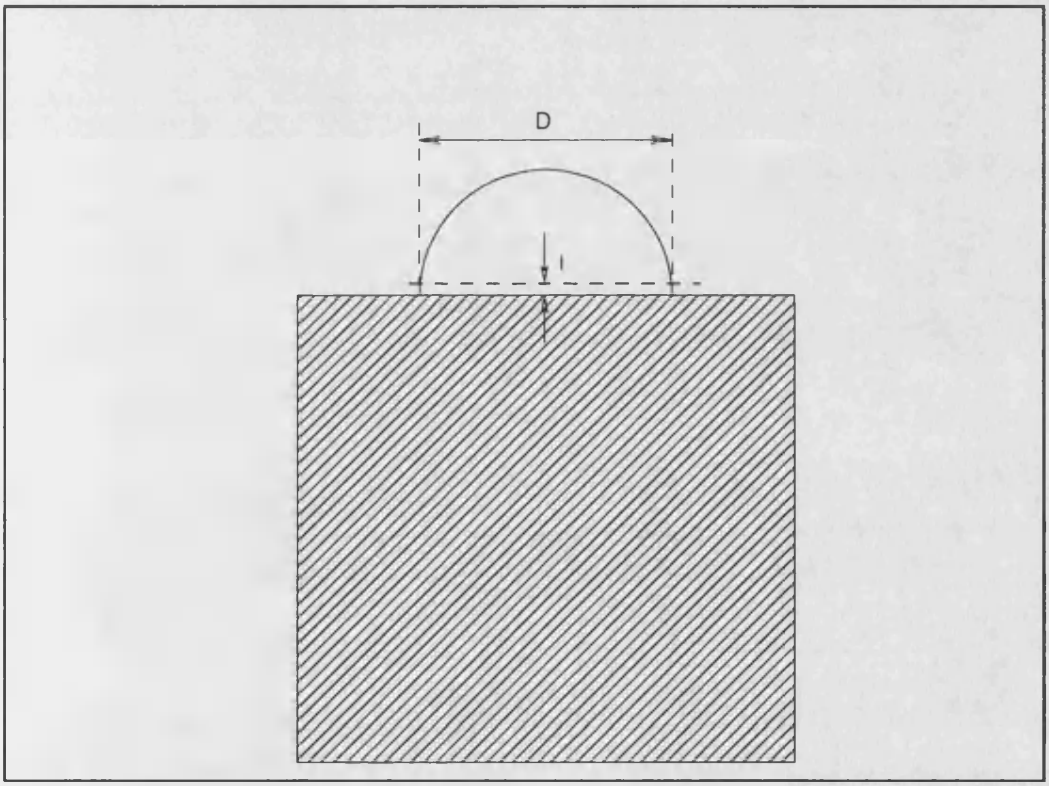

Figure 4.6: Geometry of the fibre sample (reproduced from Squire and Gibbs [1987]).

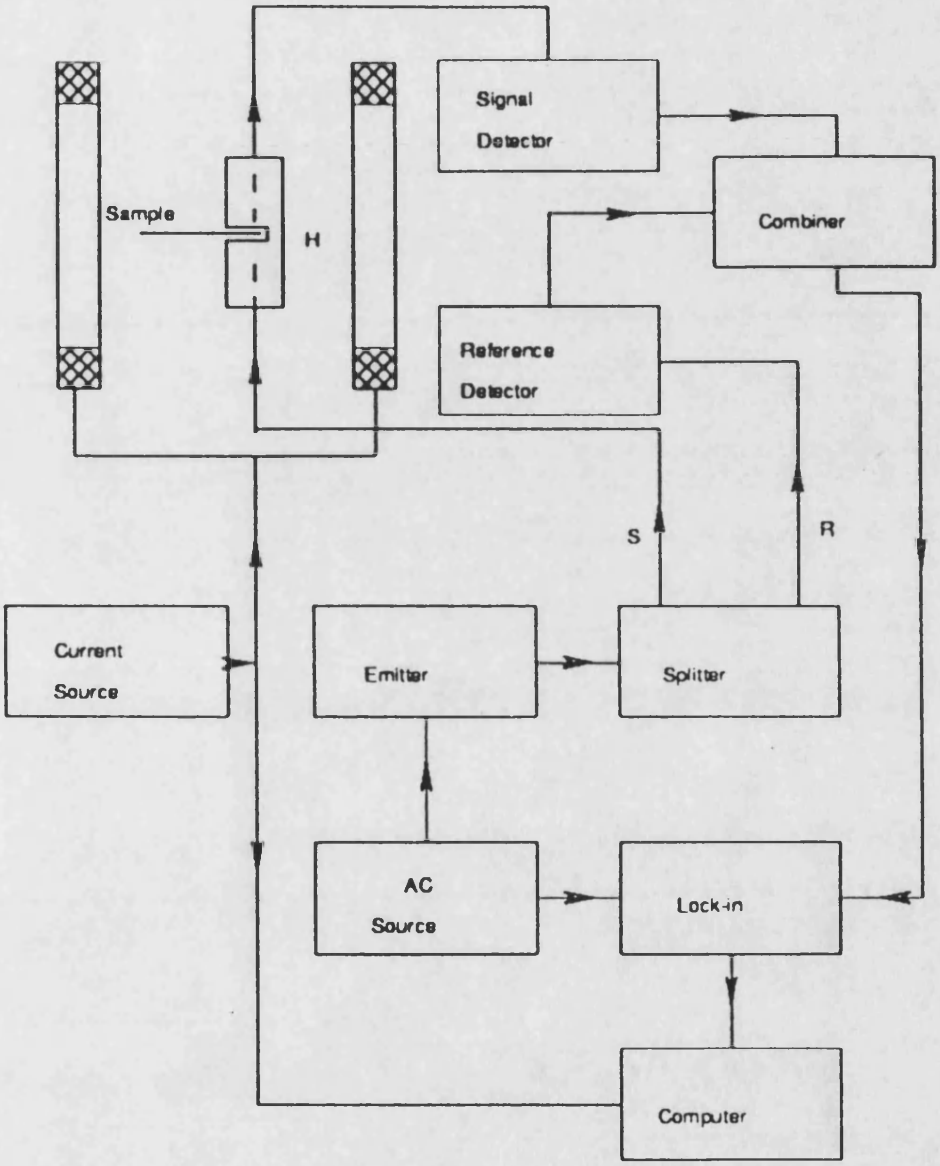

Figure 4.7: Block diagram of the λ-H system (after Squire and Gibbs [1987]).

Because of the shape and the small diameter of the amorphous wires, the method of supporting the sample during the measurement of magnetostriction in ribbons could not be used (Thomas 1991). Therefore, the wire was placed in a holder (shown in figure 4.8) which consisted of a glass slide and a glass tube. The glass tube was fixed to the glass with masking tape. A very light aluminium foil was attached by adhesive to one end of the wire. Then the wire was inserted into the glass tube (of internal diameter of 0.15mm). The free end of the wire was clamped by a Tico pad. Tico pad was used, because it is strong enough to avoid any straining and damaging of the sample. The aim of placing the wire inside a fine glass tube is to prevent the wire moving horizontally or vertically. This kind of motion leads to a change in the measured strain. Before each measurement the sample and glass tube were cleaned with acetone to remove dirt and grease which might cause static friction between the wire and the glass tube.

Calibration of the System:

The sample, with the holder was placed in an aluminium holder which was mounted on an x-table which could be moved by turning a screw. The wire was positioned with its length parallel to the x-table motion and its end connected to aluminium foil across the optical fibre. The intensity of the light beam was detected by a photo detector with respect to the relative position of sample in the x direction. The x-table was moved until the edge of the aluminium foil lay in the central region of the fibre. Then the output of the combiner was adjusted to be zero and lock-in amplification was set to a suitable position. Then the calibration factor, C, between the lock-in output, V_o, and the sample position was obtained by moving the aluminium foil edge (by moving the x-table) across the width of the fibre and meanwhile reading V_o from the lock-in. V_o as a function of the

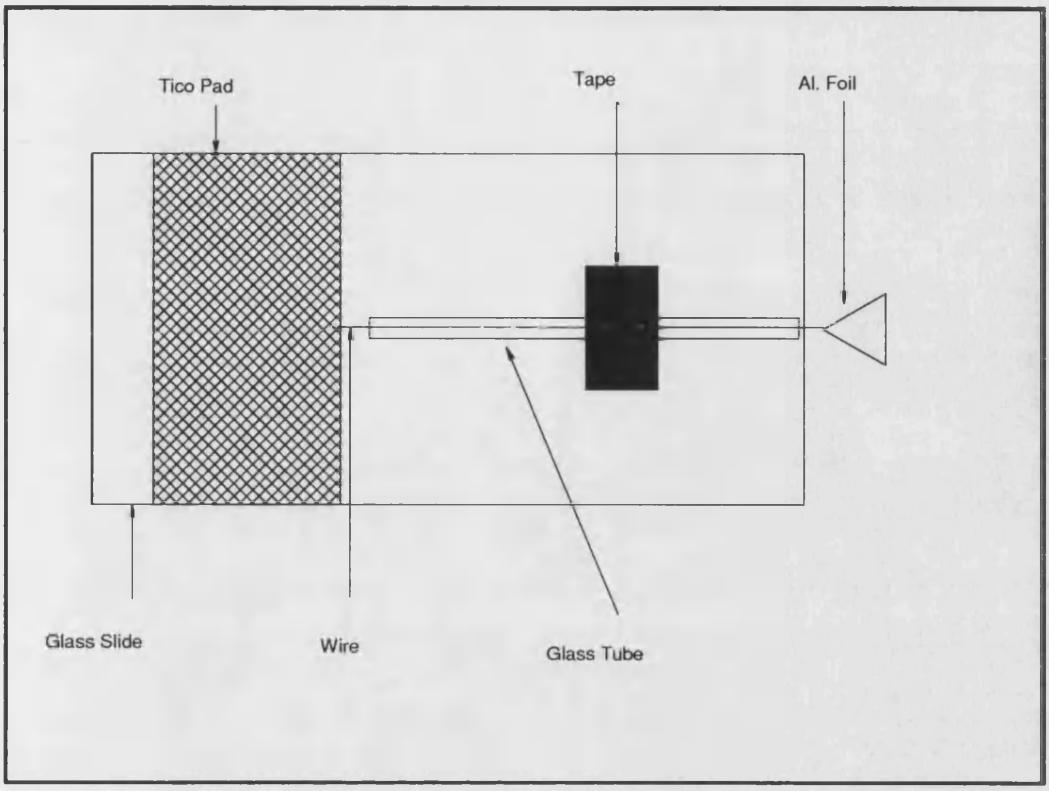

Figure 4.8: Sample holder for the λ-H system.

position of sample is linear over the whole range (figure 4.9). By calculating the gradient, dV_o/dl, C was obtained. Calibration was done before each measurement since C was different for each set-up.

Sources of Error:

The largest errors in λ-H measurements are caused by the tico pad clamping, the measurement of the sample length, the aluminium foil not being centred between the fibres, the wire length not being positioned parallel to the magnetic field axis, lateral motion of the wire and by mechanical friction between the wire and the glass tube. Another important problem is the thickness of the glass tube. If the thickness of tube is large, as shown in figure 4.10, the wire will be bent. There will be static friction between the edge of the tube and the wire. Typical λ-H loops of amorphous wires are shown in figure 4.11 with lateral motion and in figure 4.12 with no lateral motion.

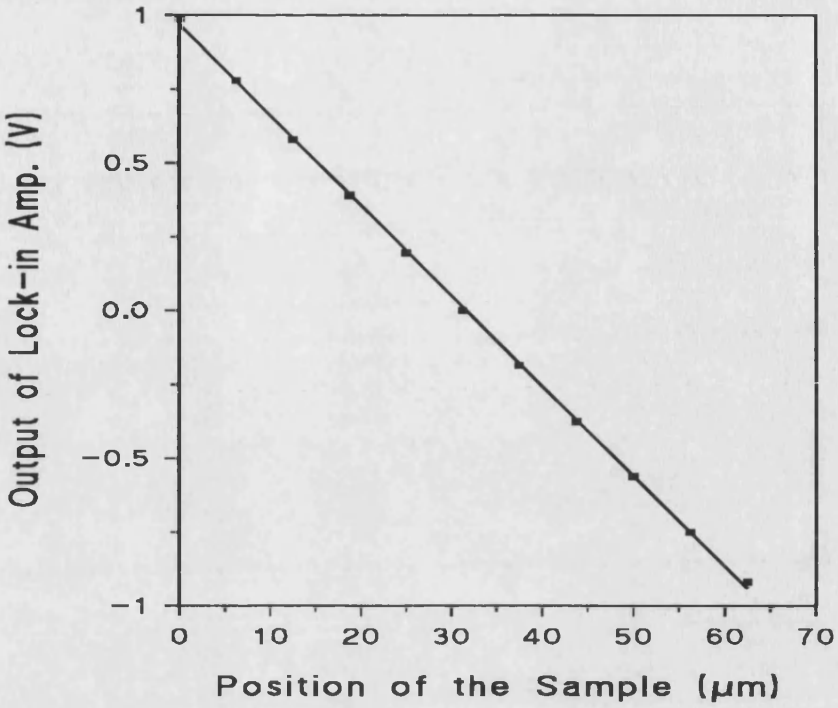

Figure 4.9: Typical lock-in amplifier output as a function of the position of the sample.

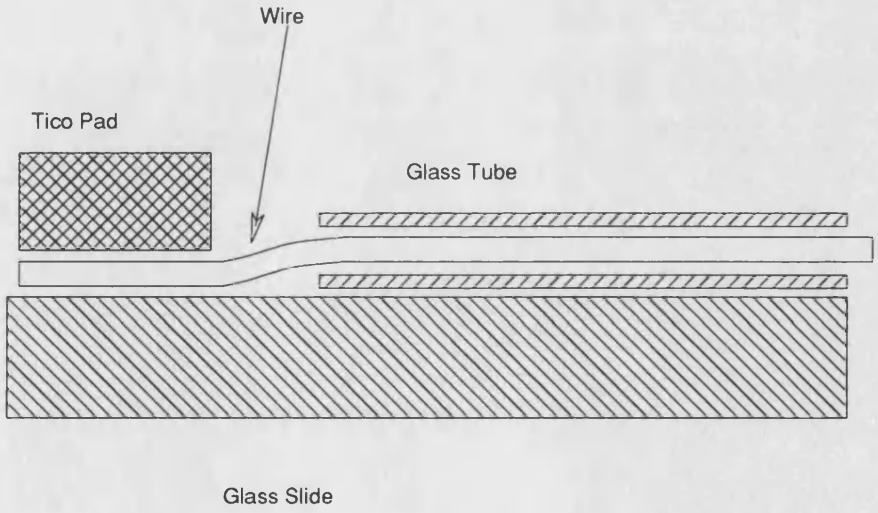

Figure 4.10: Sample holder for λ-H system where there is a friction between edge of the glass tube and sample.

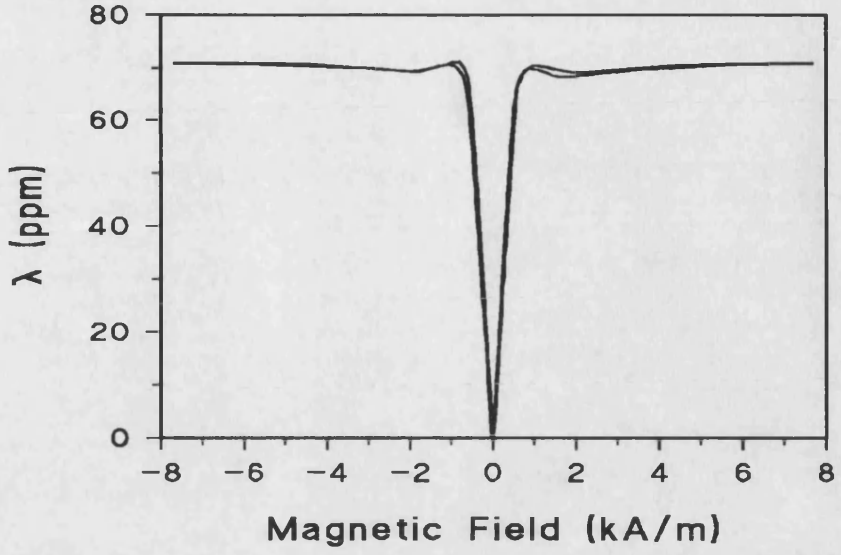

Figure 4.11: Typical measured λ-H loop of FeSiB wire with lateral motion.

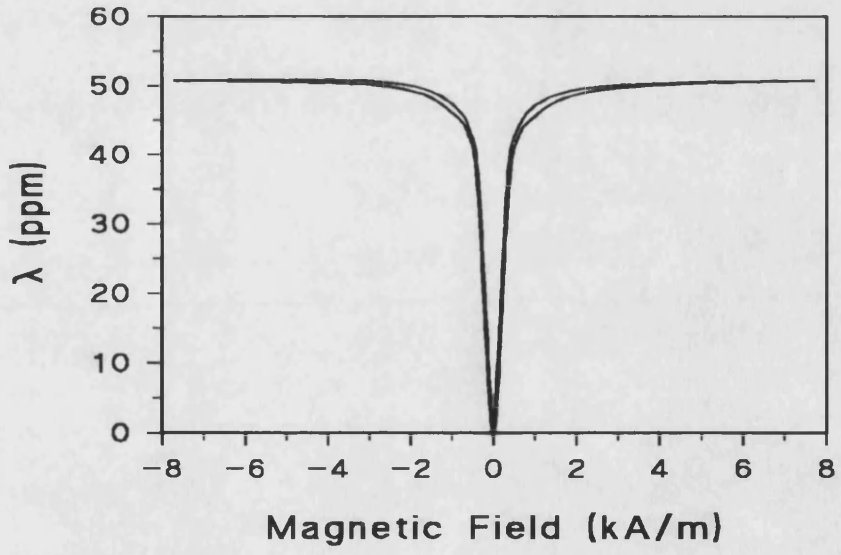

Figure 4.12: Typical valid λ-H loop of stress relieved FeSiB wire.

4.5 ΔE Measurement System

The Young's modulus, E, as a function of applied field was measured by a vibrating reed method adapted from that of Berry and Pritchet [1975]. The system was modified for wires by using an optical vibration detector in the place of the original electrostatic method (figure 4.13.a). The amorphous wire was clamped with a 2.5cm free length from one end. The clamp was connected to a mechanical vibrator driven by a variable frequency signal generator with a sinusoidal output. The vibration of the clamp leads to oscillation of the wire. The amplitude of this oscillation reaches the maximum value when the wire is driven at the resonant frequency of one of the vibrational modes.

The basis of the vibration amplitude measurement system is shown in figure 13.b where a and b are two photo diodes. The wire is placed with its axis parallel to the axis of the coil halfway between the coils and between the laser source and the photo diodes. The outputs of the photo diodes are connected to a differential amplifier. When the wire is not vibrating, the output from the differential amplifier is zero because both photo diodes receive the same amount of light intensity. When the sample starts to vibrate, the sample first moves towards one of the photo diodes (for example, diode a). In this case, the photo diode b receives a larger amount of the light, therefore $V_b > V_a$. An output is obtained from the differential amplifier, because the differential output $V_o = V_a - V_b$. Then the sample moves towards photo diode b, leading to $V_a > V_b$. At resonance frequency, this vibration gives rise to sinusoidal output from the differential amplifier at the resonant frequency. This output was connected to a phase sensitive detector (PSD). The output of the signal generator is also fed to the PSD as a reference signal (figure 4.14). The PSD output is directly proportional to the amplitude of the vibration. The resonance frequencies were read from a counter.

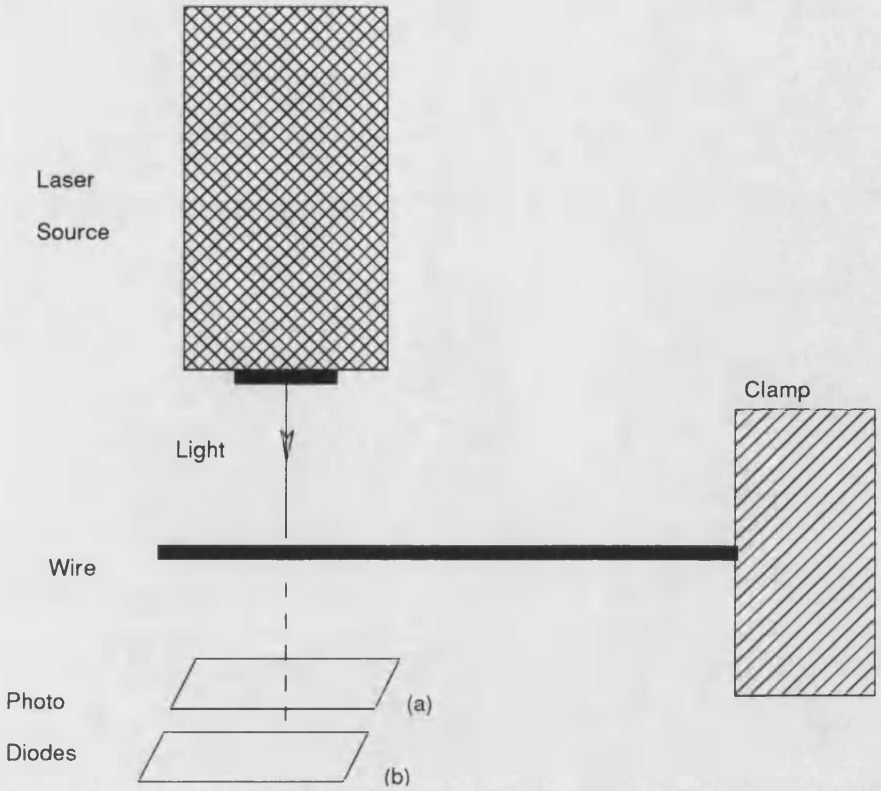

(a)

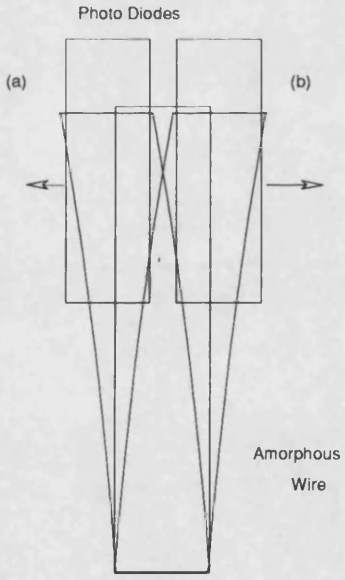

(b)

Figure 4.13: Optical detection system of the vibration of the wire.

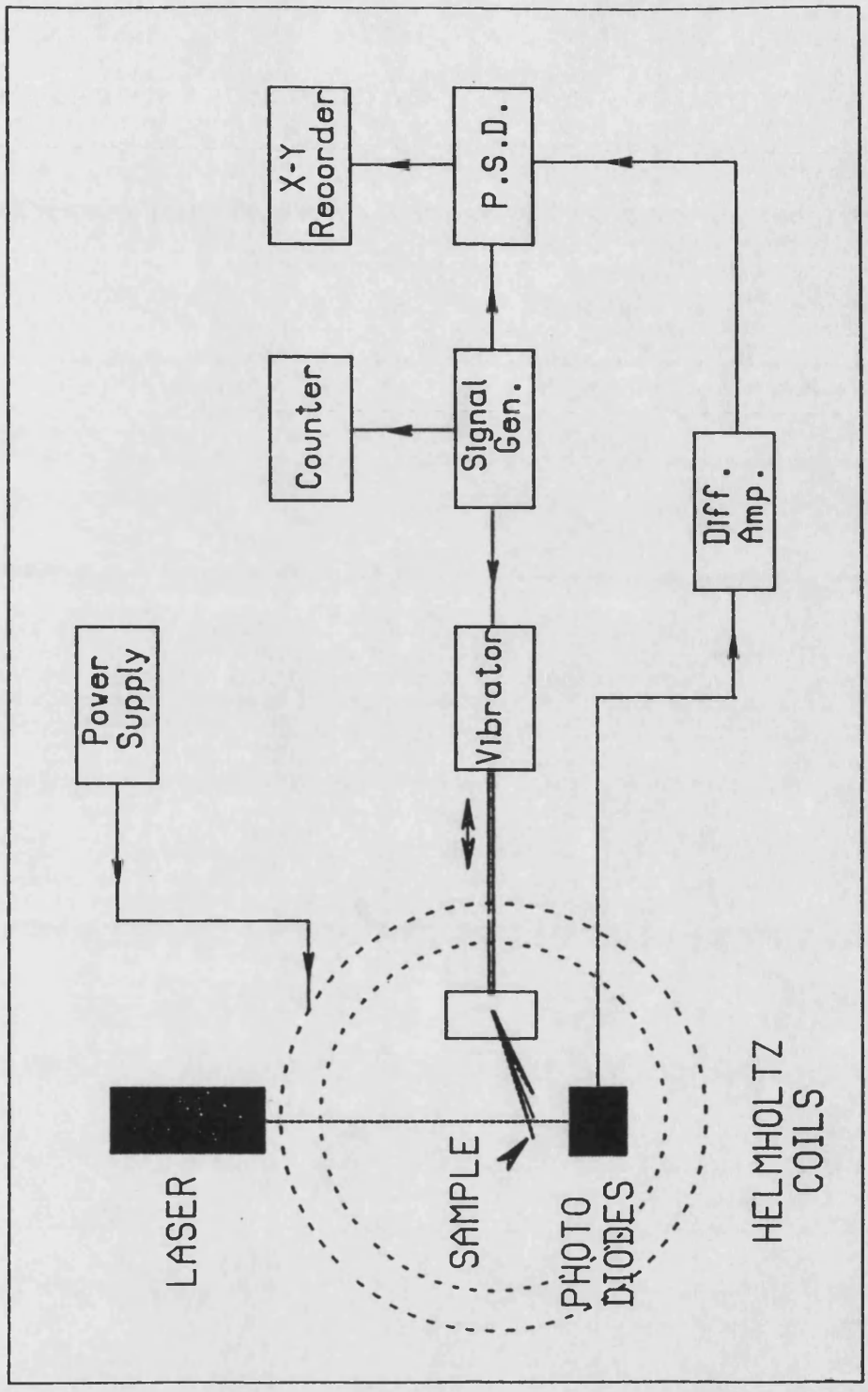

Figure 4.14: Block diagram of ΔE system.

The magnetic field was supplied by a pair of Helmholtz coils having a diameter of 20cm. The coils were driven by a dc power supply. The field was calibrated with respect to coil current using a Hall effect Gauss meter. The calibration coefficient from current to magnetic field was 3.63×10^3 A/m per Amp. The maximum field used was 7.2 kA/m which was sufficient to saturate most of the wires.

Before each measurement the sample was saturated and the frequency of the fundamental mode was measured. Then, the frequencies of the second and third modes were measured. The fundamental resonant frequency at saturation for FeSiB wire with a diameter of 125μm usually occurred between 90 and 150Hz. Under the ideal conditions the frequencies of the modes increase in sequence, as shown in table 4.2.

Vibration Mode	Ratio of Frequencies				
	1	2	3	4	5
1	1				
2	6.27	1			
3	17.55	2.80	1		
4	34.40	5.49	1.96	1	
5	56.80	9.07	3.24	1.65	1

Table 4.2. Relative ratio of vibration modes of sample (deduced from Nowick and Berry [1972]).

The magnetic field was always stepped from negative saturation to positive saturation with larger steps at higher fields and smaller steps at low fields. In this study, all the Young's modulus measurements as a function of H were performed using third mode.

For one end clamped and one end free to oscillate, the shape of the fundamental and odd modes are given by Nowick and Berry [1972] and Berry and Pritchet [1979] as,

$$y_n(x) = \frac{A_o}{2}\left\{\frac{\cosh(2\alpha_n x/l)}{\cosh\alpha_n} + \frac{\sin(2\alpha_n x/l)}{\sin\alpha_n}\right\} \qquad (4.15)$$

where n=1,3,5 ..... . The shape of even modes (n=2,4,6.....) are given by,

$$y_n(x) = \frac{A_o}{2}\left\{\frac{\sinh(2\alpha_n x/l)}{\sinh\alpha_n} + \frac{\cos(2\alpha_n x/l)}{\cos\alpha_n}\right\} \qquad (4.16)$$

In equation 4.15 and 4.16 $y_n(x)$ is the lateral displacement of the sample, of free length, l, at a distance, x, from the midpoint taken as the origin. A_o is the amplitude at the free end ($y=A_o$ at $x=l/2$). The mode parameters α_n have the values $\alpha_1=0.29843\pi$, $\alpha_2=0.74709\pi$, $\alpha_3=1.25013\pi$ and thereafter can be taken as $\alpha_n(n>3)=(n-0.5)\pi/2$.

To obtain Young's modulus, the strain energy ,W_n, stored in the sample is found by evaluating integral:

$$W_n = (EI/2)\int_{(-l/2)}^{(l/2)} (d^2y/dx^2)^2 dx \qquad (4.17)$$

where I is the second moment of area of cross-section of the wire about the neutral axis ($I=\pi r^4$, r is the radius of the wire). The results for all modes is given by,

$$W_n = \frac{1}{2}\left(\frac{4\alpha_n^4 EI}{l^3}\right)A_o^2 \qquad (4.18)$$

From $W_n=K_nA_o^2/2$ and $f_n = (1/2\pi)(K_n/m)^{(1/2)}$ where K_n is the effective spring constant and m is total mass of sample, E as a function of frequency is obtained:

$$E = \frac{\pi \mu l^4}{4\alpha_n^4 r^4} f^2 \qquad (4.19)$$

where μ is the mass per unit length of the wire. The absolute value of E can be calculated from equation 4.19, but E is proportional to l^4/r^4 and r is not uniform along the length of the wire. As a result, a small error in the measurement of l or r leads to a large error in the E value. Instead of taking the absolute value of E for different H values. $E(H)/E_s$ was measured a function of H.

The resonant frequencies in a field H, f(H), and at saturation, f_s, are related to the Young's moduli in H, E(H), and at saturation, E_s, by:

$$\frac{E(H)}{E_s} = \left(\frac{f(H)}{f_s}\right)^2 \qquad (4.20)$$

The magnetic field was changed manually from the power supply and at each different field the resonant frequency was found by manually changing the driving frequency from the signal generator. Hence $E(H)/E_s$ was obtained. A typical $E(H)/E_s$ curve as function of H is shown in figure 4.15 for stress relieved FeSiB amorphous wire.

The driving amplitude, which is applied from oscillator to the vibrator, dependence of Young's modulus was observed at low fields (figure 4.16). To minimise the amplitude dependence, the sample was driven with a very small (typically ~0.3V) signal amplitude and during the measurement, the same drive amplitude was used.

The error in setting the current through the Helmholtz coils is very small (approximately ±1A/m) which corresponds to less than 0.1% error in values of the applied field. Another source of error is reading the resonant frequency of vibration which is also very small (~0.01%). Therefore, error bars are not shown in E(H)/E versus H data sets.

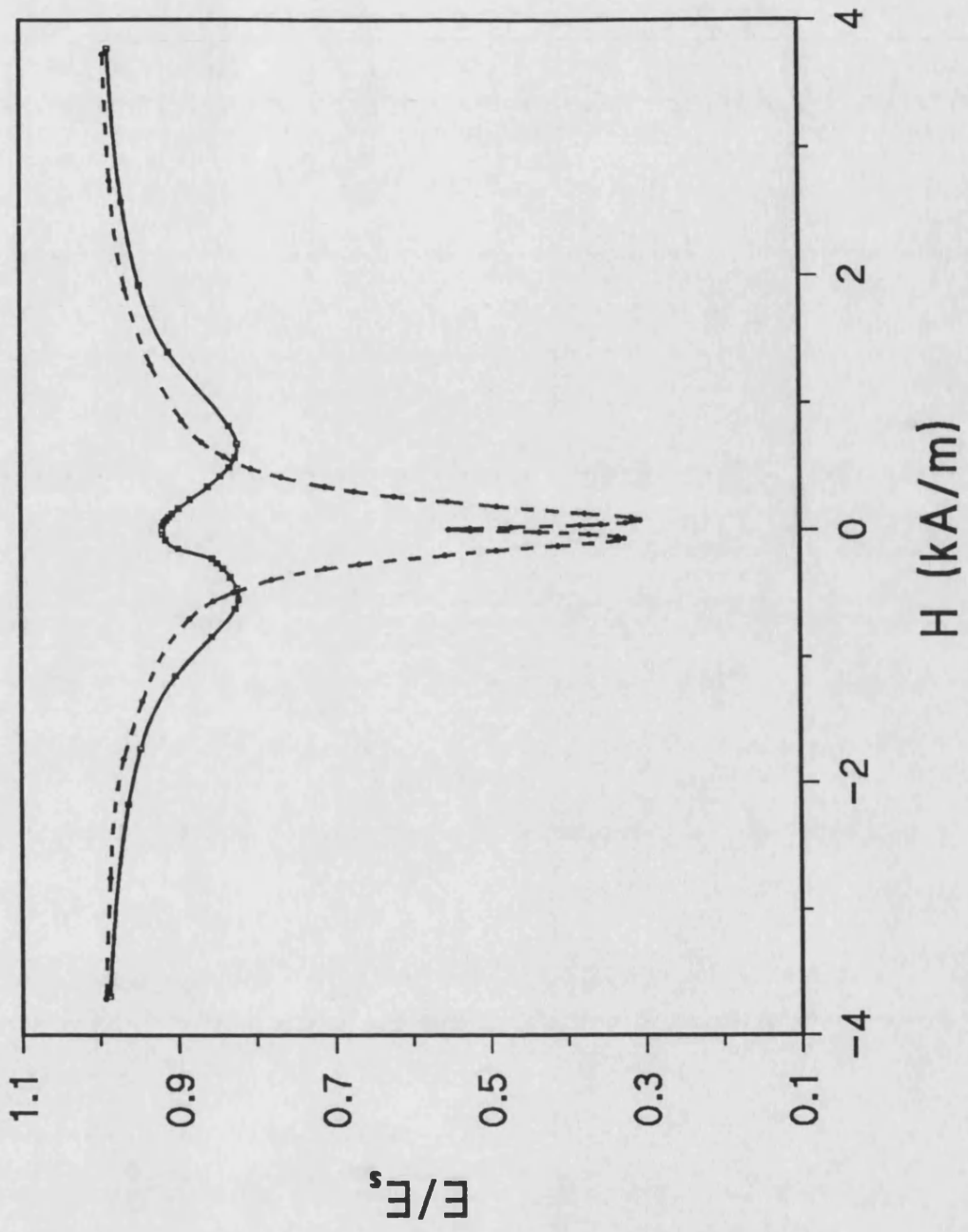

Figure 4.15: Typical ΔE data for stress relieved FeSiB wires.

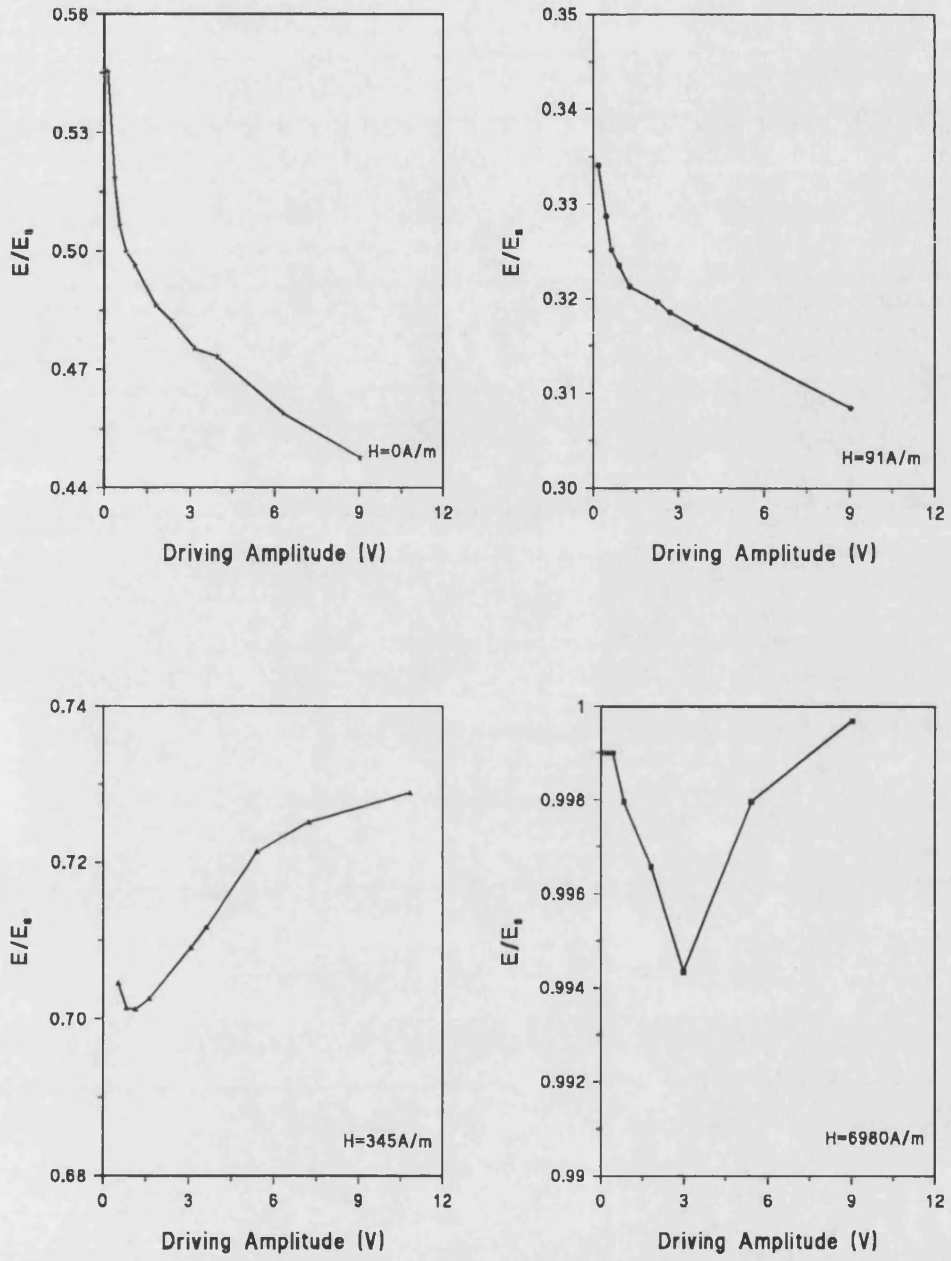

Figure 4.16: Examples of E/E_s data of stress relieved FeSiB wire as a function of driving amplitude for different applied fields.

The main problem with the $E(H)/E_s$ measurements (especially for the wire annealed at high temperature for short annealing time) was that the minimum value of E was not the same on the positive side of applied H as on the negative side (figure 4.17). It was assumed that this is due the some irreversible magnetic process in the wire.

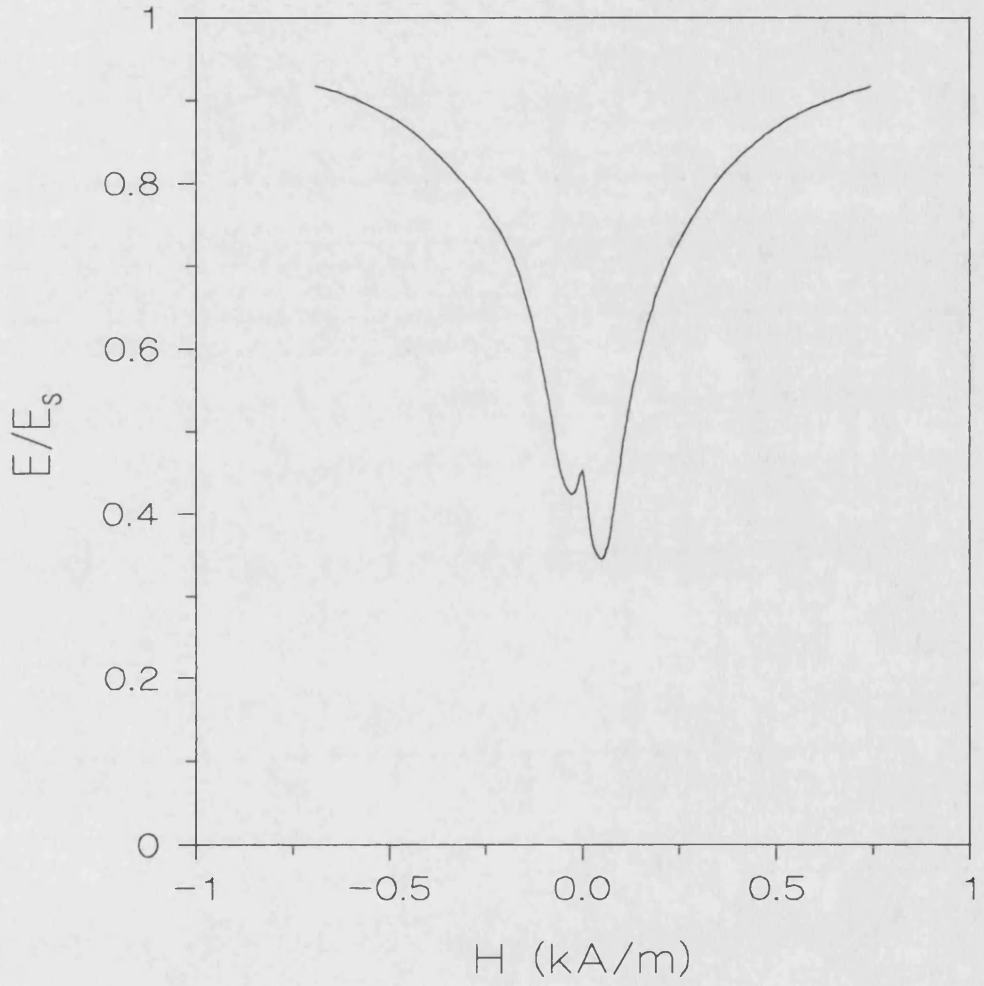

Figure 4.17: Typical ΔE for the FeSiB wire annealed at 480°C for 1 minute (notice the minimum of Young's modulus are not same).

4.6 ΔG and Damping Measurement System

A simple torsional pendulum system is one of the easiest ways to measure the shear modulus and the damping of the wires. When a wire is suspended in a such way that a torque is applied to the free end of the wire, it will be twisted; then, if the torque is removed, the restoring force generates an angular acceleration. This angular motion of the wire can be described by the differential equation (Bozorth [1951]):

$$\frac{d^2\theta}{dt^2}+2k\frac{d\theta}{dt}+\frac{\tau}{I}\theta=0 \qquad (4.21)$$

where θ is the angle of twist, k is the damping constant, I is the moment of inertia and τ is the oscillation constant. The solution of this differential equation is:

$$\theta=\theta_o\exp(-kt)\cos(\omega_o t+\phi) \qquad (4.22)$$

where θ_o is the amplitude of the oscillation and ϕ is the phase.

One of the methods of measuring the damping is to determine the rate at which the oscillations of the system die out (Cullity [1972]). If A_n is the amplitude of any one of the oscillations and A_{n+1} that of the next, then the extent of the damping is characterised by the logarithmic decrement, Q^{-1}, defined by:

$$Q^{-1}=\ln\frac{A_n}{A_{n+1}} \qquad (4.23)$$

In equation 4.22 the amplitude part of the oscillation is given by $\theta=\theta_o\exp(-kt)$. For one complete oscillation, t can be substituted by the period of the oscillation, T.

$$Q^{-1}=\ln\frac{\theta_n}{\theta_{n+1}} \qquad (4.24)$$

$$Q^{-1}=kT=\frac{2\pi k}{\omega_o} \qquad (4.25)$$

Equation 4.25 gives the damping value and the angular frequency of the oscillation is given by,

$$\omega_o = \sqrt{\frac{\tau}{I}} \tag{4.26}$$

For a twisted wire τ is:

$$\tau = \frac{G\pi r^4}{2l} \tag{4.27}$$

From equations 4.26 and 4.27, G can be obtained as a function of the period:

$$G = \frac{8\pi l I}{r^4 T^2} \tag{4.28}$$

In the experiments reported here, G was measured using two different systems: a fibre optic system and a linear rotary differential capacitance system.

In the fibre optic system, the top end of the amorphous wire was connected to an aluminium rod and the other end was connected to an aluminium tube. Also, a very light plastic tube was attached to the aluminium tube. One end of the optic fibre was the emitter of the of light, and the other end was the receiver.

The oscillation of the wire led to oscillation of the aluminium tube . Each time the plastic tube passed between the fibre optic cables, a pulse was obtained. When the plastic tube was not between fibre cables the output was zero. The time between each pulses was half the period of the oscillation. This was doubled using a D type flip-flop to obtain the period of the oscillation which was then measured using a counter. The shear modulus of the wire was then calculated from equation 4.28. All the measurements performed using the fibre optic system were done under a tensile stress of ~9MPa.

Having observed large tensile stress dependence of damping and shear modulus an inverted pendulum was designed. With the inverted pendulum system, so-called rotary differential capacitance system, damping and G as a function of magnetic field, tensile stress and torsional strain was measured. Figure 4.18 shows the general arrangement of the pendulum. The wire specimen W, of length 20cm, is held by two rods. The lower rod R_1 (aluminium) is supported by a rigid base A which has provision for fine angular adjustment. The upper rod R_2 is of telescopic brass tubing about 4mm in diameter. Its upper end is attached to the central disc of the three plate capacitor C. Therefore, rotation of the wire directly leads to rotation of the central plate of the capacitor C. The central plate is suspended by a thread T of unspun silk from a 3mm diameter brass rod B which acts as the beam of a counterbalance, pivoted on the knife edge K, and carrying a mass M at its other end. By varying the M, various tensile stresses can be applied to the wire. A and S are both mounted rigidly on a vertical optical bench to facilitate precise alignment and positioning. The solenoid S is 35cm long and has a bore of 5cm; it produces a magnetic field of up to 8kA/m. The coil is driven by a dc power supply. The variation of H along the coil axis is shown in figure 4.19. H was calibrated with respect to coil current using a Gauss meter, since H=nI, where n is number of turns per meter and I is current. The calibration coefficient is 1056 A/m per Amp. Before each measurement the sample was saturated. The applied field was then changed manually and the damping and the shear modulus were measured.

Figure 4.20 shows the capacitance rotation sensor in more detail. The design is based on the proposal of Peters [1989] for a highly linear, frictionless method of measuring angular position. The drive and pick-up (P_1 and P_3 respectively) plates are mounted rigidly on a 3-axis micromanipalator to facilitate precise alignment and positioning. The plates were fabricated from standard copper-clad laminate. Each disc is 6cm in diameter, and they are approximately 1.5mm part. The drive and rotor (P_2) plates have two semi-circular copper plates and the pick-up plate has two quarter-circle copper plates.

When the rotor plate is displaced with respect to drive and pick-up plates, leading to rotation of the wire, the capacitance is changed according to the variation of area. The change in capacitance is a linear function of the angular displacement θ, from the equilibrium position. This is a consequence of the facts that (i) the capacitance of an ideal parallel plate capacitor is proportional to the area between its plates, and (ii) the area between its plates is proportional to θ. The system is almost linear between ±45°. The maximum angle of rotation used in our measurements was about ±30°. Therefore this was not an important limitation.

Figure 4.21 is a schematic diagram of the measurement system. The equivalent circuit of the rotation sensor is a capacitance bridge, with the capacitances between the drive, pick-up and modified rotor plates. Capacitances are given as a function of θ by:

$$C_1 = C_4 = \frac{\varepsilon_o \pi R^2}{4d}\left(1 + \frac{2\theta}{\pi}\right),$$

$$C_2 = C_3 = \frac{\varepsilon_o \pi R^2}{4d}\left(1 - \frac{2\theta}{\pi}\right),$$

$$C_5 = C_6 = \frac{\varepsilon_o \pi R^2}{4d}, \qquad (4.29)$$

where R is the radius of the plate, ε_o is the permittivity of free space and d is the distance between each plate. The capacitance bridge is supplied with 5V rms at 700 kHz. In signal mode the bridge output is connected to the signal generator. The output of the lock-in is a dc voltage linearly related to the rotation angle by:

$$V_o = k\frac{2\theta}{\pi}V_i, \qquad (4.30)$$

where V_i the bridge excitation voltage and k is the system gain constant. Figure 4.22 shows the linearity of the output with angular displacement.

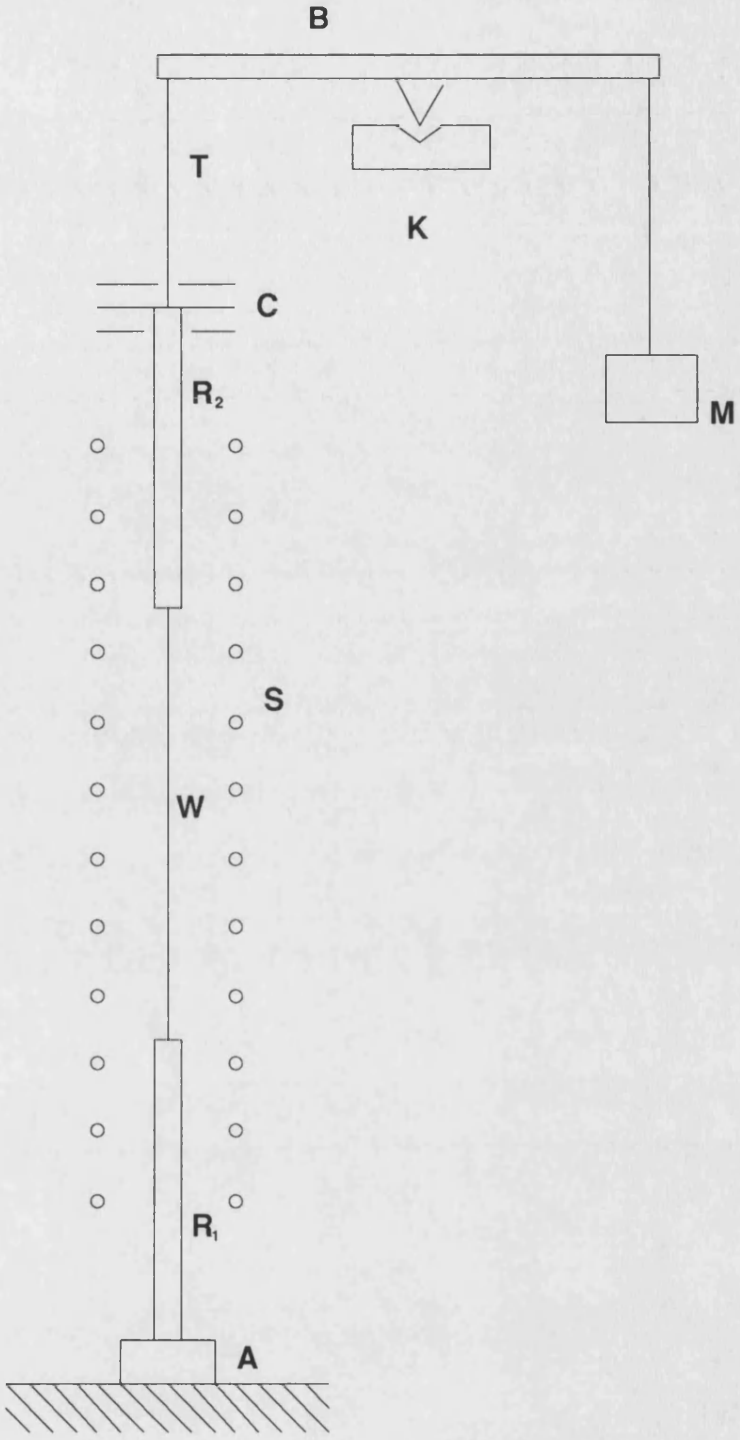

Figure 4.18: Schematic diagram of the pendulum.

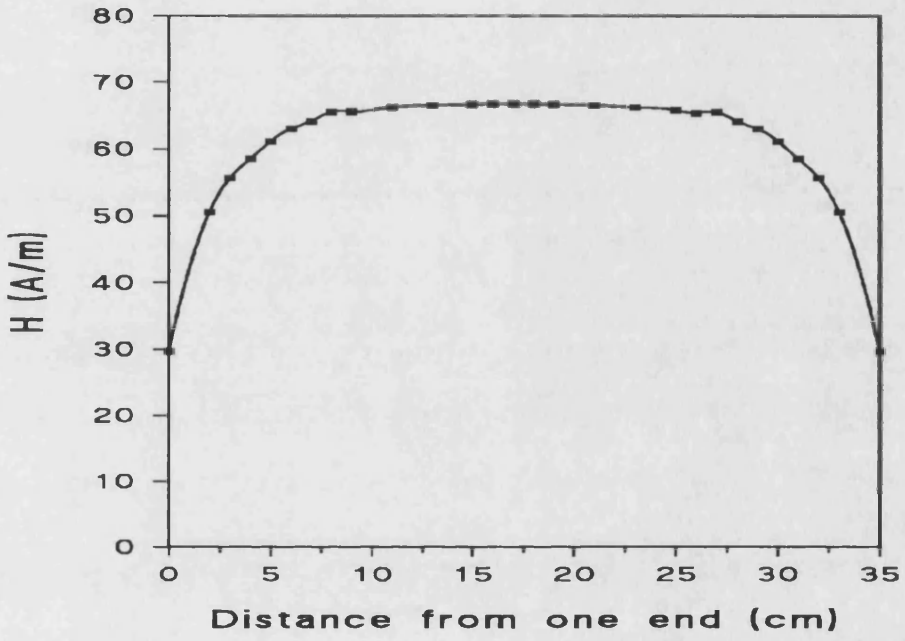

Figure 4.19: Measured profile of the coil on the ΔG system with a coil current of 57 mA.

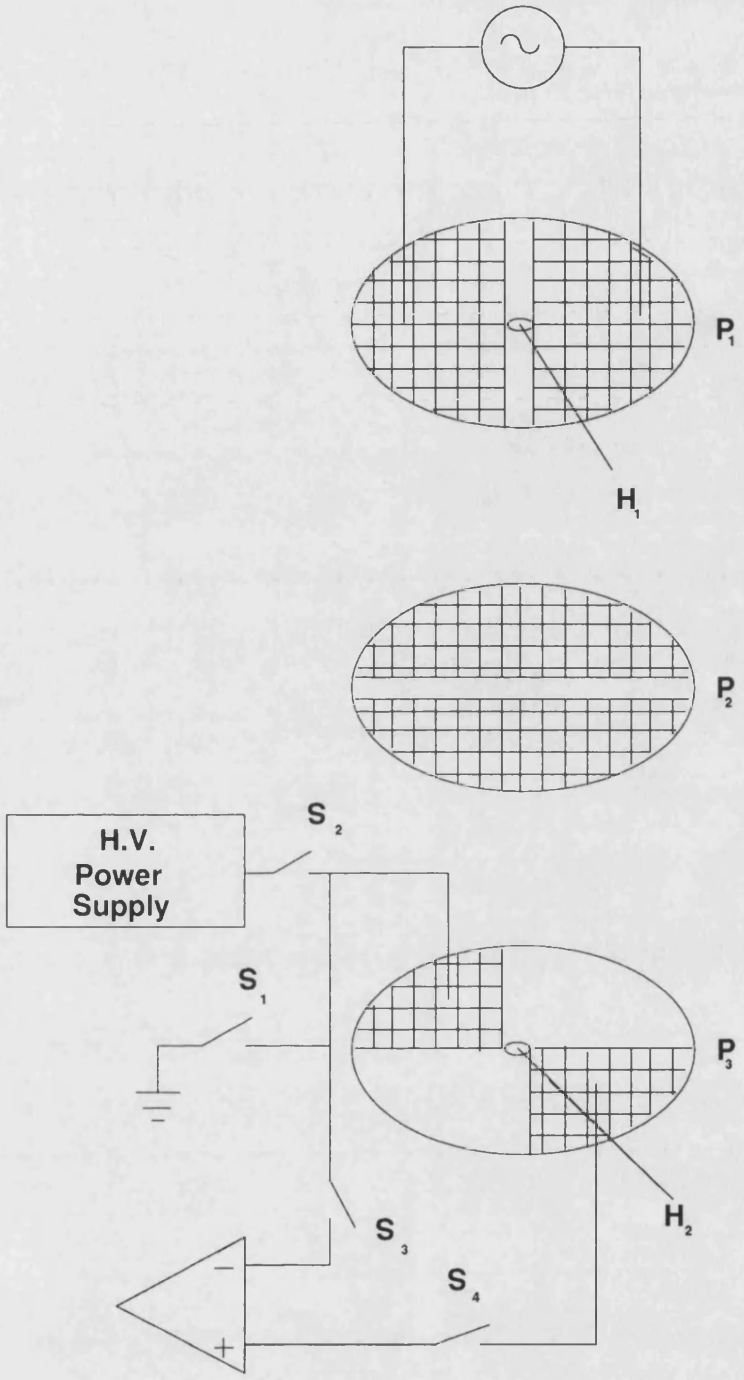

Figure 4.20: Details of the capacitive rotation sensor.

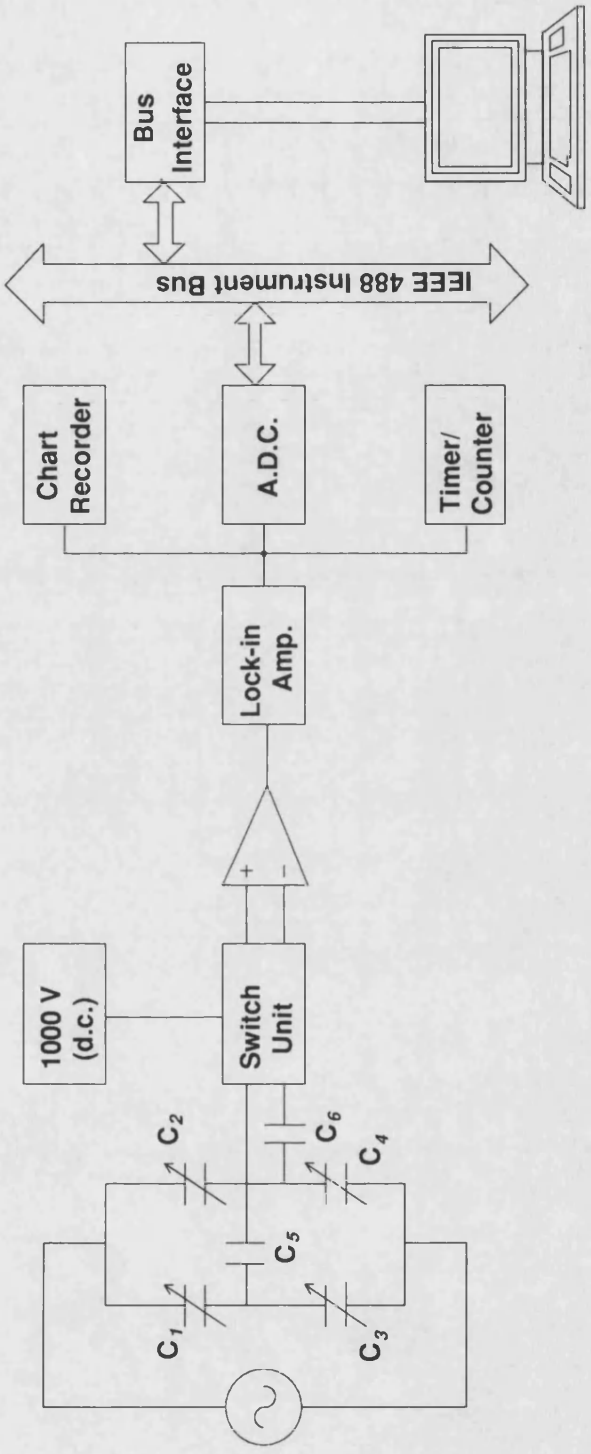

Figure 4.21: Circuit diagram of sensor bridge, signal capture, and initial displacement systems.

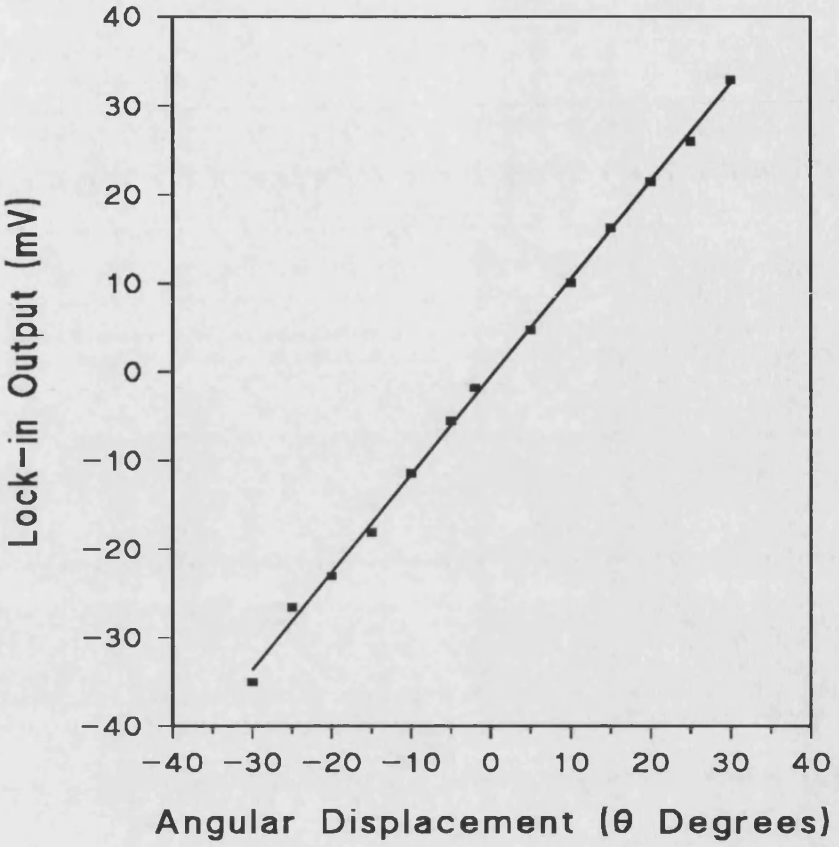

Figure 4.22: Typical lock-in amplifier output as a function of angular displacement of the rotor plate.

The output of the lock-in amplifier is then digitised and stored in the computer for analysis. For a typical case, the time period is 3-4 seconds and 7-8 cycles are stored as 400 data points. The chart recorder is for monitoring purposes only. A typical chart recorder output is shown in figure 4.23.

A useful optional feature is the high dc voltage that can be applied to the plates of the rotation sensor in order to initiate the oscillations. The application of voltages in the range 1-1.5kV across the plates produces a small torque: repeated application and removal of the voltage in synchronization with the rotation period enables the amplitude to be increased to the desired value. A switch unit containing high-voltage relays

reconnects the bridge to the signal amplifier when the oscillation has been initiated (Appendix A). Oscillation can also be initiated manually by rotating R_1 via rotation of base A (see figure 4.18).

Data Analysis:

It is assumed that the signal read from lock-in amplifier can be fitted by the function:

$$Y = b_o \exp(-kt)\cos(\omega_o t + \phi) + b_1 \qquad (4.31)$$

The right hand side represents a damped sinusoidal oscillation with a dc offset. From the parameters k and ω_o, the damping and the shear modulus were calculated from equations 4.25 and 4.28.

The reason for choosing time-domain analysis in preference to Fourier transformation (Yoshida [1981]) is that the latter requires several cycles of oscillation to give adequate resolution. In the case of large damping this obscures the strain dependence of parameters, which is a very important feature of the behaviour of amorphous wires. Also, curve fitting by using equation 4.31, gives us statistical uncertainties in the derived parameter values.

Maximum torsional strain occurs at the surface, and can be calculated from equation 4.32.

$$\varepsilon = \frac{r\theta}{l} \qquad (4.32)$$

Where ε is the torsional strain, l is the length of the wire, r is the radius and $\theta = a.b_o$ (a is a system calibration factor and b_o is the amplitude in equation 4.31). In order to obtain the torsional strain dependence of shear modulus and damping, curves were fitted using equation 4.31 to each 1 or 2 cycles.

Figure 4.24 shows portions of the digitised data together with the curves fitted using equation 4.31. Note the significant improvement in fit over a reduced time in the case of large damping. Values of the relevant parameters obtained from these fits are given in table 4.3 to illustrate the precision of the system. It can be seen clearly that the shear modulus and damping both change by significant amounts with torsional strain. The precision of the shear modulus and damping measurements depends on both the amplitude of the oscillations and the rapidity with which they die out. The maximum precision was obtained when damping was low and the oscillation amplitude was high, so that many cycles could be included in the calculation. In the case of high damping, this gave a poor fit, so the number of cycles included in the fitting was reduced.

All the results were obtained under the effect of 0.43MPa tensile stress which is the minimum tensile stress required to keep the wire straight during the measurements. The measurements were performed in air with no vibration isolation.

Data	G (GPa)	δG(GPa)	10^3Q^{-1}	$10^3\delta Q^{-1}$
Fig. 4.23.a	38.76	0.01	4.56	0.07
Fig. 4.23.b	39.37	0.01	4.44	0.37
Fig. 4.23.c	38.11	0.01	4.71	0.49
Fig. 4.23.d	30.36	0.01	27.57	0.43
Fig. 4.23.e	31.38	0.01	25.51	0.44
Fig. 4.23.f	34.19	0.03	13.9	1.3

Table 4.3: Parameters derived from the curve fitting shown in figures 4.24(a)-(f). The uncertainties, δG, are 95% confidence limits.

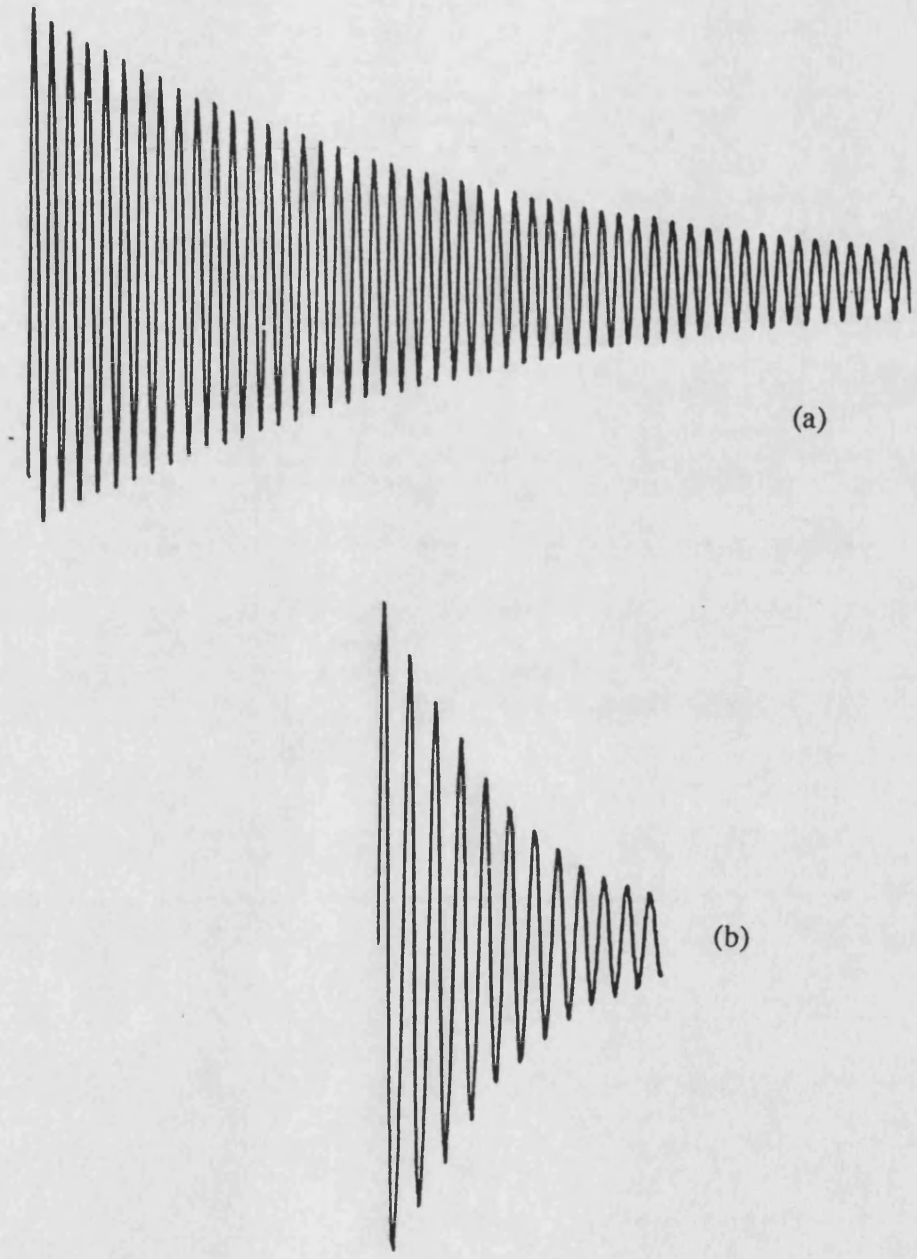

Figure 4.23: Examples of (a) low damping and (b) high damping oscillations: chart recorder traces.

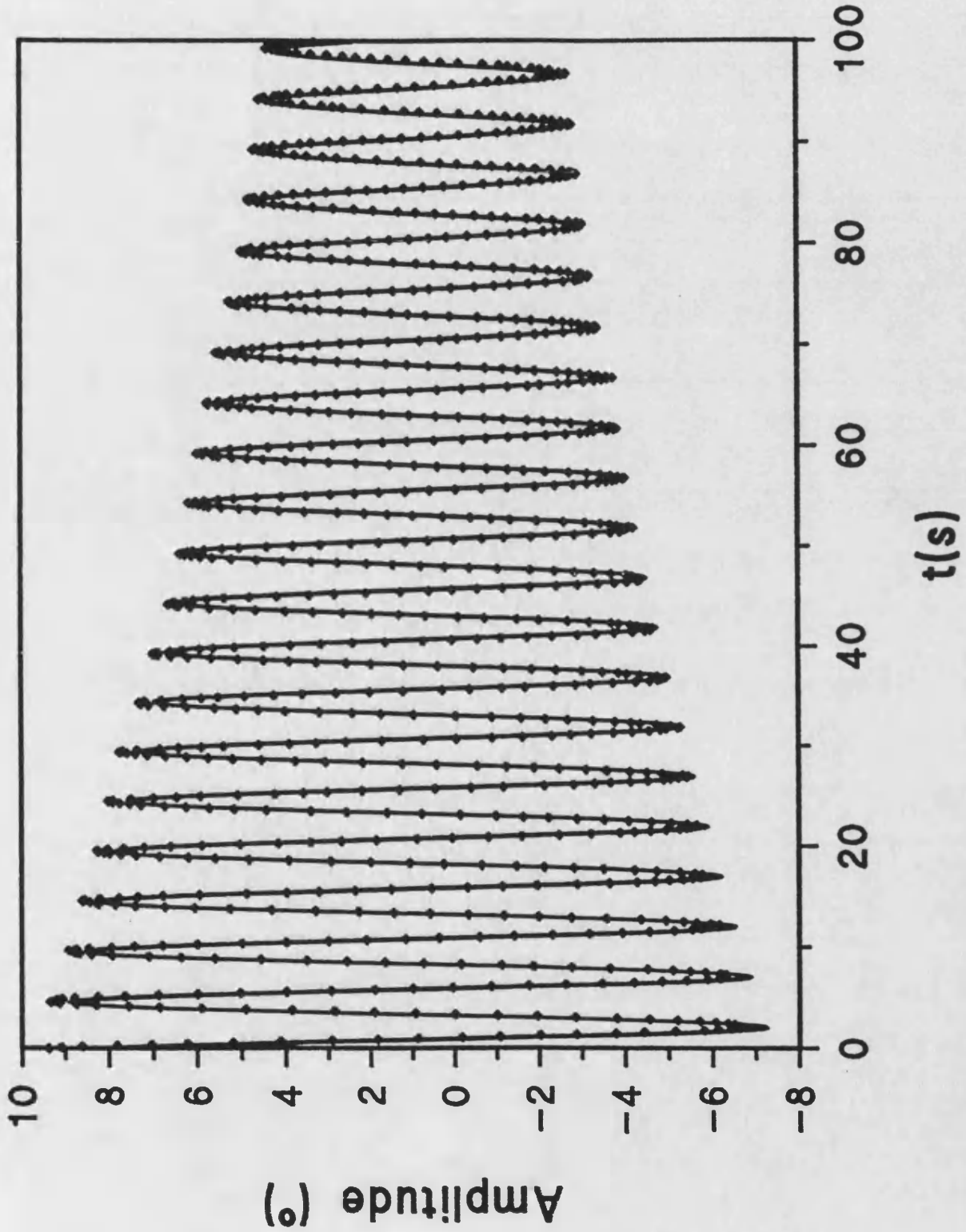

Figure 4.24.a: Entire trace (1000 points).

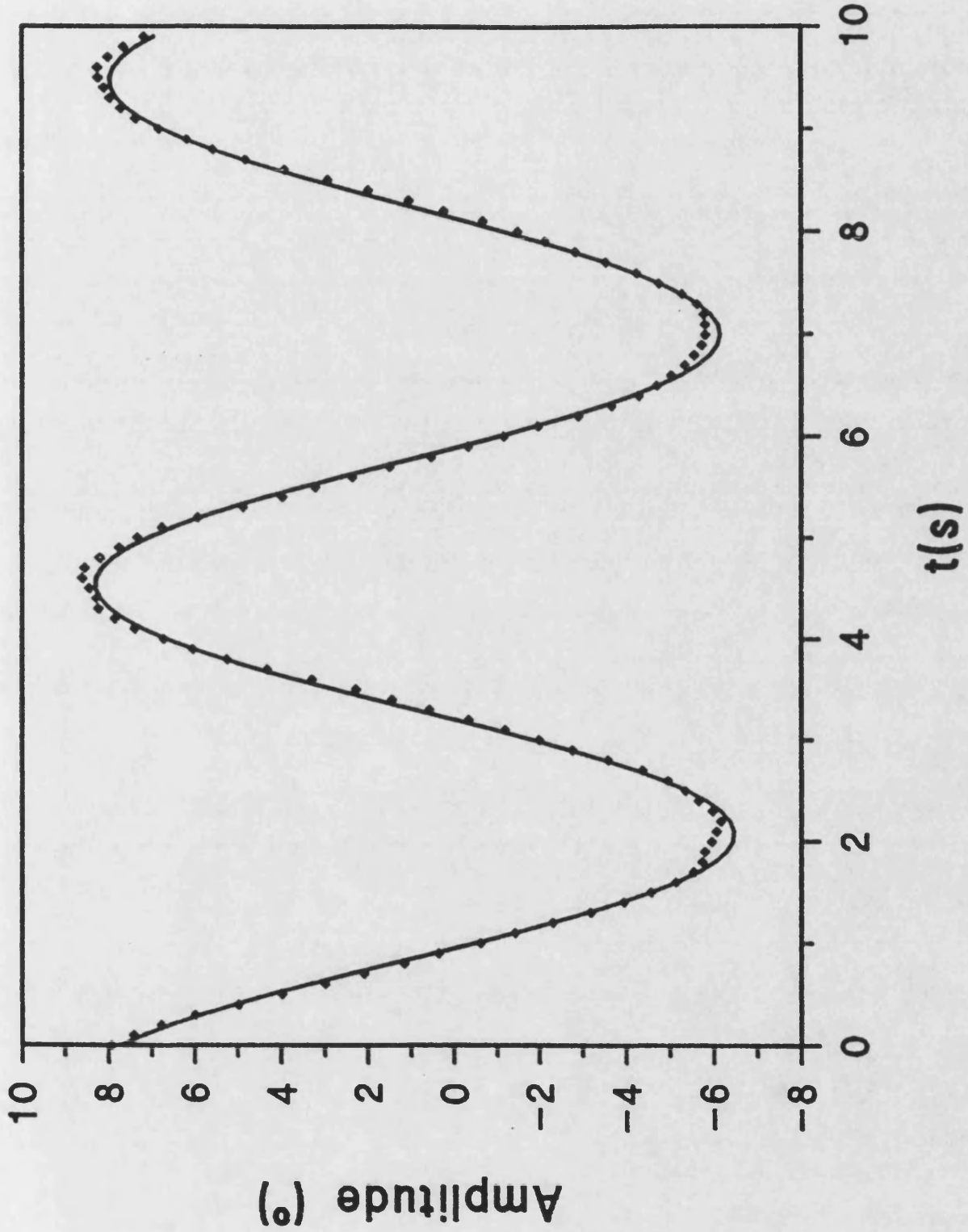

Figure 4.24.b: Section A (100 points).

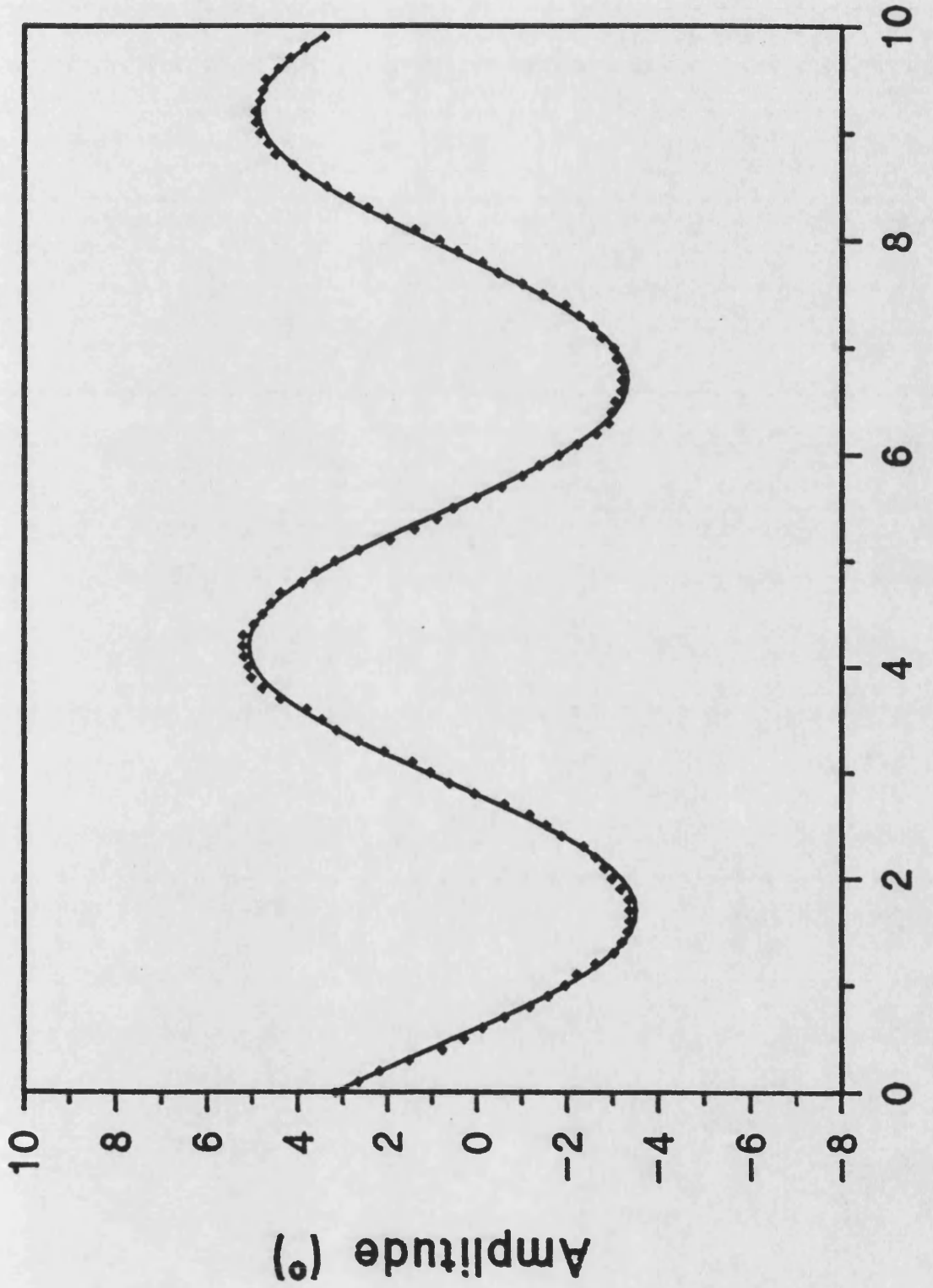

Figure 4.24.c: Section B (100 points).

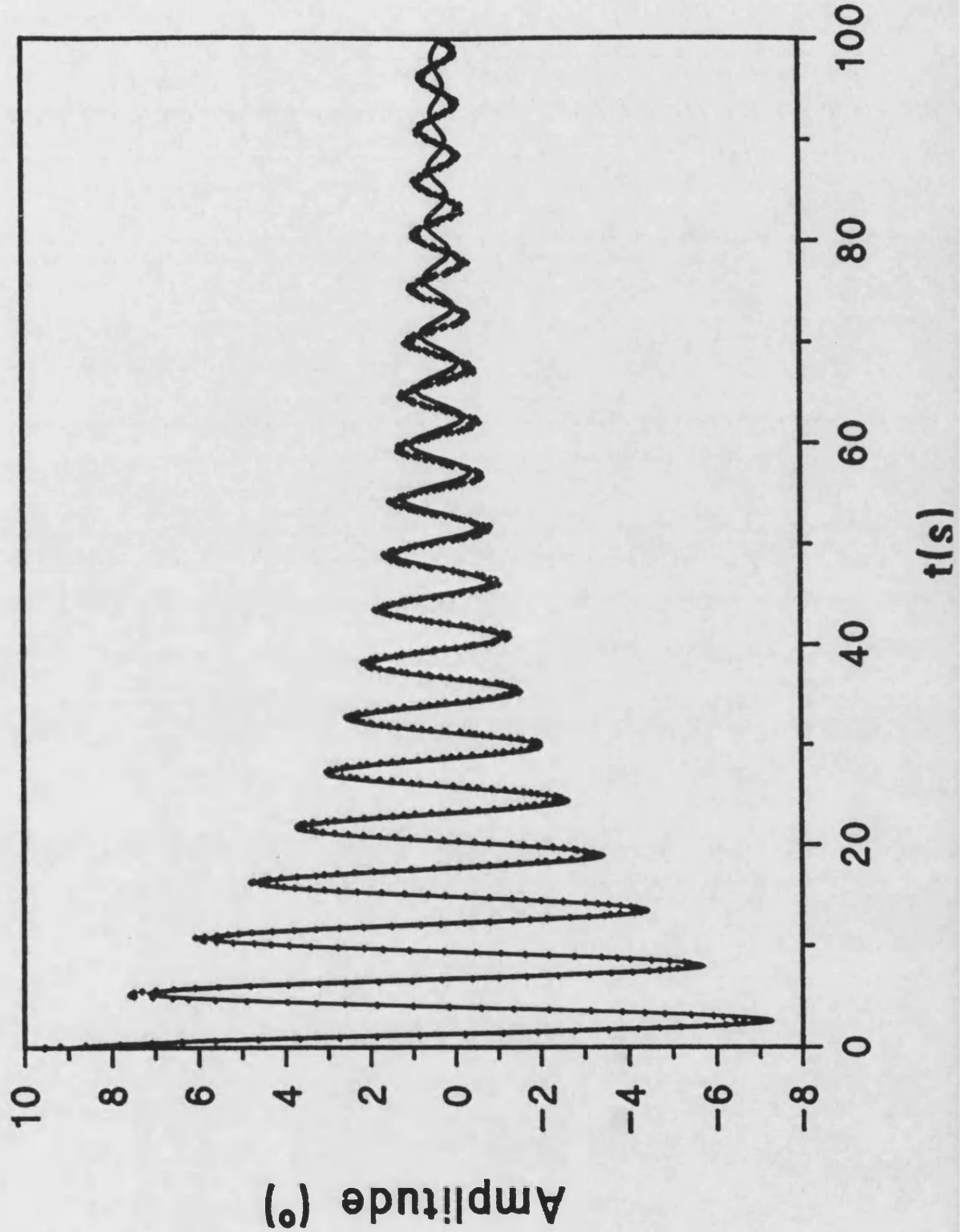

Figure 4.24.d: Entire trace (1000 points).

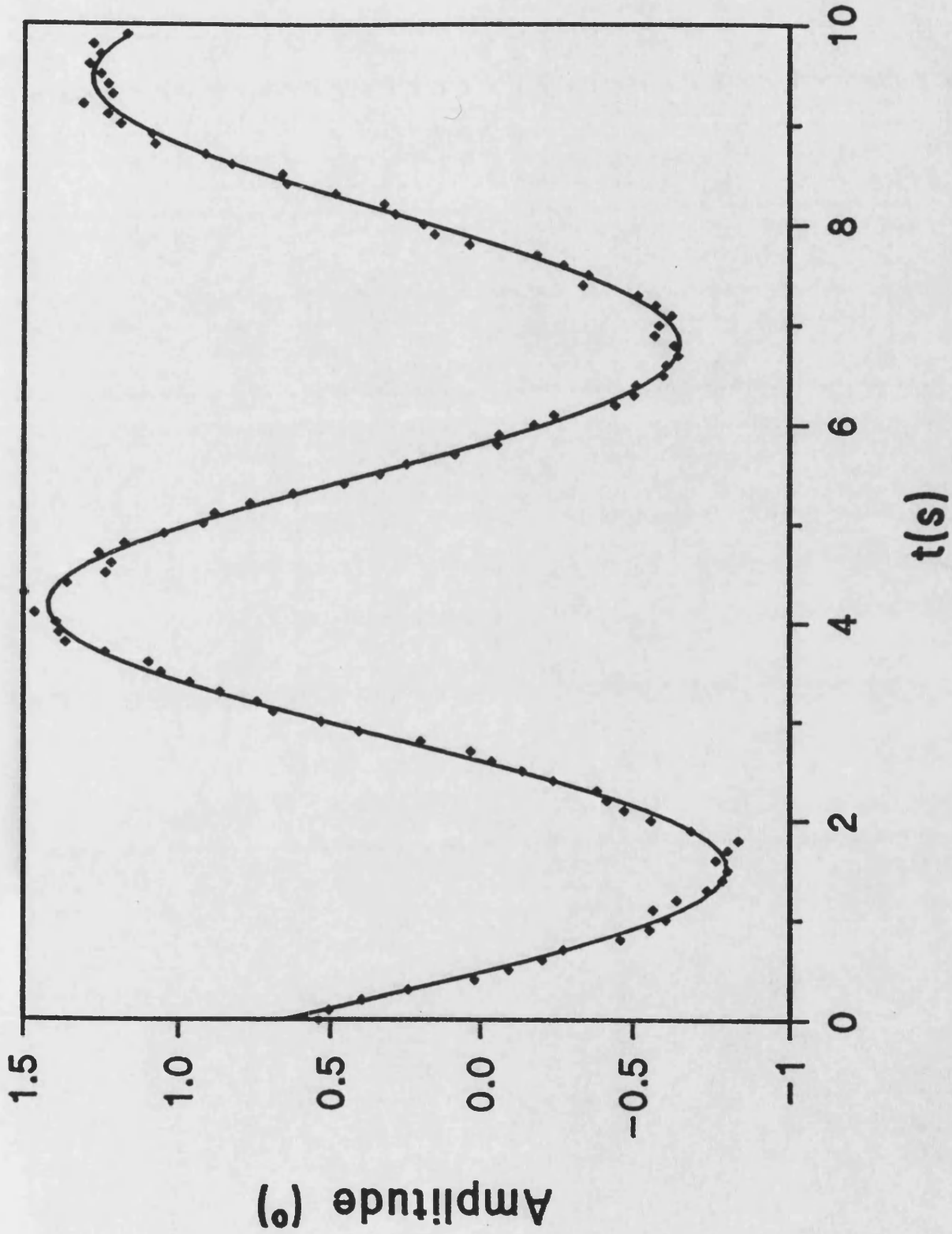

Figure 4.24.e: Section C (100 points).

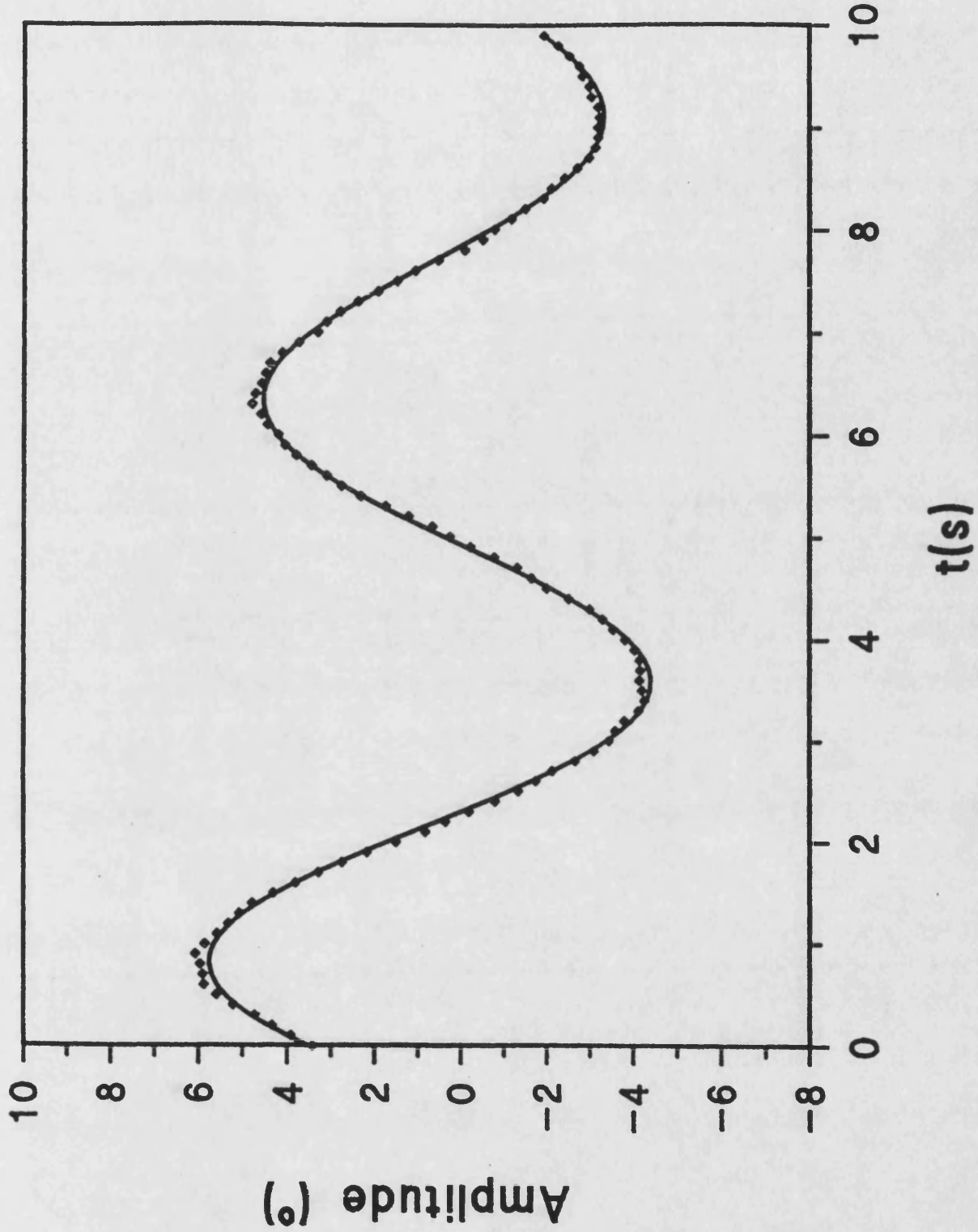

Figure 4.24.f: Section D (100 points).

Figure 4.24: Examples of equation 4.31 fitted to selected part of figures 4.23.a and 4.23.b. The dots indicate individual digitised points, and continuous lines are the fitted curves.

Sources of Errors:

The major source of error in the torsional pendulum system is the position of the rotor plate with respect to the drive and the pick-up plates. If the rotor plate is not completely parallel to the other plates, the output of the lock-in amplifier is not linear as a function of angular displacement. There are also some additional stray capacitances, such as across the insulator gaps in the each plate (i.e. edge the edge of copper plates), but the effect of these in the total capacitance is very small.

Another source of error is that when the rotor plate oscillates, it also moves slightly in the vertical plane. This can lead to large errors in the fitted parameters in equation 4.31. Figure 4.25 shows two data sets, in figure 4.25 (a) the rotor plate performs only torsional oscillation, but in figure 4.25 (b) the rotor plate oscillates also in vertical direction.

If the wire is not positioned parallel to the magnetic axis, there will be additional errors in the calculated value of the parameters as a function of magnetic field.

Shear modulus, G, was calculated from equation 4.28. But G is proportional to l/r^4 and r is not uniform along the length of the wire. As a result, the error in the absolute calculated G values is ~10%.

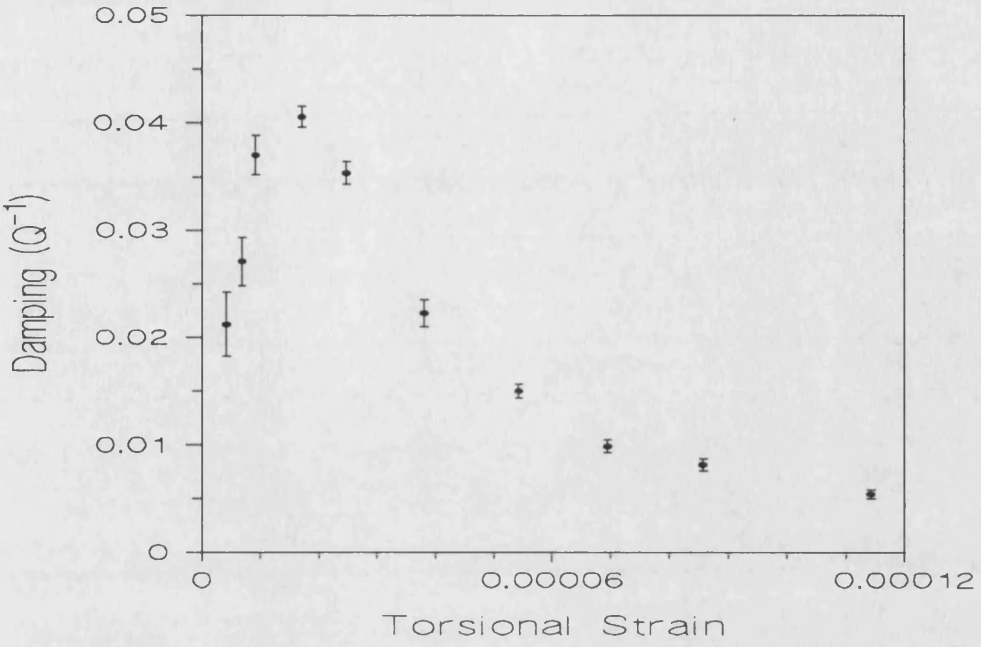

(a)

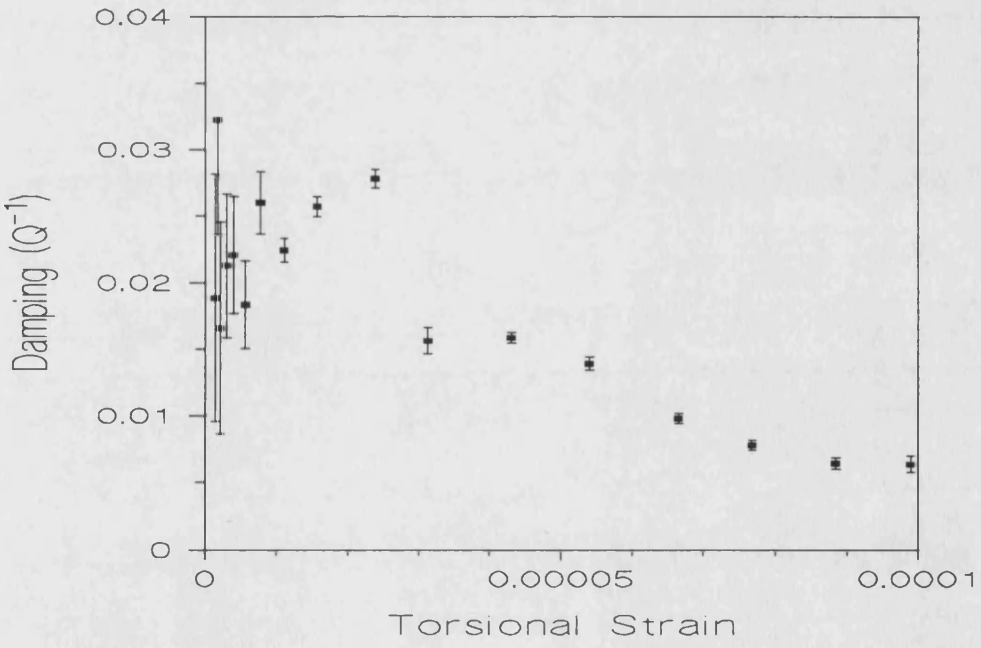

(b)

Figure 4.25: Typical damping data set as a function of applied field, (a) with only torsional oscillation (b) with also oscillation in vertical plane.

4.7 X-ray Diffraction System

In the X-ray diffraction measurements, the scattered intensity from the wire was detected by a Philips 11cm X-ray powder camera (PW 1024/10) as a function of the scattering angle 2θ. The system has a 1 kW X-ray generator with a cobalt target X-ray tube operated at 40 kV and 16mA. The measurements were taken with 2θ between 30° and 150°. The radiation has a wave length of λ_{Co}=1.7902 A°.

The Fe-based amorphous alloys have a broad peak around 2θ=45°. Partial crystallisation of the amorphous alloys leads to a sharper peak on top of the broad peak (Sheard [1989]). The relative height of the sharper peak depends on the volume fraction of the crystalline part on the surface of the amorphous alloy. Figure 4.26 shows an almost completely crystallised FeSiB amorphous wire.

4.8 DSC system

The Curie ,T_c and crystallisation ,T_x temperatures of the amorphous wires were measured by using a DuPont 9900 differential scanning calorimetry system (DSC).

The DSC system was calibrated by using the indium calibration method. One reference, which is an empty aluminium pan, and sample pan, which is aluminium pan with sample, was prepared. Then, both reference pan and sample pan were placed into the DSC and they were heated between 350°C and 600°C with a 10°C/min heating rate. The total mass of the sample was 9.7 gr. During this heating process, the temperature difference ($\Delta T=T_s-T_r$) between the sample and reference pans was measured. They were maintained at the same temperature ($\Delta T=0$). Any energy difference in the independent supplies to the sample and reference pans was recorded against the temperature via the resident

computer program. This energy difference can be in endothermic or exothermic direction, depending upon whether more or less energy has to be supplied to the sample relative to the reference material (Brown [1988]).

Figure 4.27 shows the DSC output for $Fe_{77.5}Si_{7.5}B_{15}$ amorphous wire. The Curie temperature for this wire is 425.9°C and crystallisation temperature is 537.6°C. The reaction at Curie temperature is endothermic and at the crystallisation temperature is exothermic.

Also, we measured the crystallisation temperature of a $Fe_{67}Si_{10}B_{15}Cr_8$ wire. The same heating method was used and the T_x for this wire is 587.4°C.

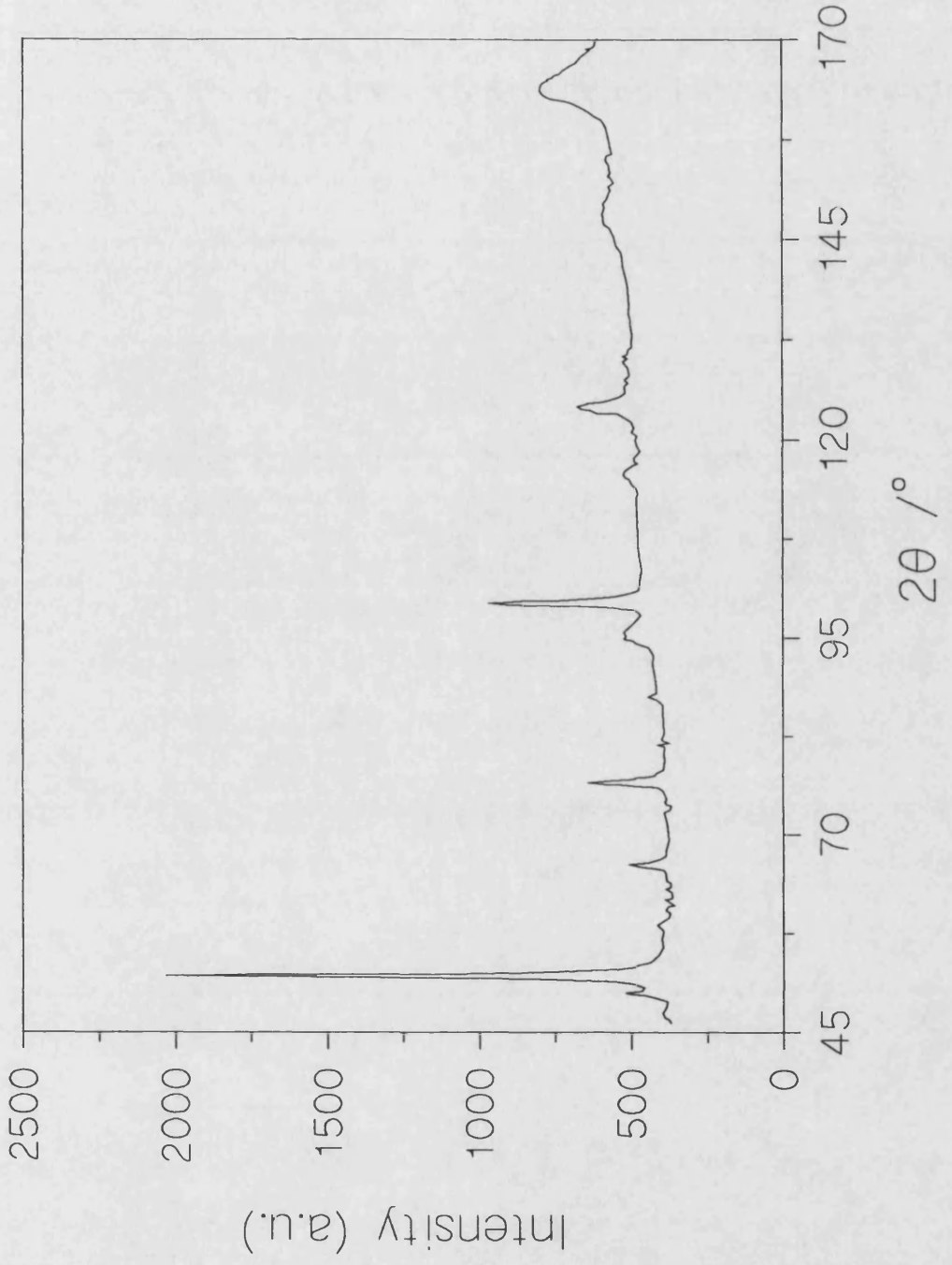

Figure 4.26: X-ray output of a partially crystallised FeSiB wire.

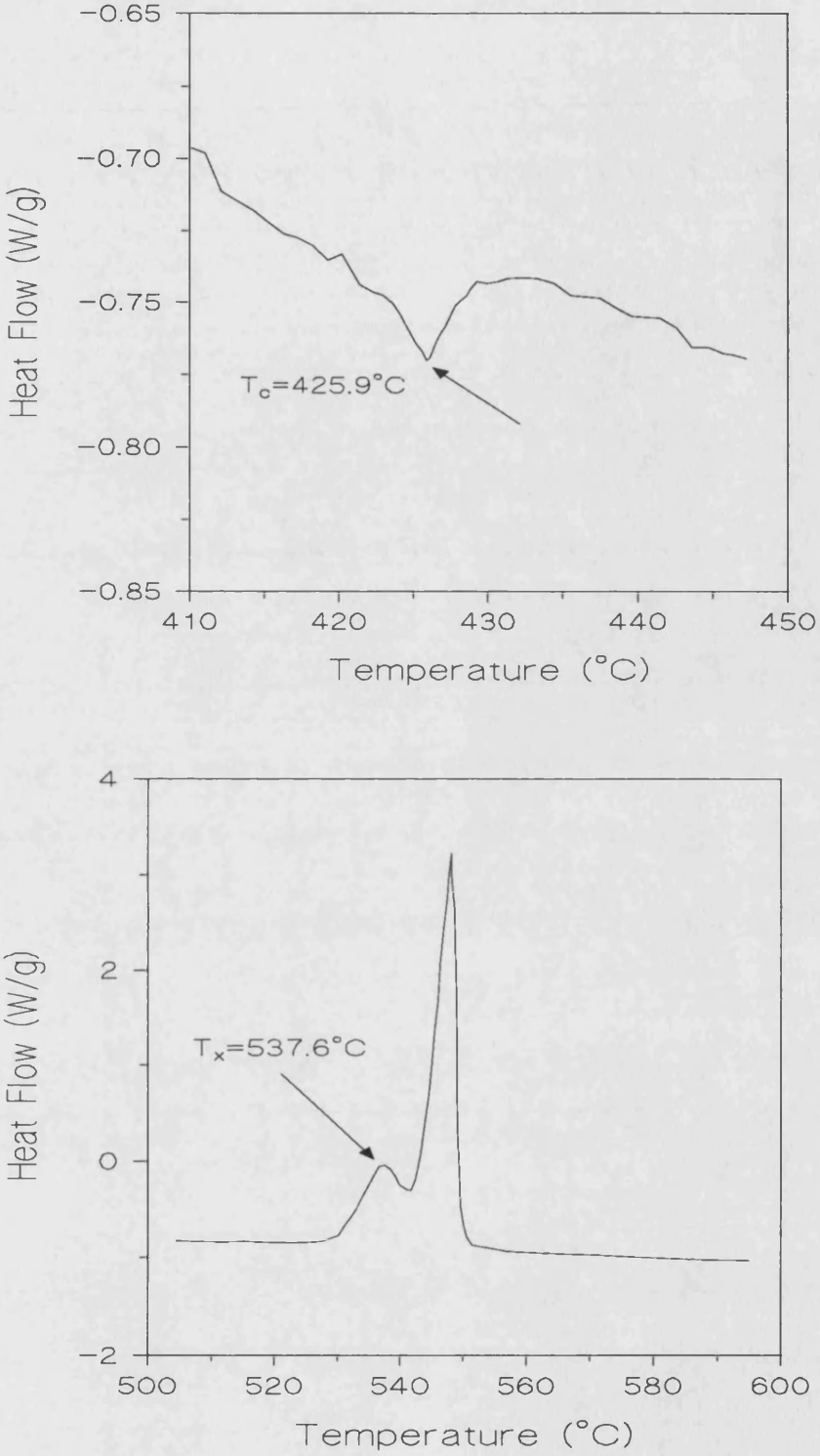

Figure 4.27: DSC output of FeSiB wire.

5 Results and Analysis for Furnace-Annealed Amorphous Wires

5.1 Introduction

In this chapter, firstly, the effects of the sample length on the magnetic properties of as-cast Fe-based wire are given. Then, the effect of furnace annealing on the magnetic and magnetoelastic properties of amorphous wires of composition $Fe_{77.5}Si_{7.5}B_{15}$ is discussed. Annealing studies were performed between 370°C and 500°C for various annealing times. Fe-Si-B wire was chosen due to the large decrease in K with annealing (to as low as $50Jm^{-3}$) and its high λ_s value (~37 ppm).

The field dependence of magnetostriction and Young's modulus is discussed using the Squire [1990] model. The magnetic field and torsional strain dependence of the damping are explained using the Smith and Birchak [1969] and Degauque and Astie [1980] models.

5.2 Effect of the Sample Length on the Properties of As-cast Wire

Figure 5.1 shows the magnetisation curves for as-cast $Fe_{77.5}Si_{7.5}B_{15}$ wire 22 cm long. The M-H loops were taken according to the method outlined in section 4.3. From figure 5.1a it can be seen that at low field the wire exhibits the characteristic Large Barkhausen Jump (LBJ), and in this region the magnetisation occurs due to the a sudden motion of one domain wall in the inner core. As the field is increased further, magnetisation occurs by both wall motion and moment rotation in the outer shell (figure 5.1b).

It has been observed that the wire length plays an important role in the magnetic behaviour of the as-cast wires. Figure 5.2 shows the effect of the wire length on the M-H loop at low fields.

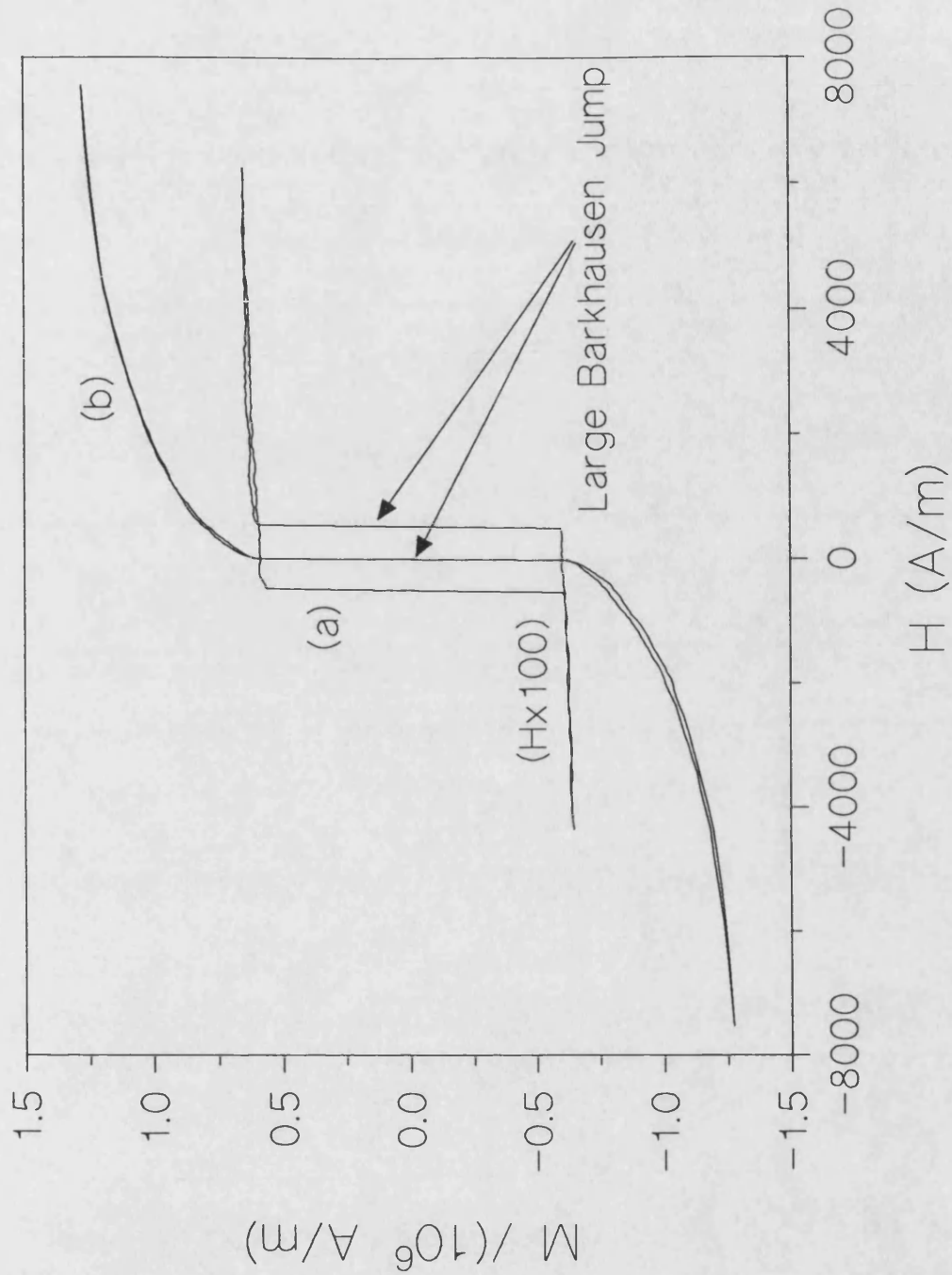

Figure 5.1: M-H loops of 22cm long as-cast $Fe_{77.5}Si_{7.5}B_{15}$ wire with a diameter of 125μm, a) maximum applied field= 75 A/m, b) maximum applied field=7500A/m (the loop a is magnified for illustration purpose).

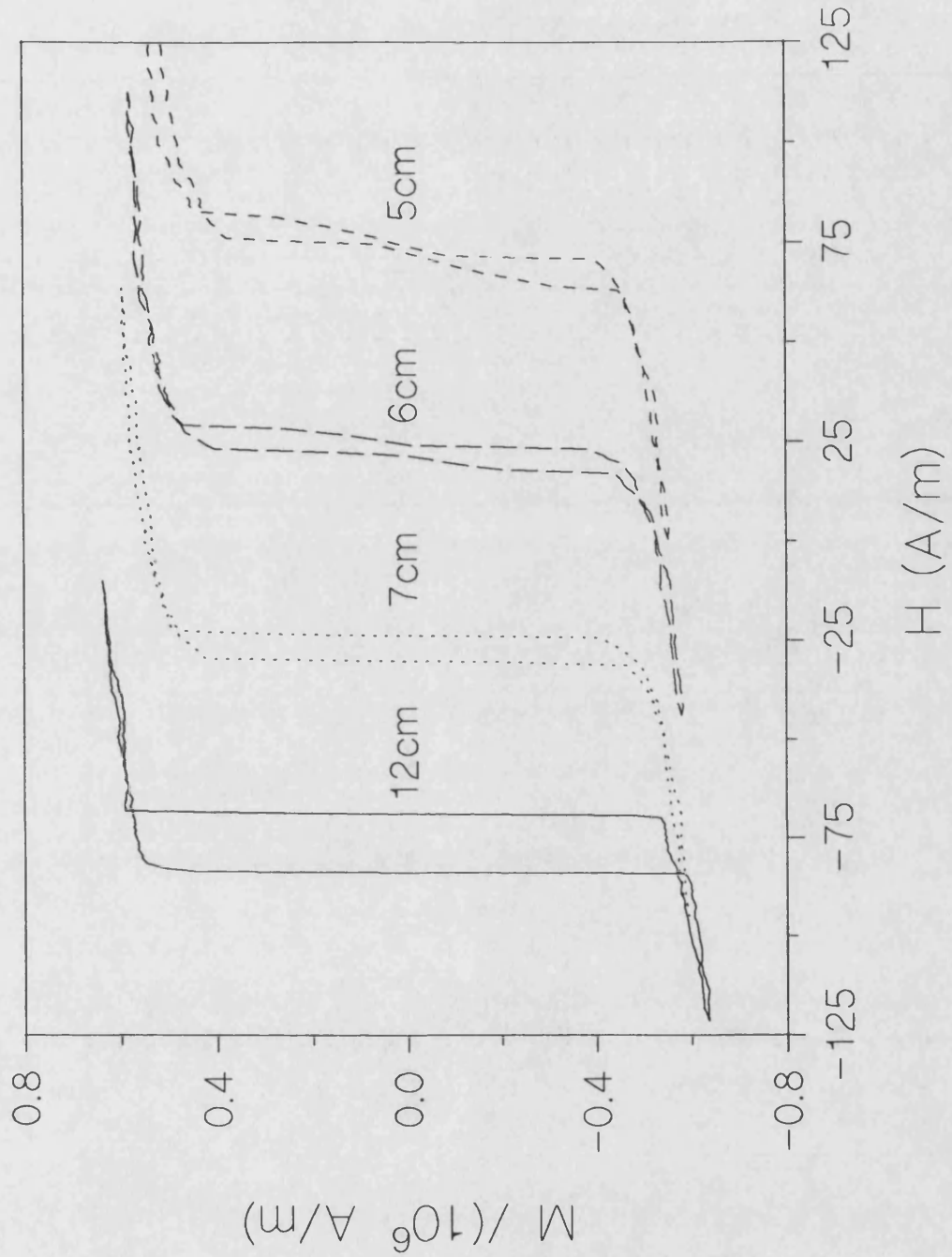

Figure 5.2: Effect of the wire length on the M-H loop of un-drawn FeSiB 125µm as-cast wire (the loops are displaced horizontally for illustration purpose only).

When the wire length is around 6.5 cm, the square shape of the M-H loop starts to disappear. With the further decrease in the length, the square shape of the M-H loop disappears completely, but loop still shows the Barkhausen jump around the remanent magnetisation, M_r. When the wire length is 3 cm no Barkhausen jump is observed. Figure 5.3 shows the effect of wire length on M_r and H_c. M_r and H_c are almost constant for wire lengths above 7 cm. When the wire length is shorter than 7 cm, M_r and H_c decrease very sharply.

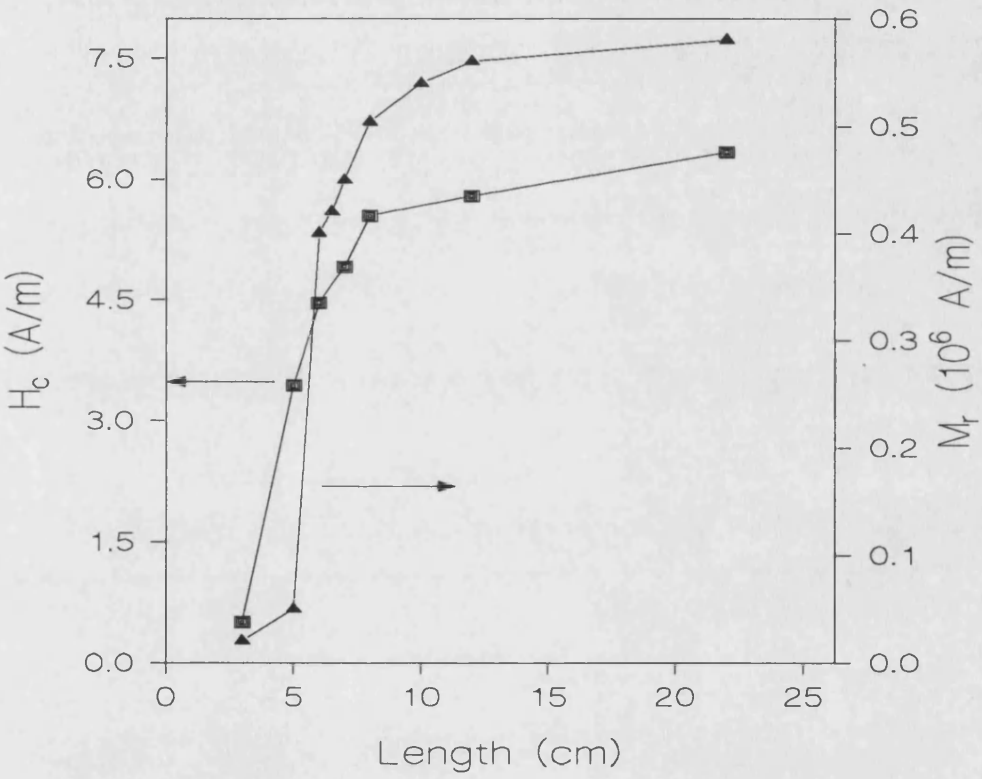

Figure 5.3: Effect of the wire length on H_c and M_r of FeSiB as-cast wire. The lines are interpolated between the experimental data points.

This magnetic behaviour of the as-cast $Fe_{77.5}Si_{7.5}B_{15}$ wire can be explained by the shape anisotropy energy. Magnetic materials arrange their domain structure in order to minimise the total anisotropy energies, which are:

$$U_T = U_{ex} + U_c + U_s + U_{me}$$

where U_c is the crystal anisotropy energy (=0 for amorphous alloys), U_s is the shape anisotropy energy, U_{ex} is the exchange energy and U_{me} is the magnetoelastic energy. When the wire length is changed, only U_s changes and it is given by:

$$U_s = \mu_o\left(\frac{1}{2}M^2N_y + \frac{1}{2}(N_y - N_x)M^2\sin^2\theta\right) \qquad (5.1)$$

where N_y and N_x are the demagnetising factors along the wire axis and in the radial direction, respectively. The shape anisotropy constant and N_x are given by (Cullity [1972]):

$$K_s = \frac{1}{2}\mu_o(N_y - N_x)M^2,$$

$$N_x = \frac{4r^2}{L}\left\{\ln\left(\frac{L}{r}\right) - 1\right\} \qquad (5.2)$$

where r and L are the radius and the length of the wire, respectively. For 10 long wire with a diameter of 125μm , K_s is of the order of $\sim 5 \times 10^5 Jm^{-3}$. Figure 5.4 shows the demagnetising factor along the wire axis for wires with diameters of 125μm and 50μm, as a function of wire length. As can be seen from equations 5.1 and 5.2, the shape anisotropy energy is a function of L/r, which determines N_y and N_x. When L is shorter than 6.5 cm, N_x increases very sharply, leading to a sharp decrease in the shape anisotropy energy in the axial direction of the wire. This leads to an important change in the total energy of the system. Therefore, the domain structure of the wire will be rearranged to minimize U_T. As a result, for the wires shorter than 6.5 cm the suggested core-sheath domain model is not valid. Ogasawara [1987] suggested that when the wire length is below the critical length (in this case 6.5 cm) inverse domains form at the end of the

wire. This changes the square shape of the M-H loop and reduces the magnitude of the Barkhausen jump. We suggest that when the wire length is shorter than 5cm there is also some moment reorientation in the inner core (i.e. easy axis in the inner core makes an angle with the wire axis) on the basis of the observed shape of the M-H loop.

In conclusion, the domain structure of the as-cast wire is not only determined by induced casting stresses (tensile stress in the outer shell and axial stress in the inner core) but also by the shape anisotropy which becomes particularly significant when the wire length is shorter than 6.5 cm.

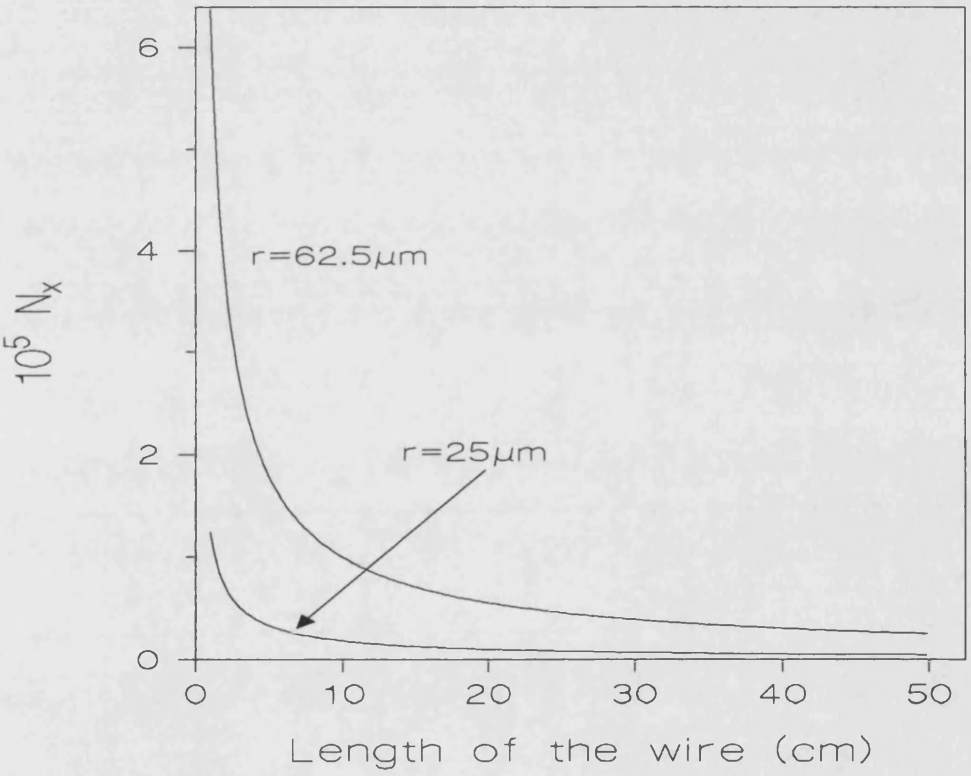

Figure 5.4: The length dependence of demagnetising factor, N_x, along the wire axis for wires of 25μm and 62.5μm radius.

5.3 Effect of Heat Treatments on the Magnetic Properties

The as-cast un-drawn wires show the characteristic LBJ, which is sensitive to the magnetostriction coupled with the internal axial stress. The relative magnitude of the Barkhausen jump with respect to the total magnetisation is affected by furnace annealing due to the reduction of the internal stress. For wires annealed at low temperatures (370-400°C) the magnitude of the Barkhausen jump changes very gradually but when the annealing temperature is high (460°C and above) the relative magnitude of the Barkhausen jump decreases very quickly and disappears at shorter anneal time.

Figure 5.5 shows the M-H loops of un-drawn $Fe_{77.5}Si_{7.5}B_{15}$ wire annealed at 460°C for various anneal times. The fractional magnitude of the Barkhausen jump decreases from the as-cast value of ~0.48 to 0.06 after annealing for 20 seconds, then with further annealing increases by a very small amount to ~0.14 and, later, again reduces. After an annealing time of 5 minutes at 460°C, the Barkhausen jump has vanished.

Figure 5.6 shows the M-H loop of cold-drawn wire with a diameter of 80μm. Due to the internal stresses induced during the drawing process the wire has a large coercivity of ~2000A/m. Cold-drawn wire does not exhibit the characteristic LBJ in non-annealed state. But when the wire is annealed at 470°C for 20 seconds, a typical Barkhausen jump is observed. Further annealing reduces the magnitude of the Barkhausen jump and it disappears after an annealing time of 3 minutes at 470°C (figure 5.7). It was assumed that annealing first relieves the stresses induced during cold-drawing so that the wire shows LBJ then the further annealing relieves the stresses induced during the solidification process.

The coercivity, H_c, is shown with respect to anneal time for annealing temperatures of

420, 460, 470 and 480°C in figure 5.8 and 5.9 for un-drawn and cold-drawn wires. The coercivity of un-drawn as-cast wire is about 4 A/m. At first, H_c decreases with annealing time at 460°C until the annealing time is ~1-3 minutes, then, it starts to increase gradually and increases very sharply when the annealing time is ~100 minutes. This sharp increase is due to the partial crystallisation of the wire. The same behaviour of H_c is observed for the un-drawn wire annealed at 480°C. But in this case, the sharp increase in H_c occurs when the annealing time is about 60 minutes.

The coercivity behaviour of cold-drawn wire is quite different from that of the un-drawn wires. The H_c behaviour of cold-drawn (CD) wires with diameters of 80μm and 100μm are however, very similar. H_c of CD 80μm wire decreases sharply from ~2000 A/m to 10 A/m after annealing for 20 seconds at 460°C. With further annealing, H_c reaches a minimum of 6 A/m after 5 minutes, then starts to increase sharply when the annealing time reaches 60 minutes. The same behaviour of H_c is also observed for an annealing temperature of 420°C but, in this case, H_c decreases more gradually and reaches a minimum of 8 A/m after 40 minutes annealing, then increases sharply after an annealing time of 1000 minutes.

The decrease in H_c is due to the relief of the internal stresses (Sheard [1989]). It was found that the maximum amount of internal stress is relieved when the CD 80μm wire is annealed for between 0.2 and 3 minutes at 460°C. With further annealing at this temperature H_c of both wires increases due to the crystallisation.

The H_c mechanism in the amorphous wires is slightly different from that in amorphous ribbons. When the wire exhibits the characteristic LBJ the measured H_c is not really the coercivity. It is the nucleation field, which is the critical field, required to nucleate a domain wall in the inner core of the wire.

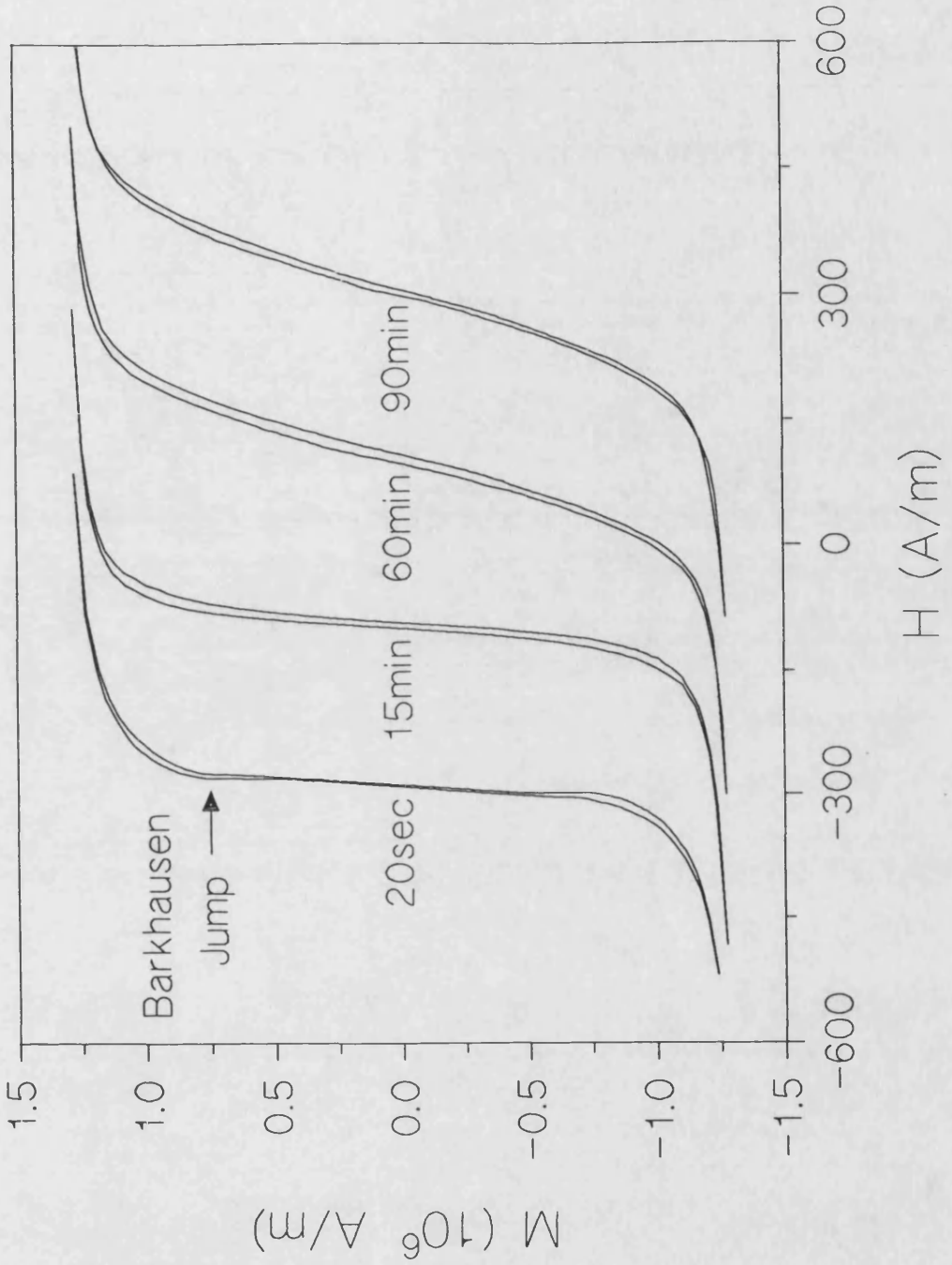

Figure 5.5: M-H loops of un-drawn 125μm wires, 7 cm long, annealed at 460°C for 20 seconds, 15 min, 60 min and 90 min (all the loops are displaced along the H axis for illustration purposes).

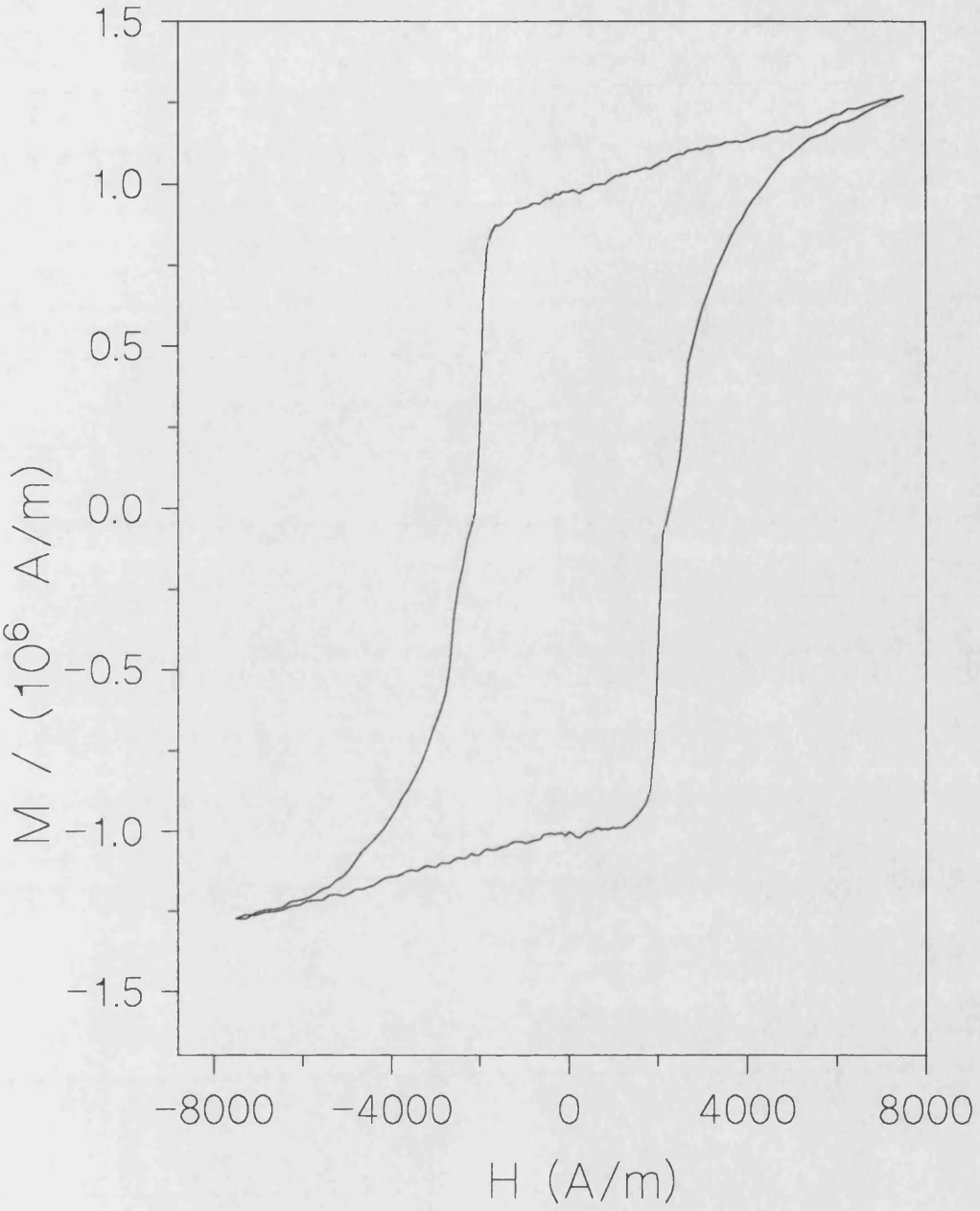

Figure 5.6: M-H loop of cold-drawn 80μm wire, 7 cm long.

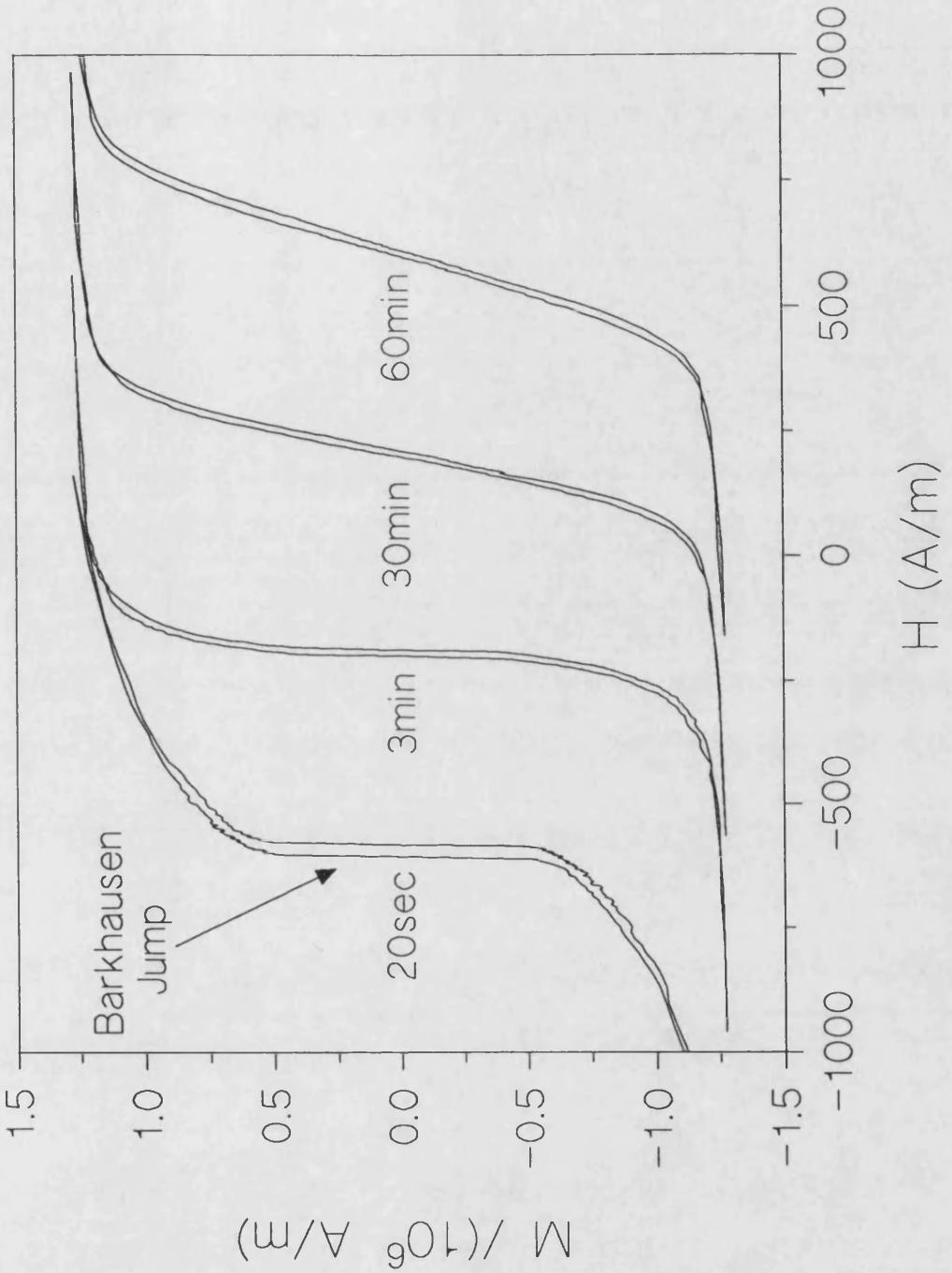

Figure 5.7: M-H loops of cold-drawn 80μm wires, 7 cm long, annealed at 470°C for 20 seconds, 3min, 30 min and 60 min (all the loops are displaced along the H axis for illustration purposes).

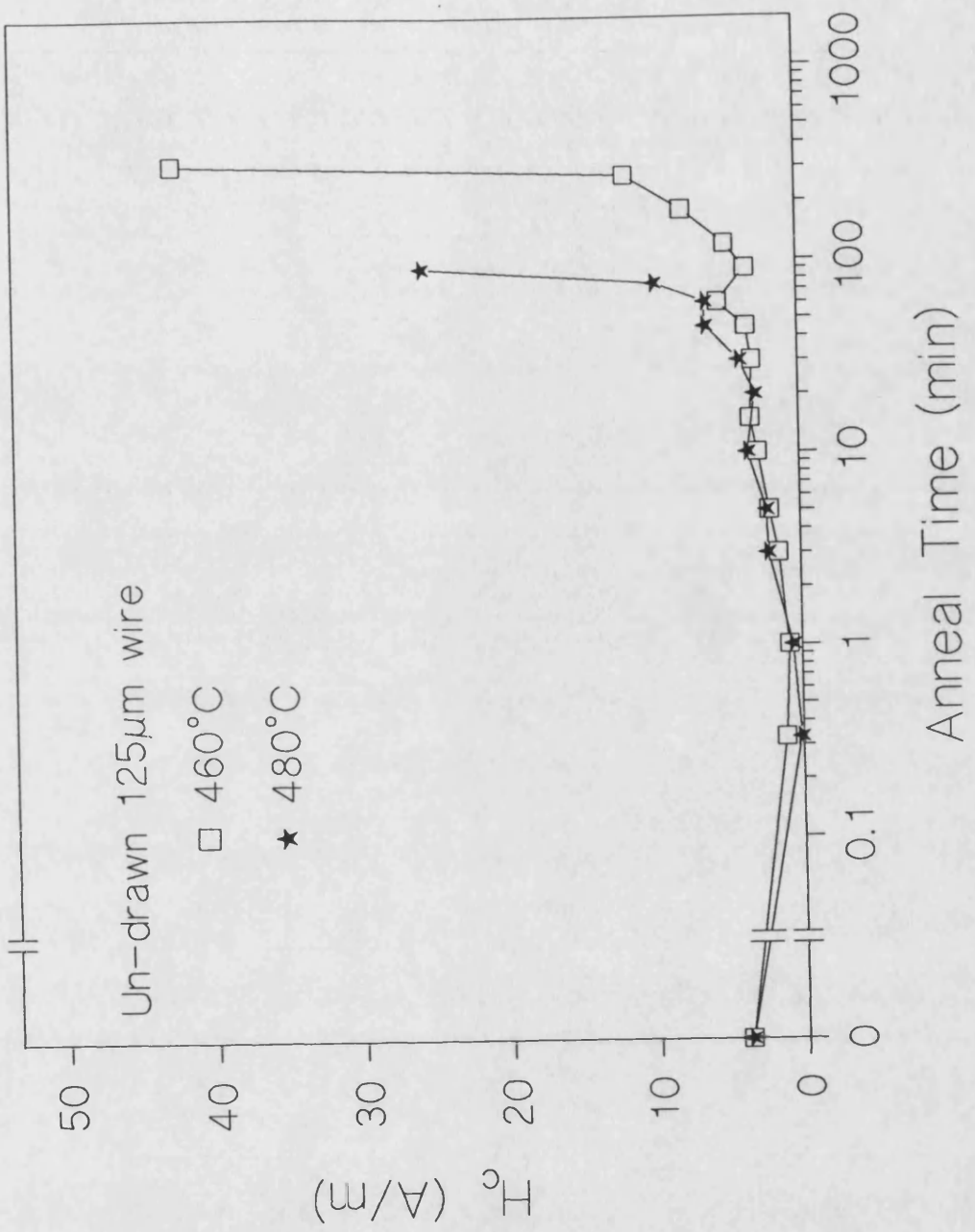

Figure 5.8: Coercivity of un-drawn 7 cm long, 125μm wires as a function of annealing time for the annealing temperatures of 460°C and 480°C. The lines are interpolated between the experimental data points.

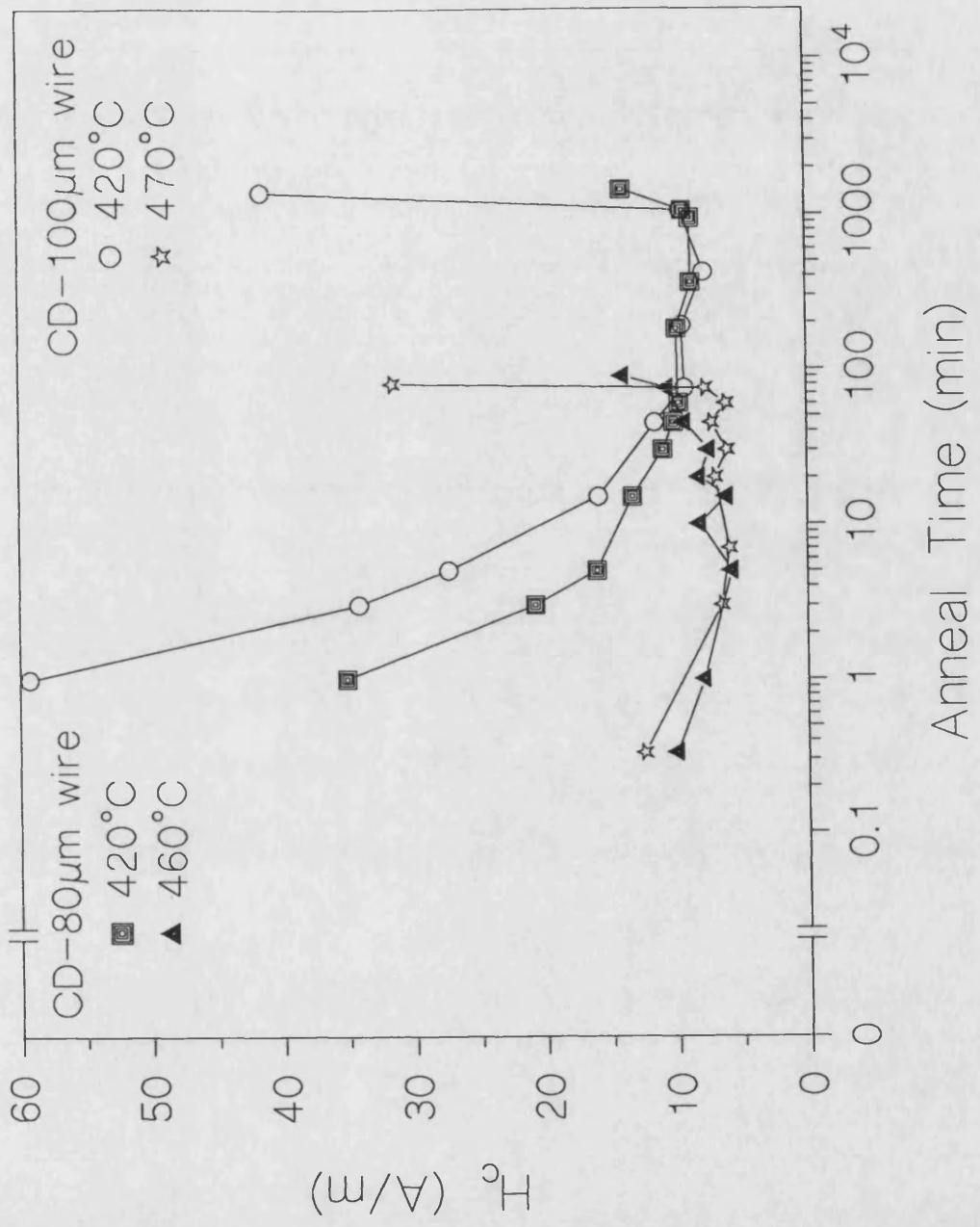

Figure 5.9: Coercivity of cold-drawn, 7 cm long, 80μm and 100μm wires as a function of annealing time. The lines are interpolated between the experimental data points.

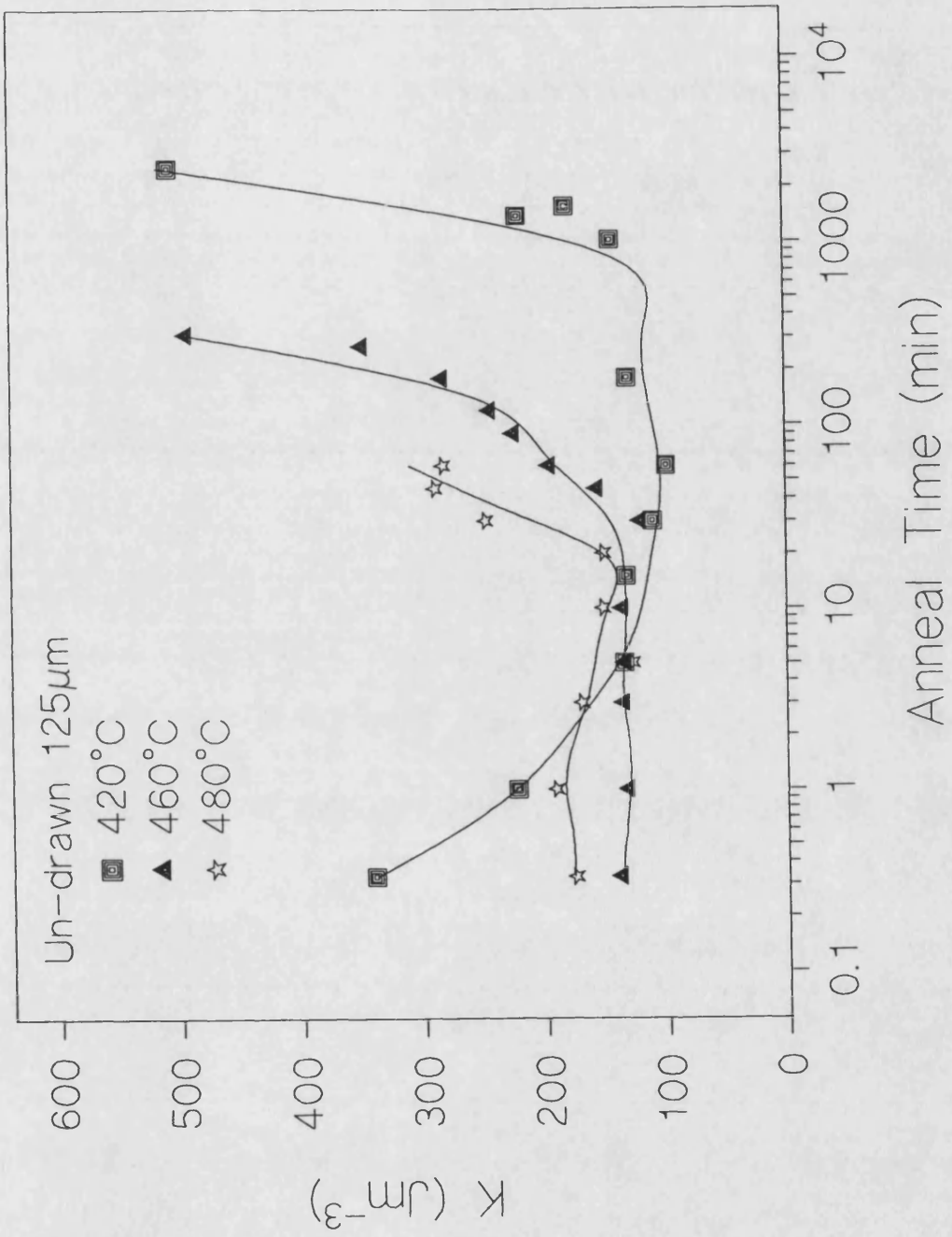

Figure 5.10: K of un-drawn 125µm wire as a function of annealing time for the annealing temperatures of 420°C, 460°C and 480°C. The lines are interpolated between the experimental data points.

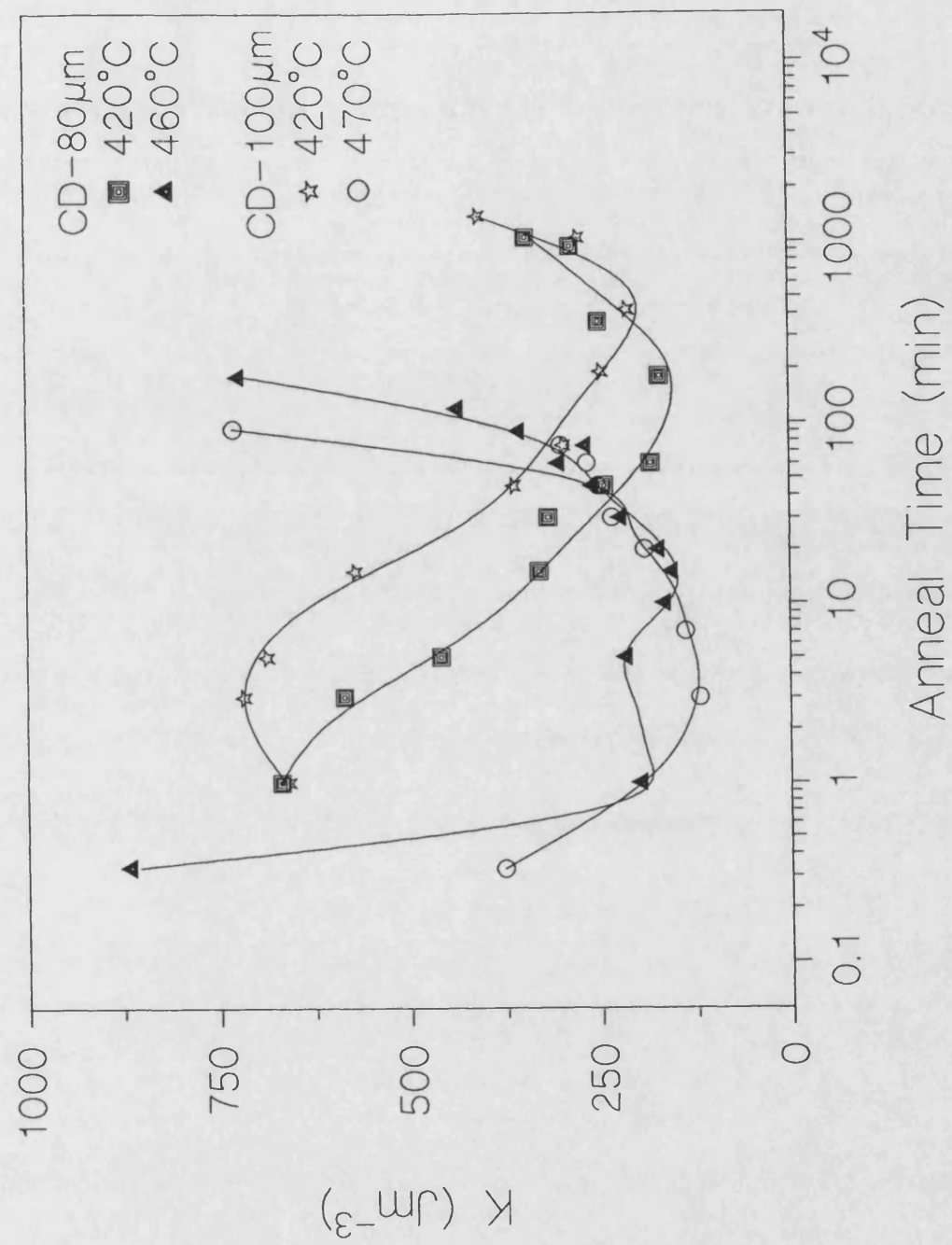

Figure 5.11: K of cold-drawn 80μm and 100μm wires as a function of annealing time.

The lines are interpolated between the experimental data points.

The anisotropy constant, K, was measured directly from the M-H loop with a maximum field of ~2500 A/m by calculating the area, as shown in figure 1.2. It was assumed that K is equal to the U_k. In the as-cast wires K arises from the interaction between the large casting stress and the magnetostriction. K is about 2200 Jm^{-3} for as-cast, un-drawn wire and is about 4000-5000 Jm^{-3} for cold-drawn wires.

K decreases gradually and reaches a minimum of 130-150 Jm^{-3} for the cold-drawn wires annealed at 420°C after an annealing time of 110 minutes. K then starts to increase due to the partial crystallisation. At high temperatures, K decreases sharply and starts to increase at low annealing time (figure 5.10 and 5.11). According to figures 5.9 and 5.11, both K and H_c of CD 80μm wire reach the minimum for anneal times of 1-10 minutes at 460°C. This shows that the best annealing time to relieve the maximum internal stress at this particular temperature is 1-10 minutes. A complete stress relief is found to be impossible due to the onset of crystallisation.

5.4 X-ray Studies

X-ray diffraction analysis was carried out using an X-ray powder camera, where the scattered intensity of X-rays from the wire is detected as a function of the scattering angle, 2θ. Figure 5.12 shows X-ray data of non-annealed CD 80μm wires and annealed at 480°C for 2 and 60 minutes. Crystallisation was not observed in the non-annealed and 2 min annealed wire. 60 min annealed wire shows a peak around 2θ=53°.

X-ray studies by Atkinson *et al* [1992] showed that the crystallisation at the surface of un-drawn wires starts after annealing at 480°C for 4 minutes. Additionally, scanning electron microscopes studies showed the existence of sub-micron crystallites on the surface of the wire annealed for 8 minutes at 470°C. Further annealing leads to growth of the crystallisation and to surface oxidation (figure 5.13).

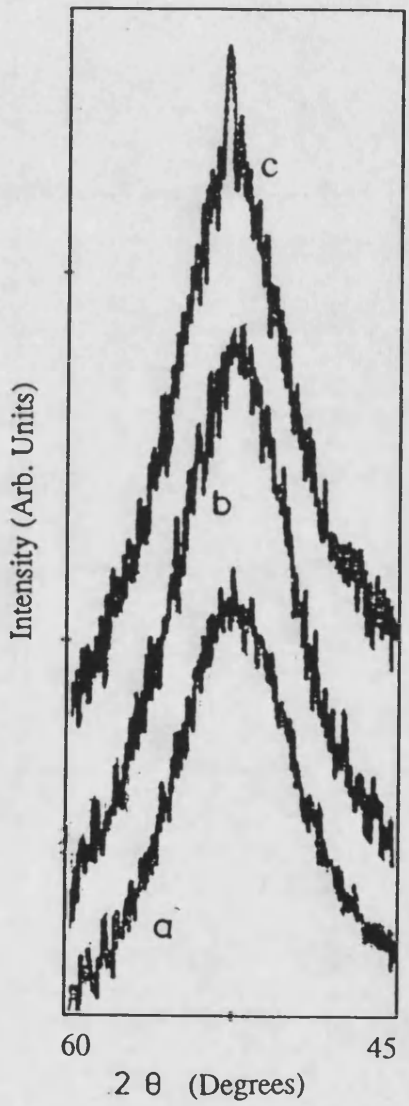

Figure 5.12: X-ray data of cold-drawn 80μm wire a) non-annealed b) annealed at 480°C for 2 minutes and c) 60 minutes.

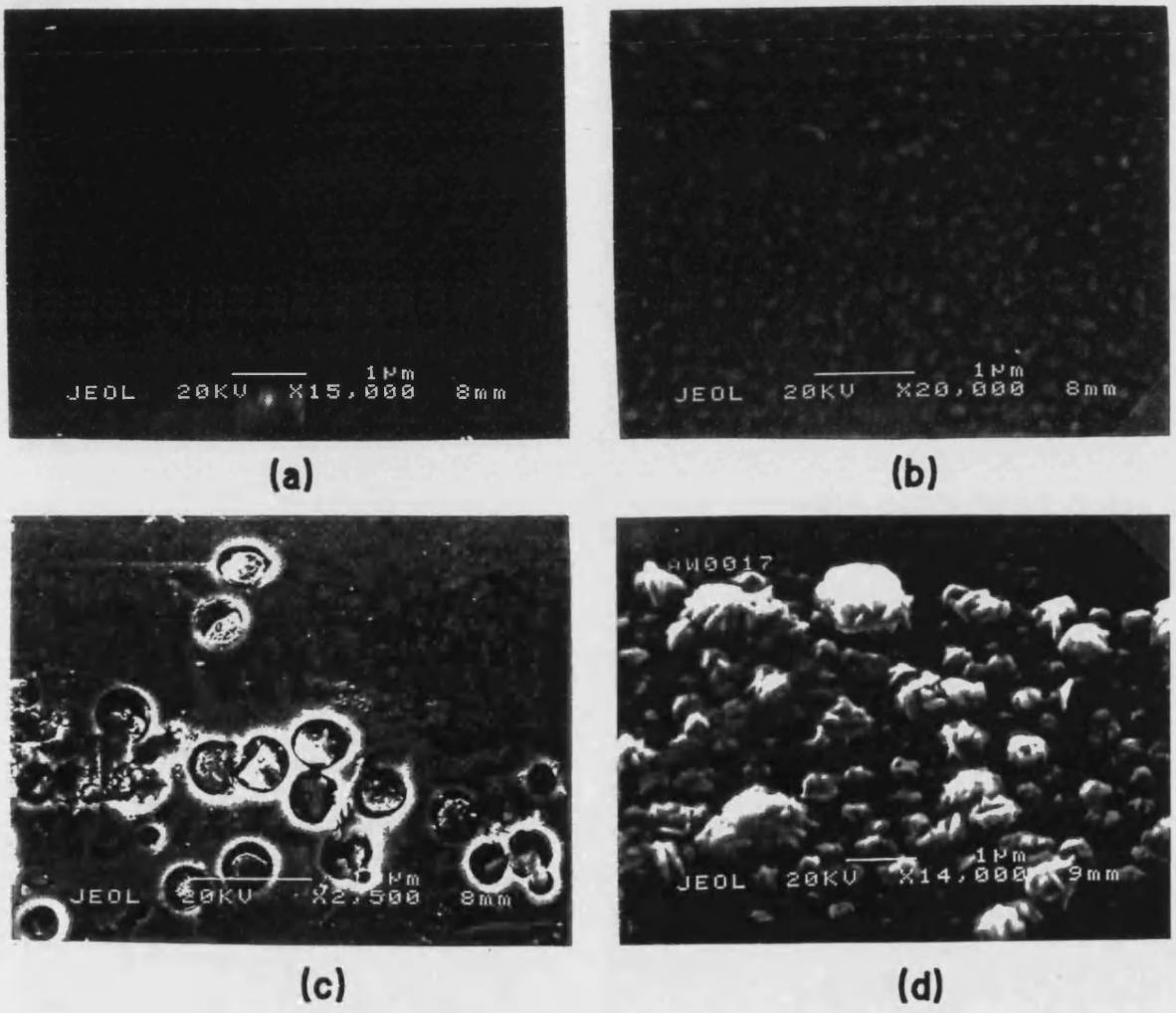

Figure 5.13: Scanning electron microscope micrographs of un-drawn 125μm wire a) as-cast, b) annealed at 470°C for 8 minutes, c) 35 minutes and d) 100 minutes (after Atkinson [1992]).

5.5 Magnetostriction

The field dependent strain, also called the engineering magnetostriction, λ_e, is related to the saturation magnetostriction constant by equation 1.9. When the wire is saturated the final angle between the magnetic moment direction and the magnetic field will be zero. So equation 1.9 can be written in the following form:

$$\lambda_e = \frac{3}{2}\lambda_s \sin^2\theta_i \qquad (5.3)$$

According to equation 5.3, in order to obtain maximum magnetostrictive strain, the initial magnetic moment direction must be perpendicular to the applied field.

Magnetostriction as a function of magnetic field was measured as explained in chapter 4, section 4. In the cold-drawn (CD) 90μm wire annealed at 480°C for 2 min, the observed LBJ from M-H loop shows that there is an axially magnetised core which cannot contribute to λ_e. Additionally, in stress relieved wires, the moments in the outer shell are not perpendicular to the wire axis and reorientation of these moments produces a net peak strain of ~48 ppm, which is slightly less than $(3/2)\lambda_s$ (figure 5.14). If the initial angle, θ_i, is calculated from equation 5.4, θ_i is about 70°.

For the 10 min annealed CD 90μm wire, the peak strain is 36 ppm, indicating a substantial number of the magnetic moments initially make an angle to the wire axis of~54°. The largest peak strain (~55 ppm) was obtained for the wire annealed for 60 min. Surface crystallisation was observed in this wire. This leads to alignment of the magnetic moments initially in a direction perpendicular to the applied field and, because $\sin\theta_i=1$, the peak strain can be identified with $(3/2)\lambda_s$, giving a value of λ_s=37ppm, similar to previously reported values (Konno [1989]). The 90 min anneal wire has a peak strain of

~52 ppm which is almost equal to the peak strain of the 60 min annealed wire. The small decrease in the peak strain is due to the increase in the size of the crystalline part of the wire.

The M-H loop of CD 100μm wire annealed at 480°C for 2 min shows the typical LBJ. M-H and λ-H curves of this wire are very similar to those for the CD 90μm wire annealed at 480°C for 2 min. CD 100μm wire has a peak strain of 46 ppm, which gives an initial angle of the moments of ~66° to the wire axis (figure 5.15). LBJ was also observed, in the case of CD 70μm wire annealed at 480°C for 1 min. It has a peak strain of 66 ppm, which is much larger than any other measured value. The diameter of CD 70μm wire is much smaller than the diameter of the glass tube (figure 4.8). Therefore, during the λ-H measurements the lateral motion of the CD 70μm wire, which increases the measured λ value, becomes unavoidable.

Measurement of the magnetostriction of as-cast wire is impossible with this method, because of the friction between the wire and glass tube. Thomas [1992] measured the magnetostriction of un-drawn wire. In order to make the wire straight and get rid of surface roughness, wires were first current annealed under a tensile stress of 815 MPa and then furnace annealed. Peak strains of 27.5 ppm and 54.7 ppm were measured for wires annealed at 0.5 A for 1 min then at 460°C for 30min, and at 0.55 A for 5 seconds then at 460°C for 60 min, respectively.

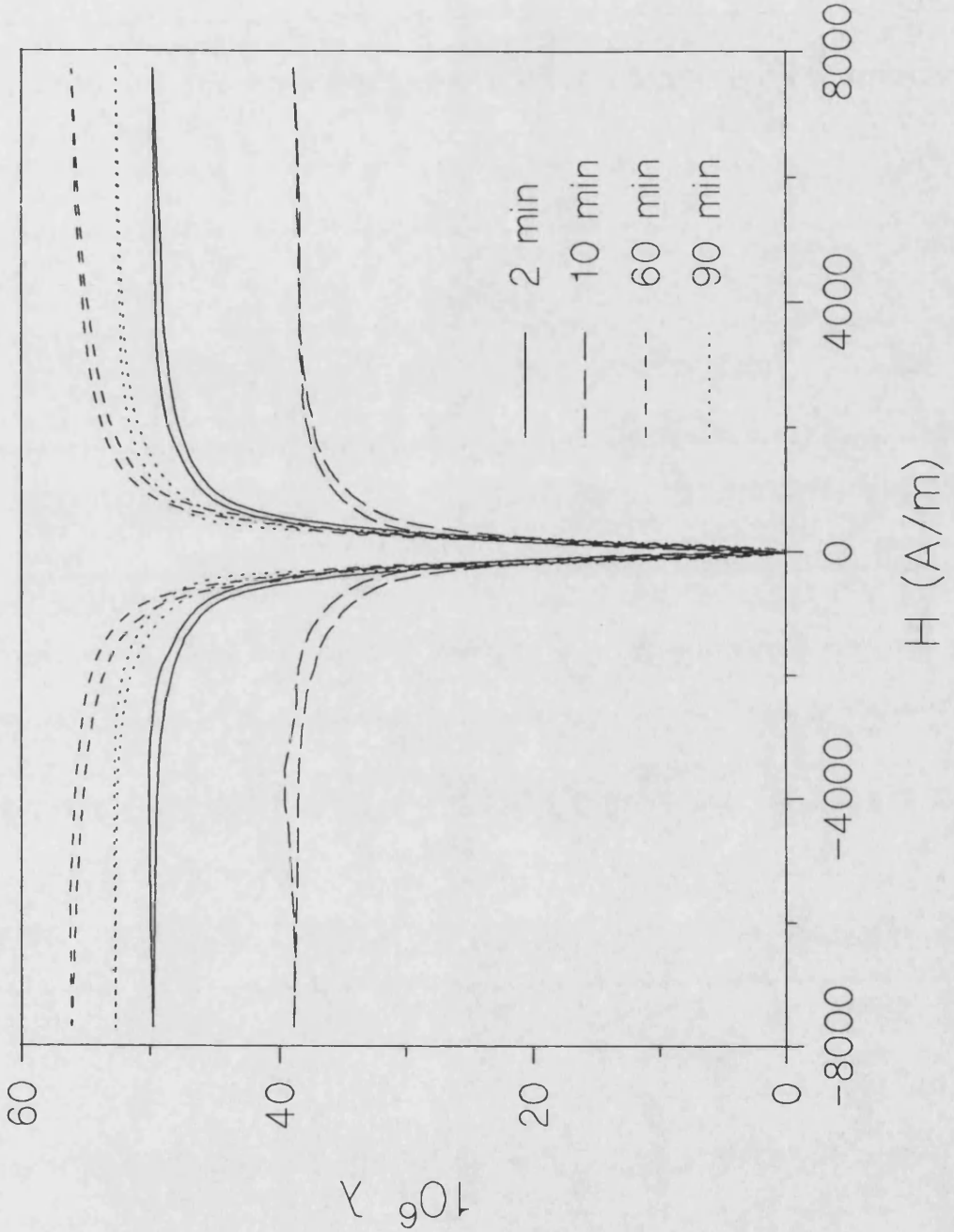

Figure 5.14: Magnetostriction of CD 90μm wire annealed at 480°C, as a function of applied field for various annealing times.

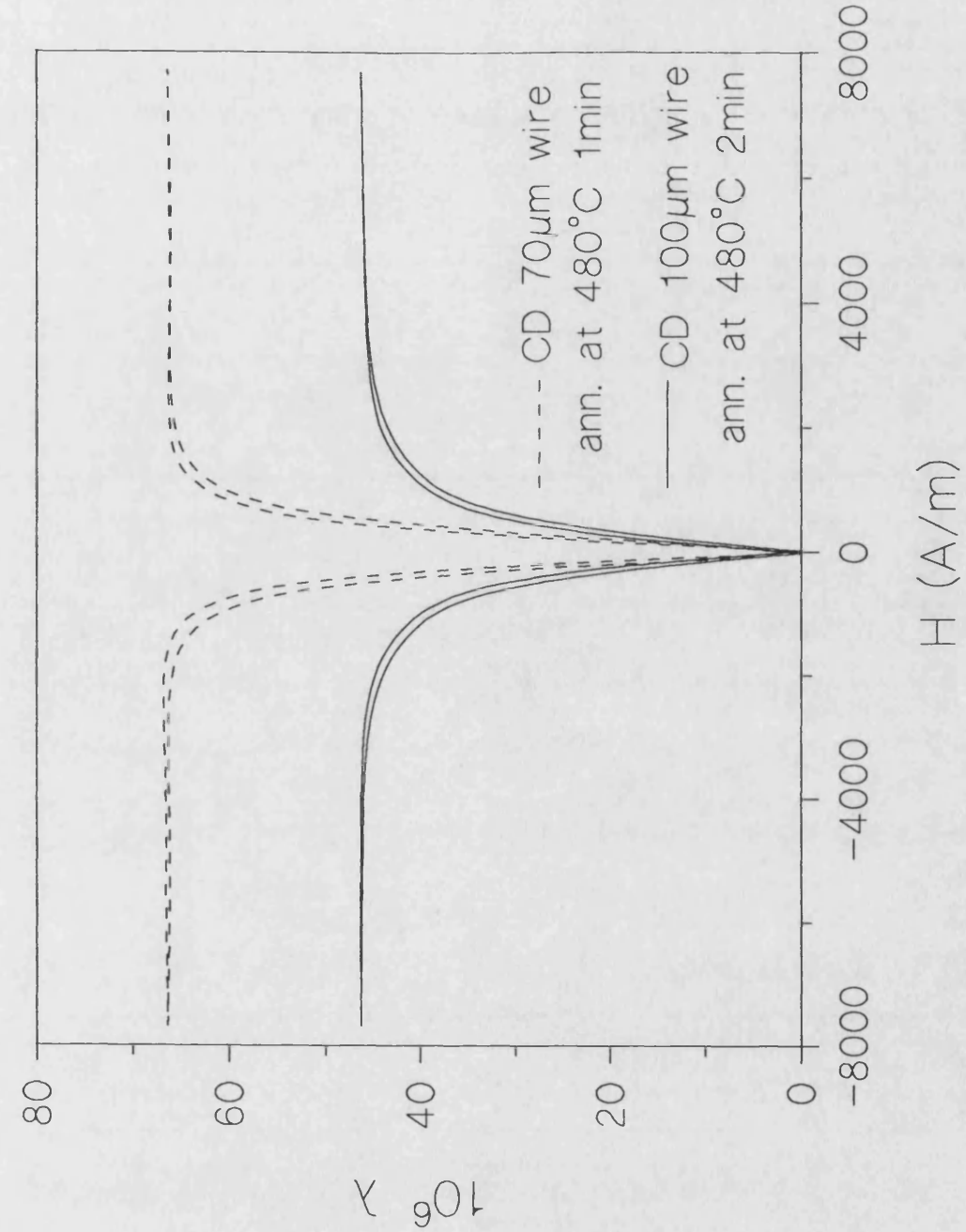

Figure 5.15: Magnetostriction of CD 100μm and CD70μm wires as a function of applied field.

5.6 Young's Modulus

5.6.1 Field Dependence of Young's Modulus

Young's modulus, E, was measured using the vibrating reed method, as explained in chapter 4 section 5. E/E_s is plotted against applied magnetic field in figure 5.16 for un-drawn wires of various diameters. The ratios of E_o/E_s and E_{min}/E_s (where E_{min} is the minimum value of E and E_o is the E at H=0) are shown in table 5.1. All the un-drawn, as-cast wires have almost same anisotropy constant, K, therefore difference in the E_{min}/E_s cannot be attributed to K. Both E_{min}/E_s and E_o/E_s increase with increasing wire diameter. Chen *et al* [1984] suggested that the quenching process varies with varying wire diameter. This would lead to a change in the size of the inner core diameter and therefore in the size of the outer shell. The inner core diameter, D_{in}, is calculated from the M_r/M_s ratio, which is ~0.5 for all as-cast wires. The ratio of the inner core diameter to the wire diameter, D, increases with increasing wire diameter. This shows a decrease in the relative size of the outer shell. Therefore it was concluded that the difference in the field dependence of E, E(H), of as-cast wires with different diameters is due to the variation in the size of the outer shell.

The field dependence of the E is explained using the Squire [1990] model. On the basis of the model, the values of E_{min}/E_s and E_o/E_s can be used as indicators of the moment angle with respect to the wire axis at H=0 and of anisotropy, respectively. To compare the experimental data with theory, the equation 3.47 can be written as:

$$\frac{E}{E_s} = \frac{1}{1+\beta F(h,\theta,\gamma)} \qquad (5.4)$$

where $\beta = \lambda_s^2 E_s/K$ and F is a numerical factor and is a function of the easy axis orientation, applied field and stress. The magnitude of E/E_s is determined mainly by the dimensionless ratio β. The measured values for un-drawn, as-cast 125μm wire are

E_{min}/E_s=0.916 and E_o/E_s=0.962 with K=2000-4000Jm^{-3} and E_s=16.2$\times 10^{10}$. β is calculated to be 0.05-0.1 and F is set to 4.5, because according to the suggested domain structure (figure 2.9) the magnetic moments in the outer shell align perpendicular to the wire axis and these are the main cause of the observed ΔE effect. E_{min}/E_s is calculated to be 0.67-0.81. If the suggested domain structure is correct, the measured E_o/E_s is expected to be 1. Neither the E_{min}/E_s nor the E_o/E_s values calculated agree with the experimental values. This difference can be explained by the domain structure of the as-cast wire. Mohri *et al* [1985] reported, from domain observation that the easy axis in the outer shell varies along the wire length showing that the moments in the outer shell are not completely perpendicular to the wire axis. Also from observation of the Matteucci effect, Velazquez *et al* [1991] and Kinoshita [1990] suggested that there must be a helical component of the moments in the inner core of the wire. This shows that the easy axis in the inner core is not in the axial direction. Therefore, there is some contribution to the ΔE effect from the inner core.

Figure 5.17 shows the field dependence of Young's modulus of the CD 100μm wire. During the cold drawing process a large internal stress is induced in the wire leading to an anisotropy of ~5000Jm^{-3}. For this wire, β is about 0.04; as a result the change in E is only a few percent.

The effect of the temperature and annealing time on E(H) was studied at annealing temperatures of 370°C, 420°C, 460°C, 470°C and 480°C with annealing times from 0.3 minutes up to 2500 minutes. The wire annealed at 370°C has a very small annealing time dependence. After annealing for 50 minutes, E_o/E_s is about 0.68, E_{min}/E_s is about 0.62 and the M-H loop shows the characteristic LBJ.

Figures 5.18, 5.19 and 5.20 show examples of E(H) behaviour of annealed un-drawn and cold-drawn wires. The field dependence of E is almost the same in both the negative

and positive applied field regions. Two minima usually occur when the field is changed from positive saturation to the negative saturation and vice versa. But the minimum values of E on the negative and positive sides of H are not exactly the same for wires annealed for shorter times. When the annealing time is increased, the difference in E_{min} values becomes smaller and then disappears.

Figure 5.21 illustrates the effect of the annealing time on E_{min}/E_s and E_o/E_s. The measurement of E_{min}/E_s as a function of annealing time gives information about the change in the anisotropy. As can be seen from figure 5.21, E_{min}/E_s behaves very similarly to K as a function of annealing time. For the un-drawn 125μm wire annealed at 420°C , both K and E_{min}/E_s decrease with increasing annealing time and reach a minimum at around 3 minutes annealing time. Both then remain the same the until annealing time reaches 1000 minutes, then they start to increase sharply. This behaviour of E_{min}/E_s and E_o/E_s is also observed for the other annealing temperatures and for cold-drawn wires. But the E_{min}/E_s behaviour of UD 125μm wire annealed at 460°C is slightly different. E_{min}/E_s first decreases from the as-cast, value then it gradually increases and starts to decrease again. With further annealing, E_{min}/E_s starts to increase sharply. However, the behaviour of K is not the same as the E_{min}/E_s behaviour for the wires annealed at that temperature. Therefore, it was assumed that the initial increase and decrease in E_{min}/E_s is due to changes in the domain structure.

E_o/E_s is determined by the initial angle of moment orientations. The decrease in E_o/E_s for short annealing times is the result of relief of the residual radial stress. Therefore, magnetic moments will try to align in the wire axis direction because of the shape anisotropy. But E_o is always bigger than E_{min} (i.e. E first decreases then increases with increasing H). This shows that the average angle of magnetic moments is always greater than 45° (figures 3.6-3.10). For wires annealed for short times the magnetic moments

align between 45° and 60° to the wire axis. But this is not correct for the cold-drawn wire annealed at 420°C for 20 seconds. The $E_o=E_{min}$ and E_{min} is very small. This indicates that the initial angle is between 20°-40°.

For the longer annealing times, E_o/E_s starts to increase and reaches a value of about 0.9-0.95 showing that the easy axis must be close to the 90° to wire axis. The increase in E_o/E_s can be related to the degree of partial crystallisation of the wire. Both X-ray and SEM studies showed that surface crystallisation starts at 30 minutes at 460°C, 8 minutes at 470°C and 4 minutes 480°C.

Density measurements (Ok and Morrish [1981]) showed that completely crystallised ribbon has a higher density than an amorphous sample. It follows that a partly crystallised layer at the surface of a wire contracts, causing a compressive stress on the internal amorphous portion of the sample. For a positively magnetostrictive material, this will result (at H=0) in orientation of moments perpendicular to the direction of the compressive stress. In the case of the surface crystallised Fe-based wire, magnetic moments will align in either the axial or circumferential direction. If the moments are in the axial direction, the change in E with magnetic field is expected to be zero. But surface crystallised wires show a large field dependence and E_o is almost equal to E_s. Therefore we suggest that in the surface crystallised Fe-based wire, magnetic moments align in the circumferential direction when H=0, as shown in figure 5.22.

Figure 5.23 shows the field dependence of E for un-drawn, annealed $Fe_{77.5}Si_{7.5}B_{15}$ and $Fe_{67}Si_{10}B_{15}Cr_8$ wires. The $Fe_{77.5}Si_{7.5}B_{15}$ wires with diameters of 95μm and 140μm show very similar E(H) behaviour to the $Fe_{77.5}Si_{7.5}B_{15}$ 125μm wire. Although $Fe_{67}Si_{10}B_{15}Cr_8$ wire was not studied comprehensively, E_{min}/E_s is about 0.67, which is smaller than E_{min}/E_s for $Fe_{77.5}Si_{7.5}B_{15}$ wires. This is because $Fe_{67}Si_{10}B_{15}Cr_8$ wire has much smaller $\lambda_s \sim 10 \times 10^{-6}$. Figure 5.24 illustrates the annealing time dependence of anisotropy field, H_k (i.e. the

field at the minimum value of E). The anisotropy field of wires annealed at 420°C first decreases then increases very gradually and then increases sharply. For the wires annealed at higher annealing temperatures, H_k first increases gradually then increases sharply. It was assumed that the variation in H_k is due to the change in K.

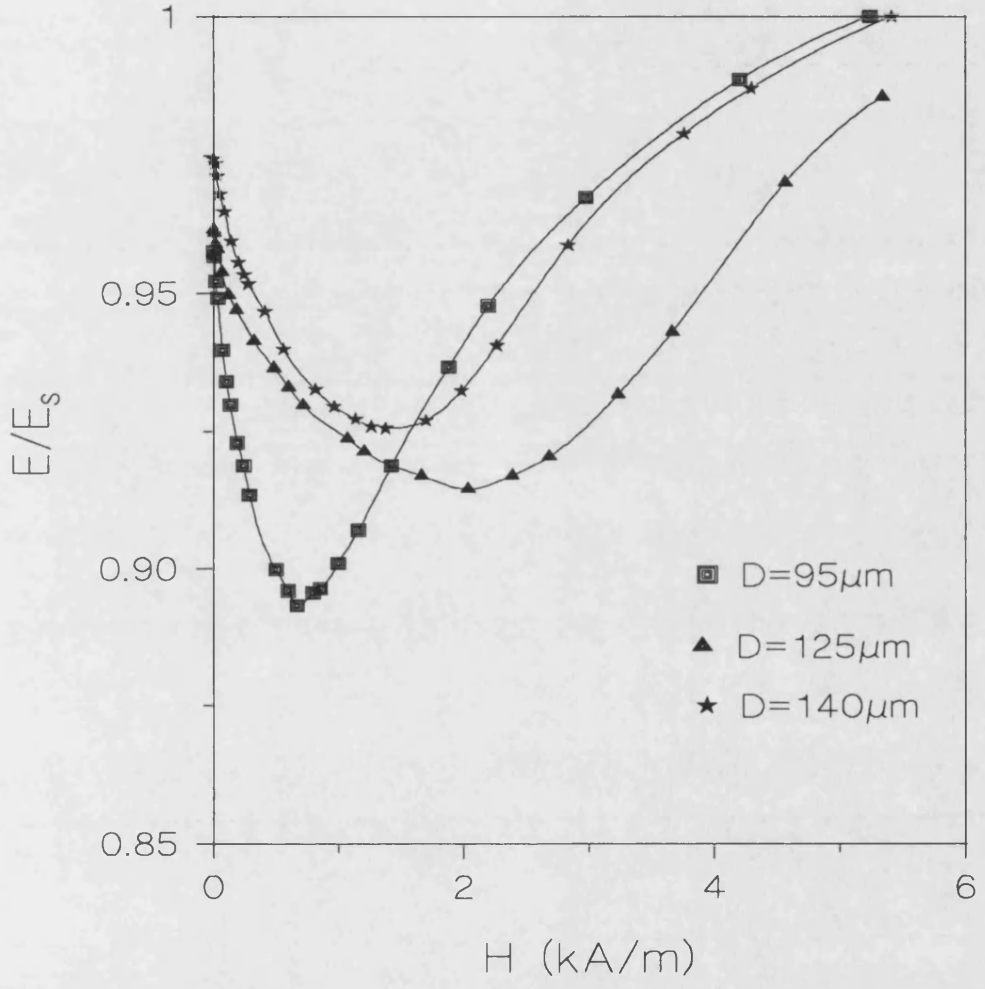

Figure 5.16: Normalised Young's modulus of un-drawn, $Fe_{77.5}Si_{7.5}B_{15}$ as-cast wires as a function of applied field. The lines are interpolated between the experimental data points.

D (μm)	D_{in} (μm)	D_{in}/D	E_o/E_s	E_{min}/E_s
95	60	0.63	0.957	0.893
125	88	0.7	0.962	0.916
140	99	0.71	0.974	0.925

Table 5.1: The estimated inner core diameters, E_{min}/E_s and E_o/E_s ratios for un-drawn as-cast wires.

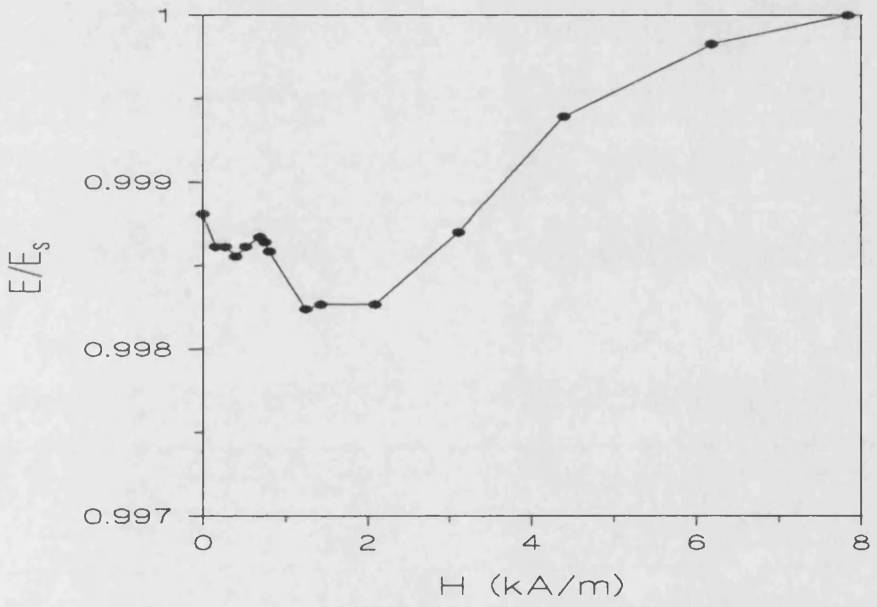

Figure 5.17: Young's modulus of cold-drawn $Fe_{77.5}Si_{7.5}B_{15}$ 100μm wire as a function of magnetic field. The lines are interpolated between the experimental data points.

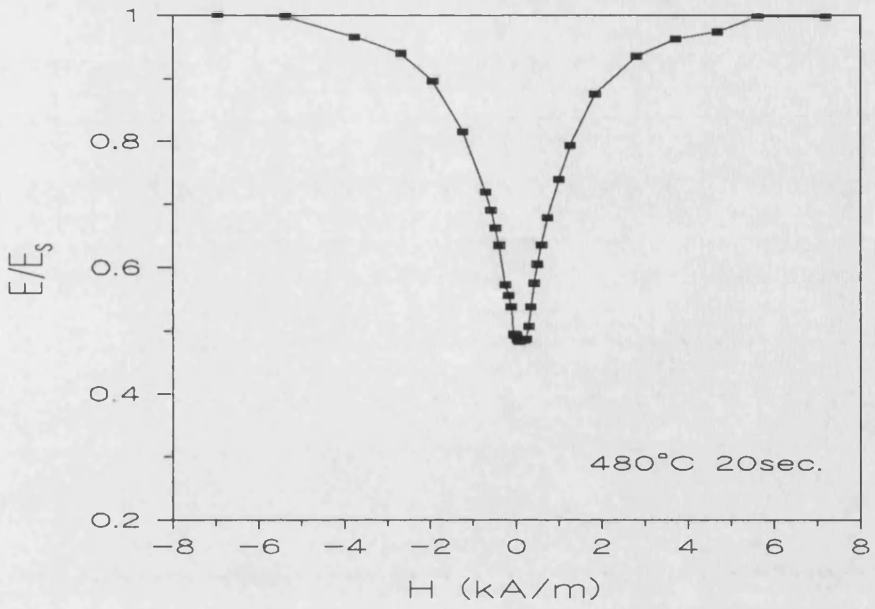

Figure 5.18a: E(H) curve of un-drawn $Fe_{77.5}Si_{7.5}B_{15}$ 125μm wire annealed at 480°C for 20 seconds.

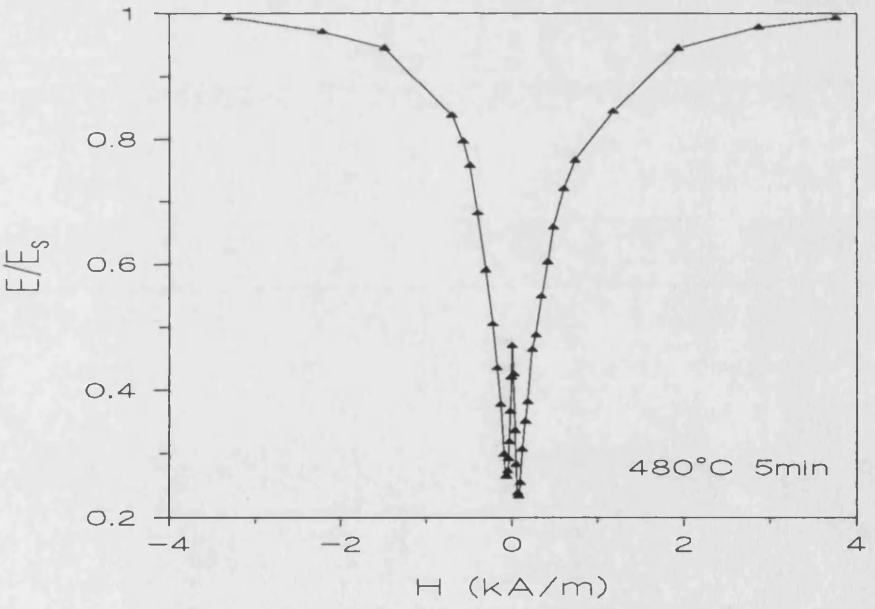

Figure 5.18b: E(H) curve of un-drawn $Fe_{77.5}Si_{7.5}B_{15}$ 125μm wire annealed at 480°C for 5 minutes.

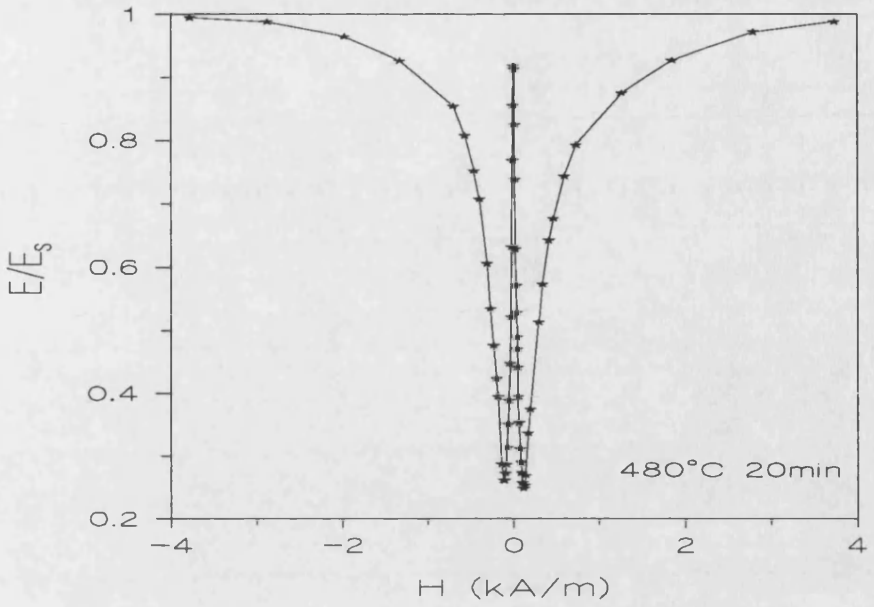

Figure 5.18c: E(H) curve of un-drawn $Fe_{77.5}Si_{7.5}B_{15}$ 125μm wire annealed at 480°C for 20 minutes.

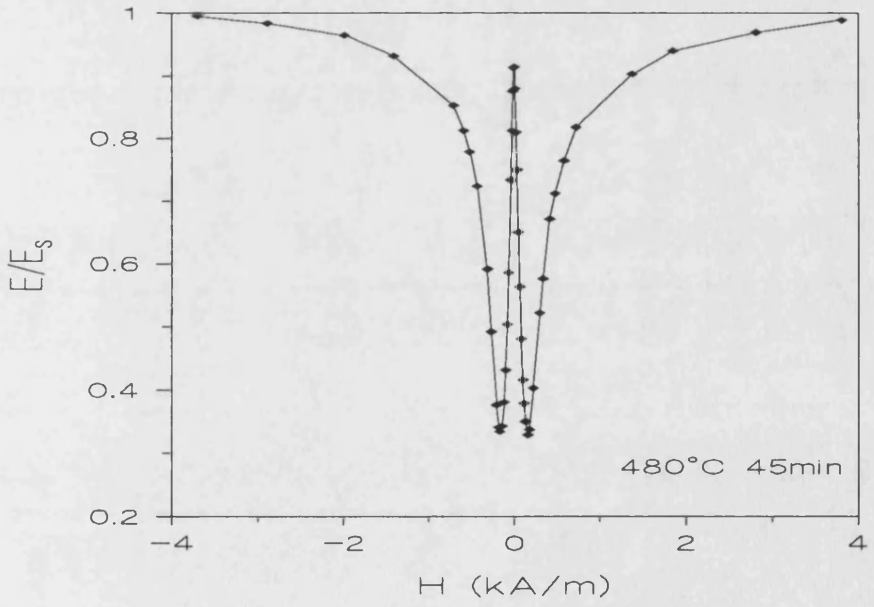

Figure 5.18d: E(H) curve of un-drawn $Fe_{77.5}Si_{7.5}B_{15}$ 125μm wire annealed at 480°C for 45 minutes.

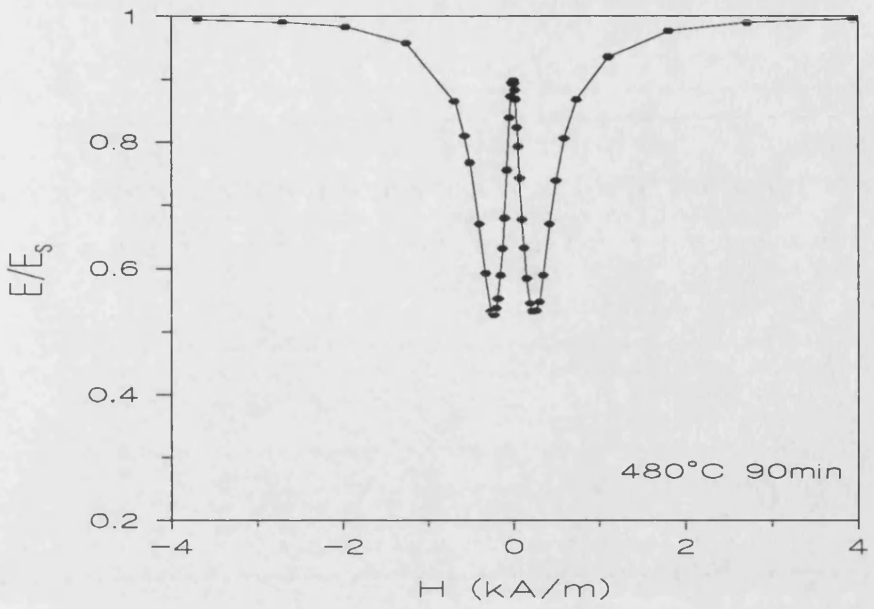

Figure 5.18e: E(H) curve of un-drawn $Fe_{77.5}Si_{7.5}B_{15}$ 125μm wire annealed at 480°C for 90 minutes.

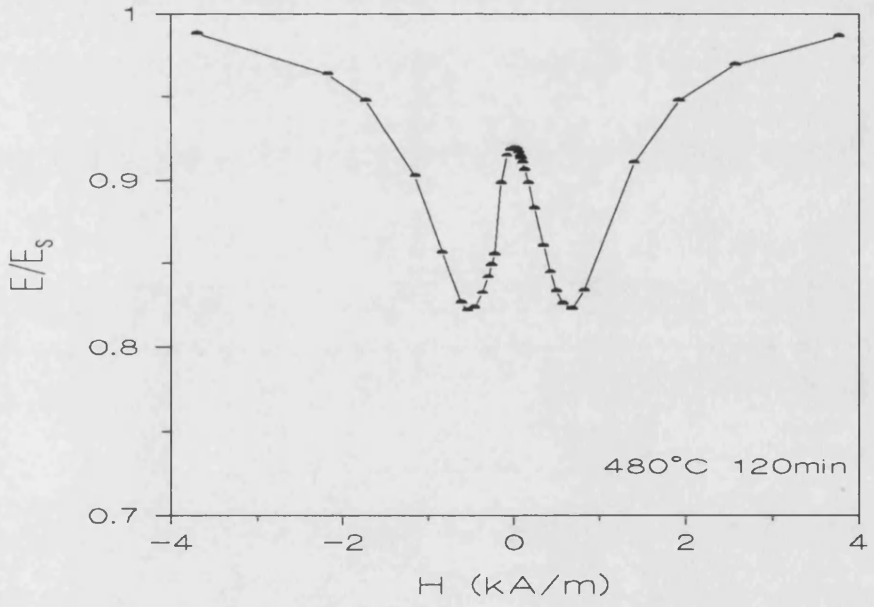

(f)

Figure 5.18f: E(H) curves of un-drawn $Fe_{77.5}Si_{7.5}B_{15}$ 125μm wire annealed at 480°C for 120 minutes. The lines are interpolated between the experimental data points.

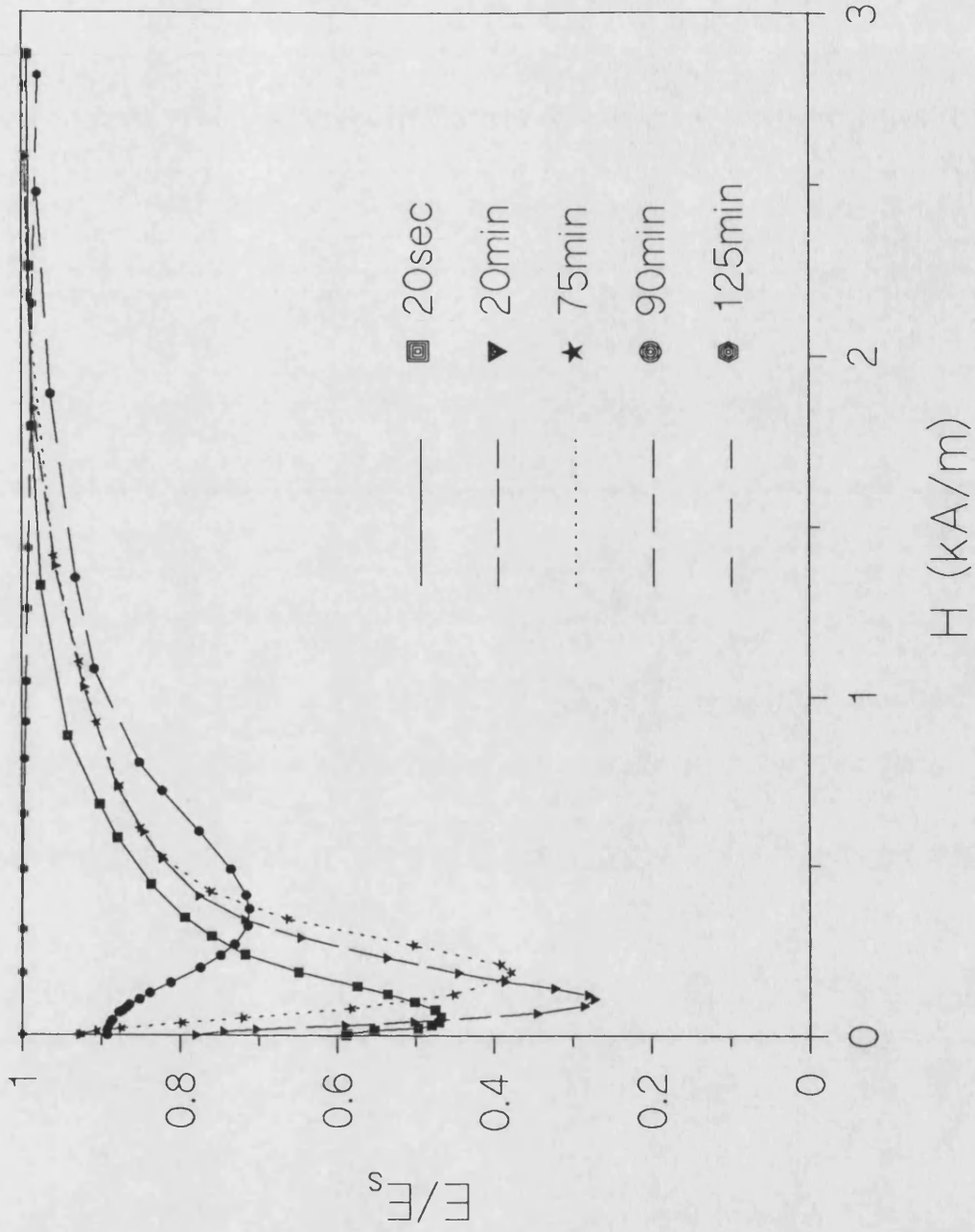

Figure 5.19: Examples of E(H) curves for cold-drawn 100μm wire annealed at 470°C for various annealing times. The lines are interpolated between the experimental data points.

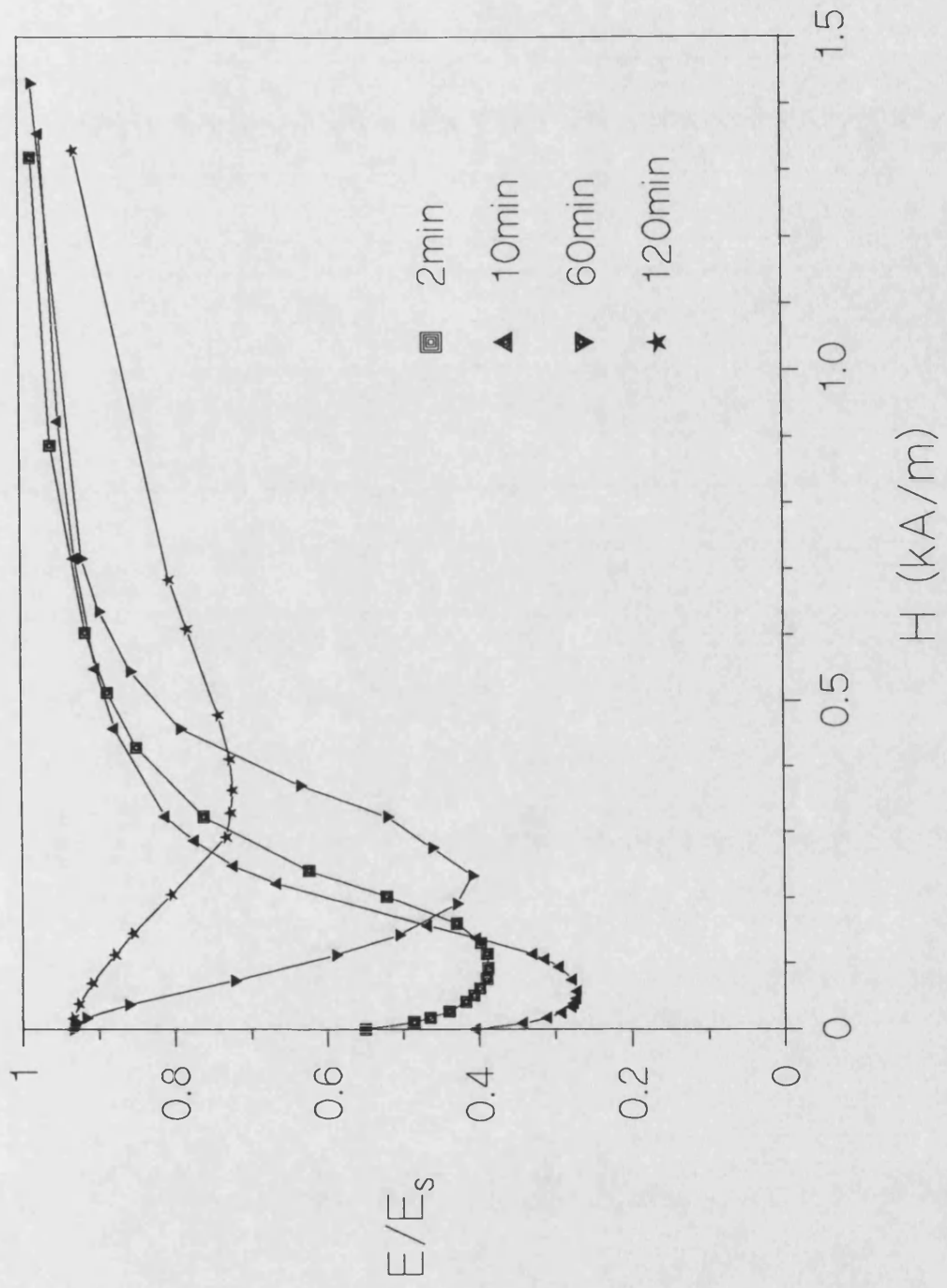

Figure 5.20: Normalised Young's modulus of CD 90μm wire annealed at 480°C as a function of applied field. The lines are interpolated between the experimental data points.

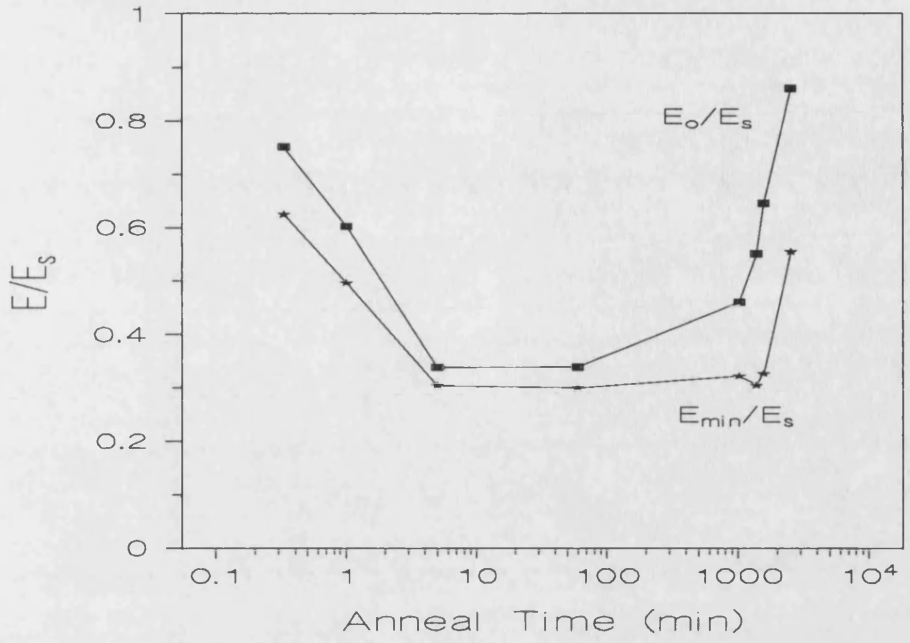

Figure 5.21a: The effect of annealing time and temperature on E_{min}/E_s and E_o/E_s.

$Fe_{77.5}Si_{7.5}B_{15}$ UD 125μm wire annealed at 420°C.

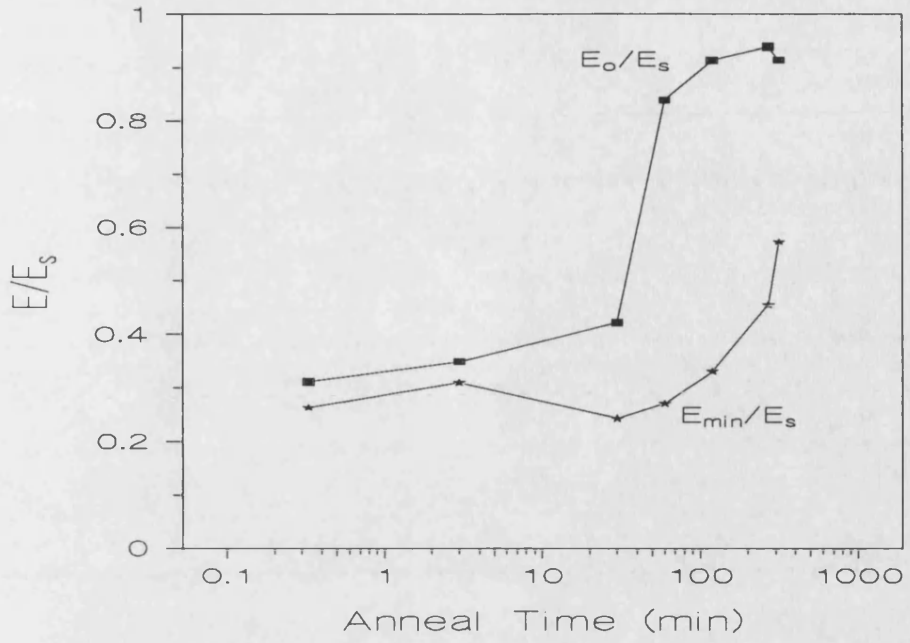

Figure 5.21b: The effect of annealing time and temperature on E_{min}/E_s and E_o/E_s. $Fe_{77.5}Si_{7.5}B_{15}$ UD 125μm wire annealed at 460°C.

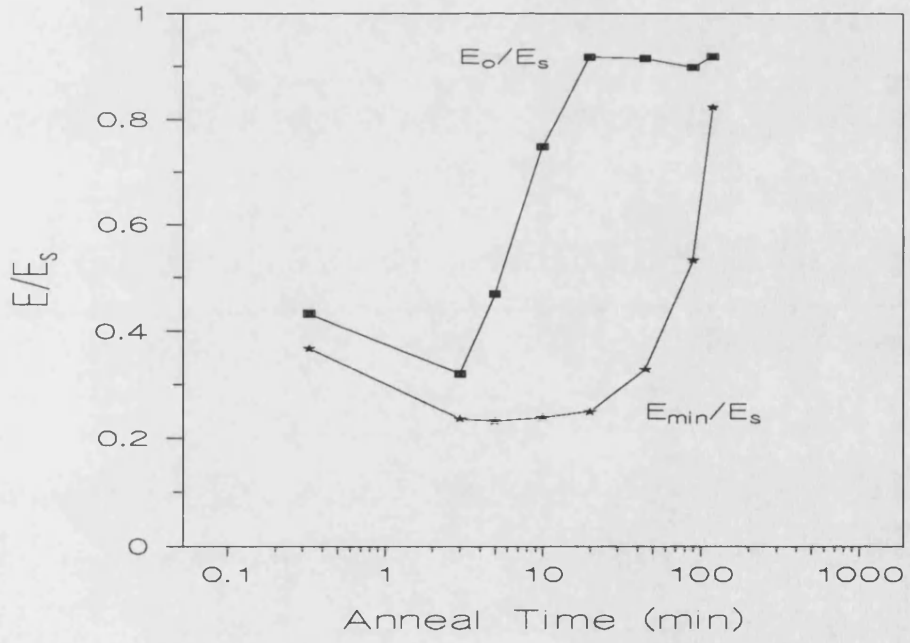

Figure 5.21c: The effect of annealing time and temperature on E_{min}/E_s and E_o/E_s. $Fe_{77.5}Si_{7.5}B_{15}$ UD 125μm wire annealed at 480°C.

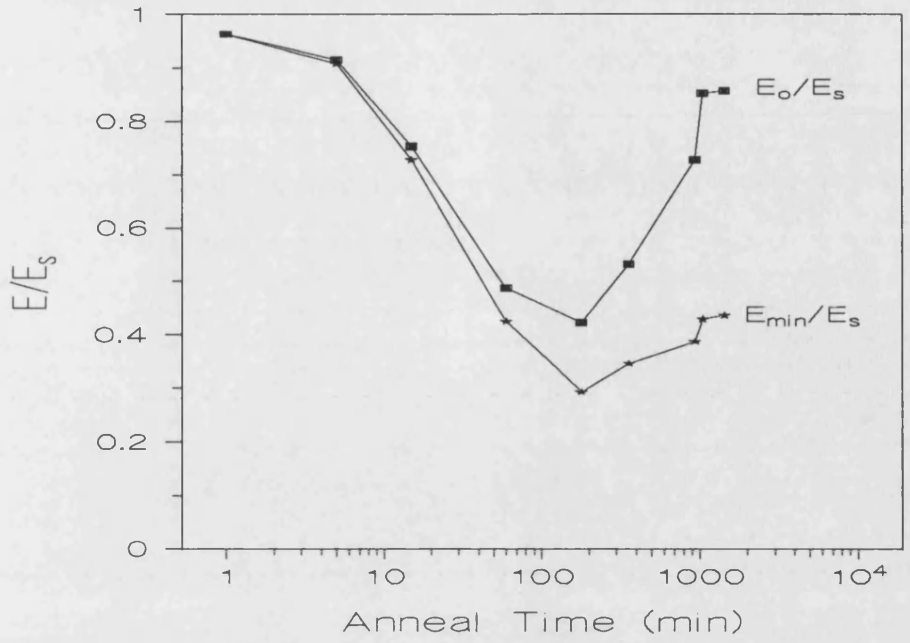

Figure 5.21d: The effect of annealing time and temperature on E_{min}/E_s and E_o/E_s. $Fe_{77.5}Si_{7.5}B_{15}$ CD 80μm wire annealed at 420°C.

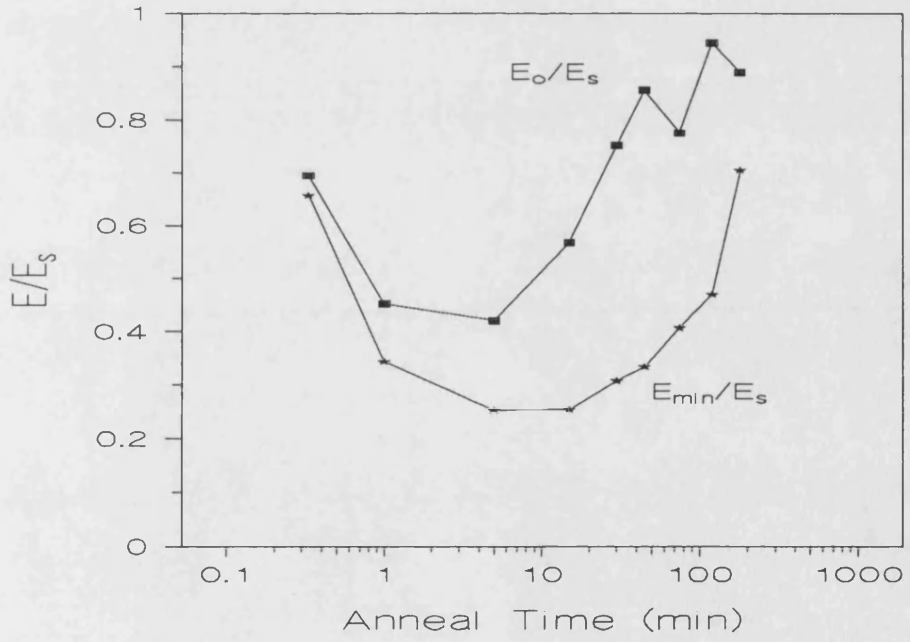

Figure 5.21e: The effect of annealing time and temperature on E_{min}/E_s and E_o/E_s. $Fe_{77.5}Si_{7.5}B_{15}$ CD 80μm wire annealed at 460°C.

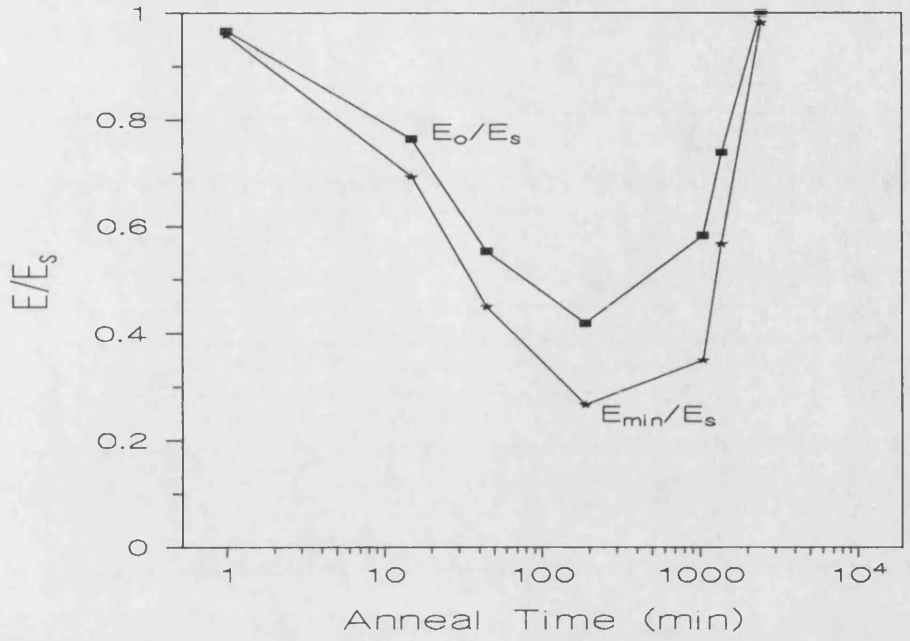

Figure 5.21f: The effect of annealing time and temperature on E_{min}/E_s and E_o/E_s. $Fe_{77.5}Si_{7.5}B_{15}$ CD 100μm wire annealed at 420°C.

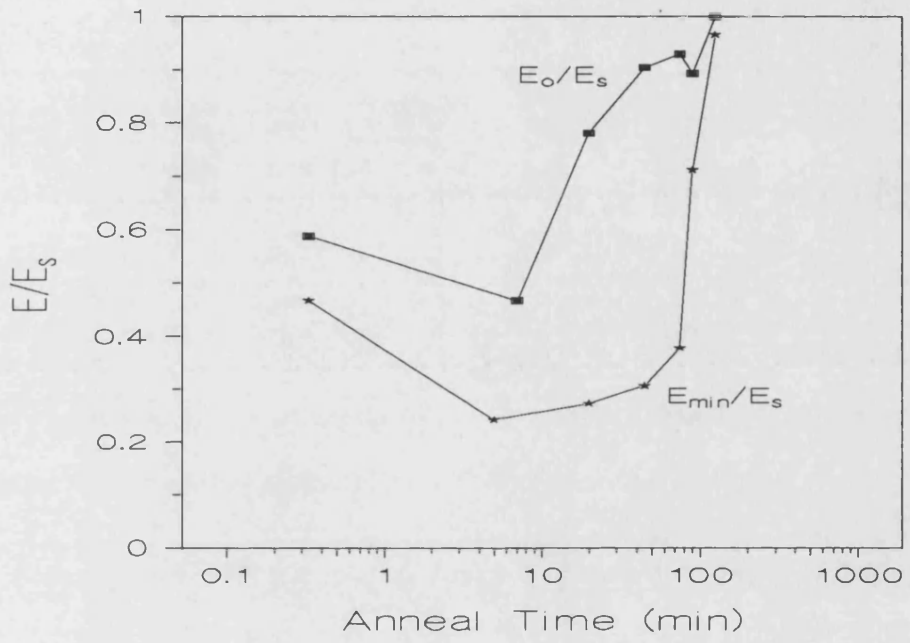

Figure 5.21g: The effect of annealing time and temperature on E_{min}/E_s and E_o/E_s. $Fe_{77.5}Si_{7.5}B_{15}$ CD100μm wire annealed at 470°C. The lines are interpolated between the experimental data points.

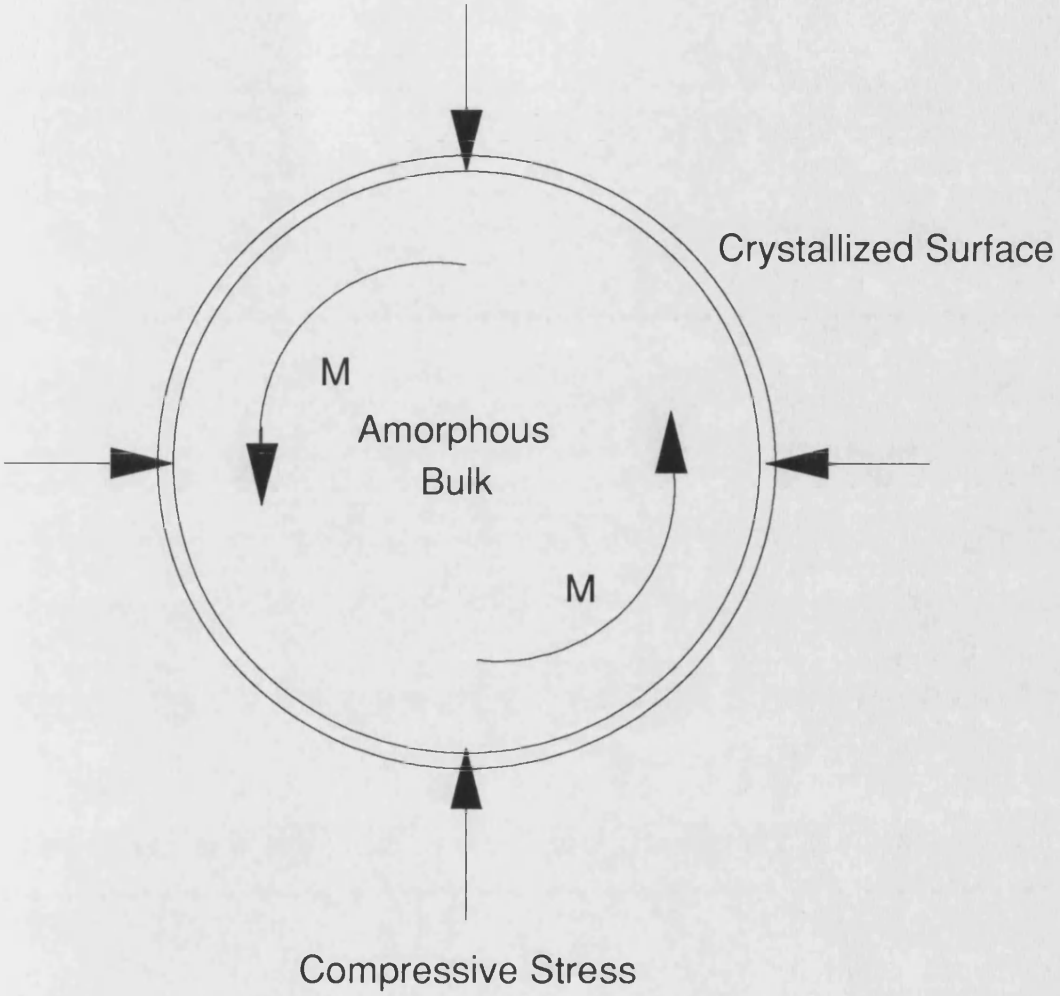

Figure 5.22: Suggested domain structure for surface crystallised Fe-based amorphous wire.

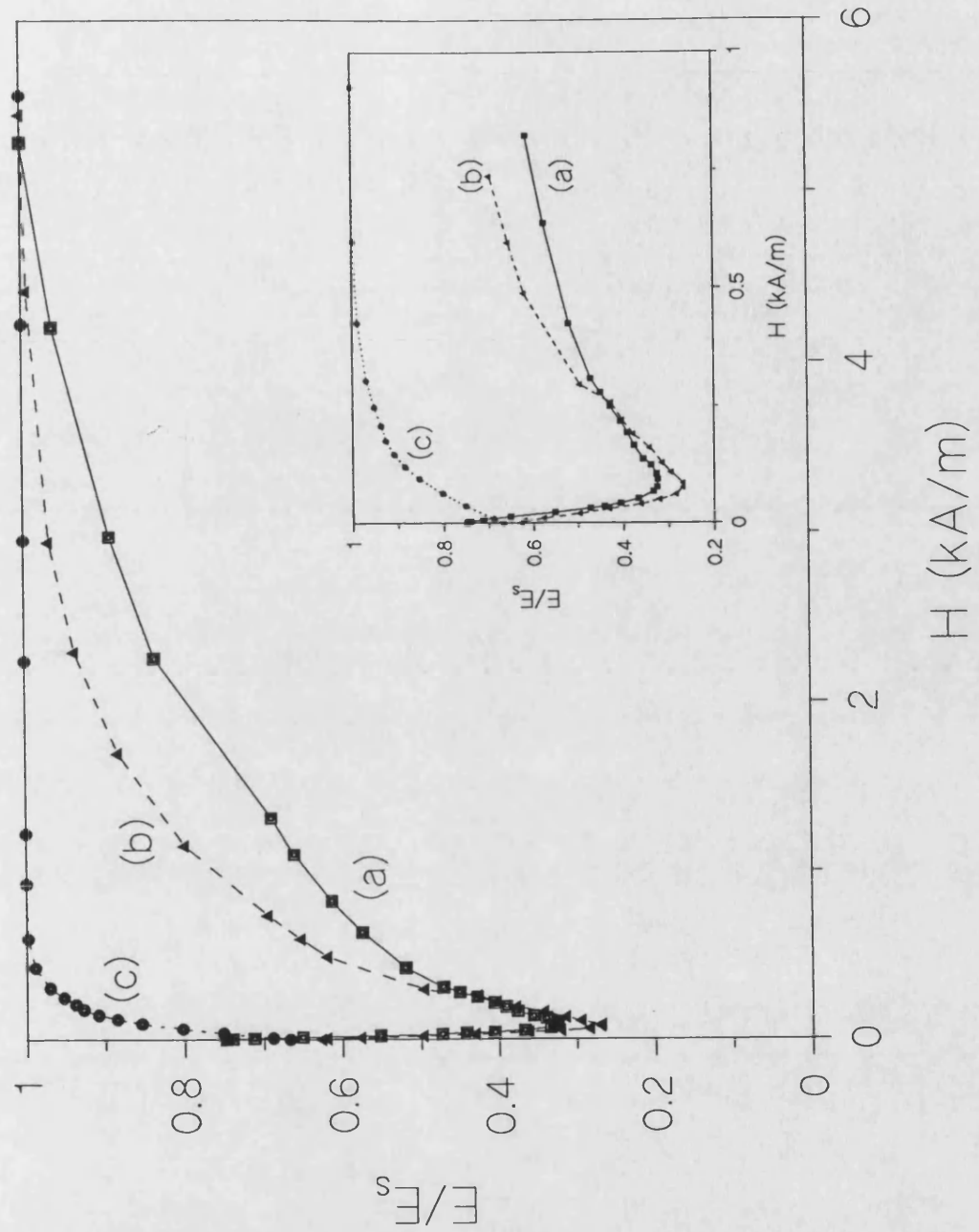

Figure 5.23: Normalised Young's modulus against applied field; a) $Fe_{77.5}Si_{7.5}B_{15}$ 140μm wire annealed at 460°C for 40 minutes, b) $Fe_{77.5}Si_{7.5}B_{15}$ 95μm wire annealed at 460°C for 30 minutes, c) $Fe_{67}Si_{10}B_{15}Cr_8$ wire annealed at 500°C for 12 minutes. The lines are interpolated between the experimental data points.

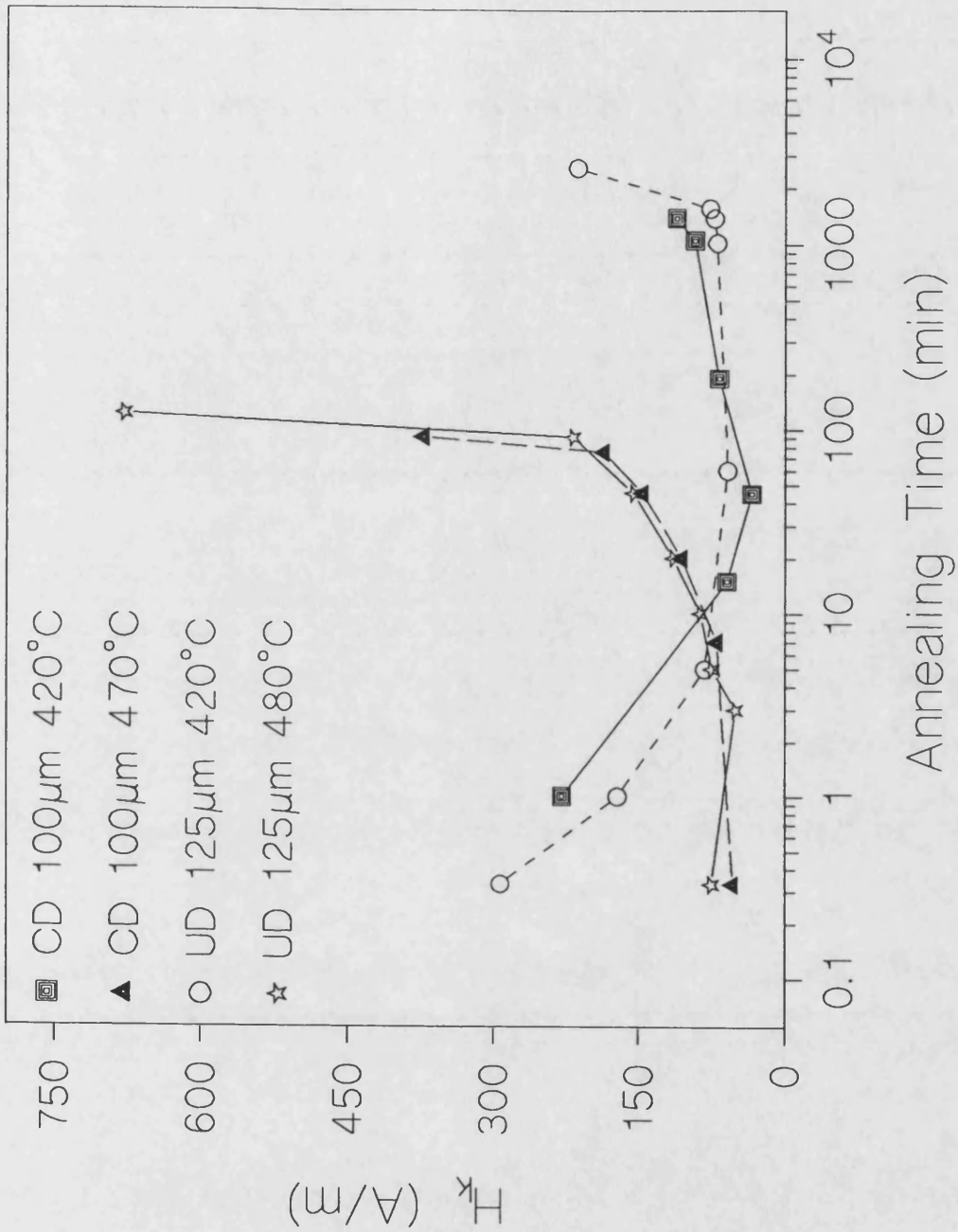

Figure 5.24: Temperature and annealing time dependence of H_k. The lines are interpolated between the experimental data points.

5.6.2 Pole Effect

When a magnetic field is applied, as shown in figure 5.25, a magnetic pole of strength m will be induced at the free end of the sample and there will be a restoring force, mHsinθ, in addition to the elastic restoring force tending to straighten the sample. This additional force increases the effective stiffness of the sample and increases its vibrational frequency (Berry and Pritchet [1979]).

If we assume that the pole force does not affect the shape of the vibrational mode, the frequency can be written as:

$$f_n = \frac{1}{2\pi}\left(\frac{K_n + S_n}{D_n}\right)^{1/2} \tag{5.5}$$

where D_n is the effective mass of the sample, S_n is the magnetic spring constant and K_n is the elastic spring constant. If the spring constant values for a wire-shaped material are calculated and inserted into equation 5.5, the following expression is obtained:

$$E = \frac{\rho\pi^2 l^4}{4\alpha_n^4 r^2} f_n^2 - \frac{1}{2}\gamma_n \frac{l^2}{r^2} MH \tag{5.6}$$

where α_n and γ_n are vibration constants. The pole effect is given in equation 5.6 by the second term on the right side. This term increases with increasing H, but the first term also changes with increasing H due to the change of frequency. The only region where a clear separation occurs is at larger fields where frequency can be taken as a constant. Then the first term becomes independent of the field. The second term becomes linear in H. γ_n in equation 5.6 varies from mode to mode. Therefore, pole effect varies from mode to mode according to the rapidly decreasing term γ_n in equation 5.6 (the calculated γ_n for different vibrational modes are γ_1=0.891, γ_2=0.0788 and γ_3=0.0165). So the pole effect becomes smaller at high vibration modes. The effect of the vibrational modes on the field dependence of E is shown in figure 5.26 for stress relieved 7 cm long FeSiB

amorphous wire with a diameter of 125μm. The geometry of the sample enters in the form of l^2/r^2. Therefore the pole effect is greater for longer and thinner samples. For the wires used in this study, the typical l^2/r^2 ratio is about 1.3×10^{-6} which is very small value. Therefore it was found that the pole effect is negligible in our measurements.

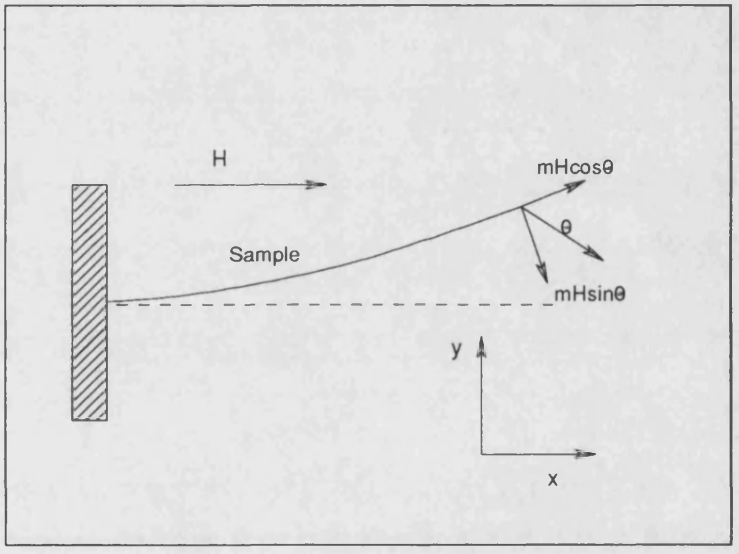

Figure 5.25: Schematic illustration of the pole effect for a wire in transverse vibration. The restoring force mHsinθ increases the stiffness and raises the vibrational frequency of the sample (from Berry and Pritchet [1979]).

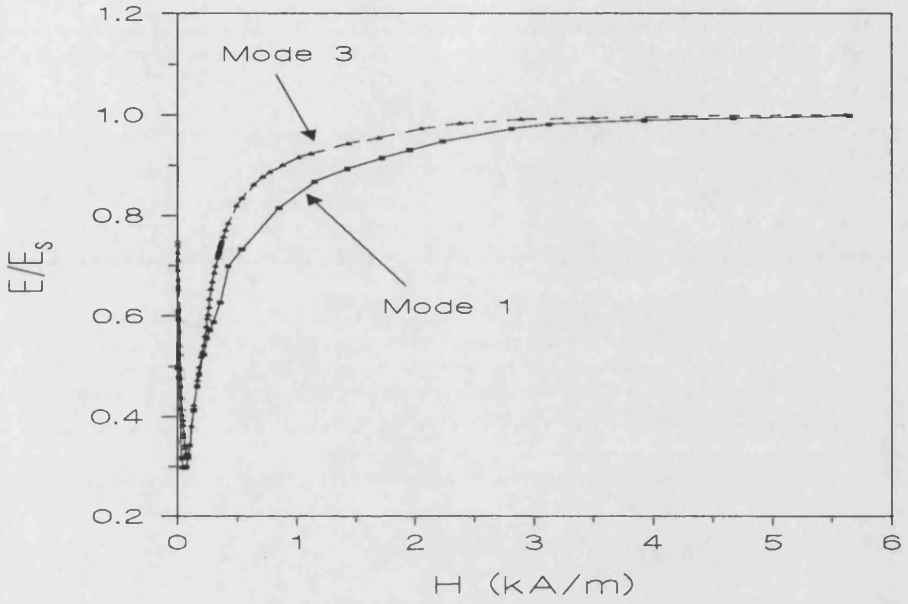

Figure 5.26: Measured Young's modulus behaviour of stress relieved amorphous FeSiB wire as a function of magnetic field for different vibrational modes (the frequencies for mode 1 ~80Hz and for mode 3 ~1530Hz at H=0). The lines are interpolated between the experimental data points.

5.7 Shear Modulus

The shear moduli, G, of amorphous wires were measured as a function of magnetic field, tensile stress, σ, and torsional strain, ε, (frequency 1-4 Hz) using a torsional pendulum. The magnetic field dependence of G, G(H), for un-drawn and cold-drawn, as-cast wires are shown in figure 5.27 and 5.28. Although a large magnetic field was applied (~10 kA/m) the as-cast wires are not saturated, due to the effect of torsion.

The general features of the magnetic field dependence of G can be partially explained using the Squire model. G/G_s is assumed to be given by:

$$\frac{G}{G_s} = \frac{1}{1 + gD(h, \theta, \gamma)} \tag{5.7}$$

where $g=\lambda_s^2 G_s/K$ which is similar to the β in equation 5.4 and D is similar to F in equation 5.4. Table 5.2 shows the minimum value of G, G_{min}; the shear modulus at H=0, G_o, shear modulus at maximum applied field, G_{max}, and the G_{min}/G_{max} ratio of $Fe_{77.5}Si_{7.5}B_{15}$ as-cast wires with various diameters. G_{min}/G_{max} increases with increasing wire diameter. G_{min}/G_o does not behave in a similar way to E_{min}/E_o. The measured values for un-drawn, as-cast 125μm wire are G_{min}/G_{max}=0.986, with K~2000-4000Jm^{-3} and G_{max}=64.16GPa. g is calculated to be 0.022-0.044 which is much smaller than the β value. From this g value, G_{min}/G_s is calculated from equation 5.7 to be 0.84-0.91, which does not agree with the experimentally measured value. This is because, firstly, the wire was not saturated, and secondly, in the calculation of G_{min}/G_s, F was set up to be 4.5 which is not correct. The reasons for this choice were given in the previous section. The shear modulus of as-cast 140μm wire decreases with increasing tensile stress. The total change in G as a function of tensile stress is only a few percent, due to the high residual stress in the wire (figure 5.29).

Figures 5.30 and 5.31 show the G(H) curves of $Fe_{77.5}Si_{7.5}B_{15}$ wires annealed at 420°C, 460°C, 480°C and 500°C. The G(H) curves in figure 5.30 were obtained using the fibre optic pendulum system under the effect of 9MPa tensile stress. It was observed that the change in the modulus was not very large due to the high tensile stress. The large effect of tensile stress on G shows why it is necessary to use an inverted pendulum with a very sensitive tensioning capability. With the inverted pendulum the axial load can be reduced to 0.5 gram, equivalent to 0.43 MPa tensile stress. Figure 5.31 shows the G(H) curves of annealed $Fe_{77.5}Si_{7.5}B_{15}$ 125μm wires under the effect of 0.43MPa tensile stress. Table 5.3 shows the G_{min}, G_o, G_{max}, G_{min}/G_{max} and G_o/G_{max} values of furnace annealed wires. G_{min}/G_{max} of the wires annealed at 480°C first decreases from the as-cast value, reaching a minimum of 0.3 after 16 minutes annealing. The ratio then starts to increase again with increasing annealing time. This behaviour of G_{min}/G_{max} as a function of annealing temperature is very similar to the E_{min}/E_s behaviour of the wire annealed at the same temperature. Hence, the magnitude of G_{min}/G_{max} is determined by K, as is E_{min}/E_s. In the case of the wires annealed at 500°C, no initial decrease in G_{min}/G_{max} is observed. This is because the temperature is very high and even a very short annealing leads to partial crystallisation of the wire.

After annealing at 530°C for 20 minutes the wire is fully crystallised. This was confirmed by X-ray diffraction and the high coercivity value (~1000A/m). The shear modulus of the wire increases from 64.5 GPa to 90 GPa with crystallisation. This is due to the increase in the density of the wire.

The G_o/G_{max} behaviour is very different from E_o/E_s as a function of annealing time. The E_o value reaches E_s after a certain annealing time. This is not observed for G_o. Two reasons can be given for this behaviour of G: a) although the applied tensile stress is very low (~0.43MPa) it is still high enough to rotate magnetic moments by some amount

in the wire axis direction leading to a reduction in the initial angle; as a result, G_o/G_{max} will be less than 1, because G_o/G_{max} is determined by the initial angle of the moment orientation; b) the torsional strain.

When a wire is twisted a torsional stress will be created. This torsional stress produces a torsional strain in the wire in a helical direction. When the magnetic strain energy density is larger than the magnetic anisotropy, the preferred magnetisation direction will be shifted into a helical path. Therefore, torsional strain will rotate the easy axis direction some amount depending on the magnitude of the applied torsional strain and the magnetic anisotropy (Hernando and Barandiaran [1975] [1978], Becker [1975]). Frank *et al* [1969] assumed that the magnetic moments are oriented at 45° to the wire axis when the torsional strain is sufficiently high.

Figure 5.32 shows the shear modulus of $Fe_{77.5}Si_{7.5}B_{15}$ 125μm wire annealed at 500°C for 6 minutes at positive and negative H values. The two minima of G, one on the either side of H=0, are not equal, as observed in the case of Young's modulus.

Figure 5.33 illustrates the effect of tensile stress on the shear modulus of wires annealed at 480°C and 500°C. The effect of tensile stress is very similar to the effect of the magnetic field. An approximate way of relating stress to magnetic field, valid for transversely field annealed ribbons, is to define an effective stress field $H_\sigma = 3\lambda_s\sigma/2\mu_oM_s$. If this is done for figure 5.33, the resulting stress field is about three times smaller than the applied field, but this discrepancy is not important in view of the completely different structure in the annealed wires.

Figures 5.34, 5.35 and 5.36 show the field dependence of G for un-drawn $Fe_{77.5}Si_{7.5}B_{15}$ 95μm and 140μm wires and for $Fe_{67}Si_{10}B_{15}Cr_8$ 135μm wire and cold-drawn 50μm wire. The G(H) behaviour of these wires is found to be very similar to that of un-drawn 125μm

$Fe_{77.5}Si_{7.5}B_{15}$ wire.

Figure 5.37 shows the dependence of shear modulus on torsional strain for different annealing temperatures and annealing times. The largest change in the shear modulus is observed in the wire annealed at 460°C for 15 minutes. The modulus at low torsional strain decreases slightly, then starts to increase with increasing torsional strain. It is also found that the change in the shear modulus is smaller at higher applied fields or greater applied tensile stresses (figures 5.38 and 5.39).

The general behaviour of the shear modulus as a function of torsional strain is similar to the behaviour of the shear modulus as a function of applied field and tensile stress. When the directions of stress and magnetic field are both parallel to the wire axis, the model proposed by Squire [1990] can be used to explain the stress and field dependences of the shear modulus. However, the torsional strain induces a more complicated stress distribution than that induced by tensile stress, so the calculation of the torsional strain dependence of the shear modulus is a more difficult problem. Smith and Birchak [1970] assumed that the change in G as function of torsional strain is only due to the motion of 90° domain wall. They expressed the ΔG effect as:

$$\Delta G = 2.5\frac{\lambda_s}{\sigma_i}\{1-\exp(-2x)\,(1+2x)/x\}, \qquad (5.8)$$

where

$$x = \frac{\varepsilon}{\varepsilon_i} = \frac{\tau}{\tau_i}.$$

σ_i is the average internal stress value, ε_i is the internal torsional strain, τ is the torsional stress and τ_i is the internal torsional stress. The model assumes $G_{min}/G_s \sim \lambda_s/\sigma_i$ which can explain the effect of the annealing, because, with annealing, σ_i is reduced, leading to a

larger change in G. The model also assumes that G_o is always equal to G_s, which does not agree with our results. Therefore, the Smith and Birchak model cannot completely explain the torsional strain dependence of the shear modulus.

Hernando and Barandiaran [1975] and Kobelev *et al* [1987] proposed that in a twisted sample, no matter what the initial moment orientation is, irreversible magnetic moment rotation is possible. As a result, the torsional strain dependence of the shear modulus can be attributed to three mechanisms: a) reversible magnetic moment rotation, b) irreversible magnetic moment rotation, c) 90° domain wall motion. The exact expression for the torsional strain dependence of the shear modulus has not been well studied. Therefore this subject needs further study to take these three effects into account.

Diameter (μm)	G_{min} (GPa)	G_o (GPa)	G_{max} (GPa)	G_{min}/G_{max}
95	56.27	57.98	58.04	0.969
125	63.25	64.7	64.16	0.986
140	61.16	62.6	61.98	0.987

Table 5.2: The G_o, G_{min}, G_{max} and G_{min}/G_{max} values of as-cast FeSiB wires with various diameters.

Temp. (°C)	Time (min)	G_o (GPa)	G_{min} (GPa)	G_{max} (GPa)	G_{min}/G_{max}	G_o/G_{max}
420	5	33.08	33.01	62.5	0.529	0.528
420	60	19.34	19.34	64.1	0.302	0.302
460	15	19.89	16.07	63.2	0.315	0.302
460	30	20.73	18.61	62.38	0.332	0.298
460	55	31.14	18.48	65.68	0.474	0.281
460	70	28.2	17.77	64.67	0.436	0.276
480	0.16	39.82	38.64	66.55	0.598	0.581
480	2	32.78	30.27	60.33	0.543	0.501
480	10	25.88	20.61	64.58	0.401	0.319
480	16	24.53	19.68	64.78	0.378	0.304
480	45	37.45	32.67	64.37	0.581	0.504
500	1	12.6	11.45	63.1	0.199	0.181
500	6	20.17	13.65	64.43	0.313	0.211
500	15	26.53	17.02	64.51	0.411	0.264
500	20	40.87	28.51	64.4	0.634	0.443

Table 5.3: The G_o, G_{min}, G_{max}, G_o/G_{max} and G_{min}/G_{max} values of annealed FeSiB 125μm wires.

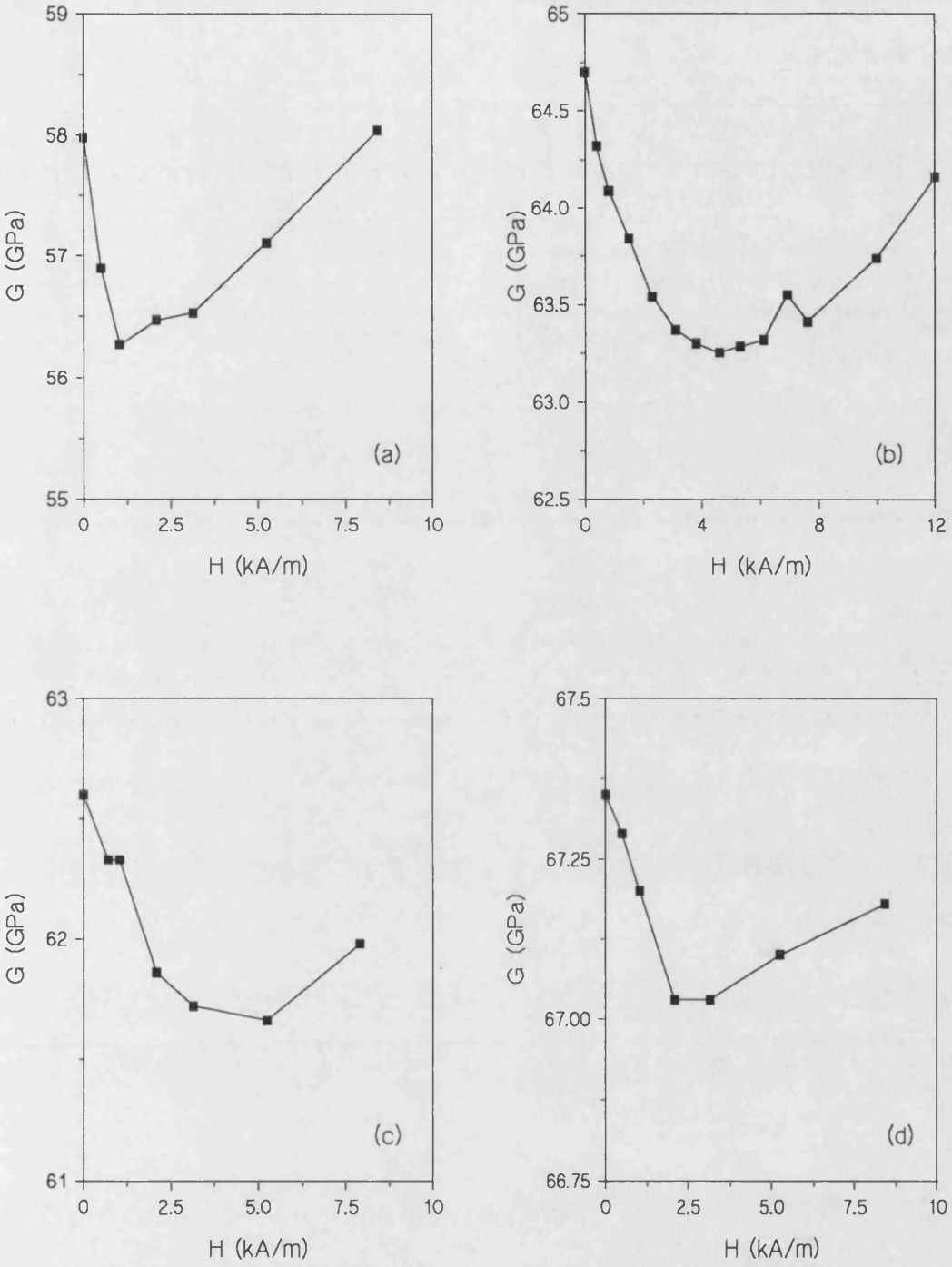

Figure 5.27: Shear modulus of as-cast wires against applied field: a) 95μm FeSiB wire, b) 125μm FeSiB wire, c) 140μm FeSiB wire, d) 140 μm FeSiBCr wire. The lines are interpolated between the experimental data points.

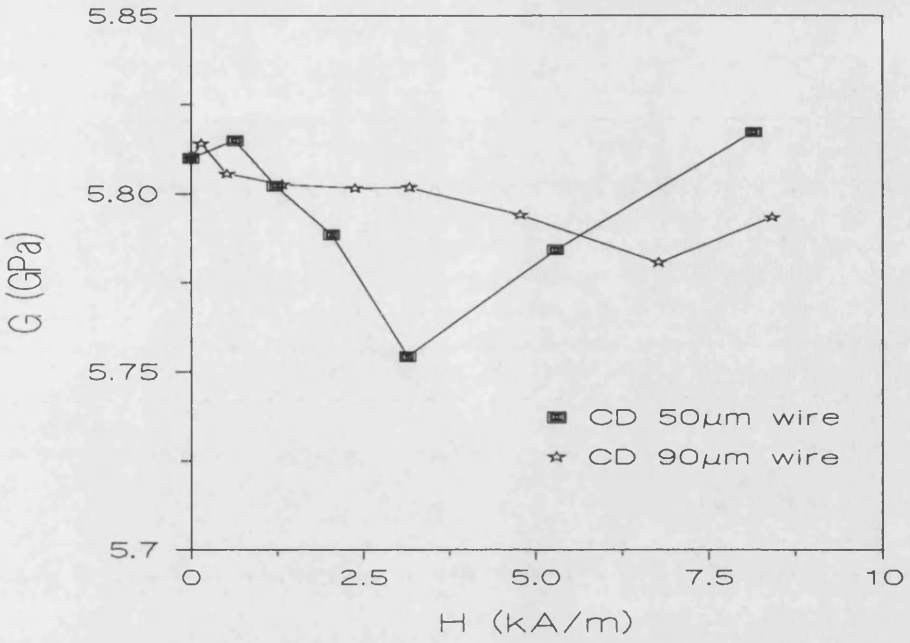

Figure 5.28: Shear modulus of cold-drawn wires as a function of applied field. The lines are interpolated between the experimental data points.

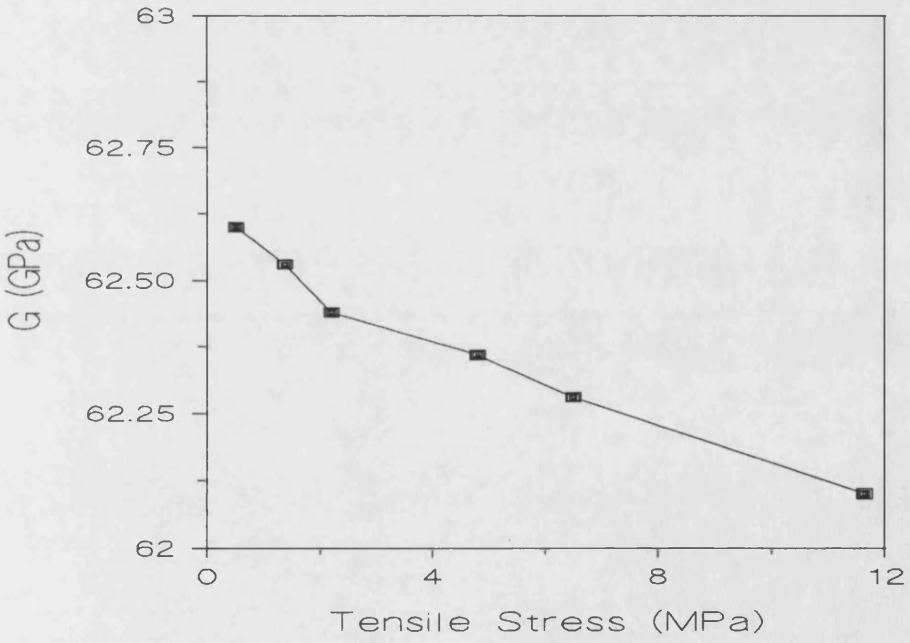

Figure 5.29: Shear modulus of as-cast FeSiB 140μm wire as a function of tensile stress. The lines are interpolated between the experimental data points.

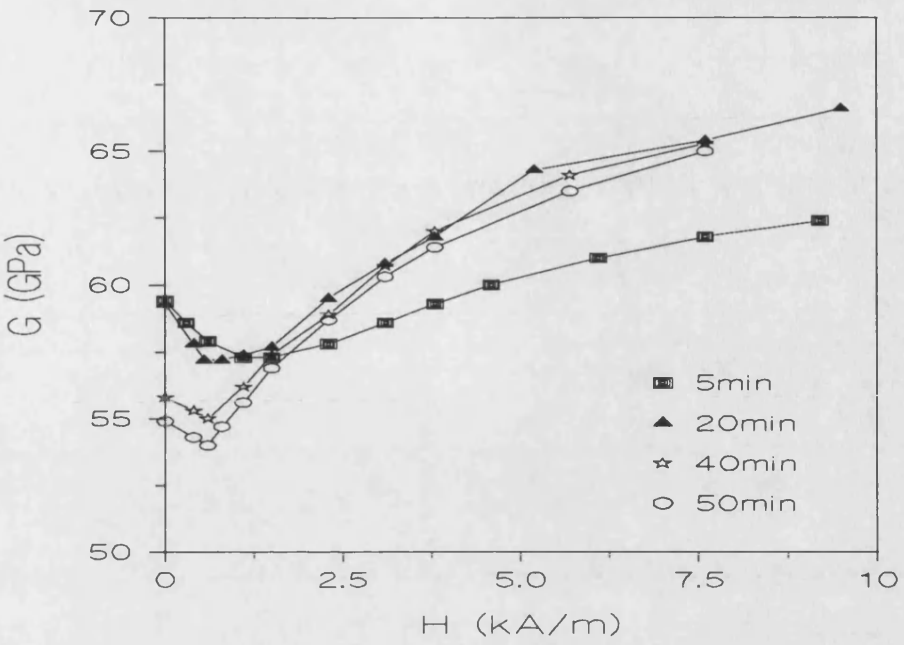

Figure 5.30a: Shear modulus of FeSiB 125μm wires annealed at 370° against applied field (tensile stress=9MPa).

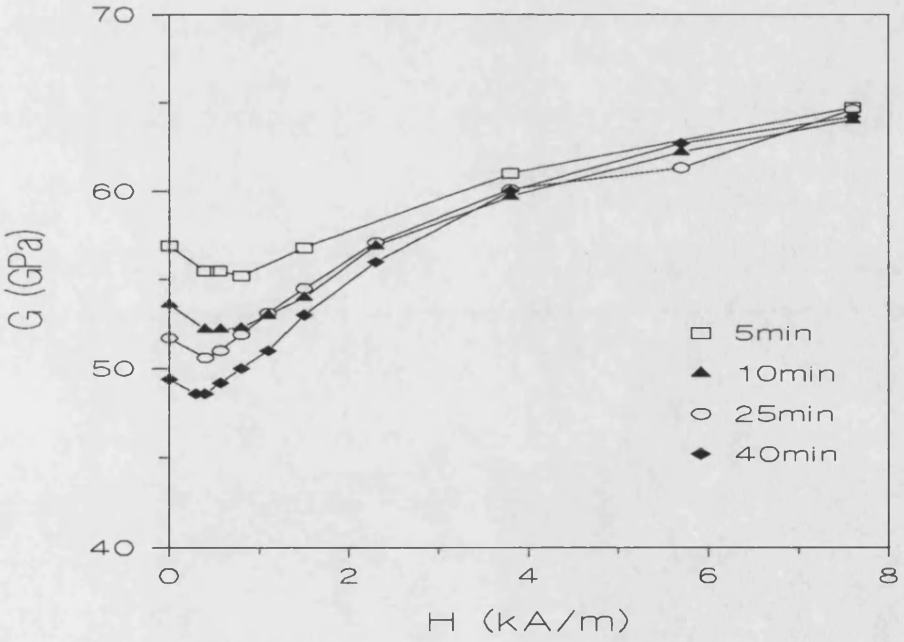

Figure 5.30b: Shear modulus of FeSiB 125μm wires annealed at 400° against applied field (tensile stress=9MPa).

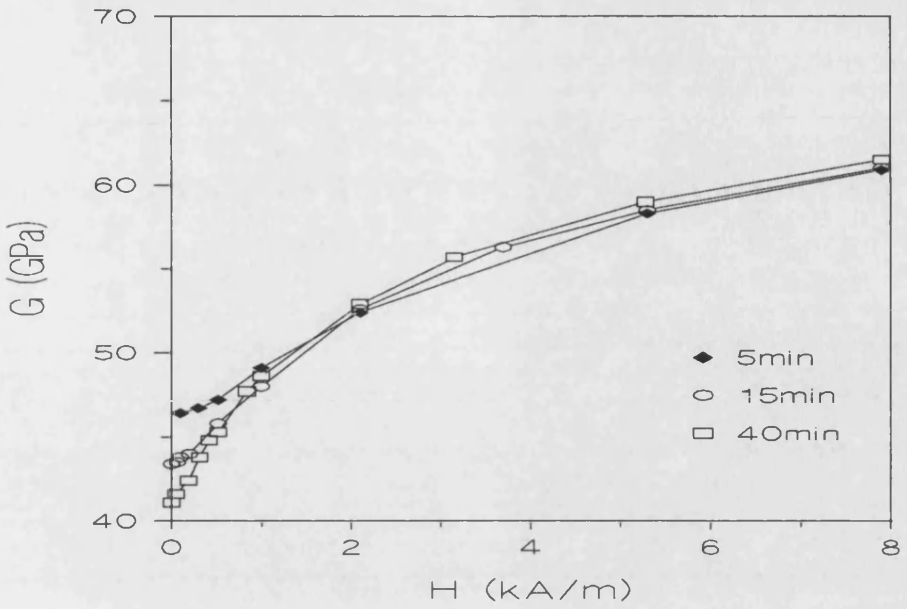

Figure 5.30c: Shear modulus of FeSiB 125μm wires annealed at 420° against applied field (tensile stress=9MPa).

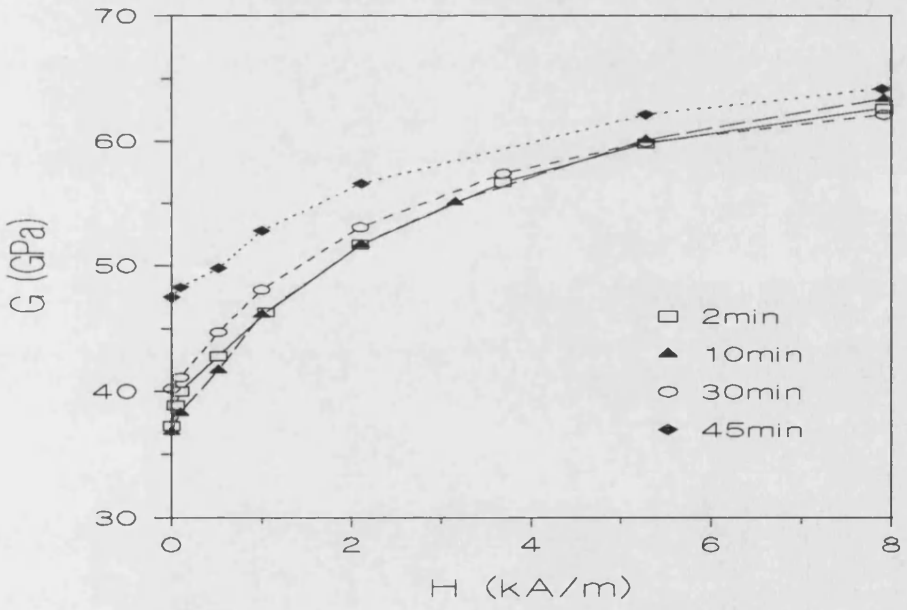

Figure 5.30d: Shear modulus of FeSiB 125μm wires annealed at 480° against applied field (tensile stress=9MPa). The lines are interpolated between the experimental points.

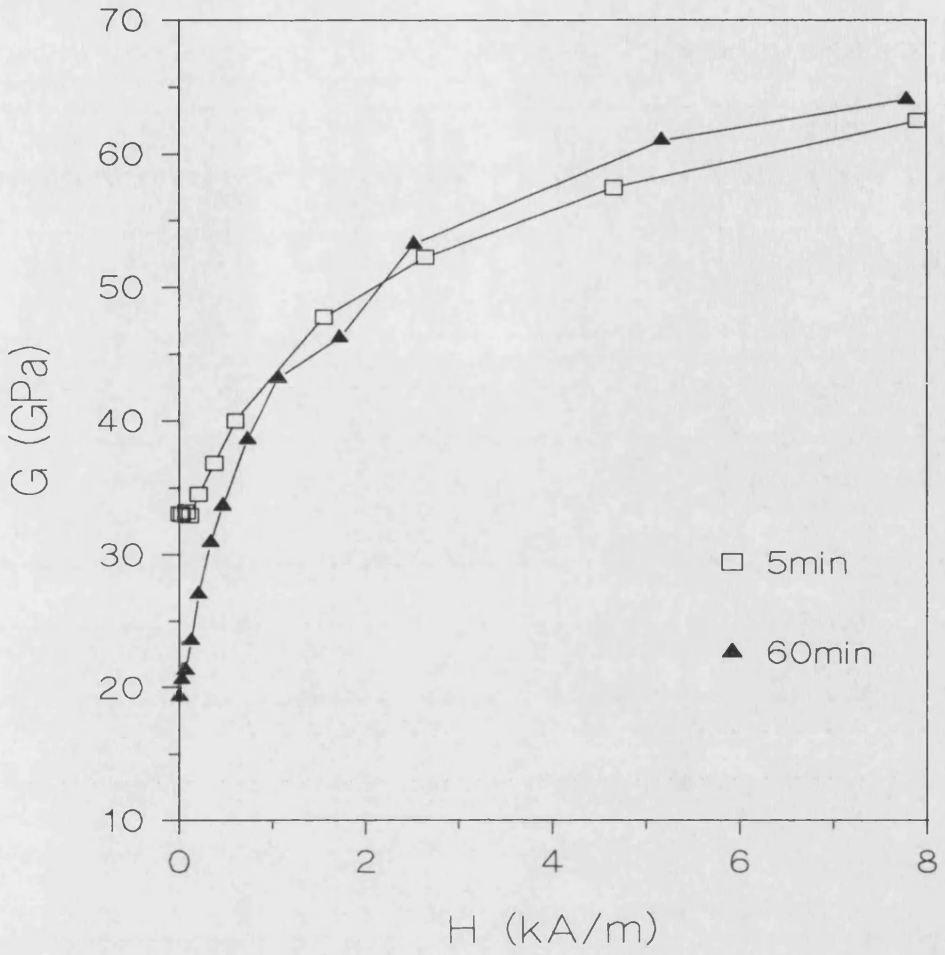

Figure 5.31a: Shear modulus of FeSiB 125μm wires annealed at 420°C against applied field (tensile stress=0.43MPa).

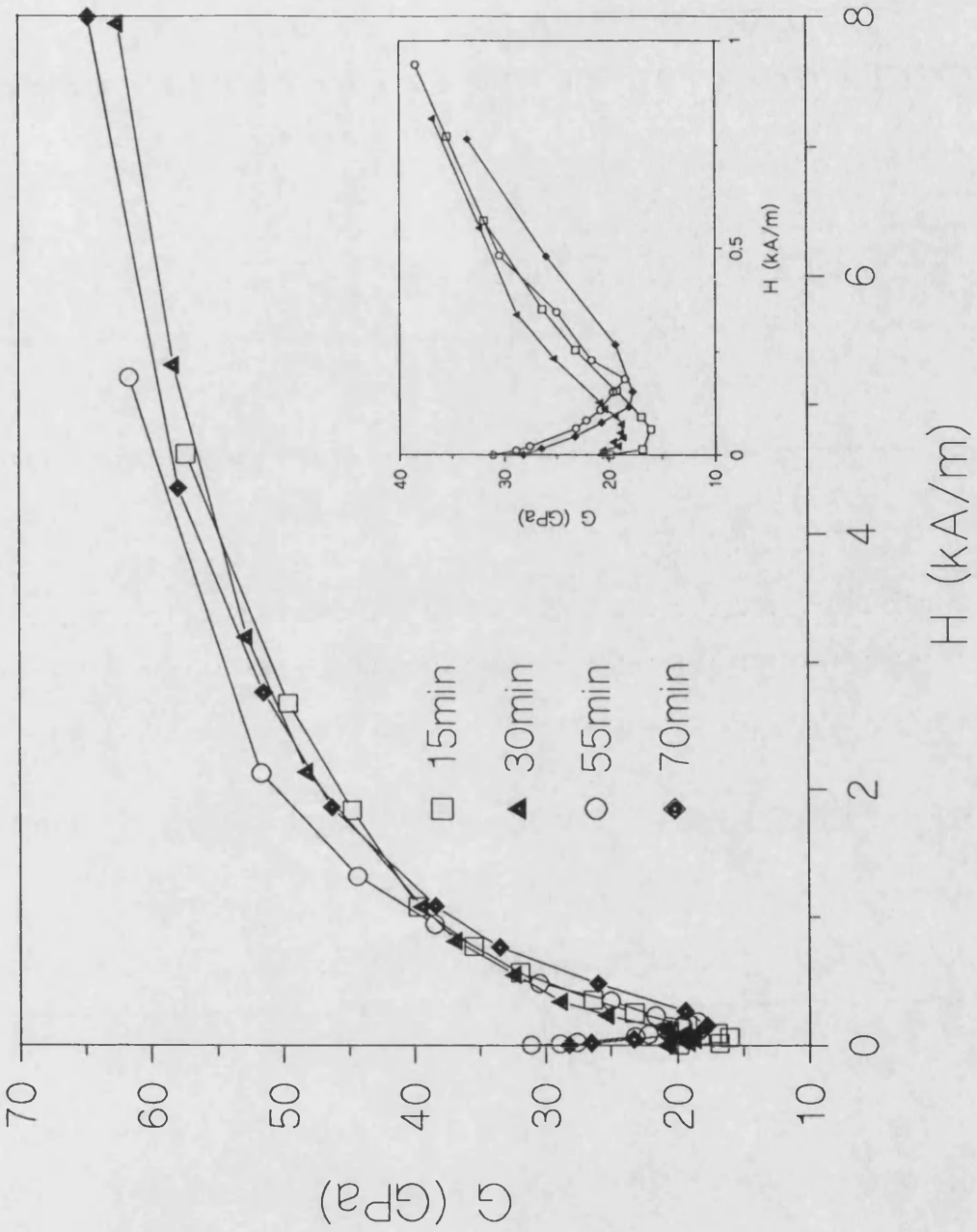

Figure 5.31b: Shear modulus of FeSiB 125μm wires annealed at 460°C against applied field (tensile stress=0.43MPa).

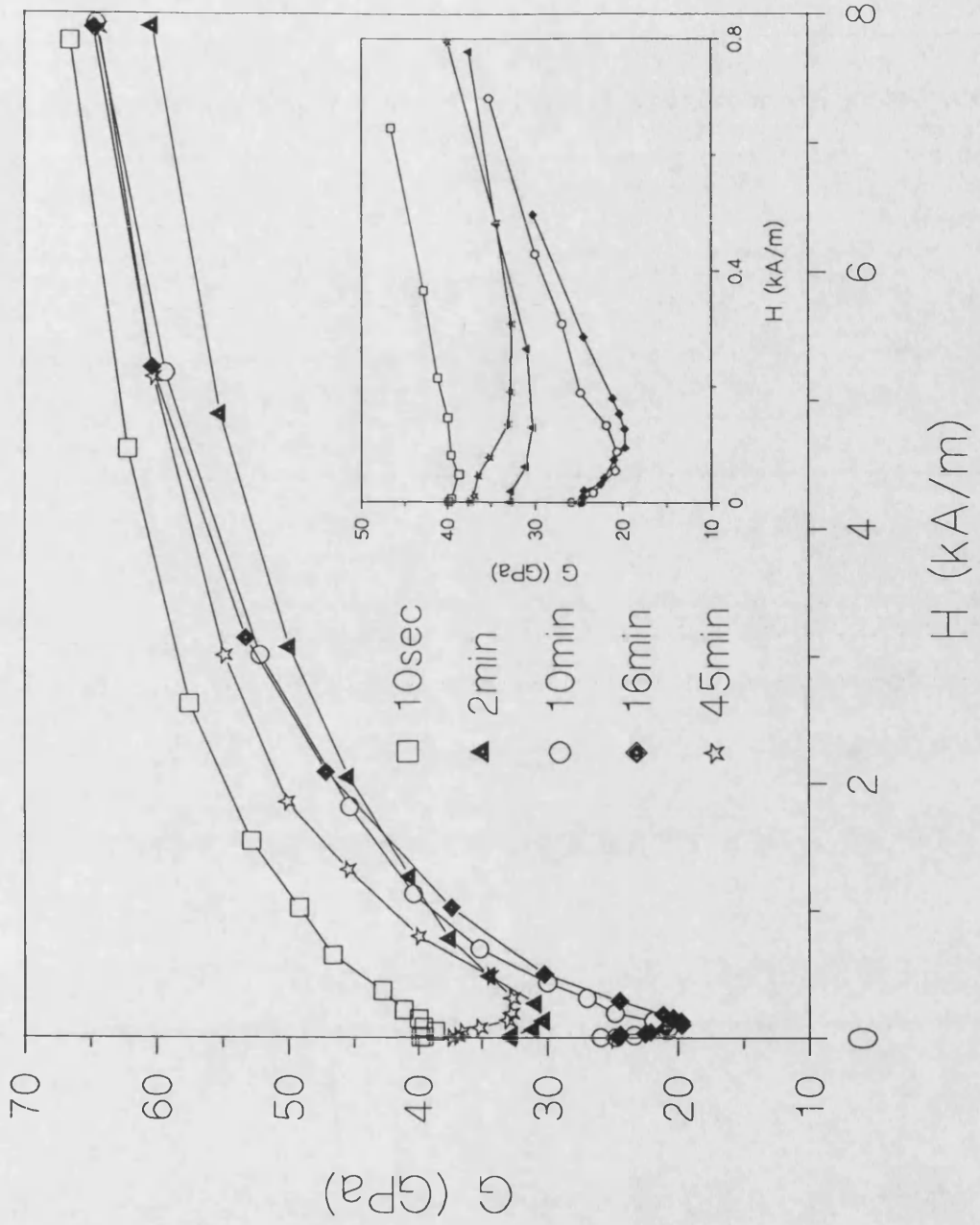

Figure 5.31c: Shear modulus of FeSiB 125μm wires annealed at 480°C against applied field (tensile stress=0.43MPa).

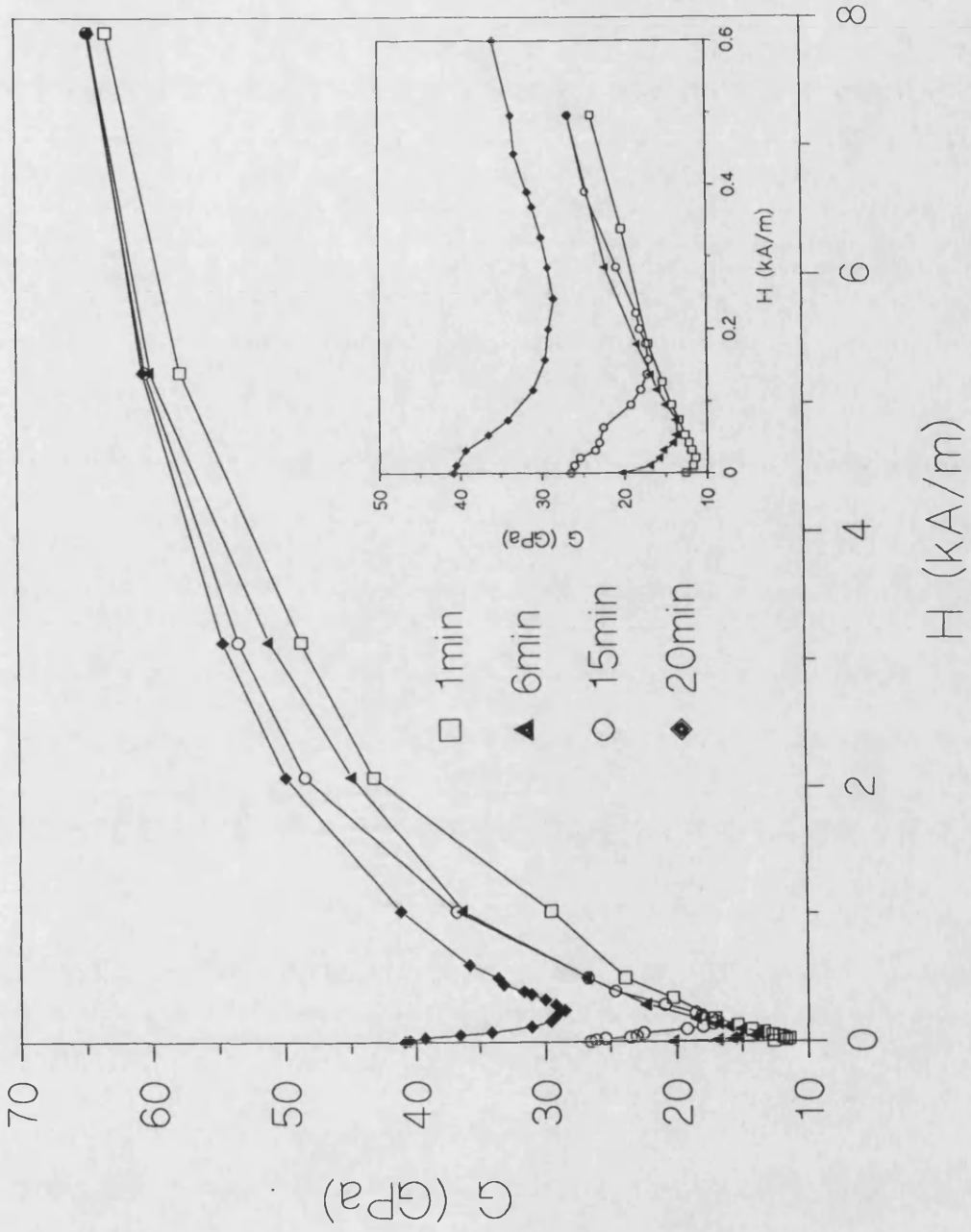

(d)

Figure 5.31d: Shear modulus of FeSiB 125μm wires annealed at 500°C against applied field (tensile stress=0.43MPa). The lines are interpolated between the experimental data points.

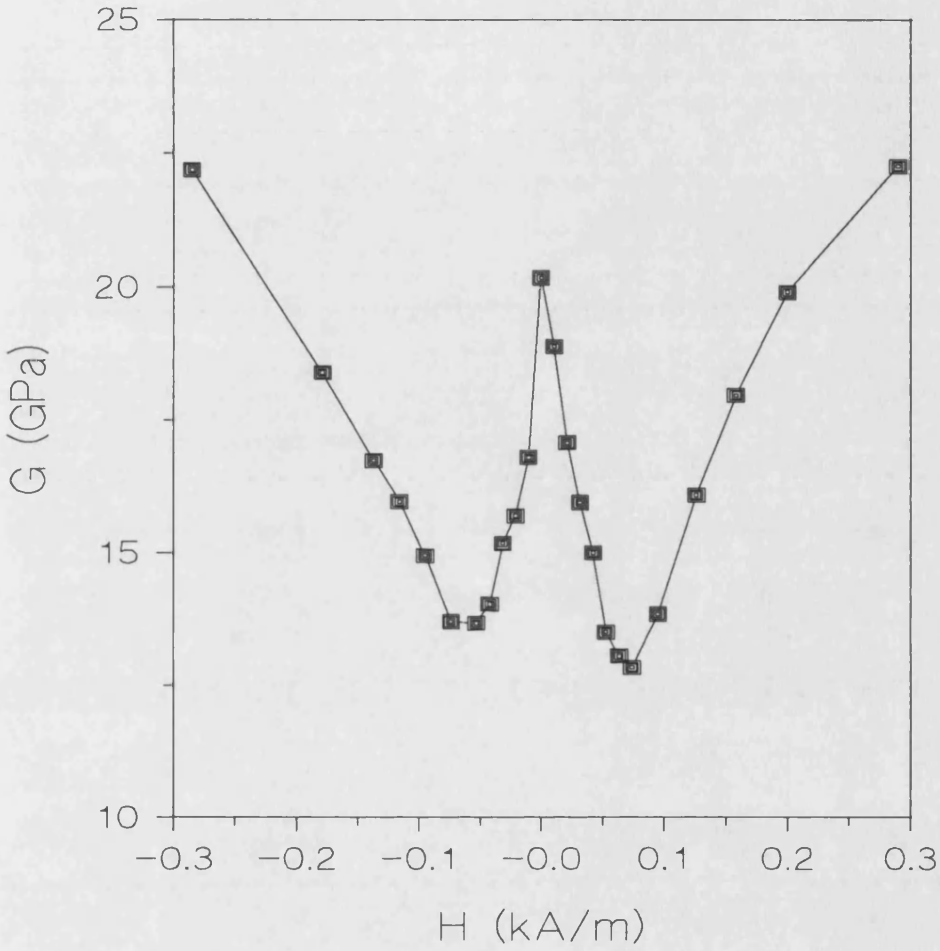

Figure 5.32: An example of a typical behaviour of G for the FeSiB wire annealed at 500°C for 6 minutes, at negative and positive applied fields. The lines are interpolated between the experimental data points.

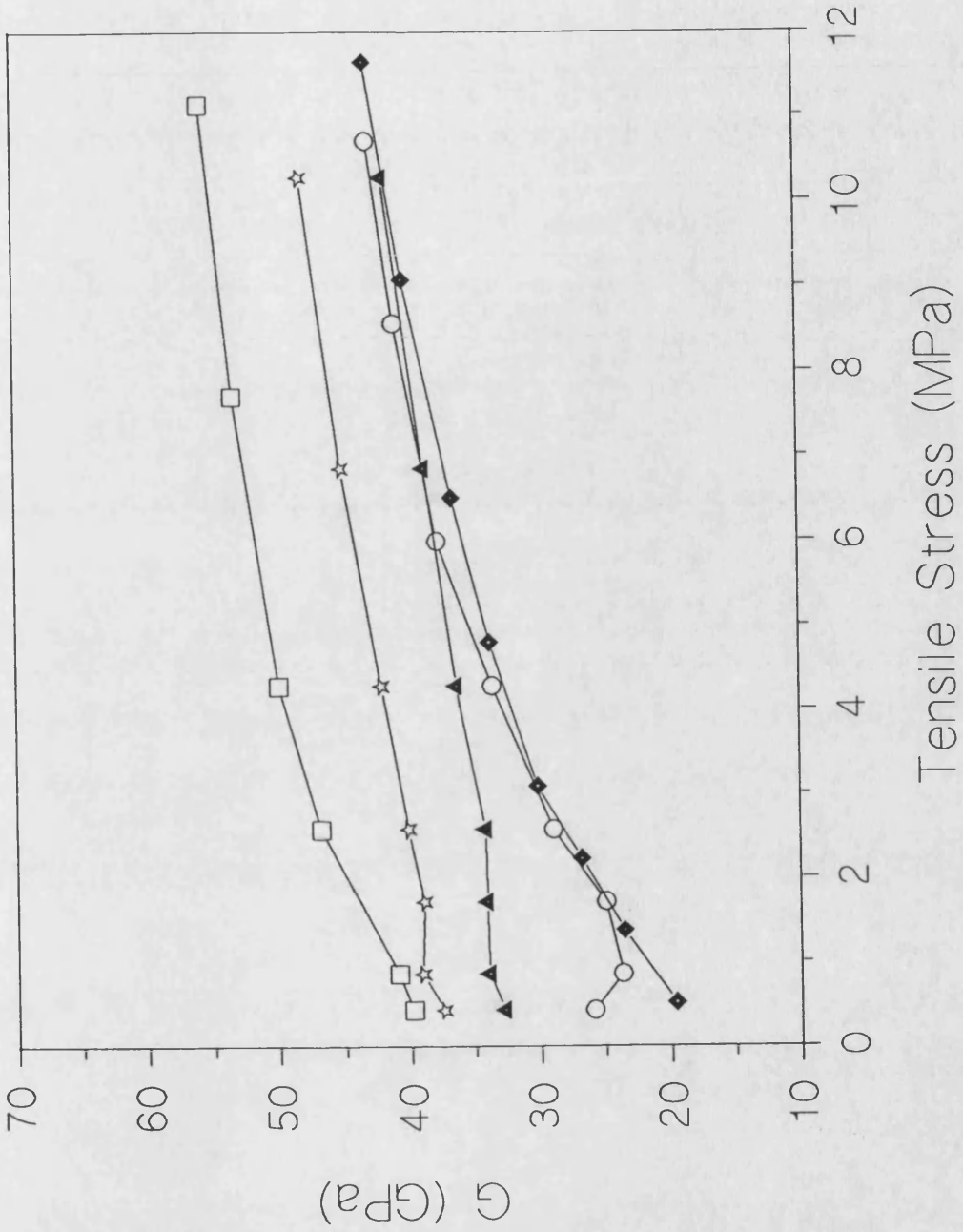

(a)

Figure 5.33: Shear modulus of FeSiB 125μm wire against applied tensile stress. The wire was annealed at 480°C. For figure captions see figures 5.31c. The lines are interpolated between the experimental data points.

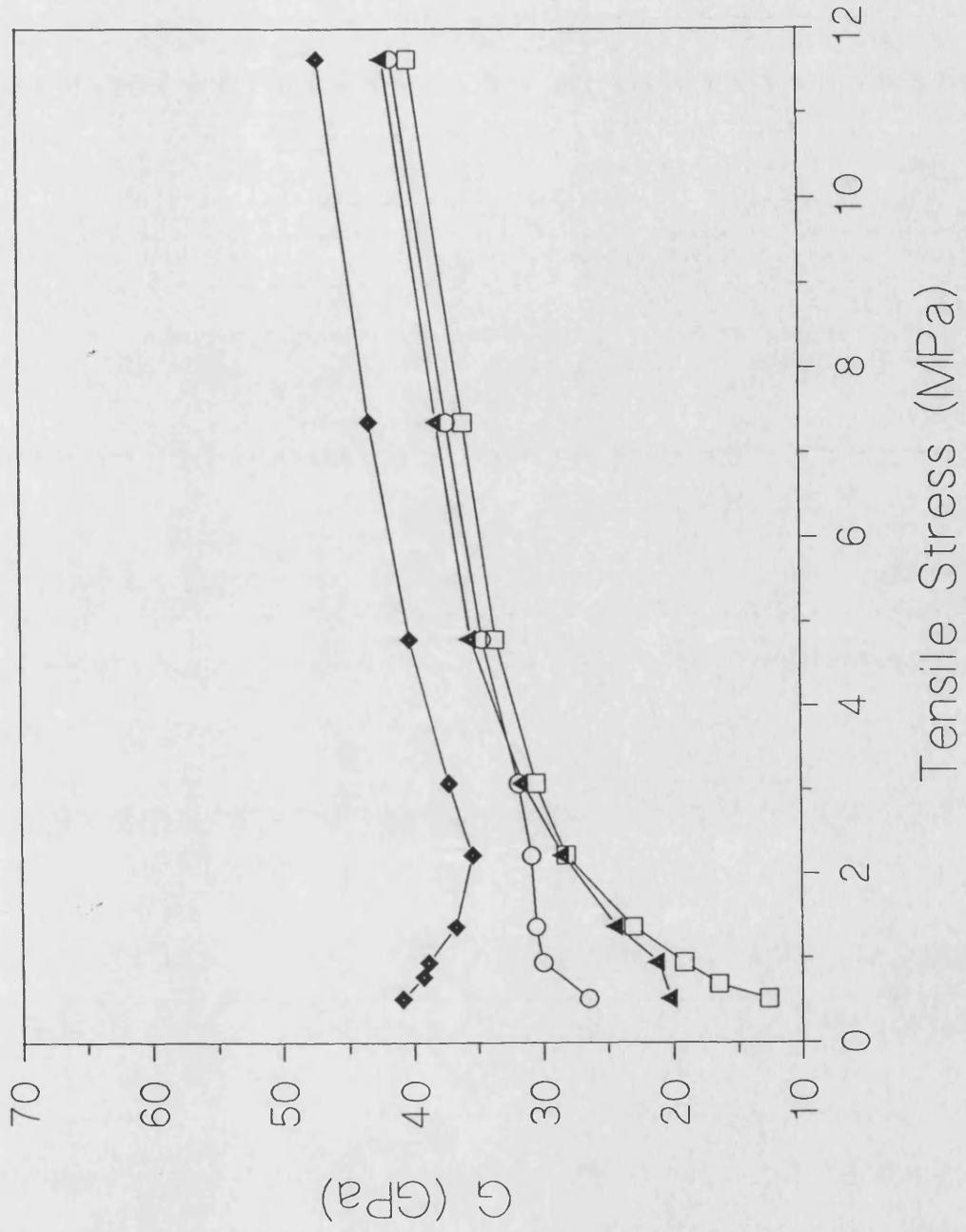

(b)

Figure 5.33: Shear modulus of FeSiB 125μm wire against applied tensile stress. The wire was annealed at 500°C. For figure captions see figures 5.31d. The lines are interpolated between the experimental data points.

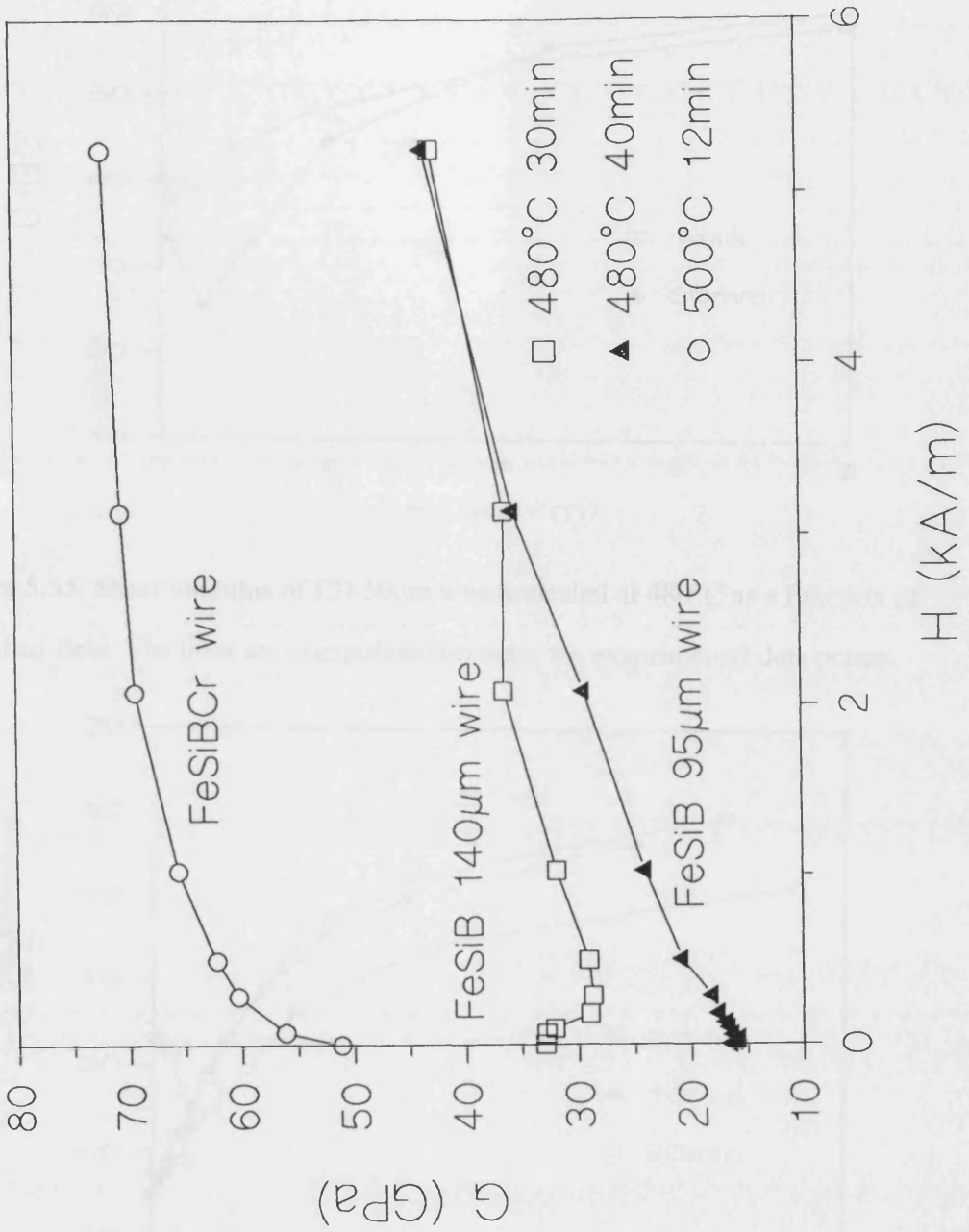

Figure 5.34: The field dependence of the shear modulus of stress relieved amorphous wires with different wire diameters and compositions. The lines are interpolated between the experimental data points.

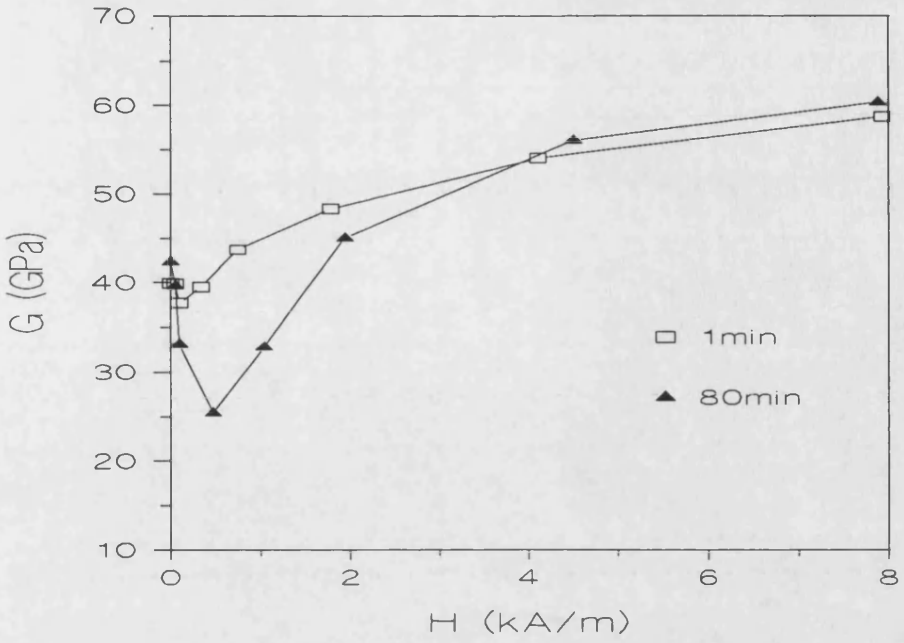

Figure 5.35: Shear modulus of CD 50μm wire annealed at 480°C as a function of applied field. The lines are interpolated between the experimental data points.

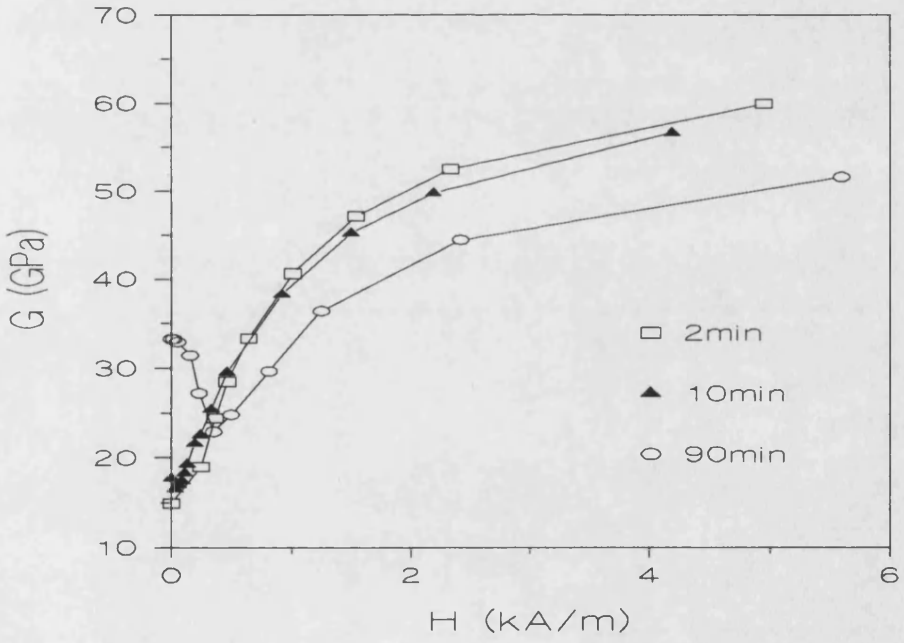

Figure 5.36: Shear modulus of CD 90μm wire annealed at 480°C as a function of applied field. The lines are interpolated between the experimental data points.

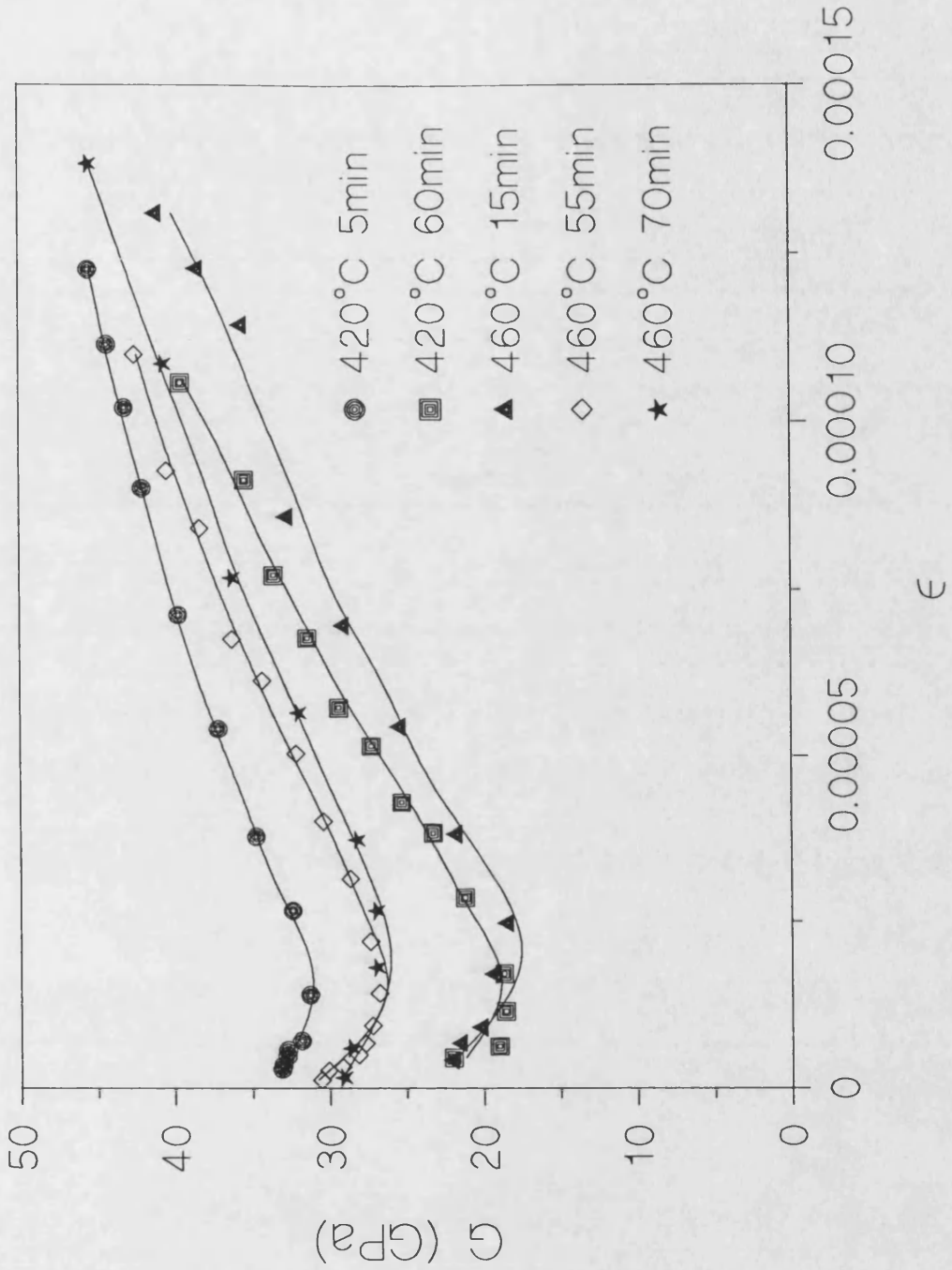

Figure 5.37: Shear modulus against torsional strain at zero applied field and 0.43MPa applied tensile stress, for different annealing times and temperatures.

The lines are interpolated between the experimental data points.

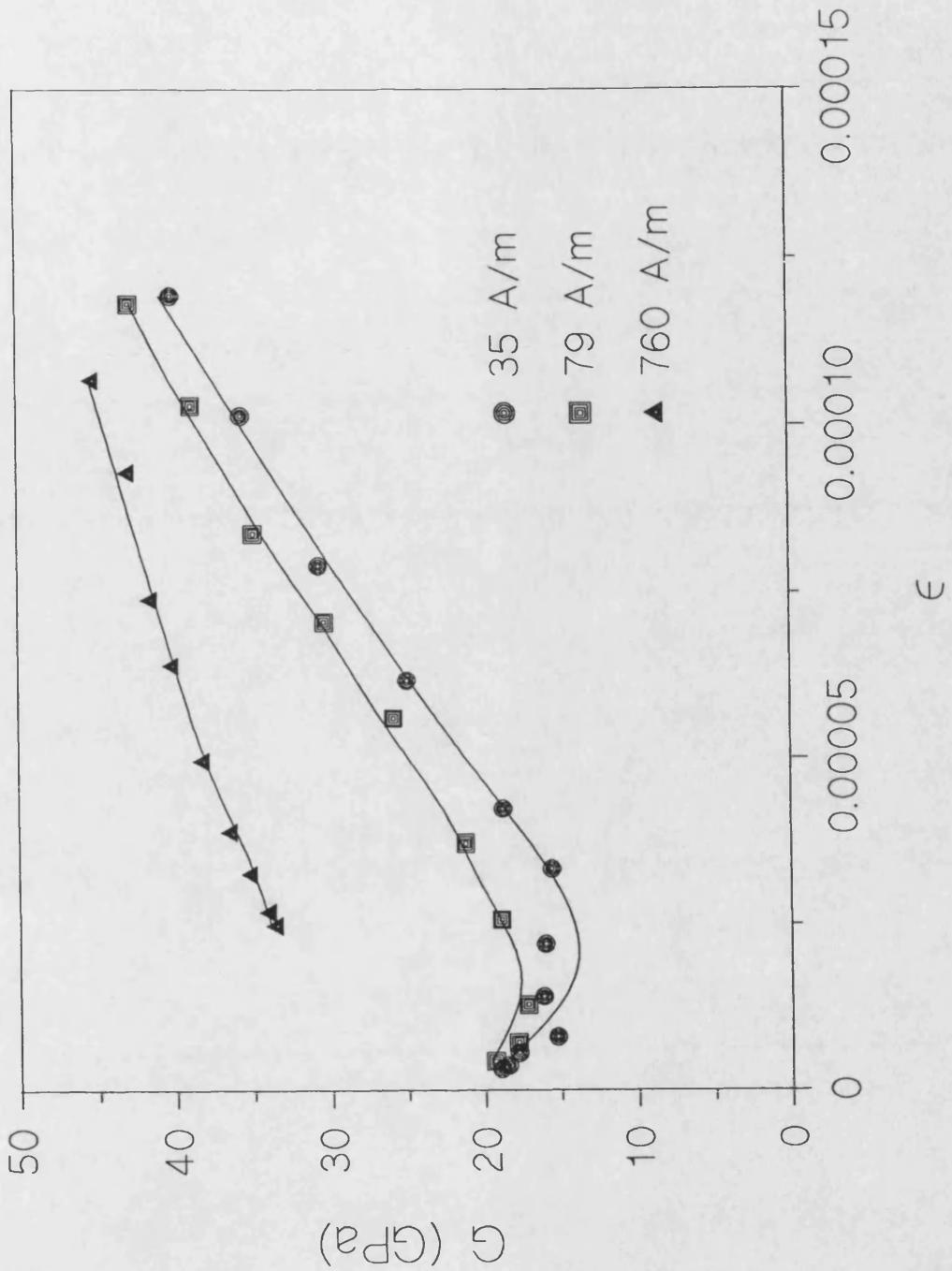

Figure 5.38: Shear modulus of FeSiB wire annealed at 460°C for 15 minutes as a function of torsional strain at different applied fields and at 0.43 applied tensile stress. The lines are interpolated between the experimental data points.

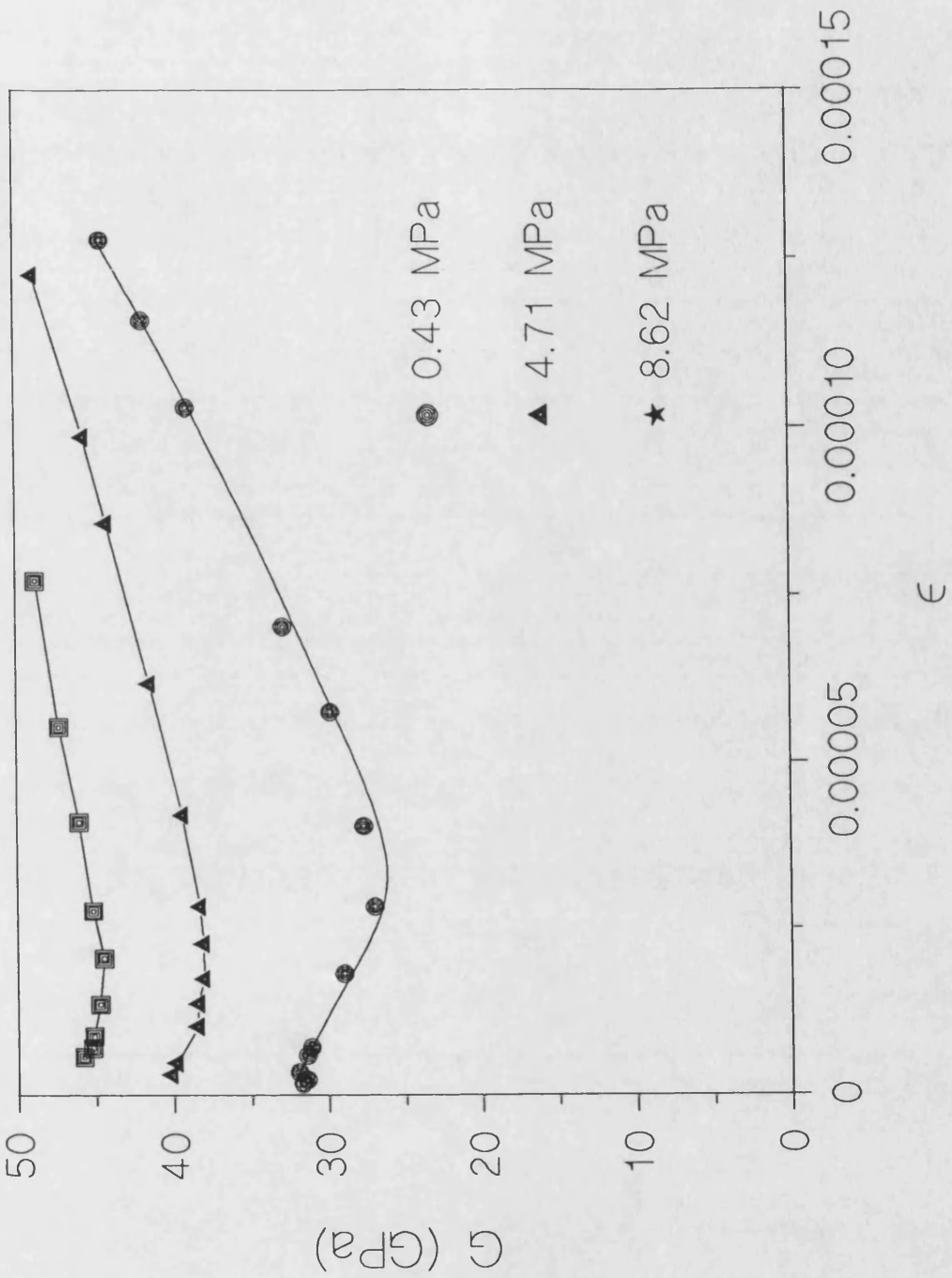

Figure 5.39: Shear modulus of FeSiB wire annealed at 460°C for 70 minutes as a function of torsional strain at different applied tensile stresses and at zero applied field. The lines are interpolated between the experimental data points.

5.8 Magnetomechanical Damping

The damping, Q^{-1}, of amorphous wires was measured as a function of applied magnetic field, tensile stress and torsional stress using an inverted pendulum. As-cast wires show almost zero damping due to the large internal stress (~200MPa) induced during the quenching in the manufacturing process. An estimate of the damping for as-cast wire by using equation 3.23 with this value of internal stress indicates that the maximum value of damping, Q_{max}^{-1}, is of the order of 10^{-4}, which is very small compared to the values found in annealed wires.

The results for wires annealed at 420°C, 460°C, 480°C and 500°C for various annealing times are shown in figure 5.40, where the damping is shown as a function of applied field. The torsional strain for these results was about $1-2\times10^{-5}$ and the tensile stress was about 0.43 MPa. In all the damping measurements, the magnetic component of the damping was obtained by subtracting from the measured damping values the value obtained for the sample in the magnetically saturated state, for which damping is mainly due to air damping. The damping as a function of applied field first increases to a maximum, then decreases, which is a typical behaviour which has been observed in crystalline materials and amorphous ribbon materials (Kiss *et al* [1989]). If the damping versus magnetic field curves are obtained under the effect of ~0 tensile stress and torsional strain, the damping would increase from zero until a maximum was reached, then it would start to decrease with increasing magnetic field (i.e. damping at H=0 is always zero). But due to the effect of tensile stress and torsional strain this behaviour has not been observed.

The Q_{max}^{-1} of wire annealed at 480°C first increases and reaches a maximum then starts to decrease with increasing annealing time. This behaviour of Q_{max}^{-1} is also observed for

other annealing temperatures. The initial increase in Q_{max}^{-1} with annealing time is due to the relief of casting stress. The decrease in Q_{max}^{-1} with further annealing is due to the onset of crystallisation.

Figure 5.41 shows Q^{-1} as function of H. The Q_{max}^{-1} values in the negative H and positive H region are almost same. The damping behaviour of cold-drawn wire is found to be similar to un-drawn wires (figure 5.42). Figure 5.43 illustrates the effect of the tensile stress on Q^{-1}. Even a very small applied tensile stress leads to a large change in Q^{-1}. It was found that the effect of tensile stress is similar to the effect of magnetic field.

The Q^{-1} measurements were performed at low frequencies (1-4 Hz). The eddy current losses are therefore negligible, so the only significant damping mechanism is magnetomechanical damping, which is amplitude dependent and is independent of the oscillation frequency. Figure 5.44 shows the amplitude of oscillation against the number of the oscillation for FeSiB wire annealed at 460°C for 15 minutes. In this figure, the slope of the curves is proportional to the damping. When the applied field is 760 A/m the slope is almost constant, so the damping does not change with amplitude. At lower applied fields, at large amplitudes, the slopes of the curves are small showing that the damping is very small. When the amplitude is between 1° and 10°, the amplitude decreases sharply, indicating large damping.

The results for wires annealed at 420°C and 460°C for different annealing times are given in figure 5.45, where the change in damping is shown as a function of torsional strain. The behaviour of the damping curve against torsional strain for amorphous wire is similar to that normally observed in crystalline ferromagnetic materials (Sumner and Entwistle [1959]). Damping first increases, then decreases with increasing torsional strain. The maximum damping peak, Q_{max}^{-1}, is about 0.042 for the wire annealed at 460°C for 15 minutes. To obtain a damping peak as high as 0.042 at 420°C, longer annealing

times are required to relieve the internal stress, in accordance with standard kinetics. Longer annealing at 460°C results in a reduction of the damping peak. This is attributed to the stress associated with surface crystallisation.

The fitted curves in figure 5.45 are from the Smith and Birchak model and are obtained using equations 3.21, 3.22 and 3.23. The parameters found from these fits are given in table 5.4. They confirm the reduction of internal stress with annealing, but show also that the heights of the peaks are not simply proportional to $1/\sigma_i$. The additional factor, K, in the model describes the shape of the magnetomechanical hysteresis loop, and therefore, indirectly, the domain structure. Since the domain structure in magnetostrictive amorphous wires is strongly affected by the internal stress, it is only to be expected that annealing will change the value of K. With the present extent of understanding of the domain structure in amorphous wires, it is not possible to give an adequate model for calculating K.

Figure 5.46 shows the same experimental data as figure 5.45, but the fitted curves are from the Degauque and Astie model (equation 3.31). The numerical parameters for Z_1 and Y_1 in equation 3.31 are selected by matching the peak value of the damping, Q_{max}^{-1}, to the peak value of ψ_1 and by matching the torsional strain value at maximum damping, ε_{max}, to Z_1 at maximum damping, Z_{1max}, at zero applied field so $Y_1=0$. This leads to two ratios, $Q_{max}^{-1}/\psi_{11max}$ and $\varepsilon_{max}/Z_{1max}$. Using these ratios and again matching the peak value by varying Y_1, theoretical curves were fitted to experimental data for different applied magnetic fields and tensile stress (figure 5.47 and 5.48). The parameters used in the curve-fitting for figure 5.46, 4.47 and 5.48 are given in table 5.5. It was assumed that the tensile stress has the same effect as the applied field and that the magnetic field is proportional to the tensile stress. The important point of the effect of the magnetic field to the damping-torsional strain curves is the initial increase in the height of the peak and the shift of it to lower torsional strain values. These features cannot be explained by the

Smith and Birchak model, which gives the lowering value of Q_{max}^{-1} and predicts that the position of the Q_{max}^{-1} peak should shift to higher torsional strain values with increasing applied field or tensile stress. This does not agree with the experimental data presented here. Therefore, the fitted curves in figures 5.47 and 5.48 are shown only for the Degauque and Astie model. As explained above, figure 4.48 shows the effect of tensile stress on the damping-torsional strain curves. The damping peak decreases with increasing tensile stress. For the reason explained above, it is not possible to measure the zero tensile stress damping curve.

Figures 5.49, 5.50 and 5.51 show the same experimental data as figures 5.46, 5.47 and 5.48, but, in this case, full least squares curve-fitting was done by a computer program, with the fitting parameters shown in table 5.6. Also, the horizontal axis is scaled by the shear modulus ratio, G/G_s, because the parameter Z_1 in the model is proportional to εG (equation 3.29). In previous studies of crystalline ferromagnetic materials, this correction has not been necessary because the change in the modulus amounted to less than 1%. In amorphous wires, by contrast, the modulus changes by a factor of more than two as the torsional strain varies, as shown in figure 5.37.

The behaviour of the damping peak of amorphous wires as a function of magnetic field or tensile stress cannot be fully explained by the Smith and Birchak model, because the effect of the magnetic field or the tensile stress on domain walls is represented as a random function. The model does not consider either domain structure or the angle between the easy axis and the field or tensile stress. The effect of magnetic field and tensile stress on the damping-torsional strain curves are explained by the Degauque and Astie model. According to this model, the magnetic field plays two roles. First, a very small field puts the domain walls in an energy position where torsional strain can perform a bigger number of irreversible domain wall jumps than in zero applied field, leading to an increase in magnitude of the damping peak. Secondly, at larger fields, the field itself

becomes strong enough to cause irreversible jumps, so irreversible jumps due to the torsional strain will be less, leading to a lower damping peak. It is possible that the application of a very small stress to a stress-free wire may increase the damping peak by analogy with the effect of an applied field. Such an effect has not been observed in this study, because even a small load produces a large tensile stress. In principle, the parameter Y_1 can be used together with equation 3.28 to estimate the mean easy axis direction; however, the precision of present data and statistics in the fitted values of Y_1 do not allow this. For the same reason, the correlation between the values of Y_1 and H, shown in table 5.6, is not as close as might be expected from the equation 3.28.

Temp. (°C)	Time (Mins)	Q_{max}^{-1}	σ_i (MPa)	K
420	5	0.016	2.6	0.021
420	60	0.024	2.3	0.052
460	15	0.042	2.6	0.105
460	55	0.024	2.4	0.041
460	70	0.027	3.4	0.058

Table 5.4: Annealing conditions for the FeSiB wires, together with the parameters σ_i, Q_{max}^{-1} and K to fit the Smith and Birchak model equations 3.22 and 3.23 to the experimental damping data shown in figure 5.45.

Temp. (°C)	Time (min)	$\frac{Q^{-1}_{max}}{\psi_{1max}}$	$\frac{\varepsilon_{max}}{Z_{1max}}$ (10^5)	Y_1	H (A/m)	σ (MPa)
420	5	0.0883	1.439	0	0	0.43
420	60	0.1163	1.410	0	0	0.43
460	15	0.1988	1.815	0	0	0.43
460	15	0.1988	1.815	0.39	35	0.43
460	15	0.1988	1.815	1.02	79	0.43
460	55	0.1202	1.583	0	0	0.43
460	70	0.1311	1.992	0	0	0.43
460	70	0.1311	1.992	1.1	0	4.71
460	70	0.1311	1.992	1.35	0	8.62

Table 5.5: Annealing conditions and parameters used to fit the Degauque and Astie model equations 3.28, 3.29 and 3.31 to the experimental damping data of figures 5.46, 5.47 and 5.48.

Temp. (°C)	Time (min)	$\frac{Q^{-1}_{max}}{\psi_{max}}$	$\frac{\varepsilon_{max}}{Z_{1max}}$ (10^5)	Y_1	H (A/m)	σ (MPa)
420	5	0.0699	7.564	0.0109±0.062	0	0.43
420	60	0.1088	5.943	0.49±0.49	0	0.43
460	15	0.1664	5.681	0.0619±0.086	0	0.43
460	15	0.1896	3.676	-0.0095±0.075	35	0.43
460	15	1.2272	6.226	2.318±12.1	79	0.43
460	55	0.0910	6.031	0.032±0.084	0	0.43
460	70	0.2647	10.416	1.293±5.136	0	0.43
460	70	0.1340	16.366	1.486±8.8	0	4.71
460	70	0.0944	16.129	1.35±5.5	0	8.62

Table 5.6: Annealing conditions and parameters used to fit the Degauque and Astie model equations 3.28, 3.29 and 3.31 to the experimental damping data of figures 5.49, 5.50 and 5.51. Uncertainties in Y_1 are 95% confidence limits.

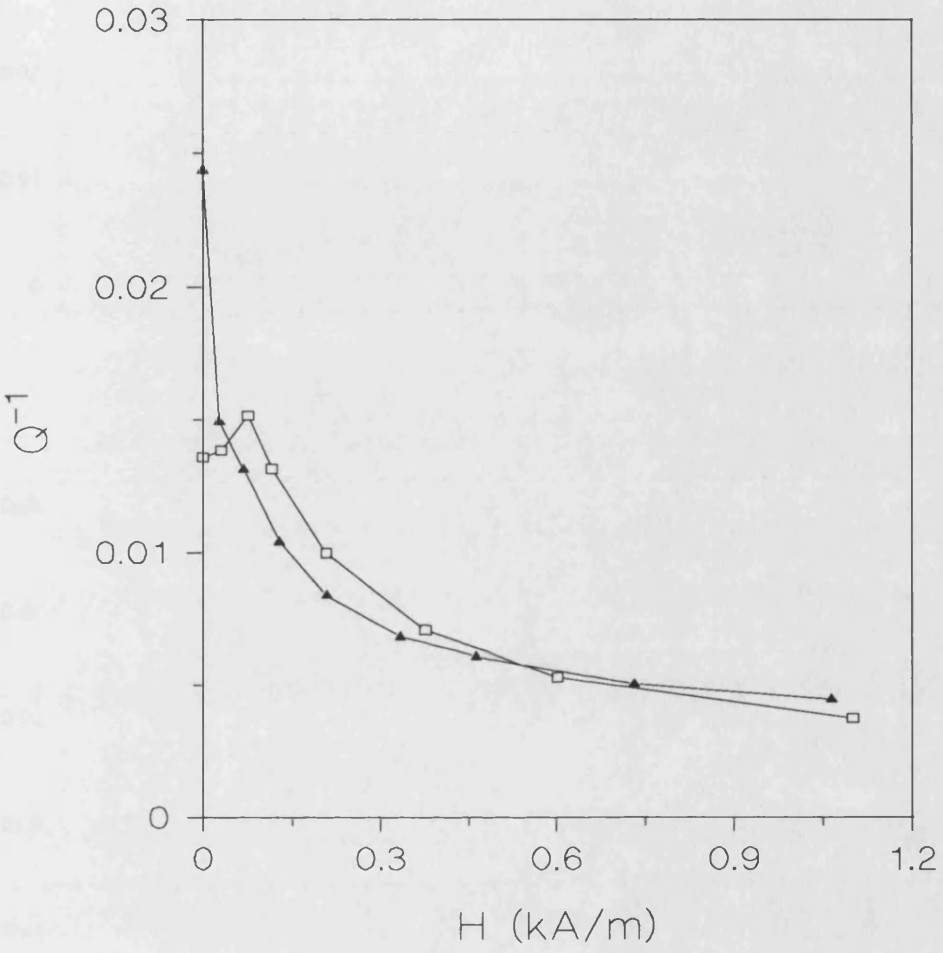

Figure 5.40a: Damping against applied field at 0.43 MPa applied tensile stress for FeSiB 125μm wire annealed at 420°C. For figure caption see figure 5.31a.

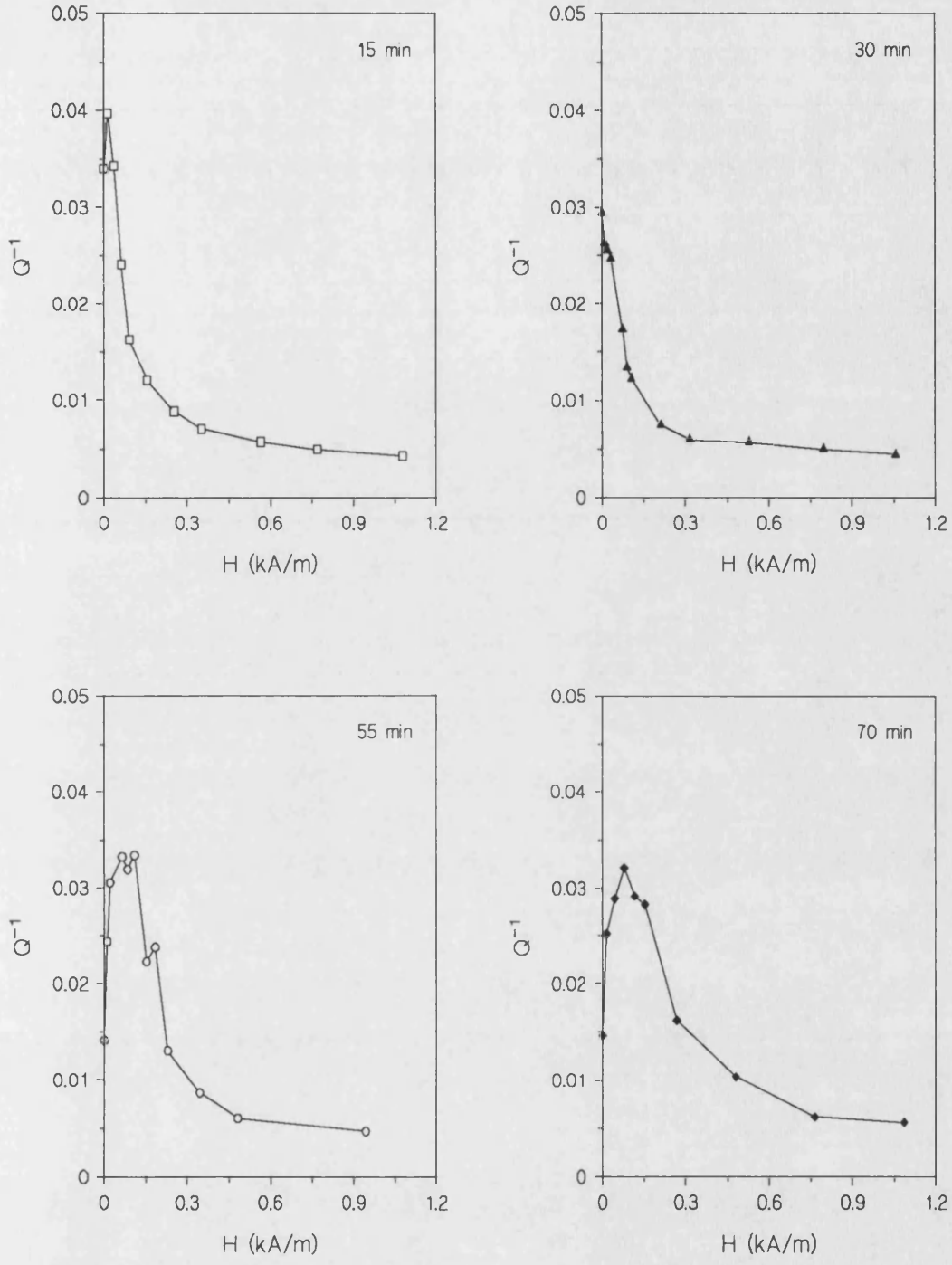

Figure 5.40b: Damping against applied field at 0.43 MPa applied tensile stress for FeSiB 125μm wire annealed at 460°C.

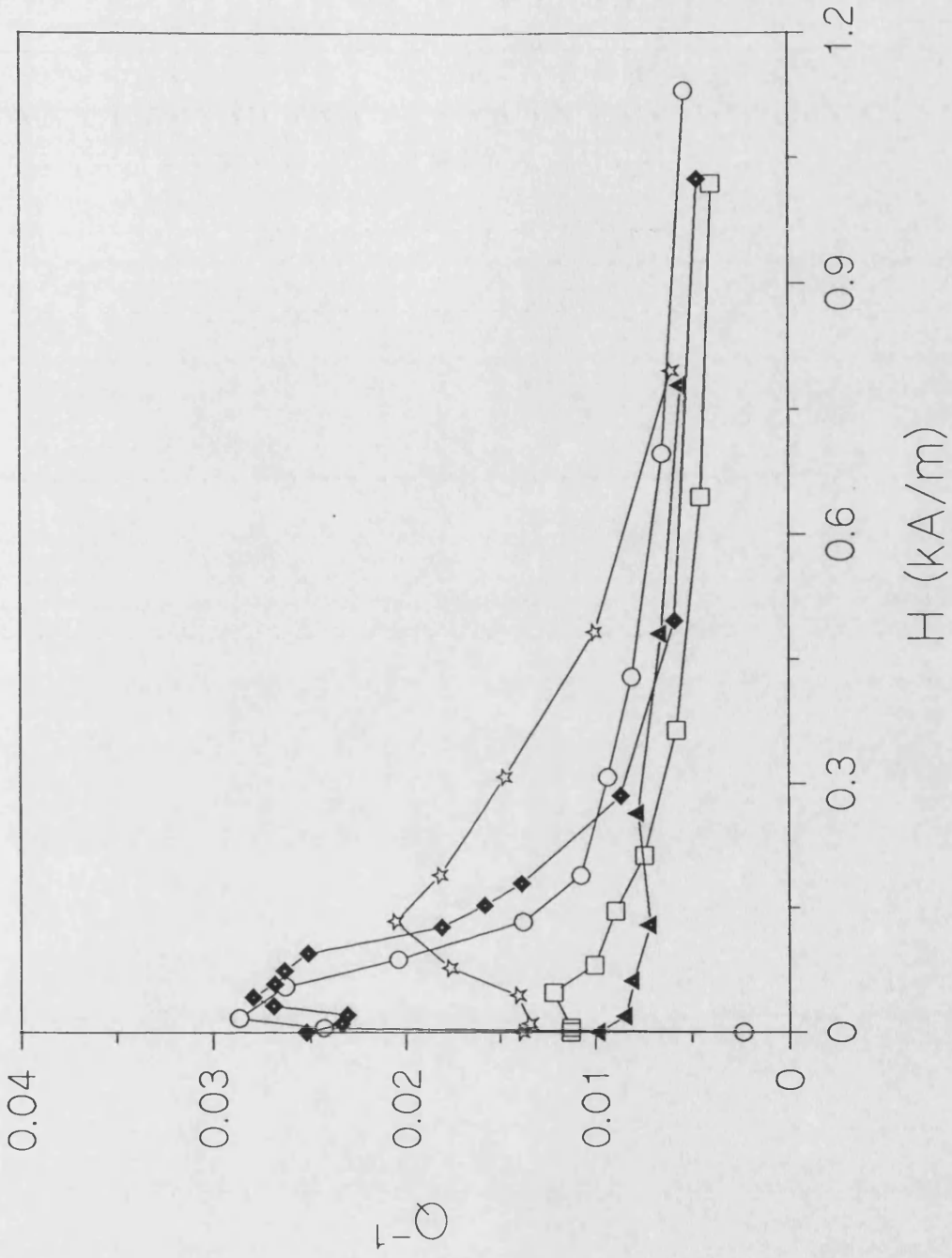

Figure 5.40c: Damping against applied field at 0.43 MPa applied tensile stress for FeSiB 125μm wire annealed at 480°C (for key see figure 5.31c).

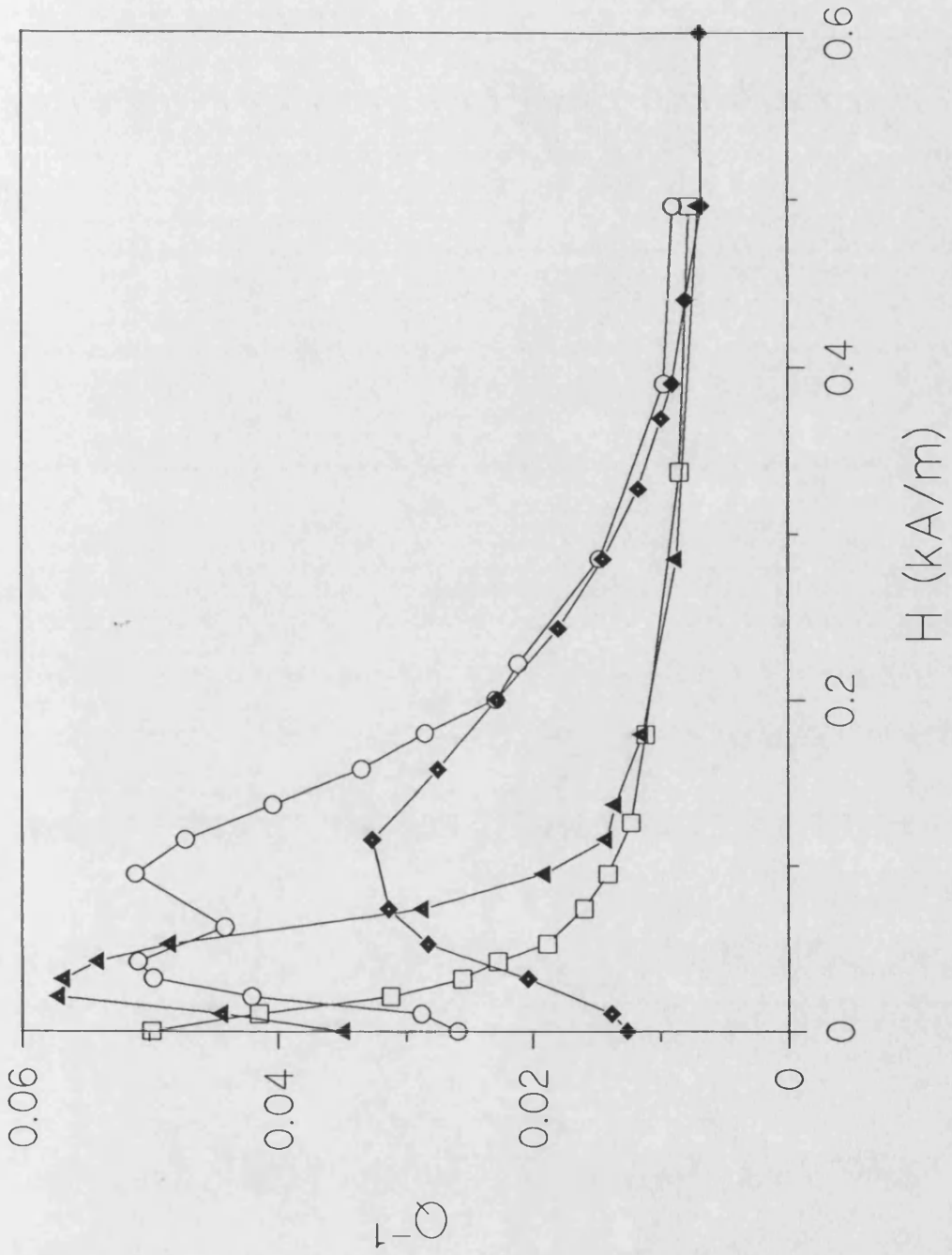

Figure 5.40d: Damping against applied field at 0.43 MPa applied tensile stress for FeSiB 125μm wire annealed at 500°C. (for key see figure 5.31d). The lines are interpolated between the experimental data points.

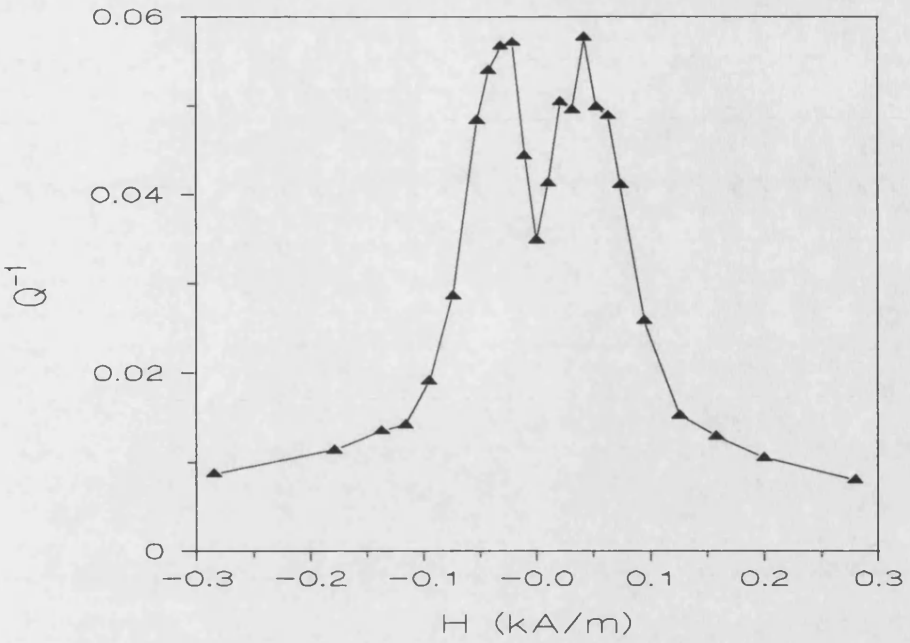

Figure 5.41: Damping against magnetic field for FeSiB 125μm wire annealed at 500°C for 6 minutes. The lines are interpolated between the experimental data points.

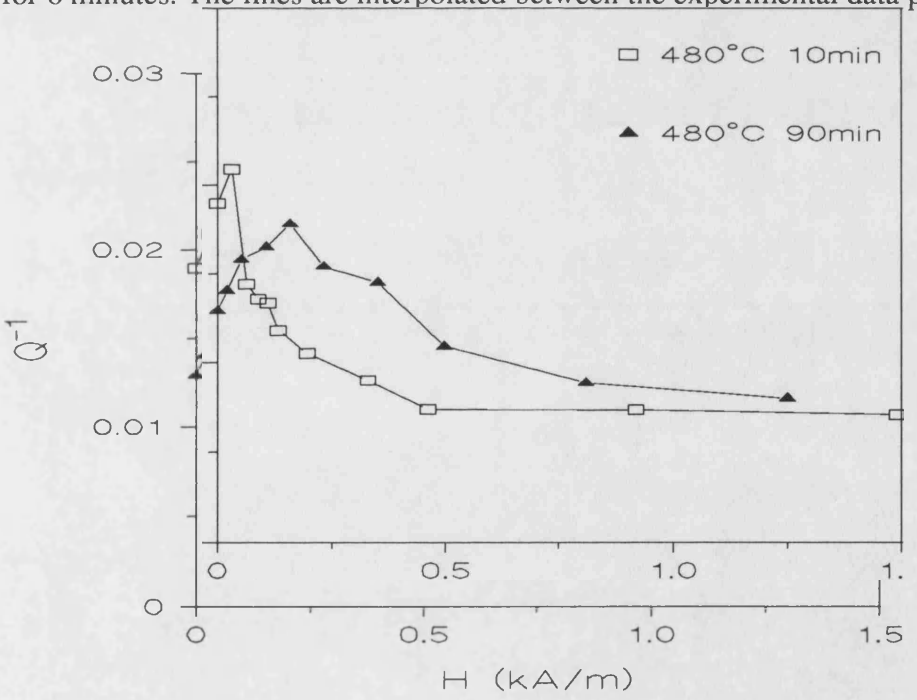

Figure 5.42: Damping against magnetic field for cold-drawn 90μm wire. The lines are interpolated between the experimental data points.

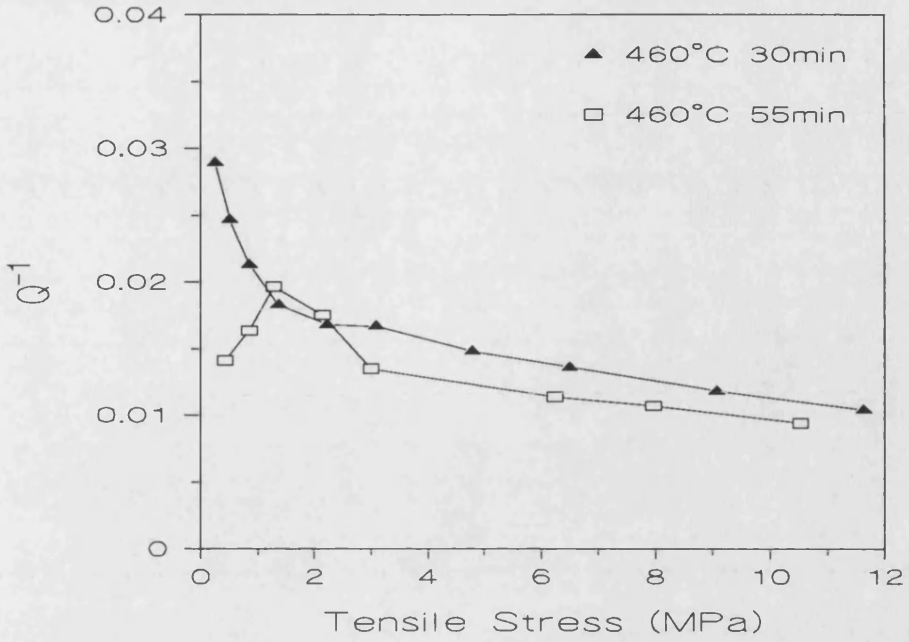

(a)

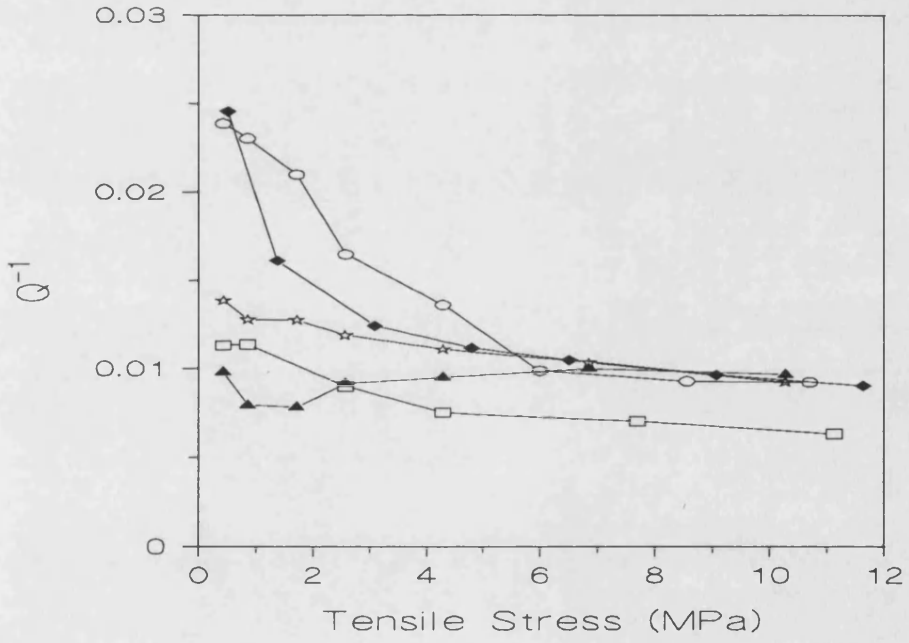

(b)

Figure 5.43: Damping against applied tensile stress at H=0 for FeSiB 125μm wire annealed at a) 460°C b) 480°C (for key see figure 5.31c). The lines are interpolated between the experimental data points.

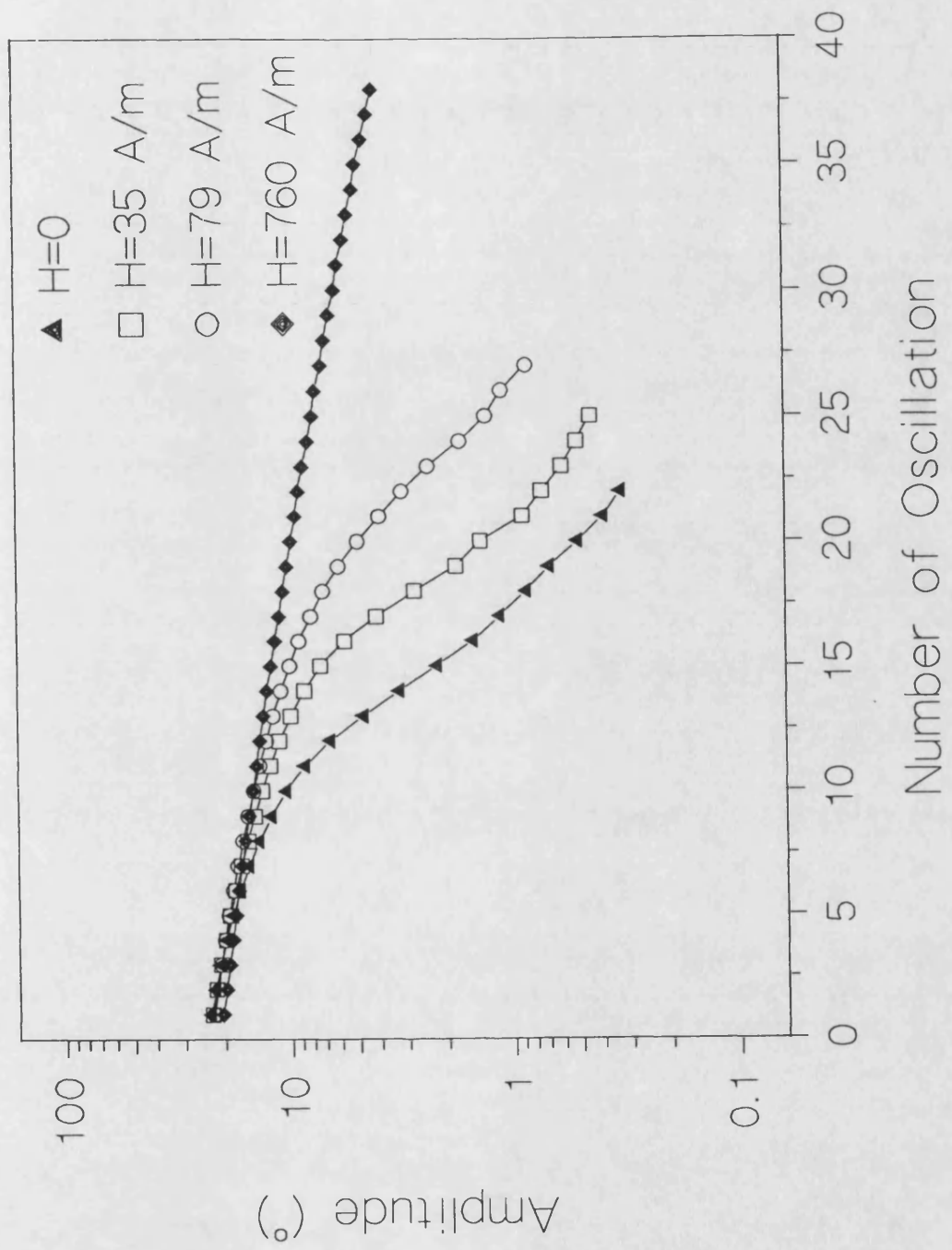

Figure 5.44: Amplitude of the torsional oscillation against the number of the oscillation for FeSiB 125μm wire annealed at 460°C for 15 minutes. The lines are interpolated between the experimental data points. A linear dependence indicates an exponential decay of amplitude corresponding to strain independent damping.

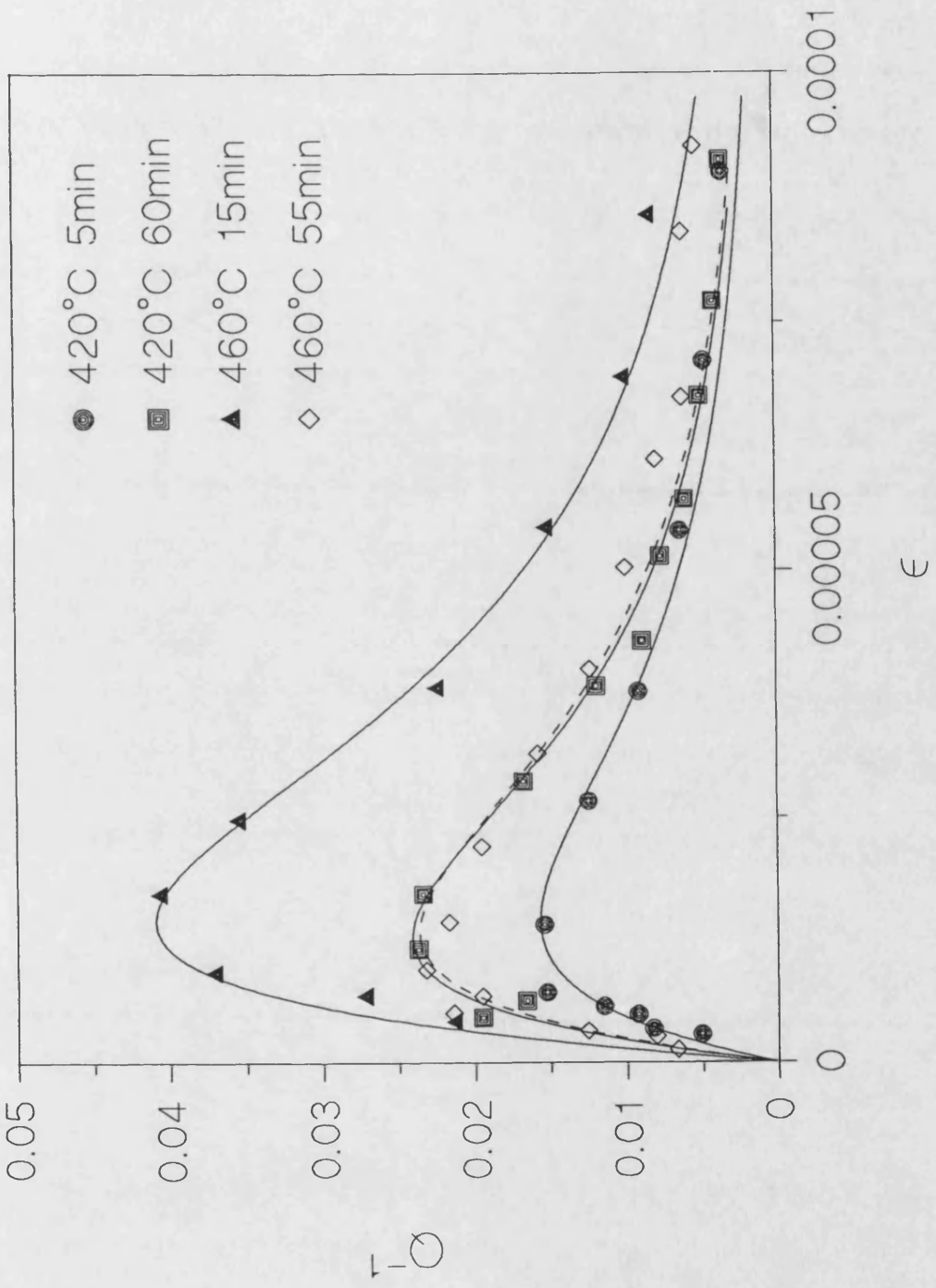

Figure 5.45: Damping against torsional strain at zero applied field and 0.43 MPa applied tensile stress for different annealing temperatures and times. The fitted curves were obtained from the Smith and Birchak model.

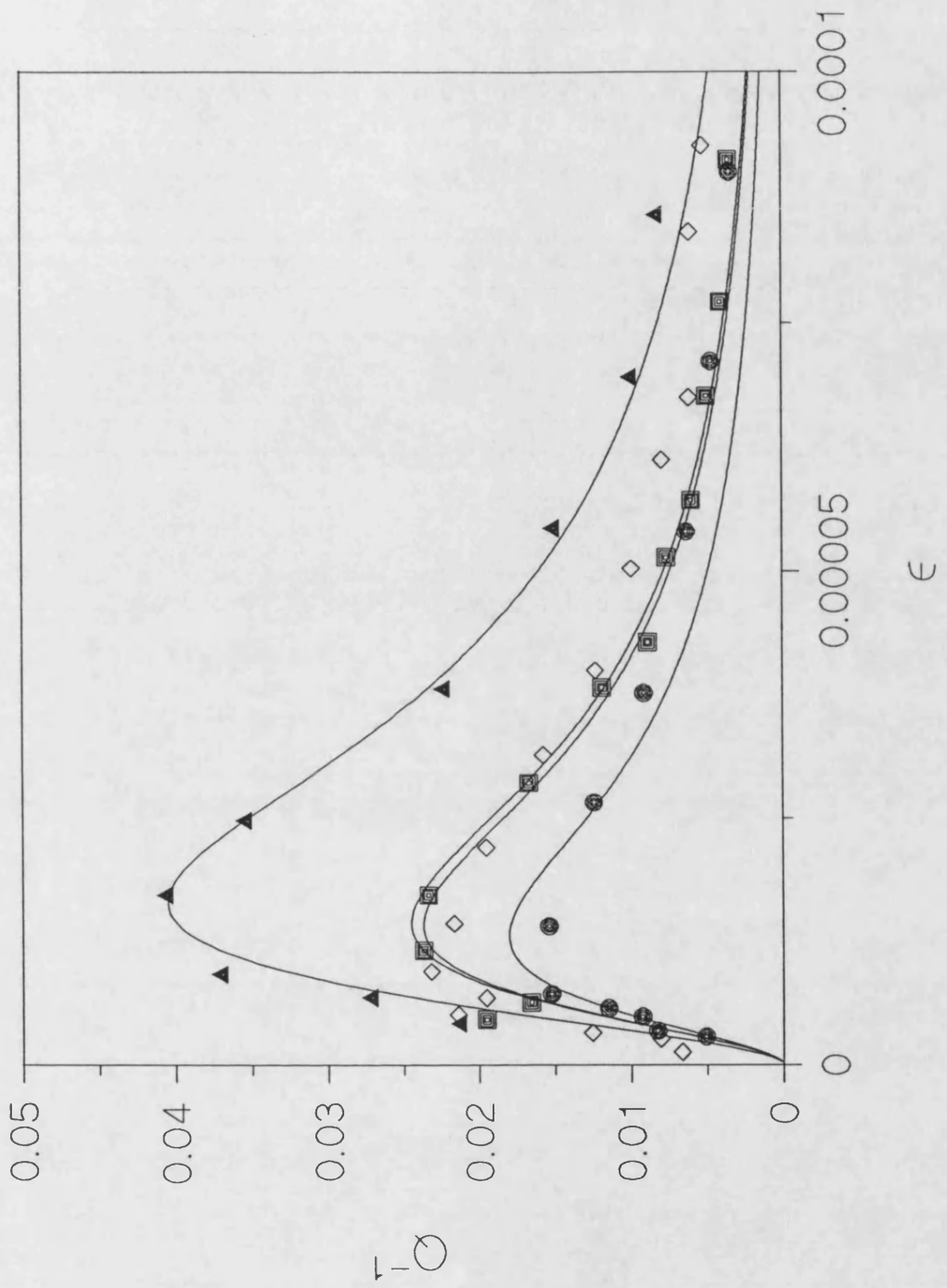

Figure 5.46: Damping against torsional strain for FeSiB 125μm wire annealed at different temperatures. For key, see figure 5.45. The fitted curves were obtained from equation 3.31.

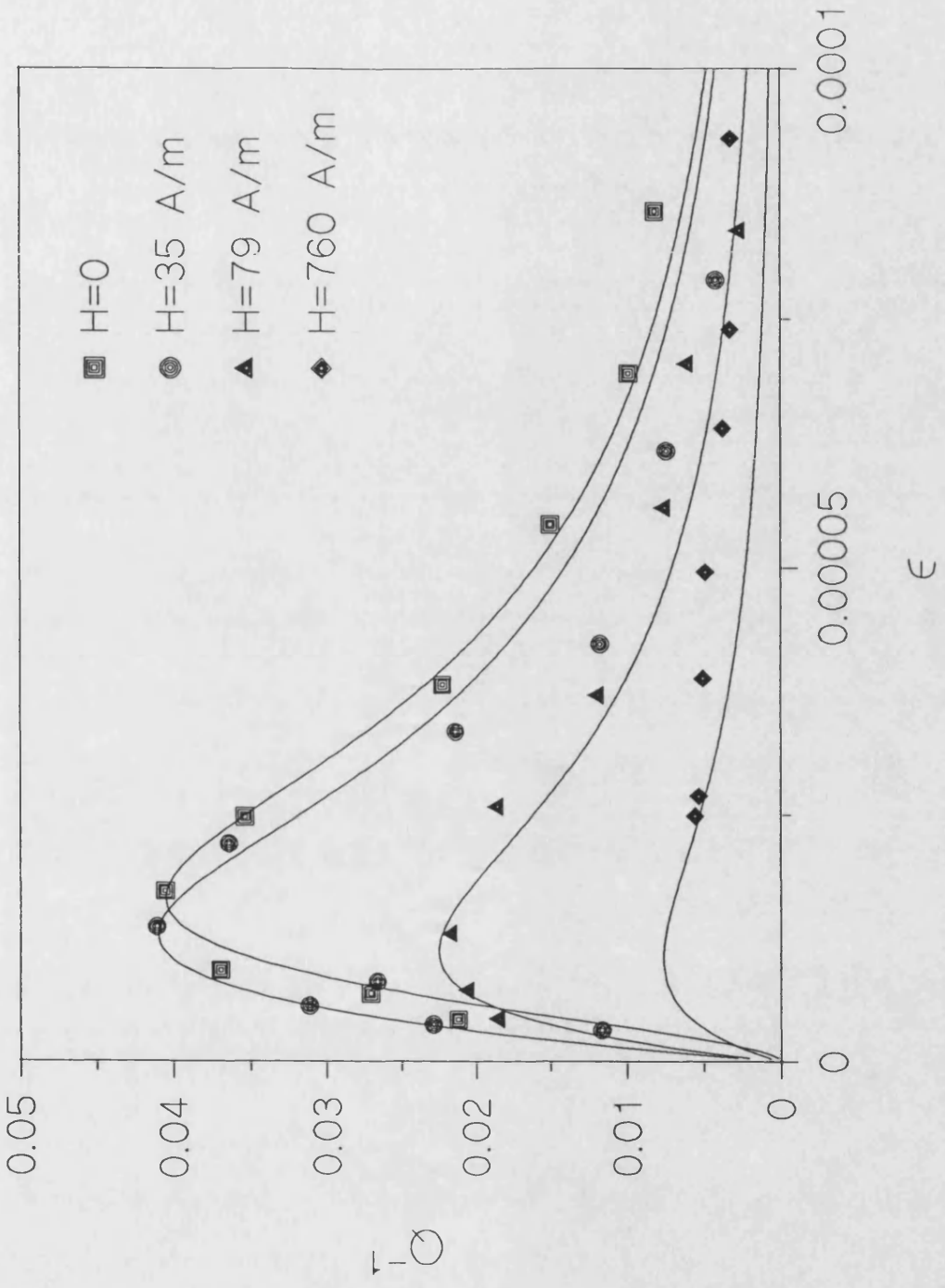

Figure 5.47: Damping against torsional strain for different applied fields for FeSiB 125μm wire annealed at 460°C for 15 minutes. The fitted curves were obtained from equation 3.31.

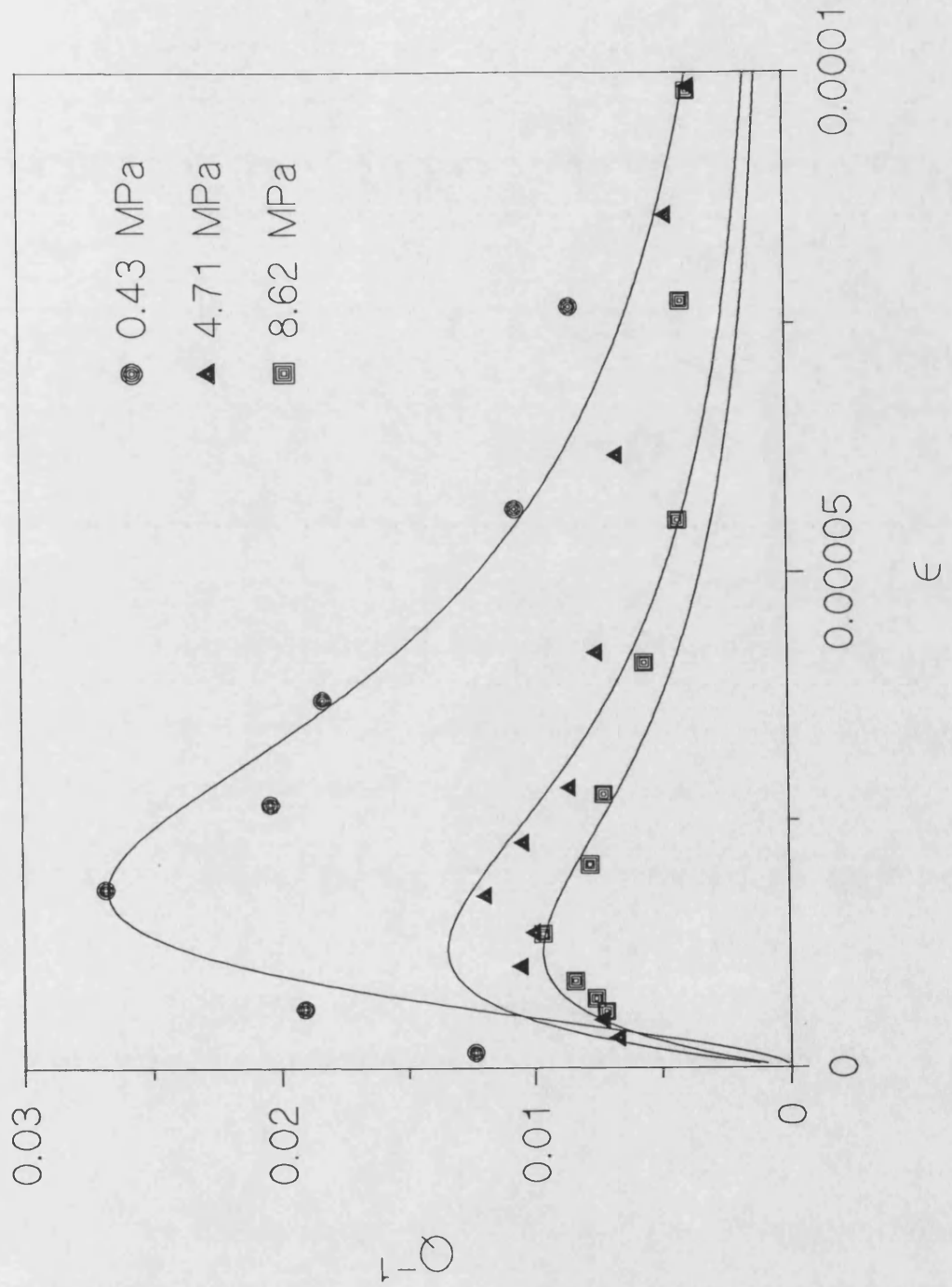

Figure 5.48: Damping against torsional strain for different applied tensile stresses for FeSiB 125μm wire annealed at 460°C for 70 minutes. The fitted curves were obtained from equation 3.31.

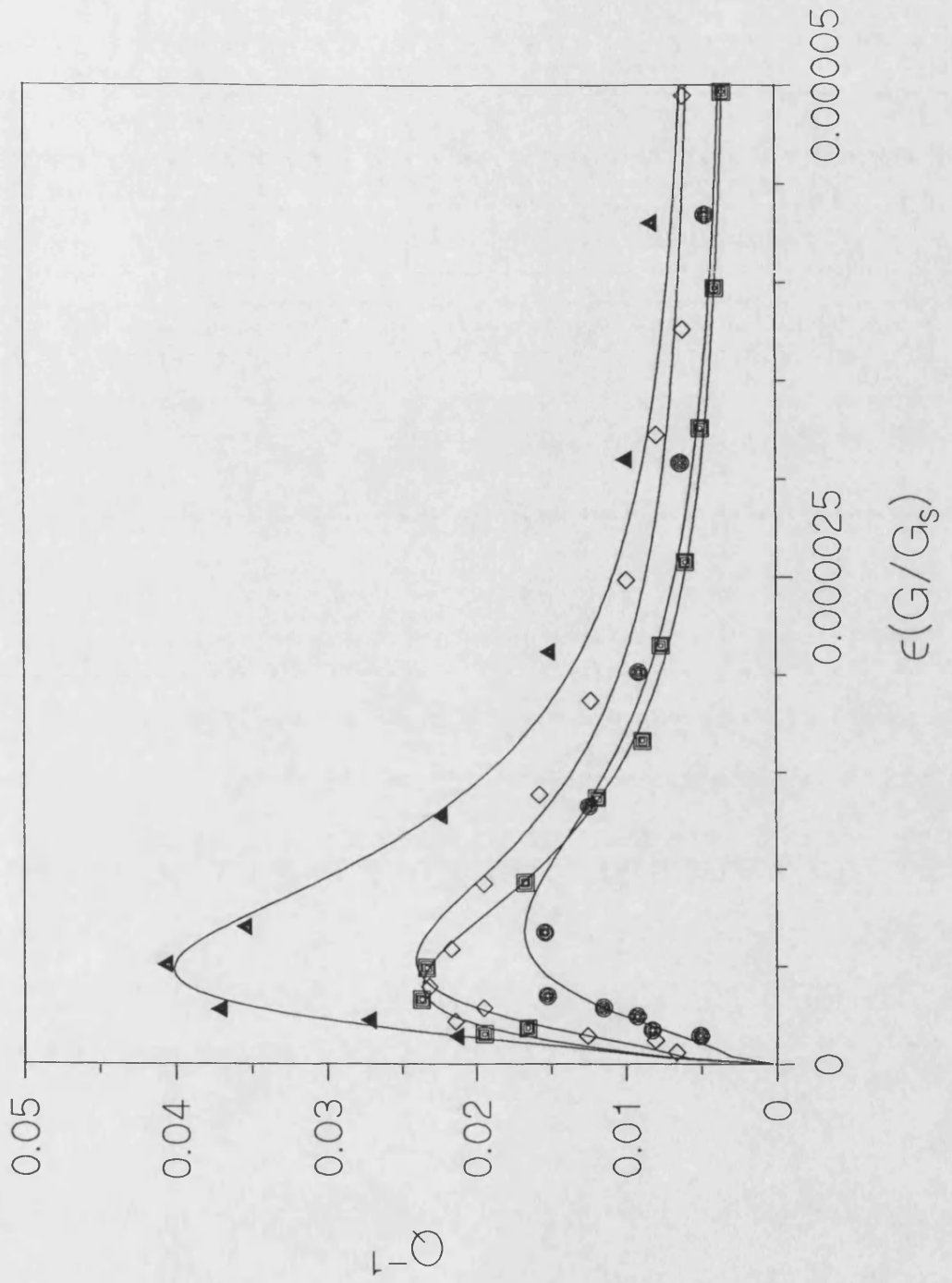

Figure 5.49: Damping against normalised torsional strain for FeSiB 125μm wire annealed at different temperatures. For key, see figure 5.45. The fitted curves were obtained from equation 3.31.

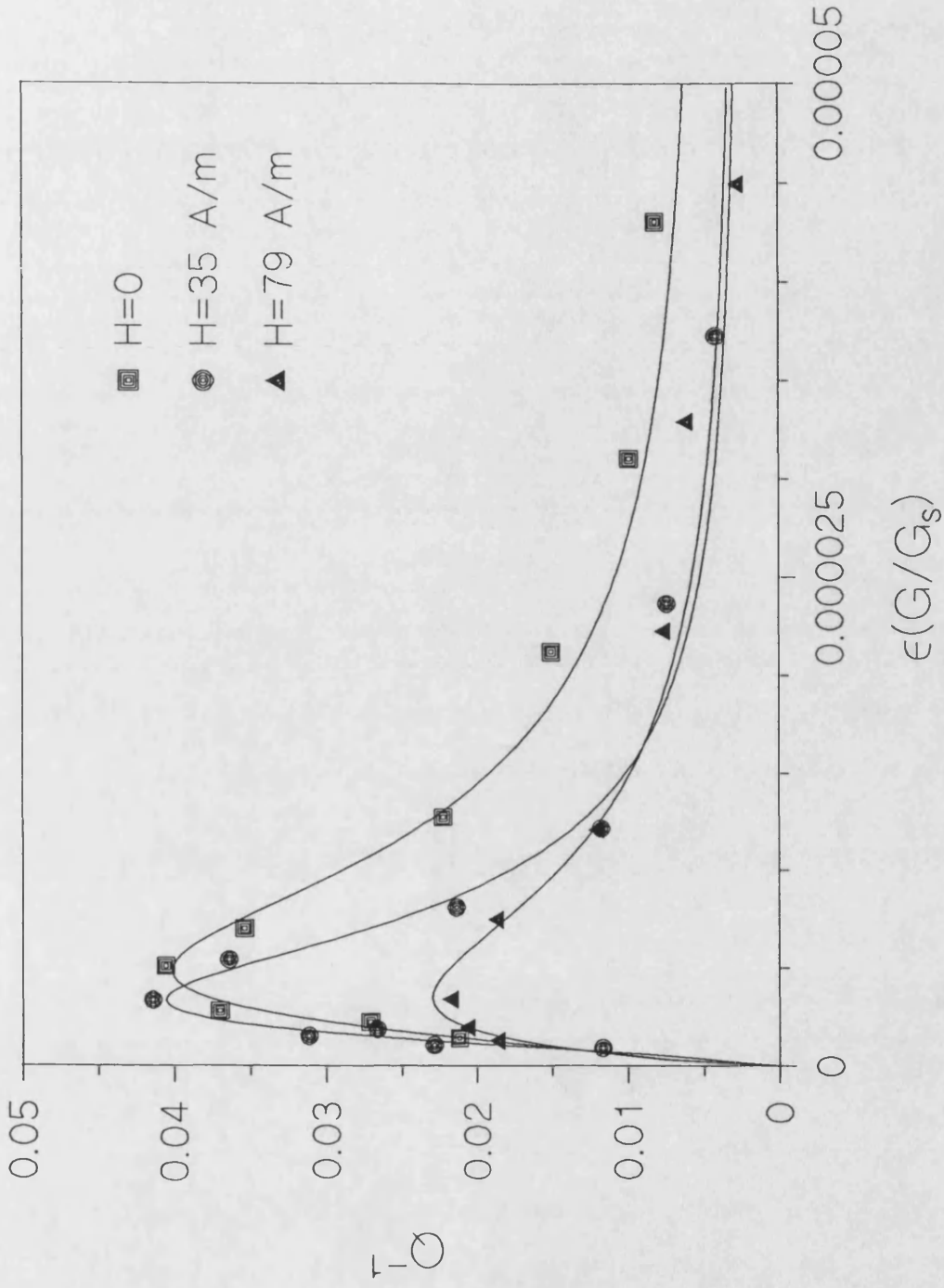

Figure 5.50: Damping against normalised torsional strain for different applied fields stress for FeSiB 125μm wire annealed at 460°C for 15 minutes. The fitted curves were obtained from equation 3.31.

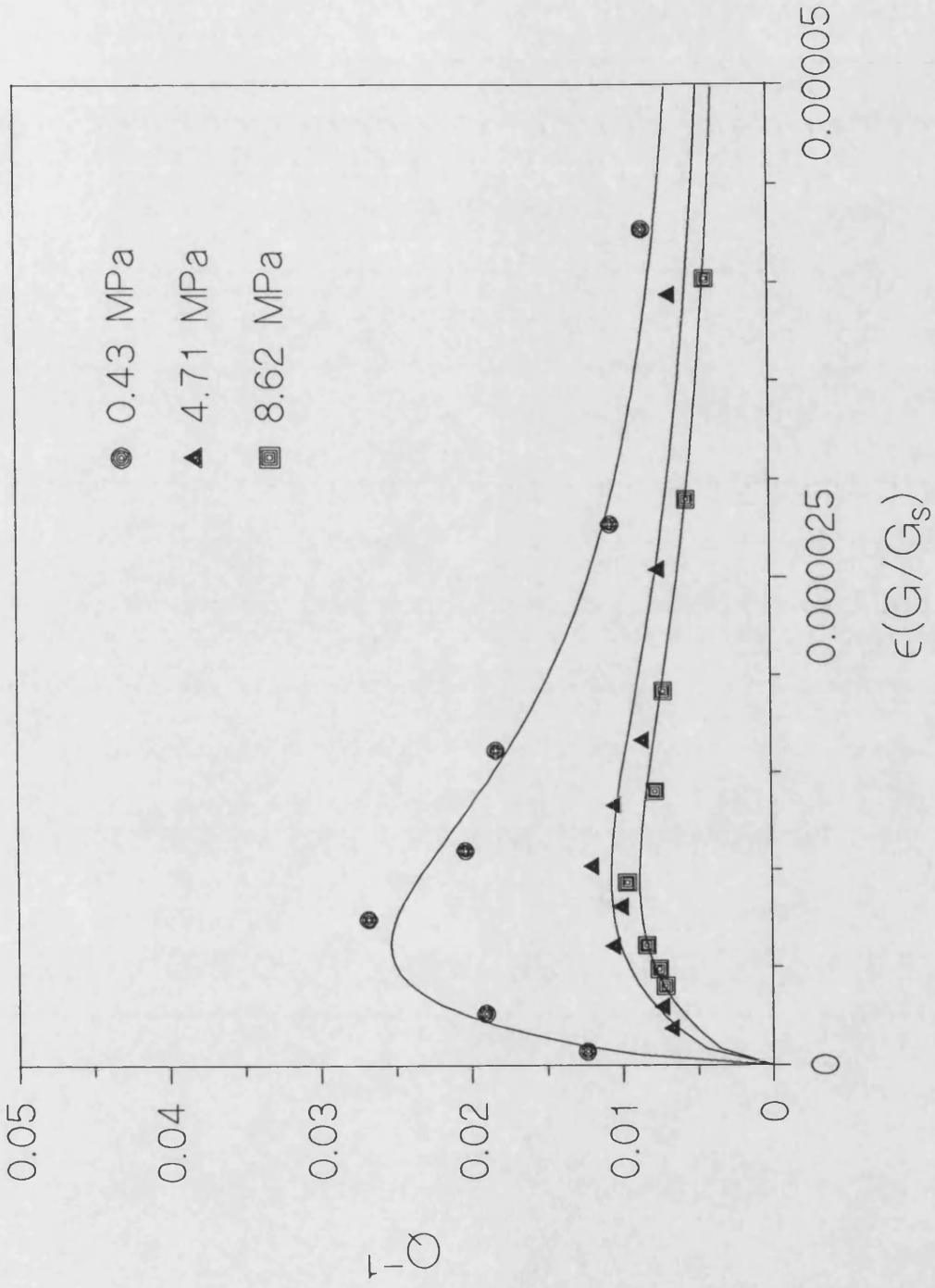

Figure 5.51: Damping against normalised torsional strain for different applied tensile stresses for FeSiB 125μm wire annealed at 460°C for 70 minutes. The fitted curves were obtained from equation 3.31.

6 Results and Analysis for Current and Field Annealed Amorphous Wires

6.1 Current Annealing

Electric current flowing through the sample has been used to heat the sample (Jagielinski [1983]). The current also creates a circumferential magnetic field in the wires. This circumferential field, H_θ, is given by:

$$H_\theta = \frac{Ir}{2\pi R_o^2} \quad (r \ll R_o) \tag{6.1}$$

where R_o is the wire radius and r is the distance from the center of the wire. Figure 6.1 shows the circular magnetic field set up in a wire with a diameter of 125μm by the applied current. Due to the variation of the wire diameter, the current density varies along the length of the wire. This leads to a temperature gradient and an inhomogeneous magnetic field along the wire length. Therefore, the induced anisotropy should be taken as the mean value. Because of this temperature gradient, the temperature generated by the current annealing should be interpreted as the average temperature within the sample.

The effects of current annealing can be observed from the modification of the magnetisation curves. The typical effects of the current annealing on the M-H loops are: 1) the high initial susceptibility becomes smaller as the annealing time increases, 2) the increase in magnetisation due to domain wall motion becomes smaller with increasing annealing time, 3) coercivity increases with increasing annealing time (Gonzalez *et al* [1988]).

The amorphous un-drawn $Fe_{77.5}Si_{7.5}B_{15}$ 125μm wires were current annealed as explained in chapter 4 section 2. Wires were annealed by ac and dc current at 737±7 mA and 605±5

mA for various annealing times. The annealing temperature during current annealing was derived from the resistance versus applied current graph, and estimated to be within the range 490±6°C for 737±7 mA and 402±4°C for 605±5 mA.

The M-H loops of 22 cm wires used in G(H) and $Q^{-1}(H)$ measurements are shown in figure 6.2 and those for 7 cm wires used in E(H) measurements in figure 6.3. As can be seen from figures 6.2 and 6.3, the wire length has a much bigger effect on the M-H loops of the annealed wire than on those of as-cast wire. This is because, in the annealed wire, the domain structure is mainly determined by the shape anisotropy whereas in as-cast wires, the domain structure is determined by the interaction between the large casting anisotropy and magnetostriction. Figure 6.4 shows the coercivity as a function of annealing time. H_c first decreases then starts to increase with increasing annealing time. There is a slight difference observed between ac and dc current annealed wires at 730-745mA. The dc current annealing leads to a slightly sharper increase in H_c than does ac current annealing. This small difference between ac and dc current annealing was also observed in the amorphous ribbons by Gonzalez *et al* [1987] and [1989].

The effect of current annealing is found to be very similar to that of furnace annealing. The current annealing first relieves the large casting stresses, then induces a circumferential easy axis due to the partial crystallisation and magnetic field created by the current. But the induced circular anisotropy due to the flowing current is almost zero. This is because the temperature is well above the Curie temperature.

The Young's modulus and shear modulus as a function of applied magnetic field are shown in figures 6.5 and 6.6, respectively. The qualitative features of E(H) and G(H) are similar. As the annealing time is increased, E_{min}/E_s and G_{min}/G_s first decrease, then increase. This corresponds to the relief of the internal stresses, followed by the onset of crystallisation.

The modulus variations of these current annealed wires are not as smooth as those obtained from furnace annealed wires. This is probably due to the temperature gradient set up along the wire length during current annealing. The nonuniformity is more obvious in the shorter wires used in the E(H) measurements, because the vibrating reed method is quite sensitive to mechanical inhomogenities in the sample. The 1 minute annealed wire does not display any drop in the modulus as H is increased from zero field. This behaviour is characteristic of easy axis directions at or less than 45° to the wire axis. The E(H) data for longer annealing times (5 and 10 minutes) do show an initial decrease in the modulus, indicating an easy axis direction between 45° and 60° to the wire axis. E_o of the wire current annealed for 15 minutes is almost equal to E_s, indicating that, initially, moments align in a direction perpendicular to the applied field.

No initial increase is observed in the damping, Q^{-1} for the current annealed wires (figure 6.7). In addition to that, the peak value of the damping for current annealed wires is found to be less than that of furnace annealed wires.

6.2 Field Annealing

The amorphous un-drawn $Fe_{77.5}Si_{7.5}B_{15}$ 125μm wires were field annealed with the field in a direction transverse to the wire axis to induce uniaxial magnetic anisotropy in the annealing field direction. The wires were cut 22 cm long and placed between two aluminium plates, which were placed between two magnets, and then heated by a heat gun, as explained in chapter 4 section 2. During the annealing a magnetic field of ~150 kA/m was applied.

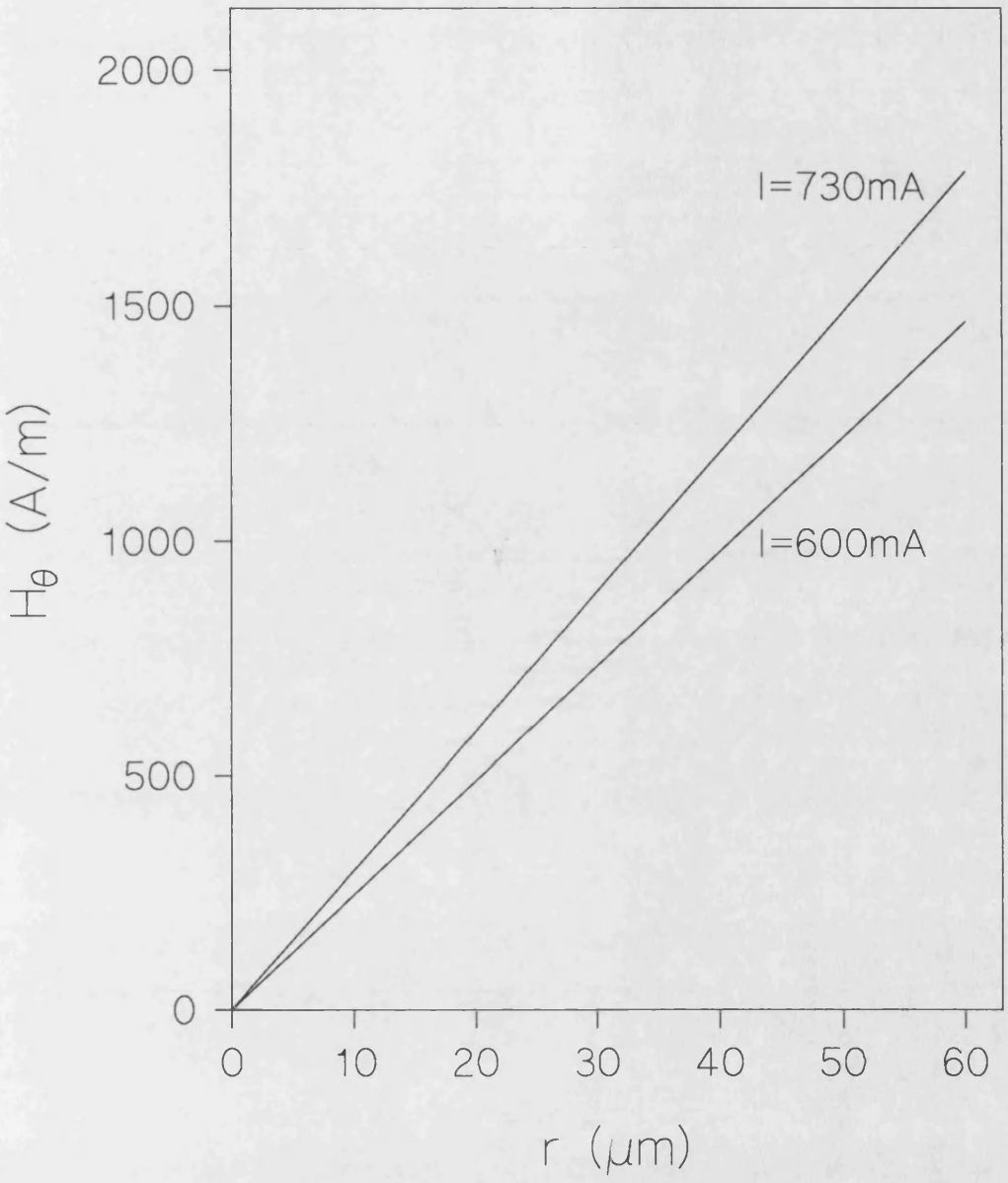

Figure 6.1: Internal magnetic field as a function of the distance from the center of the wire, r, due to the applied current.

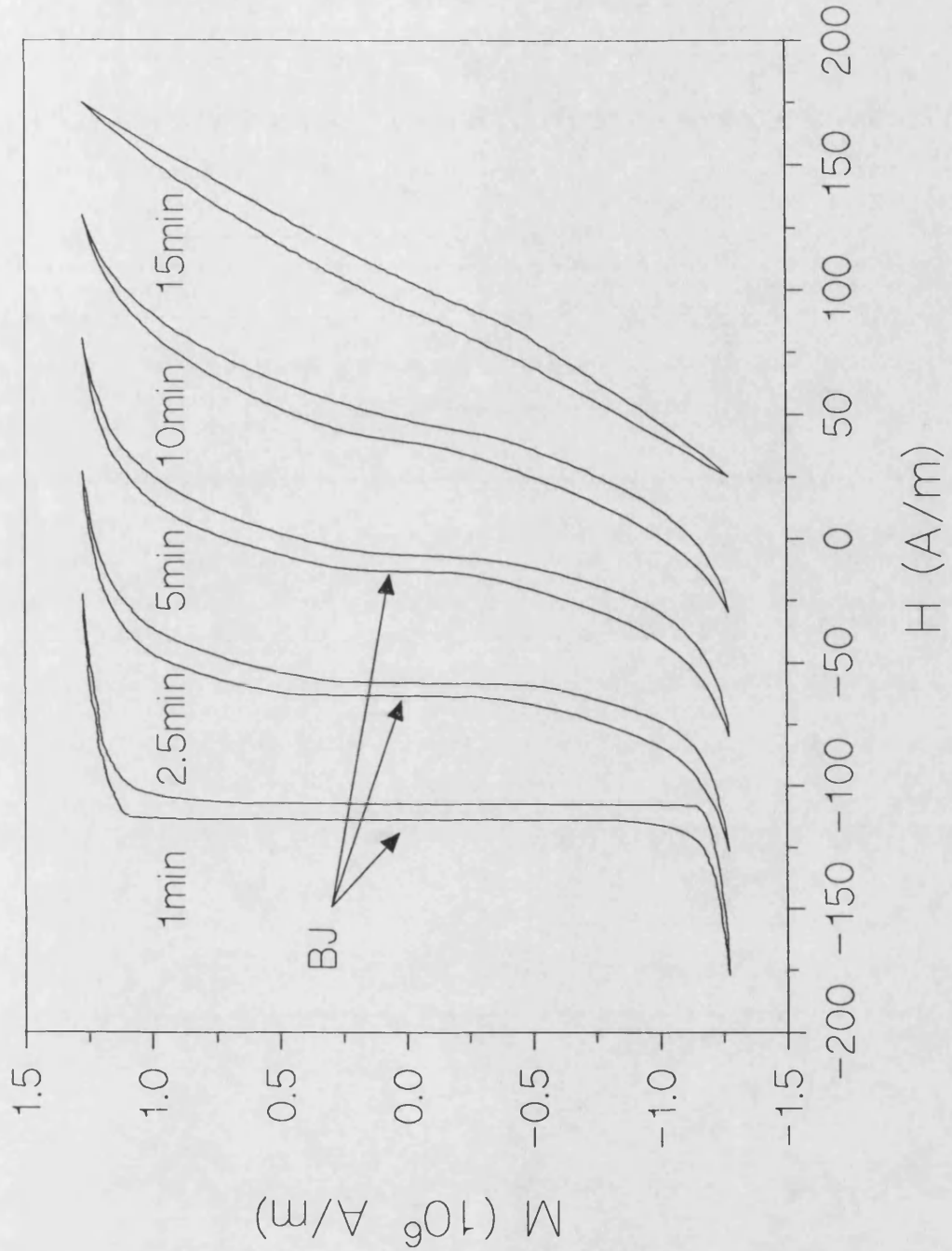

Figure 6.2: M-H loops of 22cm long FeSiB wires current annealed at 737±7 mA. Loops were displaced along the H axis for illustration purpose only.

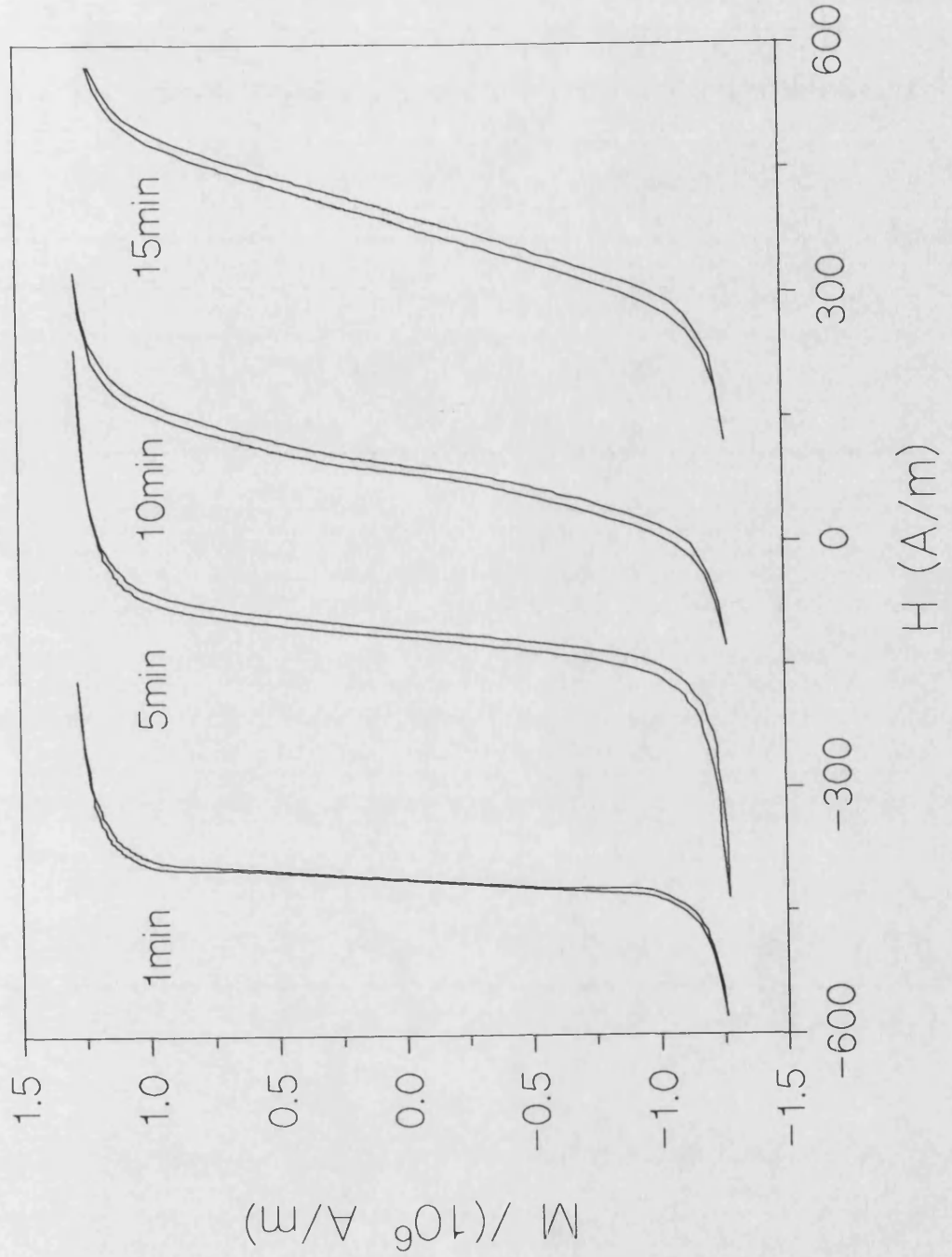

Figure 6.3: M-H loops of 7cm long FeSiB wires current annealed at 737±7 mA. Loops were displaced along the H axis for illustration purpose only.

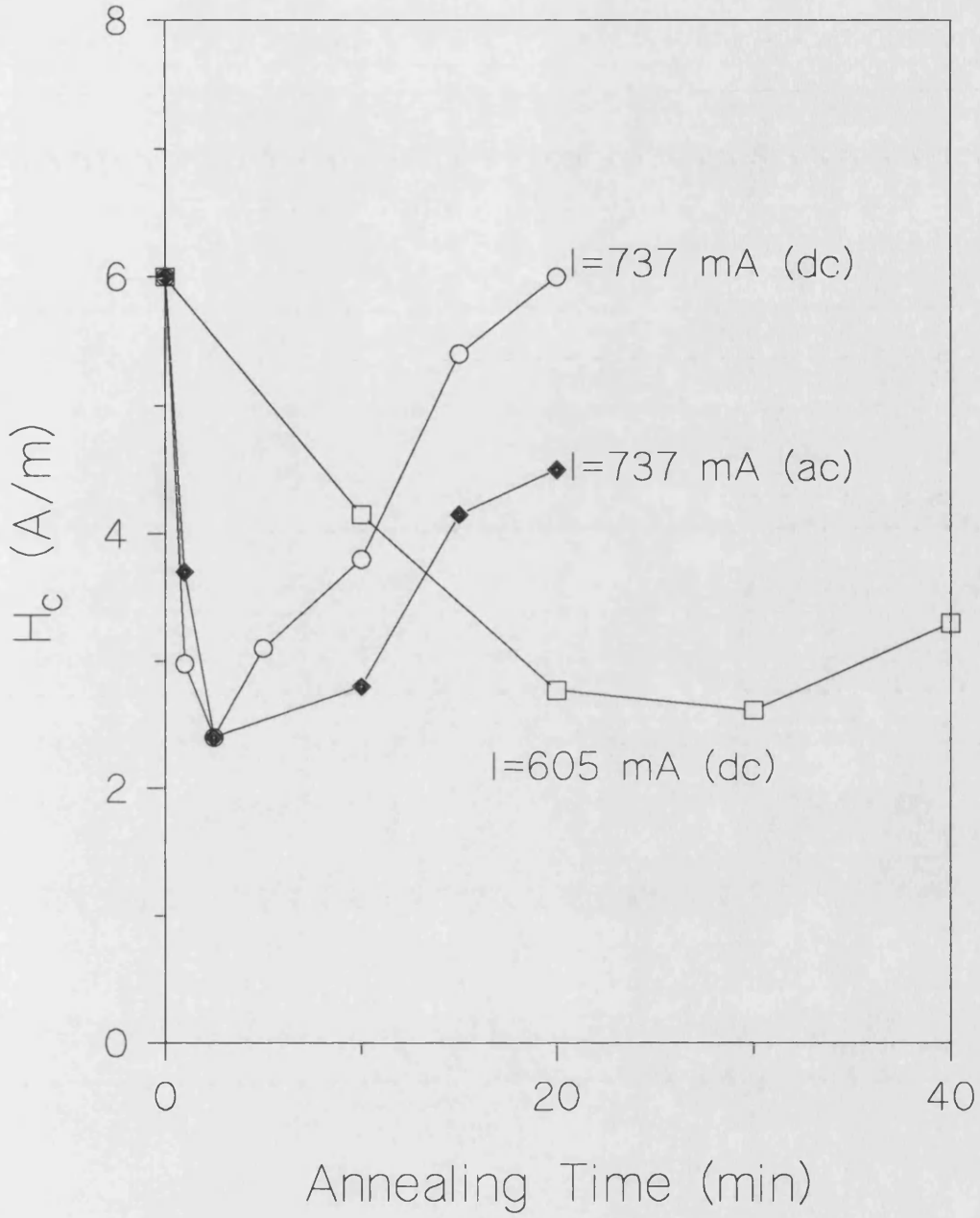

Figure 6.4: Coercivity of current annealed FeSiB wires as a function of annealing time. The data were connected with lines for guidance only.

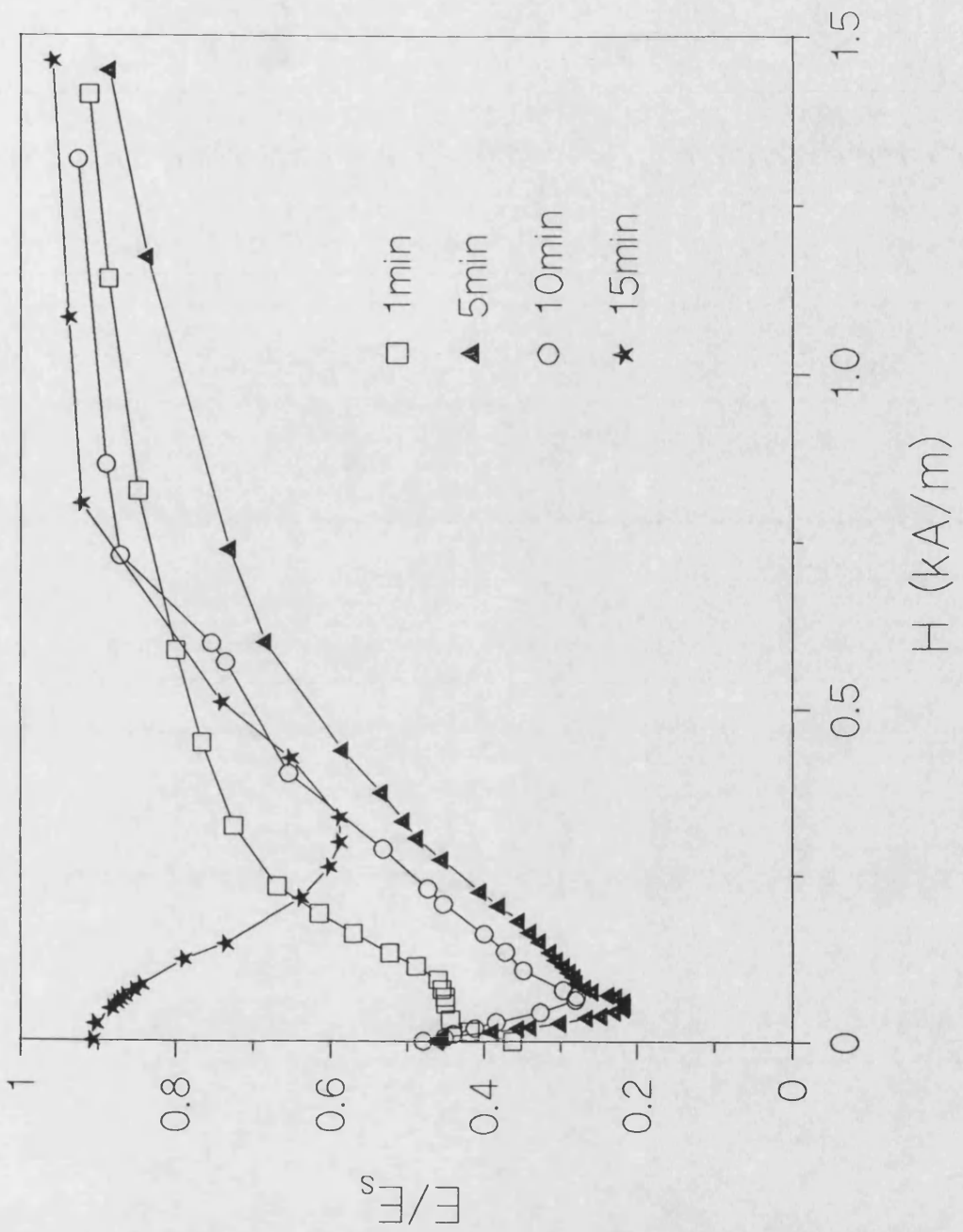

Figure 6.5: Normalised Young's modulus of FeSiB wires current annealed at 737±7 mA versus applied field. The data are connected with straight lines for guidance only.

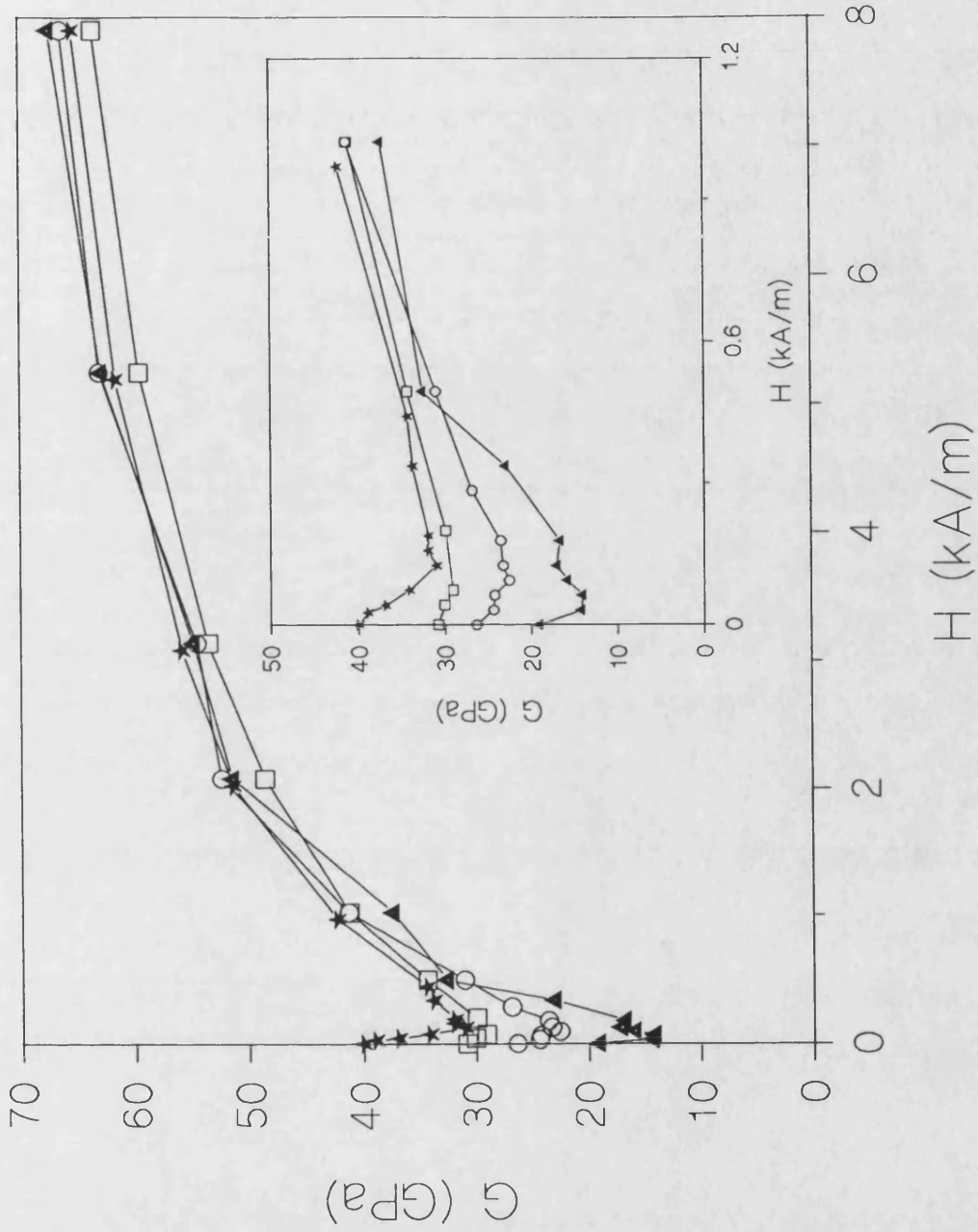

Figure 6.6: Shear modulus of FeSiB wires current annealed at 737±7 mA against applied field. The data are connected as a guide for the eye. For figure caption see figure 6.5.

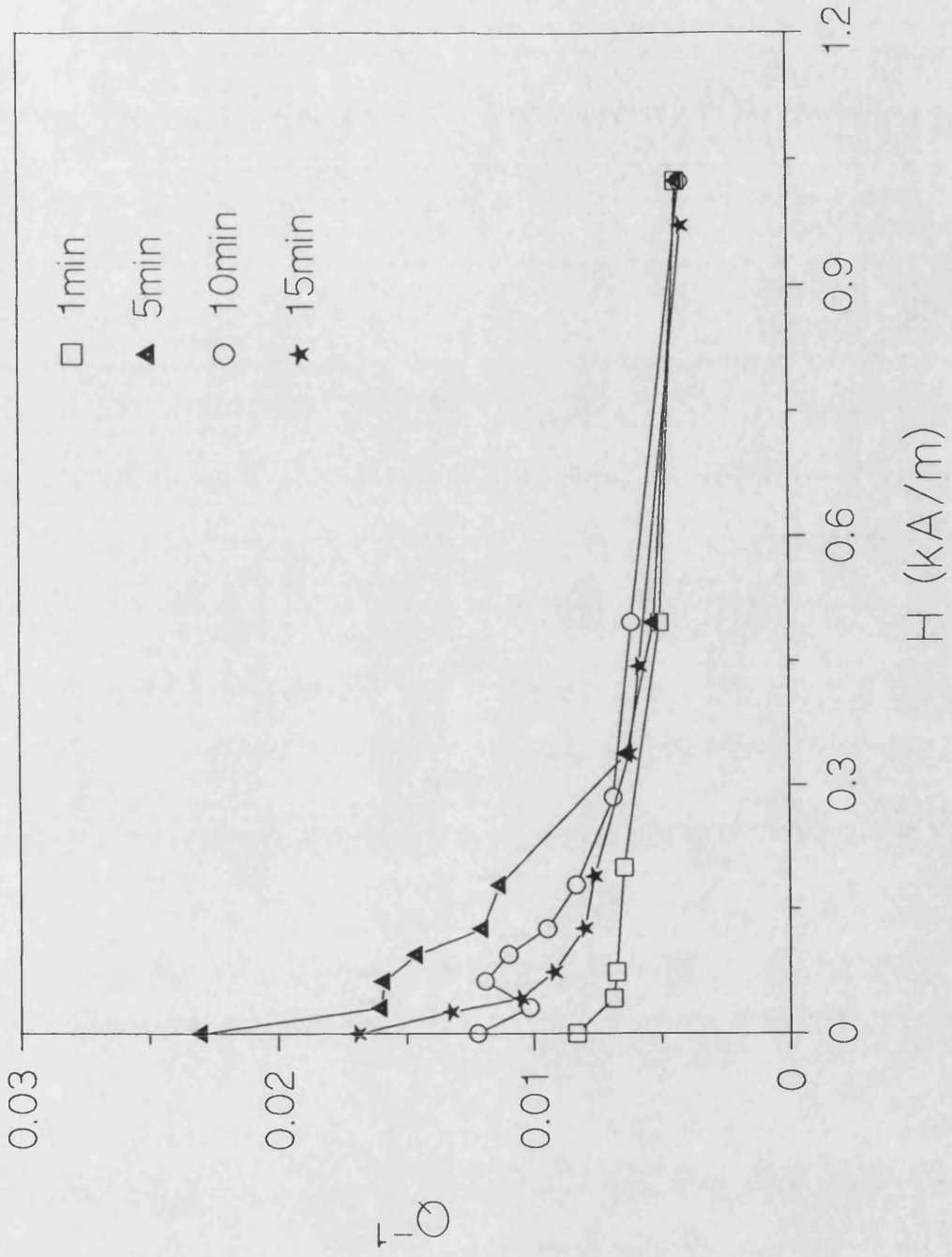

Figure 6.7: Damping of FeSiB wires current annealed at 737±7 mA against applied field. The data are connected as a guide for the eye.

FeSiB wires were field annealed at various temperatures for 60 minutes. Figure 6.8 shows the magnetic field dependence of the shear modulus of the field annealed wires. In the wires annealed between 370°C and 420°C, the internal stress was not completely relieved, so the field annealing was not successful. Although most of the internal stresses were relieved in the wire annealed at 450°C, the magnetic moments are mostly in the wire axis direction. G_o is almost equal to G_{min}, showing that the average initial angle of moments is between 35° and 45° to the wire axis.

The earlier work of Wun-Fogle *et al* [1989a] showed that the magnitude of the annealing field is very important in inducing an anisotropy in a direction transverse to the wire axis. A much larger annealing field (~900 kA/m) is required for the field annealing of the amorphous wires in order to overcome the demagnetising effects.

To obtain such a high magnetic field, the gap between the magnets shown in figure 4.4 was reduced to 0.5 cm. The amorphous wire was heated up by applying dc current. During the current annealing an 875 kA/m magnetic field was applied to the sample. The temperature of the sample was calculated as for the current annealing. The field anneals were performed around and above the Curie temperature. The annealing field was kept on while the wire was cooled down to room temperature.

Figure 6.9 shows the M-H loops of current field annealed amorphous wires. The magnitude of the linear part in the low magnetic field region decreases with increasing annealing current. Also, the coercivity first decreases from the as-cast value, then increases with increasing annealing current (table 6.1).

Figure 6.10 illustrates the magnetic field dependence of Young's modulus of the field annealed wires at various currents. The maximum change in the Young's modulus is observed for the wire field annealed at I=740±5 mA for 15 minutes, pre-annealed at

I=820±5 mA for 15 minutes. The E_o/E_s ratios show that the magnetic moments are not completely perpendicular to the wire axis (table 6.1). The average initial angle orientation angle of the moments is between 60° and 70° to the wire axis. The anisotropy constant, K, obtained from the M-H loops are also given in the table 6.1. The maximum change in the Young's modulus corresponds to the lowest value of K.

Figure 6.11 and 6.12 show magnetic field dependence of the shear modulus, G, and the damping, Q^{-1}, respectively. The change in the shear modulus as a function of applied field in the current field annealed wires is as large as that in the furnace annealed wires. No initial increase in the damping is observed.

In the current-field annealed wires, the effect of the magnetic field due to the flowing current is almost zero. This is because the field annealing is always done above the Curie temperature. In conclusion, although the annealing field was large, an easy axis in a direction transverse to the wire axis was not induced. This is for two reasons: 1) complete stress relief is impossible before crystallisation begins, 2) the annealing field was still not high enough to overcome demagnetising effects and to induce an anisotropy in a direction transverse to the wire axis.

Wun-Fogle *et al* [1989a] claimed that they succeeded in transverse field annealing amorphous wires, but their proposed domain structure for the field annealed wires (figure 2.10) shows that the magnetic moments are not in a direction transverse to the wire axis. The field annealed wire has two regions: an inner core and an outer shell. They assumed that the inner core moments align in the longitudinal direction in view of the observed sharp increase in the M-H loop at low field. They also suggested that the magnetic moments in the outer shell align in the circumferential direction because of the observed domain pictures, where the domain walls on the surface of the wires are running perpendicular to the length of the wire.

Their assumed domain structure is inconsistent with a successful transverse field anneal of an amorphous wire. It is well known that, in field annealing, an easy axis can be induced in the direction of the applied field and not in any other direction.

There is also another possibility. Earlier results showed that crystallisation starts after very short annealing times at 475°C, which is the field annealing temperature Wun-Fogle *et al* used. Therefore they should have also considered the effect of crystallisation, which aligns the magnetic moments in the circumferential direction. This may also explain why Wun-Fogle *et al* observed magnetic moments in the circumferential direction in the outer shell.

Current (mA)	Time (min)	Temp. (°C)	H_c (A/m)	K (Jm^{-3})	E_{min}/E_s	E_o/E_s
720±5	15	427±4	2.44	134	-	-
740±5	30	441±4	3.97	116	0.26	0.576
780±5	15	465±4	2.61	170	0.36	0.582
805±5	15	473±4	10.6	200	-	-
820±5	30	476±4	4.27	195	0.47	0.707

Table 6.1: Annealing temperatures, coercivities, anisotropy constant and E_{min}/E_s and E_o/E_s ratios of field annealed FeSiB amorphous wires.

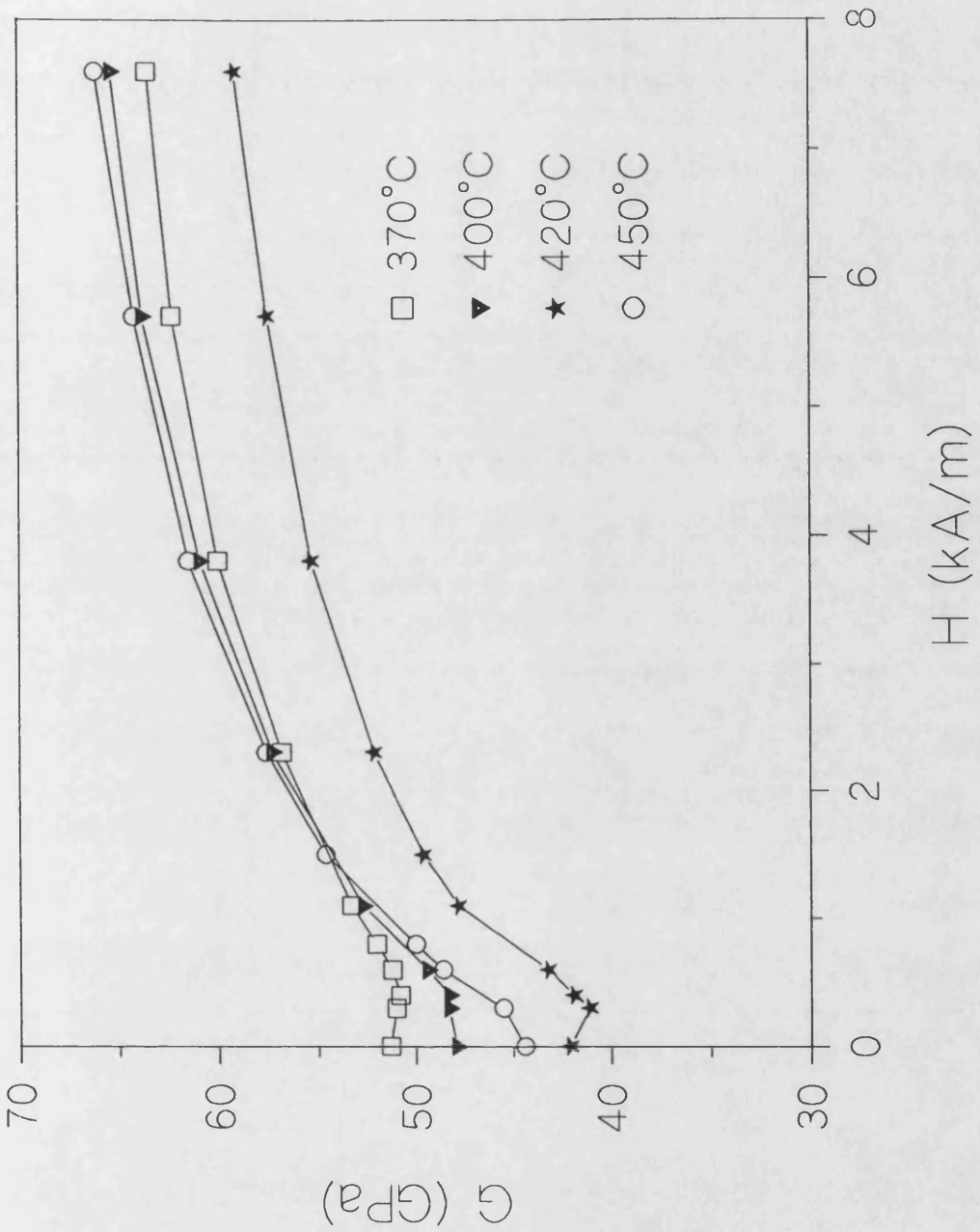

Figure 6.8: Shear modulus versus applied field for FeSiB wires annealed at various temperatures. The data are connected with lines for guidance only.

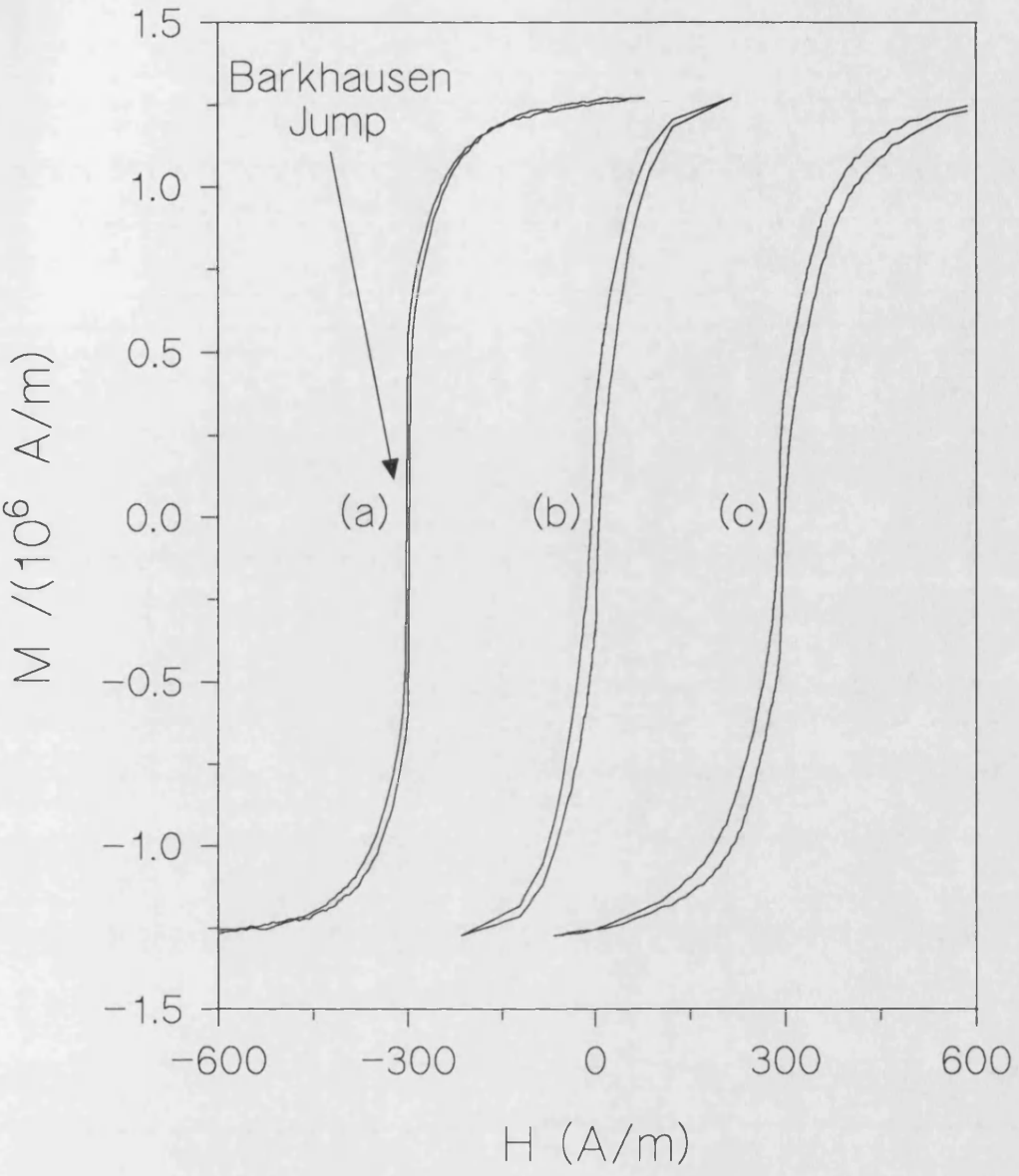
Barkhausen
Jump
(a)
(b)
(c)
1.5
1.0
0.5
0.0
−0.5
−1.0
−1.5
−600
−300
0
300
600
M /(10^6 A/m)
H (A/m)

(A)

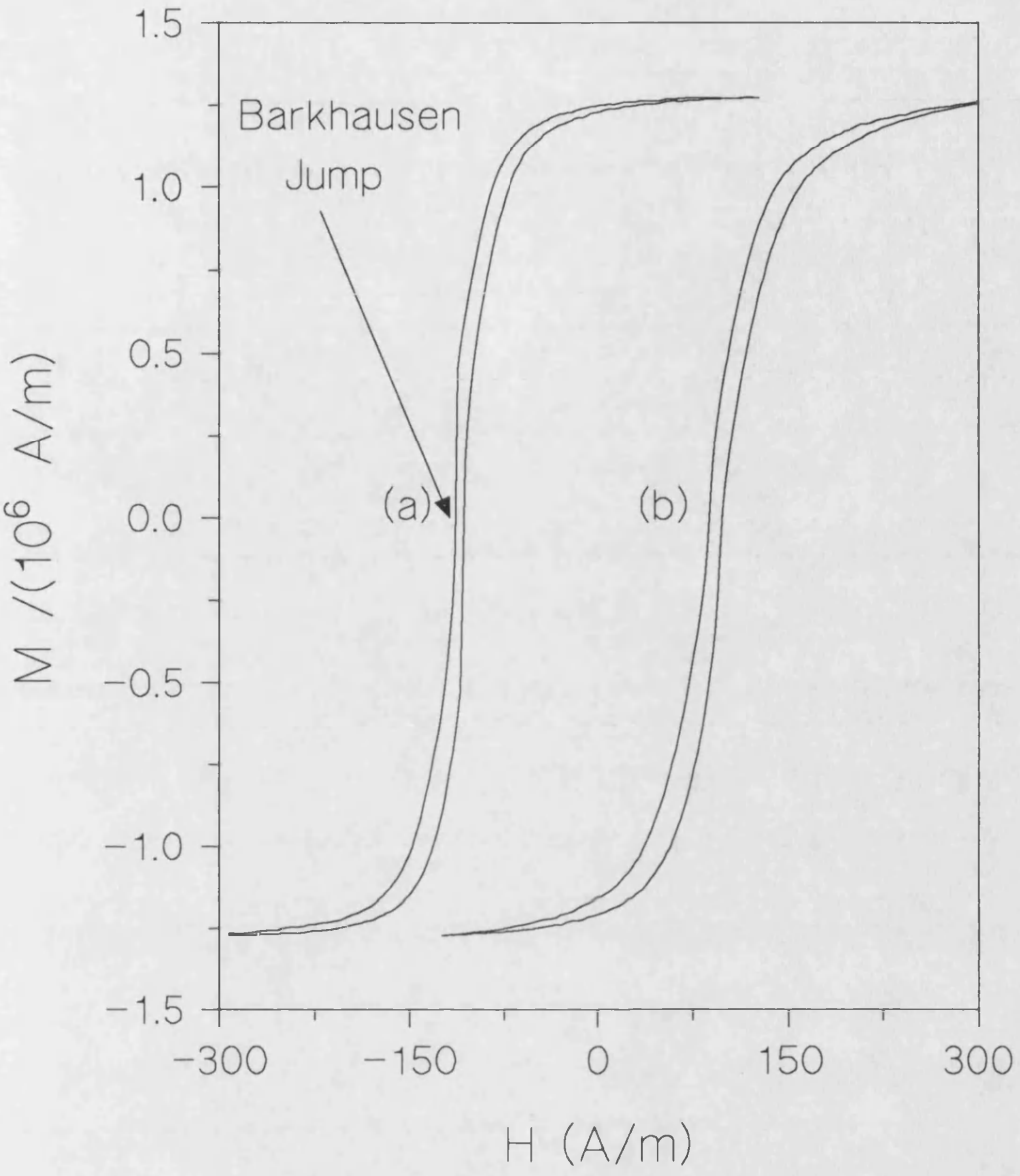

(B)

Figure 6.9: M-H loops of current field annealed FeSiB wires. Figure A: the wire was annealed at a) I=780 mA for 15 minutes, b) I=805 mA for 15 minutes, c) I=820 mA for 30 minutes, figure B: the wire, a) pre-annealed at I=820 mA for 15 minutes then annealed at I=720 mA for 15 minutes, b) pre-annealed at I=820 mA for 15 minutes then annealed at I=740 mA for 30 minutes. Loops were displaced along the H axis for illustration purpose only.

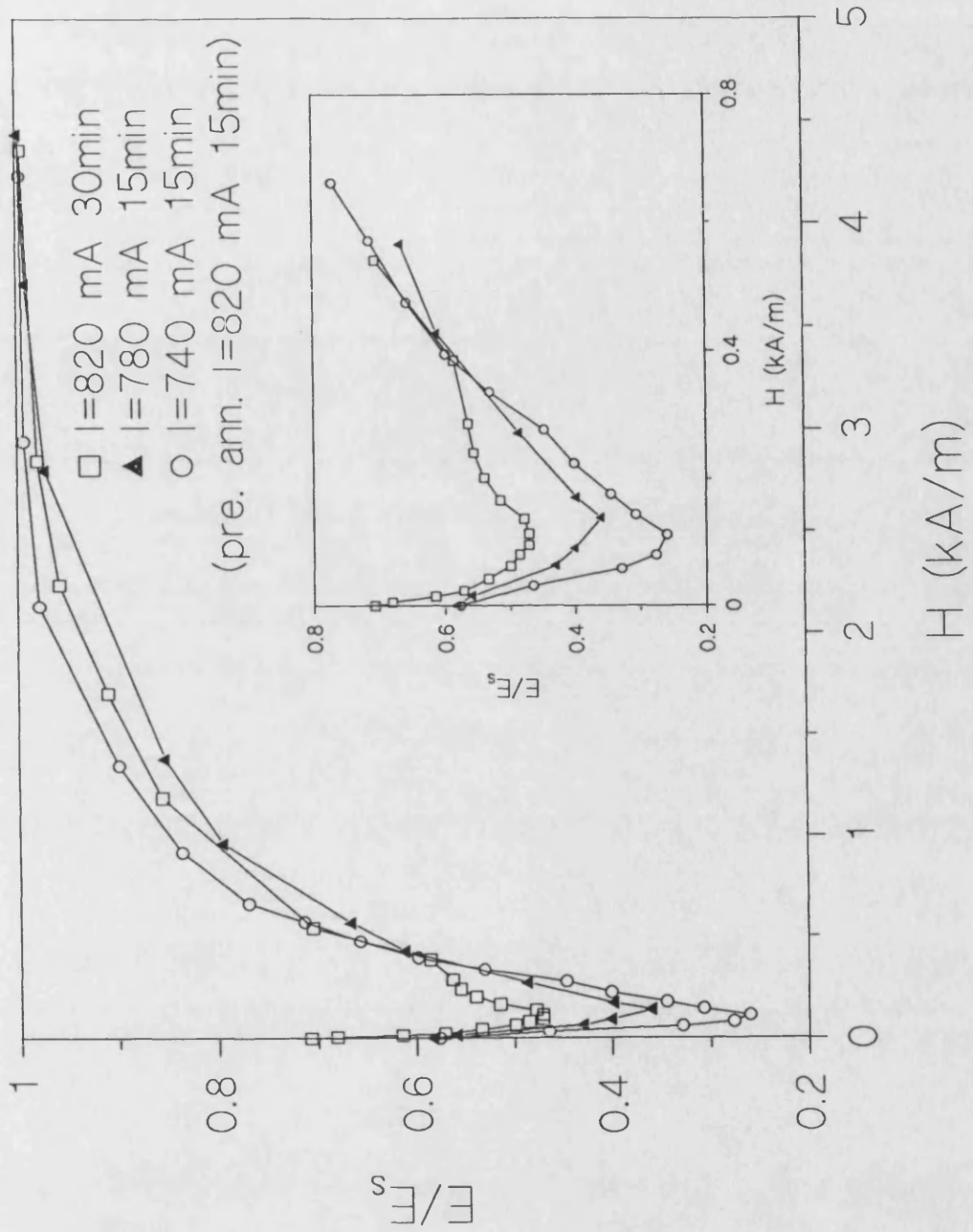

Figure 6.10: Normalised Young's modulus of current field annealed FeSiB wires, versus applied field. The data are connected with straight lines for guidance only.

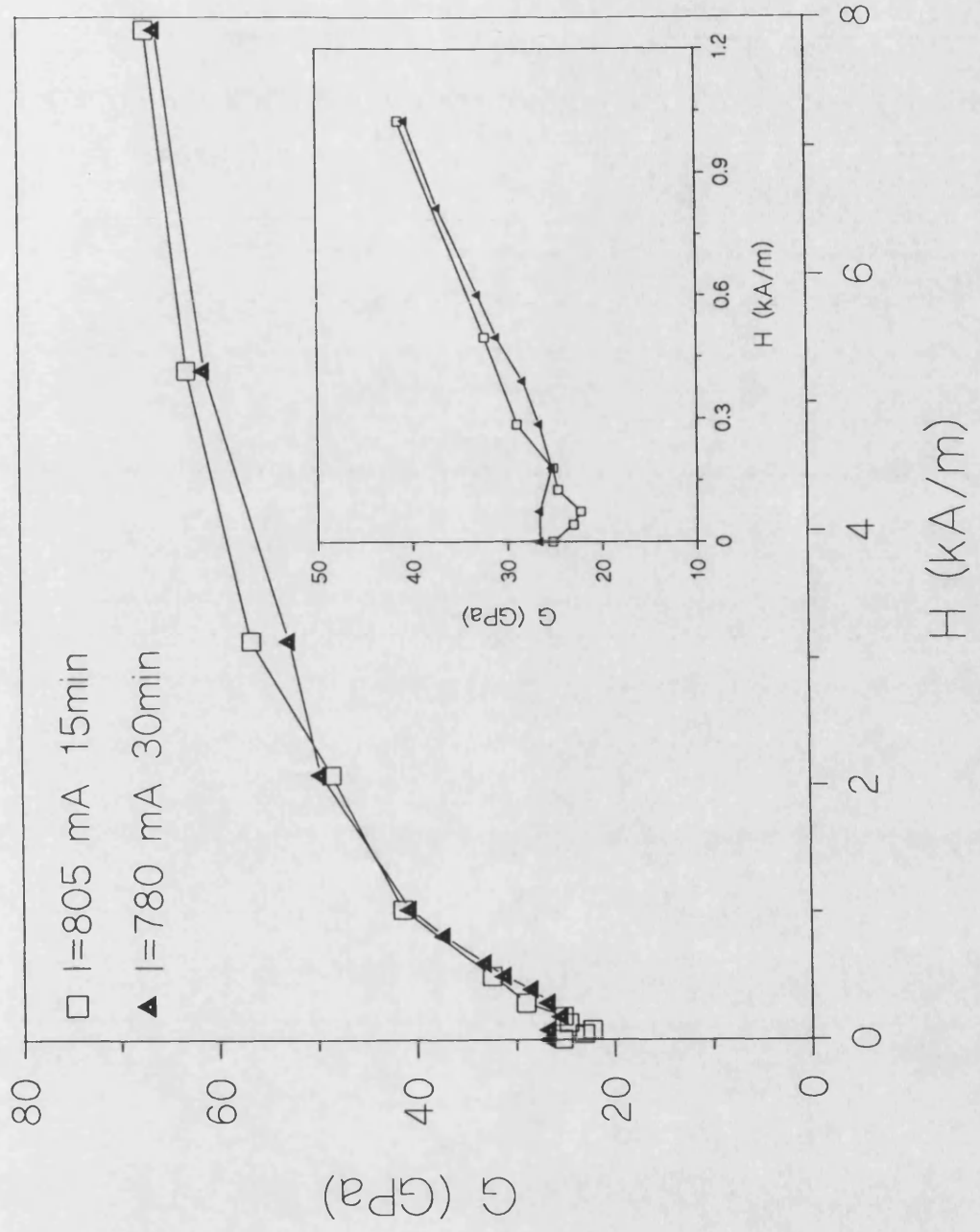

Figure 6.11: Shear modulus of current field annealed FeSiB wires against applied field. The data are connected with lines for guidance of the eye.

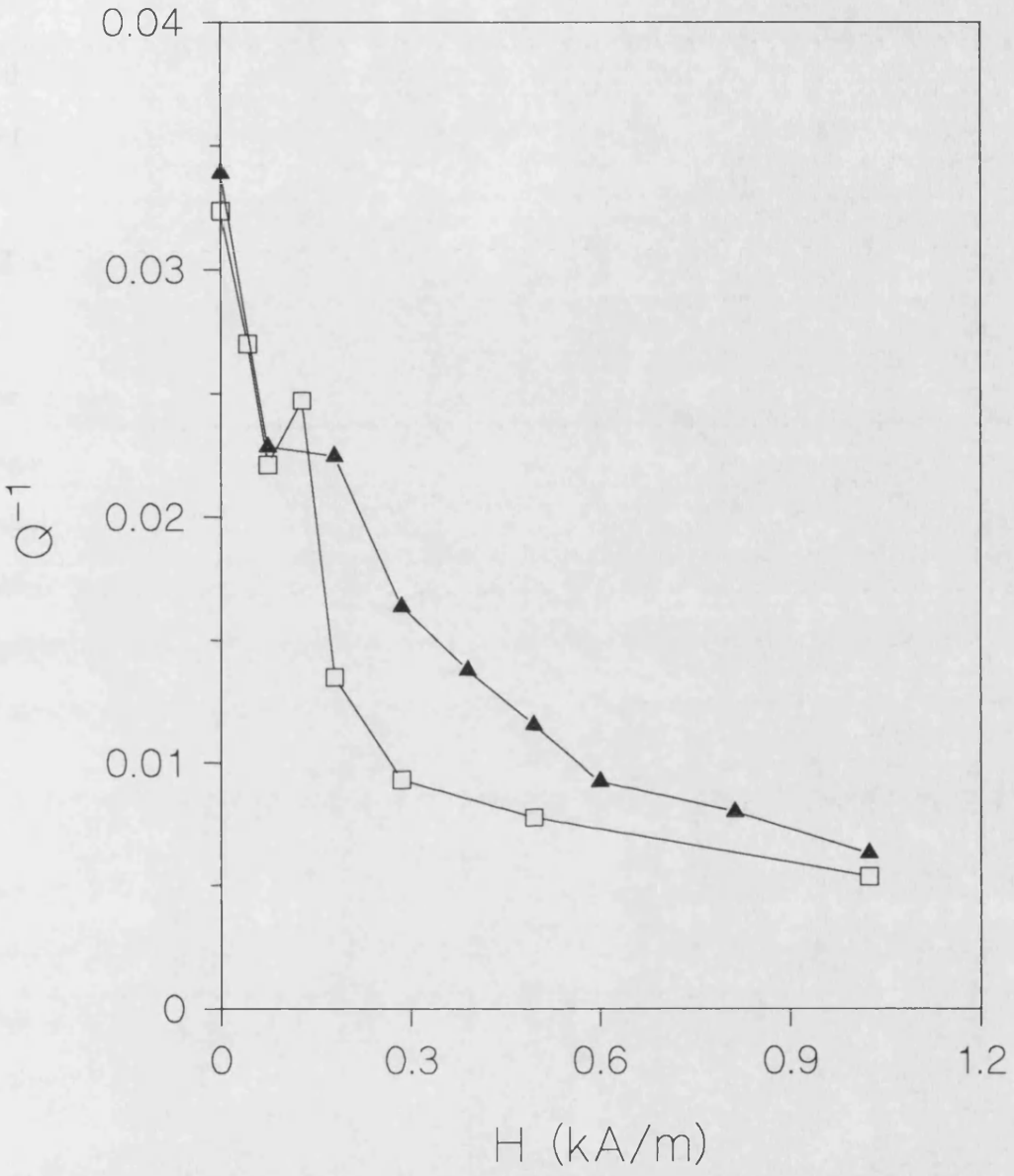

Figure 6.12: Damping of current field annealed FeSiB wires against applied field. The data are connected with lines for guidance of the eye. For figure caption see figure 6.11.

7 Conclusions

7.1 Introduction

In this chapter, conclusions are drawn from the results of this project and suggestions for future work are given. Each subject of the project is presented in a different section.

7.2 Magnetostriction

The saturation magnetostriction, λ_s, was obtained from the values of the engineering magnetostriction, λ_e, of the surface crystallised wire, where the magnetic moments align perpendicular to the wire axis. λ_s was calculated from the equation, $\lambda_s=(2/3)\lambda_e$. For the cold-drawn (CD) $Fe_{77.5}Si_{7.5}B_{15}$ 90μm wire, λ_s was measured to be 37 ppm, which is slightly higher than the value reported by others. Konno [1990] *et al* measured λ_s to be 35 ppm and Wun-Fogle *et al* [1989a] reported λ_s=30 ppm for the same wire.

It was observed that, with increasing annealing time, the peak strain decreased from 48 ppm to 36 ppm and then started to increase, reaching a maximum of 55 ppm. From the peak strain values, the initial angles of the magnetic moments were estimated. The CD 90μm wire annealed for 2 minutes at 480°C has two regions: an inner core, where the magnetic moments are aligned in the direction of wire axis, and an outer shell, where the magnetic moments are aligned at 70° to the wire axis. Further annealing reduced the peak strain and caused relief of the internal stresses, so the average initial orientation of the moments became smaller. After annealing for 60 minutes, the maximum peak strain of 55 ppm was obtained, showing that the moments were initially in a direction perpendicular to the wire axis.

Measurement of the magnetostriction of as-cast wire was found to be impossible using the fibre optic dilatometer, because as-cast wire is not straight and the surface of the wire is rough. This caused mechanical friction between the wire and the glass tube during measurement (figure 4.8).

7.3 Young's Modulus

In this study, the magnetic field dependence of Young's modulus for Fe-based wires has been presented. As-cast wire showed a very small field dependence. The E_{min}/E_s and E_o/E_s ratios for as-cast wire were found to be about 0.9 and 0.965, respectively.

Furnace annealing for short annealing times led to decreases in both E_{min} and E_o from the as-cast values. Also, the relative magnitude of the Barkhausen jump to saturation magnetisation, M_s, increased, showing that the domain structure has been rearranged. At longer annealing times, surface crystallisation occurred, leading to increases in the E_{min}/E_s and E_o/E_s ratios. For much longer annealing times, the amorphous bulk started to crystallise and the E_{min}/E_s ratio became very small.

The magnetic field dependence of Young's modulus, E(H), was explained using the Squire [1990] model. The model assumes that the magnitude of E/E_s (i.e. E_{min}/E_s) is determined by $\beta=\lambda_s^2E_s/K$. Therefore, the annealing temperature dependence of E_{min}/E_s is attributed to the anisotropy constant, K. When the wire was annealed, a large change in K was observed. K decreased from the as-cast value of ~2200Jm^{-3} to a minimum of ~100Jm^{-3}. When K was minimum, the largest E_{min}/E_s was obtained.

Using the Squire model, the initial angle of the magnetic moments were estimated from the E_o/E_s ratio. In as-cast wire the E_o/E_s ratio is about 0.965, showing that the magnetic

moments in the outer shell are not completely in the radial direction, or that the magnetic moments in the inner core are not completely aligned in the wire axis direction. The suggested domain structure for as-cast wire is not completely correct. Further work and domain imaging of the as-cast wires need to be done.

Annealing led first to an increase in the E_o/E_s ratio due to the relief of the internal stress, so magnetic moments were aligned mostly in the wire axis direction. With further annealing the E_o/E_s ratio started to decrease and the magnetic moments aligned between 45° and 60° to the wire axis. For longer annealing times, the E_o/E_s ratio increased and reached a maximum value of 0.9-0.95, showing that the magnetic moments aligned in a direction perpendicular to the wire axis.

X-ray measurements showed that, for longer annealing times, surface crystallisation occurred. This led to a compressive stress on the amorphous bulk of the wire and to the alignment of the magnetic moments in the circumferential direction in the amorphous bulk as, shown in figure 5.22.

Current annealing had a similar effect to furnace annealing on the field dependence of Young's modulus, but in the case of current annealing, the temperature was not uniform along the wire length, due to the variation of the wire diameter (and hence a variation in current density), so some irregularities were observed in the E(H) curves.

The FeSiB 125μm wires were field annealed in a direction transverse to the wire axis. The wires were heated by applying current. An easy axis in the annealing field direction was not created. This is attributed to two factors: 1) annealing field (although it was ~875 kA/m) was not high enough to overcome demagnetising effects, 2) the complete

relief of the internal stress was found to be impossible due to the onset of crystallisation. In current field annealed wires, an average initial orientation of the magnetic moments between 60° and 70° with respect to wire axis was obtained.

In conclusion, it was found that the surface crystallisation method is much better and easier than field annealing for inducing a transverse anisotropy in the Fe-based amorphous wires.

7.4 Shear Modulus

The field dependence of shear modulus, G(H), was similar to the behaviour of E(H). In particular, the G_{min}/G_s ratio behaved almost the same as E_{min}/E_s as a function of annealing temperature and time. The Squire model was used to explained the field dependence of G. But the model cannot fully explain the behaviour of G_o/G_s, because the model does not take account of the effect of the applied torque. The applied torque aligned the magnetic moments in a helical direction in the wire. So the initial easy axis was shifted, depending on the magnitude of the applied torque. This reorientation of moments changed the G_o value. It was also found that, in the G(H) curves, the sample saturated at much higher applied fields, due to the applied torque.

The general behaviour of the shear modulus as a function of applied tensile stress and torsional strain was similar to the behaviour of the shear modulus as a function of applied field. An approximate way of relating the tensile stress to the applied field is to define an effective stress field, $H_\sigma=3\lambda_s\sigma/2M_s\mu_o$, which is only valid for transversely field annealed ribbons. Torsional strain induced a more complicated stress distribution into the wire than tensile stress, so the analysis of the torsional strain dependence of the shear modulus needs more work.

7.5 Magnetomechanical Damping

Magnetic damping in ferromagnetic materials can be separated into three parts; macro-eddy currents, micro-eddy currents and magnetomechanical damping. The damping, Q^{-1}, measurements were performed at low frequencies (1-4 Hz). Therefore, the effect of the eddy currents losses were very small. The only significant damping in this frequency range was the magnetomechanical damping.

As-cast wire showed almost zero damping. When amorphous wire was annealed, the peak value of damping first increased then decreased with increasing annealing time. In a completely crystallised wire, the damping was measured to be zero. Temperature and annealing time dependence of the damping can be explained using the Smith and Birchak [1969] model, which assumes $Q^{-1} \propto \sigma_i^{-1}$. In the as-cast state, the wire has a large internal stress. So the damping for as-cast wire is zero. When the wire was annealed, the internal stress was reduced to as little as 2.3 MPa and the peak value of the damping was increased. Further annealing induced internal stresses, due to the onset of crystallisation, so the peak value of the damping decreased. However, the Smith and Birchak model cannot fully explain the effect of tensile stress and applied field on the damping versus torsional strain curves. The Degauque and Astie [1980] model was therefore used. The model assumes that the peak value of the damping is proportional to the number of 90° domain walls, S_1, which perform irreversible jumps. When the wire was annealed, S_1 was increased, so peak value of the damping increased. A low magnetic field or tensile stress put the domain walls in an energy position where torsional strain could trigger a greater number of irreversible 90° domain walls jumps, leading to an increase in the damping peak. At higher fields, the field itself became capable of triggering 90° domain wall jumps, so the number of irreversible jumps became less, leading to a decrease in the peak value of the damping.

The magnetomechanical damping behaviour of the amorphous wires cannot be fully explained by the existing models. All the models have been developed using the magnetomechanical hysteresis (torsional stress-torsional strain) loop. Direct measurement of the stress-strain loop for amorphous wires was attempted but, due to the very small wire diameter, was found to be impossible. More study is necessary in this part of the project to clarify fully the magnetomechanical damping behaviour of amorphous wires.

References

Anantharaman T., (Chapter 1-An overview) Metallic Glasses: Production, Properties and Applications (Ed. T. Anantharaman) (Trans. Tech., Netherlands, 1984).

Atkinson D., Private Communication (Bath University, 1992)

Balanzat E., J.T. Stanley, C. Mairy and J. Hillairet, "The nature of the atom species involved in the reversible relaxation of metallic glasses", *Acta Metall.*, **33(5)** (1985) 785.

Becker R. and M. Kornetzki "Some magnetoelastic torsion experiments", *Zeitschrift fur physik*, **88** (1934) 634.

Berry B.S. and W.C. Pritchet, "Vibrating reed internal friction apparatus for films and coils", *IBM J. Res. Develop.*, **19** (1975) 334.

Berry B.S. and W.C. Pritchet, " Magnetoelasticity and internal friction of an amorphous ferromagnetic alloy", *J. Appl. Phys.*, **47** (1976) 3295.

Berry B.S.,"Elastic and anelastic behaviour", Chapter 7 of "Metallic glasses", Papers presented at a seminar of the materials science division of the American Society for Metals, ASM, Metals Park, Ohio (1976).

Berry B.S. and W.C. Pritchet, "Influence of magnetomechanical pole-effect on the behaviour of thin vibrating reeds", *J. Appl. Phys.*, **50** (1979) 1630.

Bigot J, (Chapter 1-Preparation of metallic glasses and its influence on the properties)

Amorphous Metals (Ed. H. Matia and P.G. Zielinski) (World Scientific, Singapore, 1985).

Brown M.E., Introduction to Thermal Analysis (Chapman and Hall, New York, 1988).

Bozorth R.M., Ferromagnetism (Van Nostrand, New York, 1951).

Chen H.S., R.C. Sherwood, S. Jin, G.C. Chi, A. Inoue, T. Masumoto and H. Hagiwara, "Mechanical properties and magnetic behaviour of deformed metal glass wires", *J. Appl. Phys.*, **55** (1984) 1796.

Chikazumi S., Physics of Magnetism (Robert E. Krieger, Malabar, Florida, 1964).

Clark A.E. and M. Wun-Fogle, "A new method of magnetostrictivity and magnetostriction measurement", *IEEE Trans. on Mag.*, **25(5)** (1989) 3611.

Cochardt A., " The origin of Damping in High-Strength Ferromagnetic Alloys", *J. Appl. Mech. Trans. ASME*, **20** (1953) 196.

Cochardt A., " A method of measuring magnetostriction", *J. Appl. Phys.* **25(1)** (1954) 91.

Cochardt A., Magnetic Properties of Metals and Alloys (American Society for Metals, Cleveland, Ohio, 1959).

Cullity B.D., Introduction to Magnetic Materials (Addison-Wesley, Reading, MA, USA, 1972).

Degauque J. and B. Astie, "Influence of the different kinds of magnetic fields on the magnetomechanical damping of high purity iron", *Phys. Stat. Sol.*, **59** (1980) 805.

Duwez P., "Structure and Properties of alloys rapidly quenched from the liquid state", *Trans. Am. Soc. Metals*, **60**, (1967) 607.

Egami T., "Magnetic amorphous alloys: physics and technological applications", *Rep. Prog. Phys.*, **47** (1984) 1601.

Frank R.C. and J.W. Ferman, "Magnetomechanical damping in iron-silicon alloys", *J. Appl. Phys.*, **36** (1965) 2235.

Frank R.C., B.G. Johnson and C.W. Schroeder, "Crystal orientation and magnetomechanical damping of torsional vibrations", *J. Appl. Phys.*, **40(8)** (1969) 3189.

Gibbs M.R.J. and and P.T. Squire, (Chapter11-Applications) Sensors vol. 5; Magnetic sensors (Ed. R. Boll and K.J. Overshott) (VCH Publihers Inc., New York, 1989).

Gibbs M.R.J., I.E. Day, T.A. Lafford and P.T. Squire, "Domain wall mobility in amorphous wires", *J. Magn. Mag. Mater.*, **104-107** (1992) 327.

Gonzalez J., M. Vazquez, J.M. Barandiaran, V. Madurga and A. Hernando, "Different kinds of magnetic anisotropies induced by current annealing in metallic glasses", *J. Magn. Mag. Mater.*, **68** (1987) 151.

Gonzalez J., M. Vazquez, J.M. Barandiaran and A. Hernando, "Effects of current annealing on the hysteresis loop of amorphous alloys", *J. Phys. D: Appl. Phys.*, **21** (1988) 162.

Gonzalez J., M. Vazquez, J.M. Barandiaran, M.A. Illarramendi, A. Salazar and A. Hernando, "Magnetic anisotropies induced by current annealing and their dependence on annealing temperature", *Phys. Stat. Sol. (a)*, **113** (1989) 187.

Gonzalez J., J.M. Blanco, M. Vazquez, J.M. Barandiaran, G. Rivero and A. Hernando, "Influence of the applied stress on the magnetic properties of current annealed amorphous wires", *J. Appl. Phys.*, **70(10)** (1991) 6522.

Grazyk J.F., "Structure of argon sputtered Gd-Co and Gd-Co-Ho amorphous thin films", *J. Appl. Phys.*, **49** (1978) 1738.

Gutierrez J., J.M. Barandiaran and O.V. Nielsen, "Magnetoelastic properties of some Fe-rich Fe-Co-Si-B metallic glasses", *Phys. Stat. Sol.*, **111** (1989) 279.

Heck I., Magnetic materials and their applications, (Butterworths, London, 1967).

Hagiwara M., A. Inoue and T. Masumoto, "Mechanical properties of Fe-Si-B amorphous wires produced by in-rotating-water spinning method", *Metal. Trans. A*, **13A** (1982a) 373.

Hagiwara M., A. Inoue and T. Masumoto, "Production of amorphous Co-Si-B and Co-M-Si-B (M=group IV-VIII transition metals) wires by a method employing melt spinning into rotating water and some properties of the wires", *Mater. Sci. Eng.*, **54** (1982b) 197.

Hernando A. and J. Barandiaran, "The initial Matteucci effect", *J. Phys. D: Appl. Phys.*, **8** (1975) 833.

Hernando A. and J. Barandiaran, "Micromagnetics of twisted amorphous ribbons", *Phys. Rev. B*, **22(5)** (1980) 2445.

Hernando A., M. Vazquez and J.M. Barandiaran, "Metallic glasses and sensing applications", *J. Phys. E: Sci. Instrum.*, **21** (1988) 1129.

Hudson P.D., "Magnetic property control in ferromagnetic amorphous alloys", PhD thesis, University of Cambridge (1986).

Humphrey F.B., "Re-entrant flux reversal", *Satellite Symposium on Amorphous Magnetic Wires, INTERMAG'90*, London, April 1990.

Inoue A., M. Hagiwara and T. Masumoto, "Production of Fe-P-C amorphous wires by in-rotating-water spinning method and mechanical properties of the wires", *J. Mater. Sci.*, **17** (1982) 580.

Inoue A., N. Yano, H.S. Chen, M. Hagiwara and T. Masumoto, "Structural relaxation behaviour and mechanical properties of warm-drawn $Fe_{75}Si_{10}B_{15}$ and $Pd_{75}Ni_{8.5}Si_{16.5}$ amorphous wires", *Mater. Sci. Eng.*, **77** (1986) 45.

Inoue A., S. Furukawa, M. Hagiwara and T. Masumoto, "Preparation, mechanical strengths and thermal stability of Ni-S-B and Ni-P-B amorphous wires", *Metall. Trans. A*, **18A** (1987) 621.

Jagielinski T., "Flash annealing of amorphous alloys", *IEEE Trans. on Mag.*, **19(5)** (1983) 1925.

Jakubovics J.P., Magnetism and Magnetic Materials (The Institute of Metals, London, 1987).

Jiles D., Magnetism and Magnetic Materials (Chapman and Hall, London, 1991).

Kakuno K., T. Itabashi and T. Yamada, "Generation and propagation of magnetoelastic wave in amorphous wire", *IEEE Trnsl. J. Mag. Japan*, **TJMJ-2(8)** (1987) 759.

Kakuno K., H. Mochida, A. Shimodaira, S. Masuda and T. Yamada, "Effect of annealing on generation of magnetoelastic waves in amorphous wires and their application", *IEEE Transl. J. Mag. Japan*, **4(5)** (1989) 299.

Kakuno K. and S. Masuda, "Generation, propagation and detection of magnetoelastic waves in amorphous magnetic wires", *Satellite Symposium on Amorphous Magnetic Wires, INTERMAG'90*, London, April 1990.

Kawamura H., J. Yamasaki and K. Mohri, "Reinforced large Barkhausen and Matteucci effects magnetoelastic waves in cold-drawn and then torsion annealed amorphous wires", *IEEE Transl. J. Mag. Japan*, **4(6)** (1989) 368.

Kawamura H., K. Mohri, J. Yamasaki and I. Ogasawara, "Large Barkhausen effect and Matteucci effect in cold-drawn and torsion annealed amorphous magnetostrictive wires", *IEEE Transl. J. Magn. Japan*, **3(7)** (1988) 609.

Kilby C.F., P.T. Squire and S.N.M. Willcock, "Analysis and performance of a shear-wave magnetometer", (To be published in Sensors and Actuators 1993).

Kimura K., M. Kanoh, K. Kawashima, K. Mohri, M. Takagi and L.V. Panina, "Data tablet utilizing Matteucci effect of amorphous magnetic wire matrix", *IEEE Trans. on Magn.*, **27** (1991) 4861.

Kinoshita K., R. Malmhall, K. Mohri, F.B. Humphrey and J. Yamasaki, "Influence of applied tensile and compressive stress on large Barkhausen and Matteucci effects in amorphous wires", *IEEE Trans. on Magn.*, **Mag-22(5)** (1986) 445.

Kinoshita F., "Estimation of the radius of the inner core and the angle of easy axis of its magnetisation for as-prepared amorphous magnetostrictive wire", *IEEE Trans. on Magn.*, **25(1)** (1990) 1786.

Kiss S., L. Malkinski, G. Posgay and L. Pogany, "Influence of tensile stresses on magnetic field dependences of internal friction and of shear modulus of the Fe-Si-B metallic glass", *Acta Phys. Pol.*, **A76(1)** (1989) 157.

Kobelev N.P. and Y.M. Soifer, "Magnetic field induced changes in the damping and velocity of acoustic waves in amorphous ferromagnetic metals", *Sov. Phys. Solid State*, **28(2)** (1986) 236.

Kobelev N.P., Y.M. Soifer, V.G. Shteinber and Y.B. Levin, "Giant ΔE effect and magnetomechanical damping in amorphous ferromagnetic ribbons", *Phys. Stat. Sol. (a)*, **102** (1987) 773.

Konno Y. and K. Mohri, "Magnetostriction measurements for amorphous wires", *IEEE Trans. on Magn.*, **25(5)** (1989) 3623.

Konno Y., K. Mohri and S. Uchiyama, "Magnetostriction measurements for amorphous wires", *IEEE Transl. J. on Magn. Japan*, **5(5)** (1990) 402.

Kornetzki M., "The damping of mechanical vibrations due to magnetic hysteresis", *Zeitschrift fur Physik*, **121** (1943) 363.

Letcher M., G.A. Jones, D.G. Lord, M. Wun-Fogle and H.T. Savage, "Domain structure of as-cast and annealed FeSiB amorphous wires", *J. Appl. Phys.*, **69(8)** (1991) 5331.

Livingston J.D., "Magnetomechanical properties of amorphous metals", *Phys. Stat. Sol. (a)*, **70** (1982) 591.

Liu J., R. Malmhall, L. Arnberg and S.J. Savage, "Theoretical analysis of residual stress effect on the magnetostrictive properties of amorphous wires", *J. Appl. Phys*, **67** (1990) 4238.

Lu J., J.T. Wang, B.Z. Ding and S.L. Li, "Cooling rate effect on anelastic properties and Young's of FeSiB alloys", *Scripta Metall.*, **24** (1990) 1879.

Luborsky F.E., "Magnetic annealing of amorphous alloys", *IEEE Trans. on Mag.*, **MAG-11(6)** (1975) 1644.

Luborsky F.E., "Magnetic anneal anisotropy in amorphous alloys", *IEEE Trans. on Mag.*, **MAG-13(2)** (1977) 953.

Luborsky F.E. (Ed.), Amorphous Metallic Alloys, (Butterworths, London) (1983).

Madurga V. and A. Hernando, "Radial stress distribution generated during rapid solidification of amorphous wires", *J. Phys. Condensed Matter*, **2** (1990a) 2127.

Madurga V., J.L. Costa, A. Inoue and K.V. Rao, "Magnetostrictive influence on the bistability of amorphous wires", *J. Appl. Phys.*, **68(3)** (1990b) 1164.

Malmhall R., K. Mohri, F.B. Humphrey, T. Manabe, H. Kawamura, J. Yamasaki and I. Ogasawara, "Bistable magnetisation reversal in 50μm diameter annealed cold-drawn amorphous wires", *IEEE Trans. on Mag.*, **Mag-23(5)** (1987) 3242.

Manabe T., H. Kawamura, K. Mohri, J. Yamasaki, R. Malmhall and I. Ogasawara, "Large Barkhausen effect and Matteucci effect in cold-drawn amorphous magnetostrictive wires", *IEEE Transl. J. Magn. Japan*, **3(3)** (1988) 288.

Masumoto T., I. Ohnaka and M. Hagiwara, "Production of Pd-Cu-Si amorphous wires by melt spinning method using rotating water", *Scripta Metall.*, **15** (1981) 293.

Mitra A. and M. Vazquez, "Stress and annealing dependent magnetic properties of amorphous wires", *to appear J. Phys D: Appl. Phys.*, **23(2)** (1990) 228.

Mitra A., A. Hernando, G. Rivero and M. Vazquez, "Susceptibility and Coercivity of amorphous wires", *J. Magn. Mag. Mater.*, **83** (1990a) 339.

Mitra A. and M. Vazquez, "Measurement of the saturation magnetostriction constant of amorphous wire", *J. Appl. Phys.*, **67(9)** (1990b) 4986.

Mitra A., K. Mandal and S.K. Ghatak, "DC magnetic properties of as-quenched and flash annealed amorphous magnetic wires", *J. Magn. Mag. Mater.*, **110** (1992) 135.

Mohri K., "Review on recent advances in the field of amorphous-metal sensors and transducers", *IEEE Trans. on Mag.*, **MAG-20(5)** (1984a) 942.

Mohri K., F.B. Humphrey, J. Yamasaki and K. Okamura, "Jitter-less pulse generator elements using amorphous bistable wires", *IEEE Trans. on Mag.*, **MAG-20(5)** (1984b) 1409.

Mohri K., F.B. Humphrey, J. Yamasaki and F. Kinoshita, "Large Barkhausen effect in amorphous magnetostrictive wires for pulse generator elements", *IEEE Trans. Mag.*, **MAG-21(5)** (1985) 2017.

Mohri K., "Applications using re-entrant flux reversal and Matteucci effect", *Satellite Symposium on Amorphous Magnetic Wires, INTERMAG'90*, London, April 1990.

Moorjani K. and J.M.D. Coey, (Chapter ?- title) Metallic Glasses (Ed. S.P. Wolsky and A.W. Czanderna) (Elsevier, Amsterdam, 1984).

Morito N., "Internal friction study on structural relaxation of a glassy metal $Fe_{32}Ni_{36}Cr_{14}P_{12}B_6$", *Mater. Sci. Eng.*, **60** (1983) 261.

Morito N. and T. Egami " Correlation of shear modulus and internal friction in the reversible structural relaxation of glassy metals", *J. Non-Crystalline Solids*, **61-62** (1984a) 973.

Morito N. and T. Egami "Internal friction and reversible structural relaxation in the metallic glass $Fe_{32}Ni_{36}Cr_{14}P_{12}B_6$", *Acta Metall.*, **32** (1984b) 603.

Motogi S., "A phenomenological theory of hysteresis damping of vibrations in ferromagnetic materials", *Int. J. Eng. Sci.*, **20(7)** (1982) 823.

Newman F.H. and V.H.L. Searle, The General Properties of Matter (Edward Arnold Ltd., London, 1957).

Nowick A.S. and B.S. Berry, Anelastic Relaxation in Crystalline Solids, (Academic press, New York, 1972).

O'Dell T.H., "Measurement of magnetomechanical coupling factor in amorphous ribbons", *Phys. Stat. Sol. (a)*, **74** (1982) 565.

Ogasawara I., "Magnetic properties of amorphous metal wires", *IEEE Transl. J. on Magn. Japan*, **TJMJ-2(8)** (1987) 756.

O'Handley R.C., "Physics of ferromagnetic amorphous alloys", *J. Appl. Phys.* **62(10)** (1987) R15.

Ok H.M. and A.H. Morrish, "Surface crystallisation and Magnetic anisotropy in amorphous $Fe_{40}Ni_{38}Mo_4B_{18}$ ribbons", *J. Appl. Phys.*, **52** (1981) 1835.

Overshott K.J., "Rapidly cooled materials", *Inst. Phys. Conf. Ser.*, **No:89, Session 6,** 1987, 189.

Peters R.D., "Linear rotary differential capacitance transducer", *Rev. Sci. Instrum.*, **60** (1989) 2789.

Savage H.T., "Application using magnetostriction", *Satellite Symposium on Amorphous Magnetic Wires, INTERMAG'90*, London, April 1990.

Sheard S.M., "Metallic glasses for pulse compression", PhD thesis, University of Bath (1989).

Smith C.J., The General Properties of Matter (Edward Arnold Ltd., Belfast, 1960).

Smith G.W. and J.R. Birchak, "Effect of internal stress distribution on magnetomechanical damping", *J. Appl. Phys.*, **39** (1968) 2311.

Smith G.W. and J.R. Birchak, "Internal stress distribution theory of magnetomechanical hysteresis an extension to include effects of magnetic field and applied field", *J. Appl. Phys.*, **40** (1969) 5174.

Smith G.W. and J.R. Birchak, "Application of internal stress distribution theory to ΔE effect, initial permeability and temperature dependent magnetomechanical damping", *J. Appl. Phys.*, **41** (1970) 3315.

Smith G.W. and J.R. Birchak, "Magnetomechanical damping and magnetic properties of iron alloys", *J. Appl. Phys.*, **43** (1972) 1238.

Spano M.L., K.B. Hathaway and H.T. Savage, "Magnetostriction and magnetic anisotropy of field annealed metglass 2605 alloys via dc M-H loop measurements under stress", *J. Appl. Phys.*, **53** (1982) 2667.

Squire P.T. and M.R.J. Gibbs, "Fibre-optic dilatometer for measuring magnetostriction in ribbon samples", *J. Phys. E*, **20** (1987) 499.

Squire P.T., S.M. Sheard, C.H. Carter and M.R.J. Gibbs, "Digital M-H plotter for low-coercivity metallic glasses", *J. Phys E*, **21** (1988) 1167.

Squire P.T., "Phenomenological model for magnetization, magnetostriction and ΔE effect in field-annealed amorphous ribbons", *J. Magn. Mag. Mater.*, **87** (1990) 299.

Squire P.T. and M.R.J. Gibbs, "Shear-wave magnetometry using metallic glass ribbon", *Electron. Lett.*, **23** (1987) 147.

Sumner G. and K.M. Entwistle, " The stress-dependent damping capacity of ferromagnetic metals", *J. Iron and Steel Institute*, **192** (1959) 238.

Thomas A.P., "Magnetostriction in transition metal-metalloid metallic glasses", PhD Thesis, University of Bath (1991).

Thomas A.P., Private Communication (Bath University, 1992)

Vazquez M., J. Gonzalez and A. Hernando, "Induced magnetic anisotropy and change of the magnetostriction by current annealing in Co-based amorphous alloys", *J. Mag. Mag. Mater.*, **53** (1986) 323.

Velazquez, M. Vazquez, A. Hernando, H.T. Savage and M. Wun-Fogle, "Magnetoelastic anisotropy in amorphous wires due to quenching" *J. Appl. Phys.*, **70(10)** (1991) 6525.

Wun-Fogle M., H.T. Savage, L.T. Kabacoff, K.B. Hathaway, J.M. Merchant and B. Beihoff, "Magnetoelastic effects in amorphous wires and amorphous ribbons with non-magnetic thin film coatings", *J. Appl. Phys.*, **64(10)** (1988) 540.

Wun-Fogle M., H.T. Savage, L.T. Kabacoff, M.L. Spano and J.R. Cullen, "Effect of applied stress on the magnetisation of amorphous magnetoelastic wires", *IEEE Trans. on Mag.*, **25(5)** (1989a) 3617.

Wun-Fogle M., H.T. Savage and M.L. Spano, "Enhancement of magnetostrictive effects for sensor applications", *J. Mater. Eng.*, **11** (1989b) 103.

Yamasaki J., H. Soeda, T. Manabe and K. Mohri, "Compositional variation of magnetic properties in amorphous wires prepared by in-rotating-water spinning method", *IEEE Transl. J. on Magn. in Japan*, **TJMJ-1(2)** (1985) 233.

Yamasaki J., F.B. Humphrey, K. Mohri, H. Kawamura, H. Takamure and R. Malmhall, "Large Barkhausen discontinuities in Co-based amorphous wires with negative magnetostriction", *J. Appl. Phys.*, **63** (1988) 3949.

Yamasaki J., "Magnetic properties of Fe-Co based amorphous wires", *Satellite Symposium on Amorphous Magnetic Wires, INTERMAG'90*, London, April 1990.

Yamasaki J., Y. Ohkubo and F.B. Humphrey, "Magnetostriction measurement of amorphous wires by means of small-angle magnetisation rotation", *J. Appl. Phys.*, **67(9)** (1990) 5472.

Yoshida I., T. Sugai, S. Tani, M. Motegi, K. Minamida and H. Hayakawa, "Automation of internal friction measurement apparatus of inverted torsion pendulum type", *J. Phys. E.: Sci. Instrum.*, **14** (1981) 1201.

Appendix A-Torque on the Capacitor

The rotor plate in figure 4.20 is rotated by applying about 1000V to one of the pick-up plates. One of the driving plates is connected to ground. Therefore, an energy, U, will be induced between the plates, given by:

$$U = \frac{1}{2}CV^2 \tag{A.1}$$

where C is the capacitance between the plates and V is the applied voltage. The capacitance is:

$$C = \varepsilon_o \frac{A}{d}, \quad A = \frac{\pi r^2}{4} \tag{A2}$$

A is the area of the pick-up plate, ε_o is the permittivity of free space ($\varepsilon_o = 8.85 \times 10^{-12}$ F/m), r is the radius of the plate (r=3 cm) and d is the distance between the plates (d=1.5mm). C is therefore about 4pF. When a voltage is applied, there will be a torque which rotates the rotor plate. The torque is given by:

$$\Gamma = \frac{dE}{d\theta} = \frac{1}{2}V^2 \frac{dC}{d\theta} \tag{A3}$$

$$\frac{dC}{d\theta} \sim \frac{4pF}{1.57rad} = 2.5pF/rad$$

The torque is calculated from equation A3 for V=1000V to be $\Gamma = 1.25 \times 10^{-6}$ Nm. The shear modulus of the wire is:

$$G = \frac{\sigma}{\varepsilon}, \quad \sigma = \frac{a\phi}{l} \tag{A4}$$

where ϕ is the angular displacement, l is the length of the wire, a is the radius of the wire and σ is the shear stress. The torque as a function of the stress is given by:

$$d\Gamma = \sigma a \, dA, \quad \Gamma = \frac{\pi \phi G a^4}{2l} \tag{A5}$$

If we take G=60GPa, l=20cm and a=61μm, the angular displacement will be approximately 0.2 rad. This is a suitable initial angular displacement and it can be increased if required by using a series voltage pulses.

To apply 1000V to one of the pick-up plates a circuit was designed as shown in figure A. S_1 was used to apply 1000V, S_4 was used to discharge the pick-up plate and S_2 and S_3 were used to protect the differential amplifier and to bring the circuit to the operating position.

In the switching process, four steps are used:

1) Close all the switches to connect all of them to earth.

2) Keep close S_1 and open the other switches to apply high voltage.

3) Open S_1, S_2 and S_3 and close S_4 to discharge the pick-up plate.

4) Open S_1 and S_4 and close S_2 and S_3 to bring the circuit back to the operating position.

After the third step the rotor plate starts to rotate and, at step 4, the output of the transducer system goes directly to the differential amplifier. In this position, data are collected by a computer.

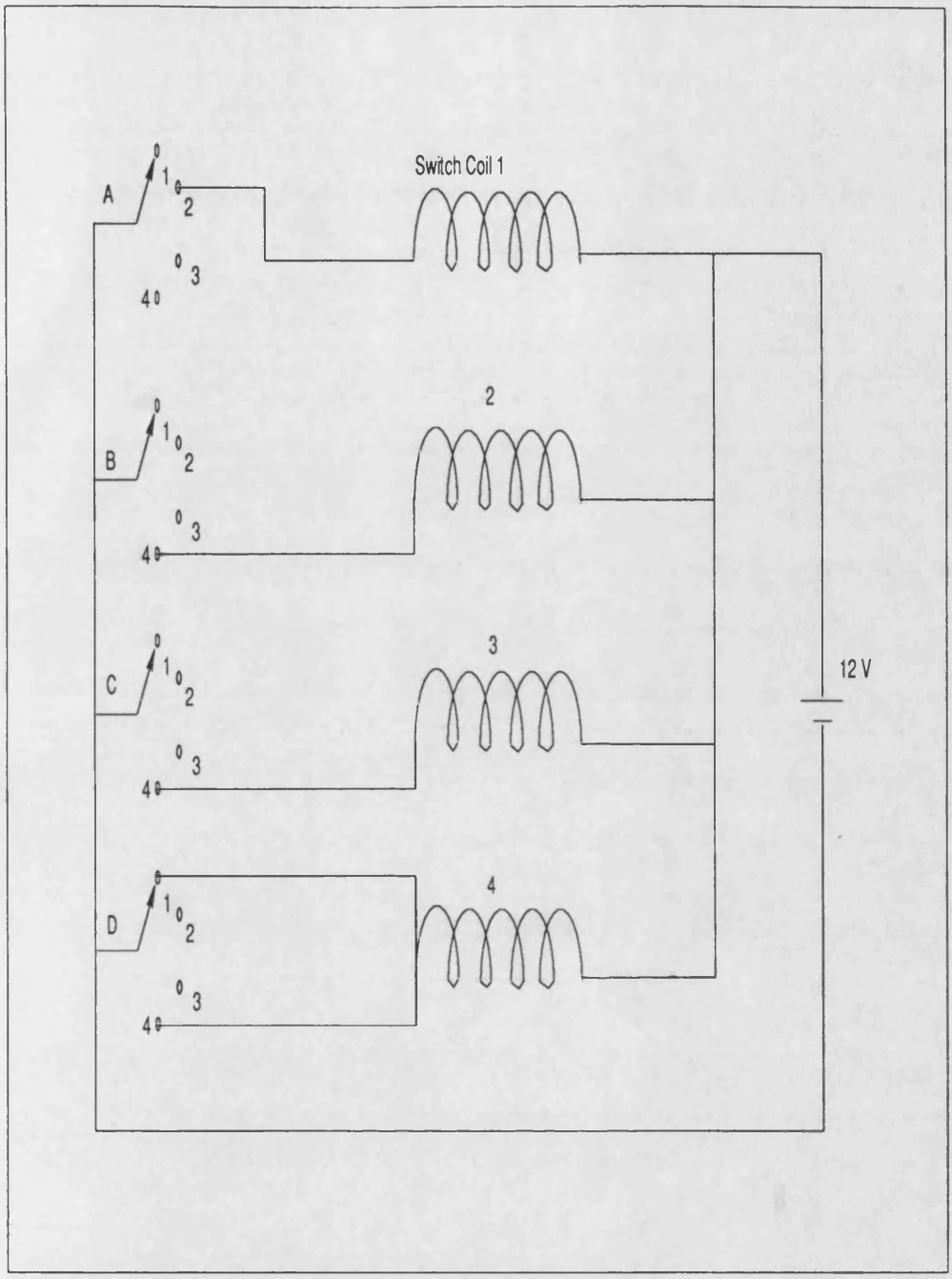

Figure A: Switch circuit to apply high voltage to the one of the pick-up plates.

Reprinted from

journal of magnetism and magnetic materials

Journal of Magnetism and Magnetic Materials 132 (1994) 10–21

Review Article

Amorphous wires and their applications

P.T. Squire [a,*], D. Atkinson [a], M.R.J. Gibbs [a,1], S. Atalay [b]

[a] *School of Physics, University of Bath, Bath BA2 7AY, UK*
[b] *Inönü Universitesi, Fen-Edebiyat Fakultesi, Fizik Bölömü, Malatya, Turkey*

(Received 5 October 1993; in revised form 4 December 1993)

N·H

ELSEVIER

JOURNAL OF MAGNETISM AND MAGNETIC MATERIALS

Journal of Magnetism and Magnetic Materials (ISSN 0304-8853). For 1994, Volumes 126–137 are scheduled for publication. Subscription prices are available upon request from the publisher. Subscriptions are accepted on a prepaid basis only and are entered on a calendar year basis. Issues are sent by surface mail except to the following countries where air delivery via SAL is ensured: Argentina, Australia, Brazil, Canada, China, Hong Kong, India, Israel, Japan, Malaysia, Mexico, New Zealand, Pakistan, Singapore, South Africa, South Korea, Taiwan, Thailand, USA. For all other countries airmail rates are available upon request. Please address all your requests regarding orders and subscription queries to: Elsevier Science, Journal Department, P.O. Box 211, 1000 AE Amsterdam, The Netherlands. Telephone: +31-20-5803642, Telefax: +31-20-5803598. Claims for issues not received should be made within six months of our publication (mailing) date.

US mailing notice – The Journal of Magnetism and Magnetic Materials is published monthly except semimonthly in January, March, May, July, September and November (total 18 issues) by Elsevier Science, Molenwerf 1, P.O. Box 211, 1000 AE Amsterdam, The Netherlands. The annual subscription price is US$ 3347 (valid in North, Central and South America only), including air speed delivery. Application to mail at second class postage rate is pending at Jamaica, NY 11431.

US POSTMASTERS: Send address changes to Journal of Magnetism and Magnetic Materials, Publications Expediting, Inc., 200 Meacham Avenue, Elmont, NY 11003. Airfreight and mailing in the USA by Publications Expediting.

Cover design by Jonathan Eric Freeman (d) **Printed in The Netherlands**

ELSEVIER

Journal of Magnetism and Magnetic Materials 132 (1994) 10–21

journal of magnetism and magnetic materials

Review Article

Amorphous wires and their applications

P.T. Squire [a,*], D. Atkinson [a], M.R.J. Gibbs [a,1], S. Atalay [b]

[a] *School of Physics, University of Bath, Bath BA2 7AY, UK*
[b] *Inönü Universitesi, Fen-Edebiyat Fakultesi, Fizik Bölömü, Malatya, Turkey*

(Received 5 October 1993; in revised form 4 December 1993)

Abstract

The basic physical and magnetic properties of Fe and Co based amorphous wires are summarised, together with post-production treatments used to modify the properties of the as-quenched alloys. The current status of the core–shell domain model is reviewed in the light of recent studies of the internal stress and easy axis distributions. Finally, a survey of recently proposed applications is presented.

1. Introduction

Amorphous ferromagnetic alloy wires produced by in-rotating-water quenching have been available for more than a decade. The magnetic properties of amorphous wires, with a wide range of compositions, have been investigated with a view to understanding both the basic behaviour and the potential for application [1].

It is generally accepted that the basic behaviour of the as-cast wires is associated with the coupling between the magnetostriction and the stresses induced during the rapid quenching process. On the basis of magnetization measurements, surface domain imaging, and domain wall propagation experiments, models of domain structure have been proposed for both negative and positive magnetostriction compositions [2]. However, an increasing volume of evidence clearly indicates that such models, in particular for the positive magnetostriction composition, are oversimplified and should be refined.

A considerable number of potential applications utilizing the magnetic properties of amorphous wires have been reported. Such applications have been based primarily upon what can be termed *pulse effects*, which are associated with the rapid switching of magnetization, while other applications are based on *magnetomechanical effects*.

The magnetic properties of amorphous wires were the subject of a special symposium in 1990 [1] which provided a review of the field up to that time; unfortunately the proceedings were not published. This paper presents a review of recent developments in the study of the amorphous wires. It summarises the developments in sample treatment and measurements, brings together the theoretical work describing the internal stresses associated with quenching, presents refinements to the suggested domain structure and describes the developments in device applications.

* Corresponding author.
[1] Now at the University of Sheffield, UK.

SSDI 0304-8853(94)00018-M

2. Basic physical properties

The compositions of amorphous wires with magnetically interesting properties are of the form $(Fe, Co, Ni)_x Si_y B_z$, where the transition metal content is in the range 70–80% and the Si and B contents are in the range 10–20% [3]. Occasionally additional elements, such as Cr, may be added to improve corrosion resistance. There are three families of composition that will be considered in this review: Fe-based, having large positive magnetostriction, Co-based, having small negative magnetostriction, and alloys having about 6% of the Co replaced by Fe to produce nearly zero magnetostriction. Magnetostriction plays a decisive rôle in determining the magnetic and magnetomechanical behaviour of amorphous wires, because the dominant anisotropy is the result of residual stress and magnetostriction.

Some of the basic physical properties of selected alloys are shown in Table 1. Caution is advised in using published magnetostriction data, because the values are rather sensitive to the exact composition, and to the casting conditions; published data also vary. The data in Table 1 refer to the as-cast, or as-quenched state; some variation in all parameters can be expected after annealing, especially in the values of Young's modulus E and longitudinal acoustic wave velocity v_L, which can develop strong field dependence after annealing.

3. Magnetic characteristics

Much of the interest in amorphous wires has been stimulated by their remarkable magnetic properties. In this section we summarise the main magnetic features of amorphous wires, which may be broadly classified as pulse effects and magnetomechanical effects.

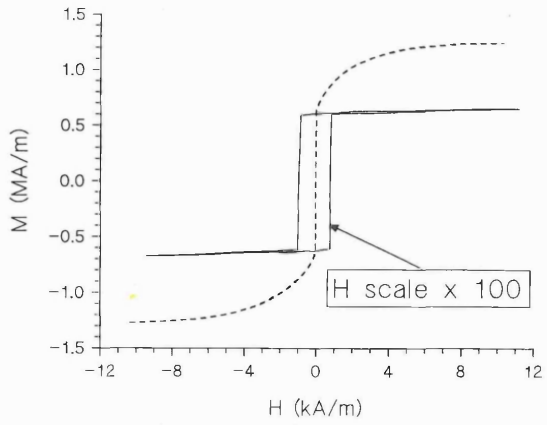

Fig. 1. Large Barkhausen effect in as-cast $Fe_{77.5}Si_{7.5}B_{15}$ wire. Solid line is low-field $M-H$ loop showing switching field; broken line is high-field $M-H$ loop showing approach to saturation. Loop time = 30 s.

3.1. Pulse effects

The most striking feature of the hysteresis loop of many amorphous wires is the *Large Barkhausen Effect* (LBE), that shows as a vertical step in the hysteresis loop (Fig. 1). The magnitude of this step is typically half of the full magnetization change, expressed as a remanence ratio $M_r/M_s \approx 0.5$ [6]. It is observed in many compositions in the as-quenched state, whenever the magnetostriction is large enough, coupled with the casting stress, to produce the characteristic 'core–shell' domain structure (Fig. 2). The low-field loop is essentially bistable in character; the exact nature of the bistability depends on the alloy and the internal stress [6]. The field at

Table 1
Basic physical properties of representative amorphous wires in the as-cast state [3–5] (figures in brackets are interpolated from data in [3])

Composition	ρ (Mg/m^3)	E (GN/m^3)	v_L (km/s)	$\mu_0 M_S$ (T)	$10^6\lambda_S$
$Fe_{77.5}Si_{10}B_{12.5}$	7.21	164	4.77	1.6	35
$Co_{72.5}Si_{12.5}B_{15}$	7.74	174	4.73	0.64	−5.6
$(Fe_{0.06}Co_{0.94})_{72.5}Si_{12.5}B_{15}$	(7.70)	(173)	4.74	0.8	−0.08

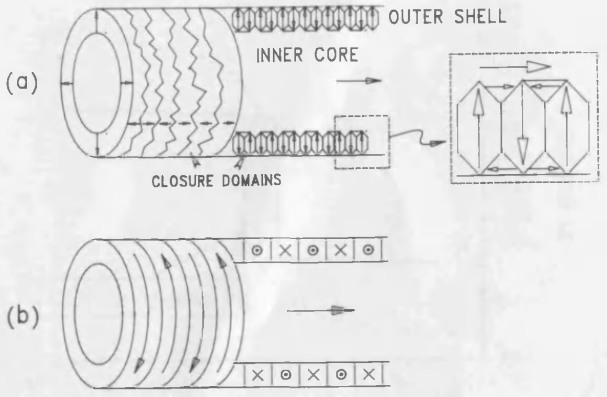

Fig. 2. Simplified diagram of the core–shell domain model for (a) positive magnetostriction, and (b) negative magnetostriction (after [6]).

which the core switches from one stable state to the other is called the *switching field*, and is usually denoted by H^*.

The LBE is generally explained in terms of the switching of the axially magnetized core by the propagation of a single 180° domain wall along the wire. The propagation of this domain wall can be directly observed by positioning one or more short sensing coils along the wire. The shape of the resulting voltage pulses, and their time difference can be used to infer the shape and size of the wall and its speed [7–10]. A related effect is the generation of a voltage across the ends of a twisted wire when it is placed in an alternating magnetic field (Fig. 3a); this is known as the *Matteucci Effect* [11]. The magnitude of this in amorphous wires can amount to several tens of mV, making it potentially useful for sensor applications. The normal arrangement for observing the Matteucci effect is with the applied field produced by an external coil along the wire axis. An alternative arrangement, requiring no coils [6], uses an alternating current along the wire to produce a circumferential or helical field at the wire surface. If this is sufficiently large it can induce core switching, resulting in a Matteucci voltage; this can be distinguished from the low-frequency driving voltage by high-pass filtering (Fig. 3b). A third arrangement [6], (Fig. 3c) uses an alternating field perpendicular to the wire axis to produce local core switching. This results in a Matteucci voltage at twice the exciting frequency,

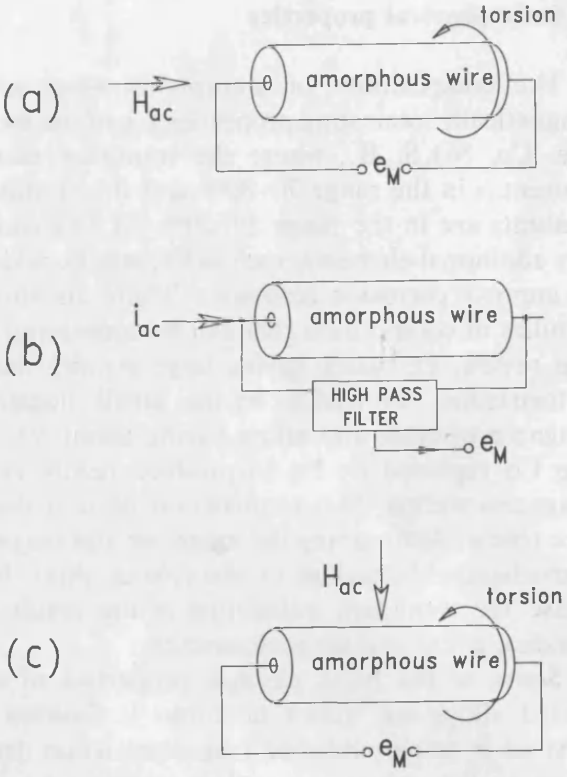

Fig. 3. Matteucci effects in amorphous wires. (a) Normal arrangement with externally applied axial alternating field. (b) Coil-free arrangement [6]. (c) Perpendicular effect [6].

which has been used to demonstrate a data tablet [11].

The other pulse effect that has the potential for device applications is the *Inverse Wiedemann Effect* [12,13]. In its general form this is a change in the magnetic induction of a material caused by an applied torsion. The particular form that is observed in amorphous wires is a torsion-induced change in the switching field of a bistable wire, as shown in Fig. 4.

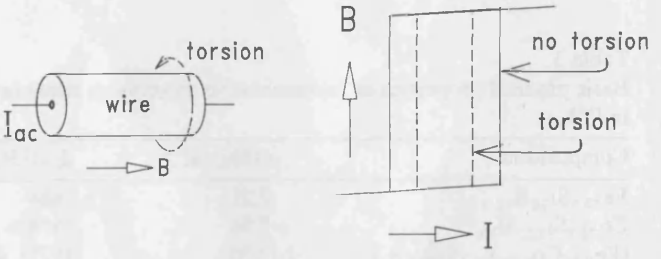

Fig. 4. Inverse Wiedemann effect.

A particular advantage of the pulse voltages that are produced by these effects is that they depend only weakly on the frequency of the exciting field, since they arise from the propagation of a domain wall, not on the rate at which the applied field changes.

3.2. Magnetomechanical effects

Magnetomechanical effects are here taken to include any interaction between the magnetic and mechanical properties of a material. The most direct magnetomechanical effect is magnetostriction. As shown in Table 1, the saturation magnetostriction λ_S can vary from a few ppm negative for cobalt-based wires to nearly 40 ppm positive in iron-based wires. In suitably annealed samples this can result in rates of change of strain $\partial\lambda/\partial H$ and quadratic dependence $\lambda = cH^2$ that are as large as those found in amorphous ribbons [14], and much greater than those found in crystalline materials (Fig. 5).

A consequence of magnetostriction is the field dependence of the elastic moduli, in particular the Young's modulus: the *ΔE effect*. The magnitude of the ΔE effect in wires can approach that of optimally annealed amorphous ribbons, with a maximum variation by as much as a factor of five [16]. Typical results are shown in Fig. 6. Similar behaviour is observed with the shear modulus, leading to a *ΔG effect* of comparable magnitude [17].

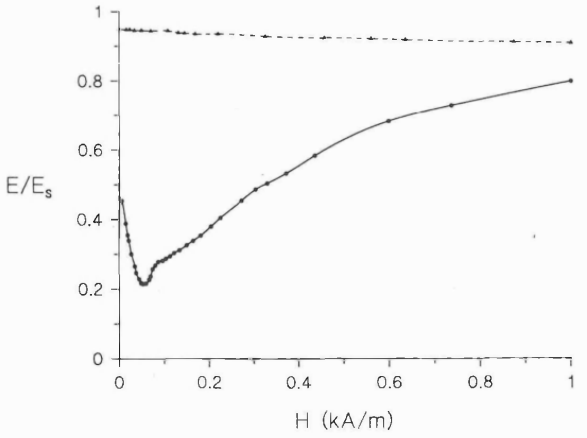

Fig. 6. ΔE effect in current-annealed $Fe_{77.5}Si_{7.5}B_{15}$ wires (solid line) with the data for as-cast wire (broken line) for comparison [16].

A less well known effect is *magnetomechanical damping*. This is the damping of mechanical oscillations by coupling between the mechanical displacement and irreversible wall movements. It can be a very large effect in suitably prepared, magnetostrictive amorphous wires [18].

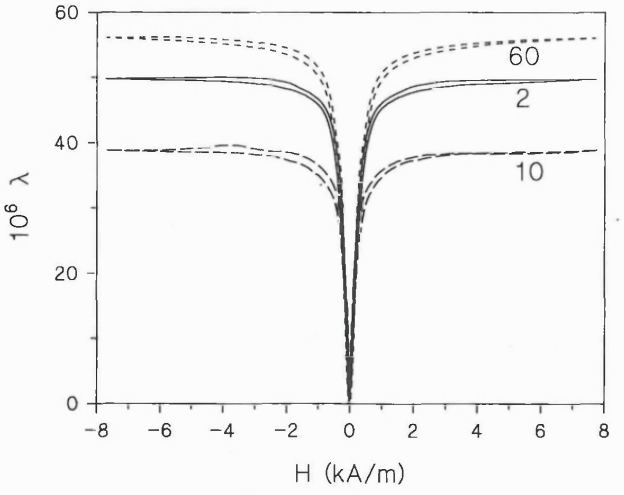

Fig. 5. Engineering magnetostriction of cold-drawn and annealed $Fe_{77.5}Si_{7.5}B_{15}$ wires annealed at 480°C for various times in minutes [15].

4. Post-production treatments

The metallurgy of amorphous wire production determines the diameter of the as-cast wires to be in the range 100–200 μm for the compositions that are magnetically interesting [3]. The rapid quenching process leaves a substantial residual stress in the as-cast wires. Estimates based on the measured anisotropy constant and saturation magnetostriction ($K_u = \frac{3}{2}\lambda_S\sigma$) put the residual stress σ_r at between 40 and 330 MPa for a wide range of compositions [6]. As-cast wires commonly exhibit the LBE and the associated Matteucci and inverse Wiedemann effects, and so may be used directly for applications based on these effects.

Features of as-cast wires that may make them unsuitable for other applications include the large anisotropy (typically $\sim 10^3$ J/m^3 [6]) and spatial inhomogeneity [19]. In order to overcome the

limitations set by these features, several kinds of post-production treatment have been used. Another reason for post-production treatment of amorphous wires is to induce bistability in compositions that are not bistable in the as-cast state, particularly the near-zero magnetostriction Co-rich composition [20]. Surprisingly large anisotropies (~ 100 J/m^3) can be induced by annealing this alloy under stress [21]. The variety of treatments and effects is too large for a full description here; a summary is given in Table 2.

5. Domain models

The basic core–shell model of magnetic domain structure (Fig. 2) has proved very effective for understanding the magnetic behaviour of amorphous wires. However, as a result of recent studies it is necessary to refine the model. In this section we review these studies and discuss their implications for domain models.

5.1. Internal stress distribution

In its simplest form the core–shell model assumes a residual radial tensile stress in the as-cast state. Combined with positive magnetostriction this produces a radial easy axis. On the other hand, shape anisotropy favours axial magnetization. The resulting domain structure (Fig. 2a) consists of radially magnetized domains in the outer shell. The large demagnetization energy that would result from a pure radial domain structure is reduced by axial closure domains on the surface and along the core. The easy axes are thus either along the wire axis or perpendicular to it, and the moments in zero applied field make angles of either 0 or 90° to the axis, except in domain walls. Negative magnetostriction results in the 'bamboo' domain structure shown in Fig. 2(b), with the easy axis circumferential.

The actual stress distribution inside as-cast wires has been the subject of some debate. Kinoshita et al. [31] studied the effect of applied tensile and compressive stresses on the Matteucci voltage and nucleation field, and deduced that, in addition to the radial tensile stress, there is an axial stress that changes progressively from compressive at the surface to tensile at the centre. This would be completely consistent with the above domain structure. Attempts to calculate the residual stress by considering the temperature gradients during quenching have resulted in conflicting pictures. Madurga and Hernando [32] modelled the quenching process with radial heat flow and a series of concentric solidifying shells. They calculated the radial stress in arbitrary units, and showed that it is positive for all radii, with a maximum near 0.7 times the wire radius r_W. Liu et al. [33] also modelled the cooling process; their results for wire with a radius of 60 μm show what appears to be the residual axial stress falling rapidly from ~ 1200 MPa compressive at the

Table 2
Post-production treatments of amorphous wires

Treatment	Purpose	Comments	Refs.
Cold-drawing	Improve surface quality. Improve cross-sectional uniformity. Reduce demagnetizing factor	Produces large residual stress, so annealing is required for magnetic use	[1,3,19]
Furnace annealing	Reduce residual stress and anisotropy to improve magnetic softness. Induce controlled surface crystallization	Good temperature uniformity. No magnetic field. Limited to short samples	[15,23,24]
Current annealing	As furnace annealing. The current can be steady or pulsed ('flash annealing')	Quick and convenient. Temperature nonuniform because of local inhomogeneities; also difficult to measure	[15,16,25,26,27]
Current + stress annealing	Induce controlled anisotropy	Difficult to obtain uniformity	[1,21,28,29,30]

surface to zero at a depth of about 20 μm. It then rise gradually to about 150 MPa tensile halfway in, finally falling to zero at the core (Fig. 7). Velázquez et al. [34] calculated three components of stress: axial, radial and azimuthal. Their results (Fig. 7) for the axial and radial components are qualitatively consistent with those of [32] and [33], but the quantitative agreement with [33] is not close. The existence of the predicted azimuthal component is supported by measured asymmetry in the M_φ–H_z hysteresis loops.

Experimental studies of the internal stress have mainly involved measuring the dependence of the remanence M_r and switching field H^* on applied axial stress (e.g. [24,31,35–37]). Typical of these studies is [35], in which the authors assume radial stress with a Gaussian distribution. They fit the experimental curves with various values of mean stress and dispersion, obtaining values of 6 MPa and 200–250 MPa respectively for best fit. Fig. 7 indicates that the dispersion is of the right order of magnitude, but neglect of residual axial and azimuthal stress components, and the assumption of a Gaussian distribution, are not well founded. A more recent study [36] deduces a mean internal stress of 150 ± 15 MPa from the stress dependence of the switching field, based on calculation of the wall energy. The distribution of radial stress within the outer shell is derived from the stress dependence of the remanence; the results show a broad, non-Gaussian distribution between 0 and 450 MPa.

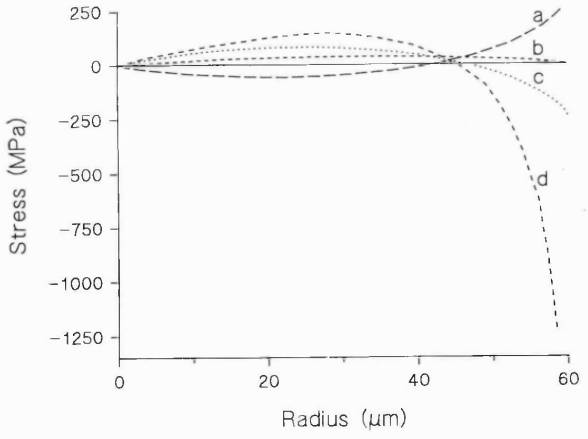

Fig. 7. Calculated stress distributions in as-quenched wires; (a) azimuthal, (b) radial, (c) axial [34], (d) axial [33]. Radius 60 μm.

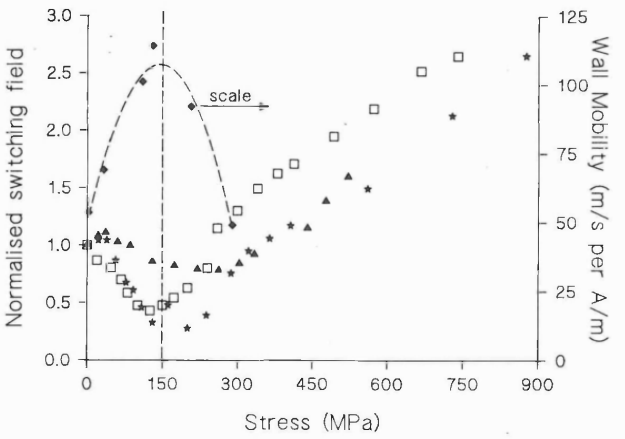

Fig. 8. Stress dependence of the switching field H^* in as-cast $Fe_{77.5}Si_{7.5}B_{15}$ wires. □[36]; ▲ [25]; ⋆ [31]. Also shown is the wall mobility (♦) [7].

The appearance of a minimum in the stress dependence of the switching field at an applied axial stress of about 150 MPa [36] is matched by a maximum in the stress dependent wall mobility at the same stress [7]. Both effects are consistent with a mean internal stress value of this magnitude. Fig. 8 shows some of these data.

5.2. Easy axis distributions

It is generally accepted that the dominant anisotropy mechanism in amorphous wires is that caused by stress and magnetostriction. In principle, therefore, it should be possible, given the internal stress distribution, to calculate the internal anisotropy at any point; in particular, the easy axis distribution should be calculable. Some care is needed in this step. The principle danger is in treating stress as a vector, rather than a tensor. This can result in easy axes at angles intermediate between the principle stresses [34], whereas the easy axis for positive magnetostriction is always in the direction of the largest orthogonal stress component. Consequently, the easy axis directions for principal stresses along and orthogonal to the wire axis should also be along and orthogonal to the wire axis; that is, in zero applied field, all moments should lie at angles of 0

or 90° to the axis. This is the situation represented in the original core–shell model (Fig. 2).

There is strong evidence that this picture is oversimplified. Three types of experiment support the existence of a significant spread of easy axis angles in as-cast wires: second harmonic voltage measurements, the Matteucci effect and field dependent elastic modulus measurements.

When a small ac field is applied along the axis of a wire, moments in the core inclined at nonzero angles to the axis induce voltages in an axial pickup coil at twice the excitation frequency. Kinoshita [37] has used this effect to estimate the easy axes in the core of as-cast Fe-based wires to be inclined at angles between 40° and 65° to the wire axis. Supplementary measurements of the pulse voltages induced in short pickup coils are interpreted by assuming angles between 40° and 48°. The shell moments are not involved in these measurements because of the closure domain structure.

The Matteucci effect normally appears when a sample is twisted, thereby inducing helical anisotropy. The measurement of small Matteucci voltages in untwisted wires (e.g. [10]) shows clearly that some helical anisotropy exists in the as-cast state.

The third type of measurement that confirms a range of easy axis angles is the ΔE effect. It has been shown [38], that moment rotation through a full 90° results in a zero-field Young's modulus E_0 equal to the saturation value, accompanied by a fall to a minimum at the anisotropy field H_K, and a sudden return to the saturation modulus above H_K. The field dependence of the ratio E/E_S is a sensitive function of the easy axis orientation [39]; the shear modulus can be used in a similar way. Measurements of the field dependent elastic moduli have been used to study the behaviour of the easy axis distribution in as-cast and annealed amorphous wires [16,17,23, 26]. Fig. 9 shows the field dependence of Young's modulus for an as-cast Fe-based amorphous wire. The value of E_0/E_S is substantially less than one on the scale of the small overall effect; the modulus also shows a pronounced minimum. This behaviour can only be explained in terms of moment rotations between 45° and 90°; that is, easy

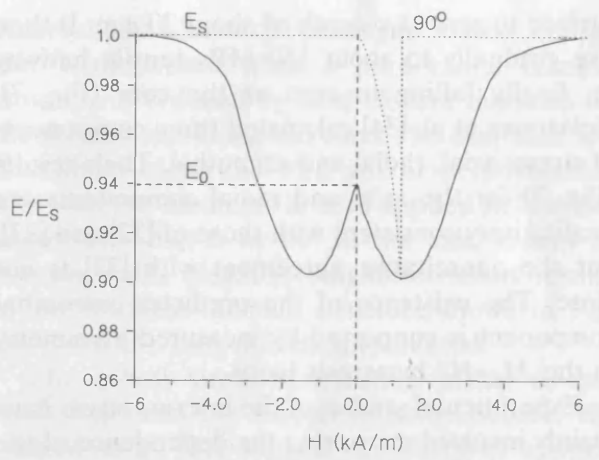

Fig. 9. Field dependence of the Young's modulus of as-cast $Fe_{77.5}Si_{7.5}B_{15}$ wire, normalised to the saturation value. The ideal behaviour of a material with pure moment rotation through 90° [38] is shown for comparison.

axes inclined between 45° and 90° to the wire axis. In this case, the moments responsible for the effect are predominantly in the shell, not the core, because the measured modulus is overwhelmingly determined by the material at larger radii for purely mechanical reasons. Similar results have been obtained with Co-based wire. It is interesting to note the suggestion, based on direct domain observations in [40], that the surface closure domains may not be exactly parallel to the surface. This supports the above argument.

The dispersion of easy axis angles throughout the volume of as-cast amorphous wires shows that the dominant stress axis must also vary. One mechanism that has been suggested [10] to explain this is that during the solidification process random twisting stresses are introduced. A further possibility is afforded by the microscopic voids that have been reported in the bulk of fractured amorphous wires [41]. Although these are estimated to occupy less than 0.1% of the volume, the distortion of the stress field around them could extend to a significantly greater fraction of the material.

5.3. The current status of domain models

The basic validity of the core–shell model has been established by extensive indirect experimen-

tal studies, and is consistent with direct surface domain observations that have been reported. A major problem with direct domain observations is that they can only be made on the surface, either of unpolished wires (e.g. [42–44]) or of polished flats [40,44,45]; the domain structures inside the wire can only be inferred. However, by combining direct and indirect evidence it has been possible to build up a fairly detailed picture of the domain structure, especially in as-cast $Fe_{77.5}Si_{7.5}B_{15}$ wire. A Bitter colloid domain image taken on the surface of an as-cast $Fe_{77.5}Si_{7.5}B_{15}$ wire is shown in Fig. 10. The helical pattern is not observed at all positions along the surface; at other places the dominant bands run at various angles to the axis, as shown in [10]. The smaller lines are thought to correspond to the closure domains shown in Fig. 2(a). What these images show is that the shell domain magnetization vectors are not aligned exactly at 90° to the wire axis, and that there are random variations in the domain geometry, presumably controlled by local variations in the casting stresses, as mentioned in Sections 5.1, 5.2 above.

Recent studies of the variation of remanence near the ends [46], and ac loss [47] in as-cast Fe-based wires suggest that the core does not consist of a single cylindrical domain. Instead the authors propose a zero-field tubular domain structure, consisting of an inner core magnetized in the opposite direction to the remanent magnetization, and an outer tube magnetized parallel to the remanent magnetization. There is no independent evidence for this suggestion and, since the argument is rather indirect, it is safer to retain the existing picture (Fig. 2) of a single core domain over the central part of a wire long enough to be bistable. The evidence [8,45,46] for the existence of reverse spike domains at the ends is stronger. There is a significant magnetostatic energy reduction associated with such an arrangement. The length of the reverse domains can be estimated from the critical length for bistability [36], if it is assumed that bistability disappears when the reverse domains at the two ends meet in the middle. This estimate suggests a length of about 3 cm for the reverse spikes.

The picture that emerges from the studies reviewed here is that in the as-cast state of the highly magnetostrictive Fe-based amorphous wires, the domain structure is basically as shown in Fig. 2, but modified by (a) reverse spike domains at the ends; (b) a helical component of magnetization in the core; and (c) a distribution of easy axes in the shell. An attempt to depict these refinements is shown in Fig. 11. Further

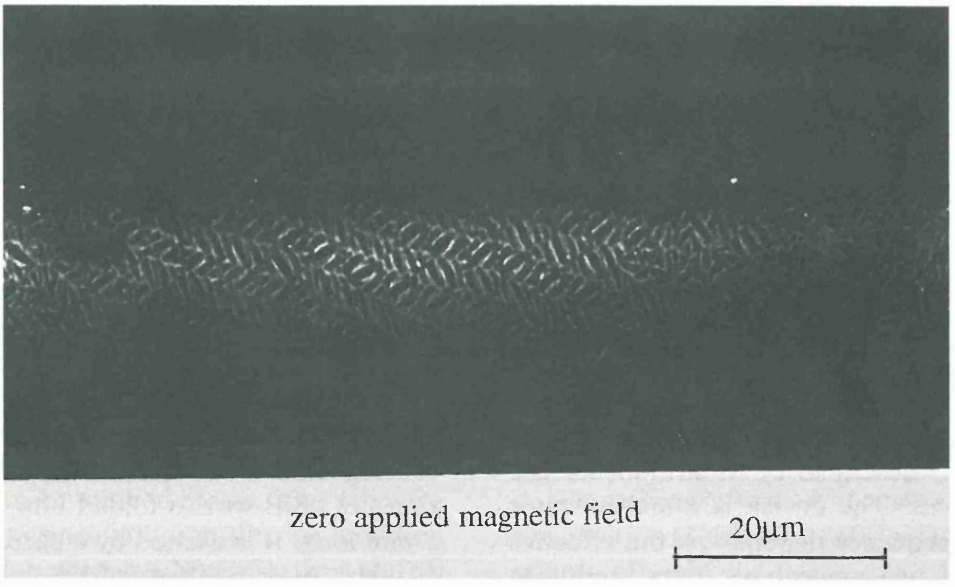

Fig. 10. Domain image taken by the Bitter colloid technique on the surface of an as-cast $Fe_{77.5}Si_{7.5}B_{15}$ wire.

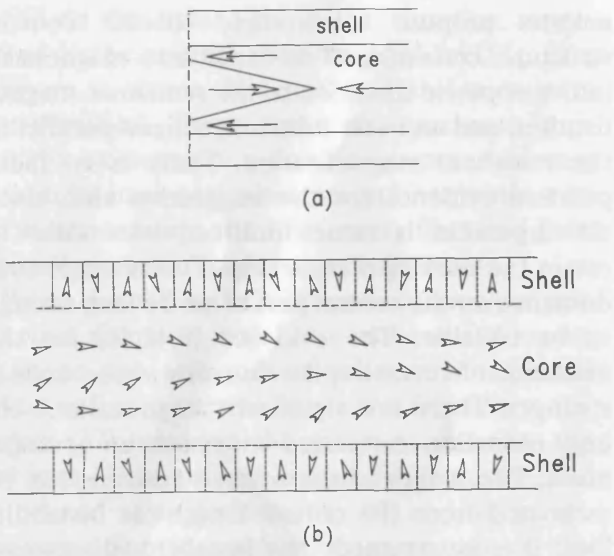

Fig. 11. Postulated domain structures for as-cast $Fe_{77.5}Si_{7.5}B_{15}$ wires (not to scale): (a) Reverse spike domain structures in the core at the ends. (b) Spread of moment directions in the core and sheath; the closure domains (cf. Fig. 2) are omitted for clarity.

study is needed to clarify our understanding of the internal domain structure.

6. Applications

Applications of amorphous wires have been proposed that utilise all the basic phenomena described in Section 2. A good review of applications proposed up to 1990 has been given in [1]. This survey attempts to supplement and update that review.

6.1. Applications based on effective permeability

Amorphous wires are attractive as magnetic cores because they are small, can have high permeability and good frequency response. Several applications based on amorphous wire cores have been demonstrated.

The largest group of applications is based on a device originally described by Mohri [48] for use with ribbon cores. The device is a multivibrator circuit whose frequency depends on the effective permeability of two amorphous cores, acting in push–pull. The effective permeability depends on the applied dc magnetic field, and the output of the device, in a suitable feedback arrangement, is a voltage that varies linearly with field. By adjusting the feedback circuit a voltage of ± 15 V can be obtained for fields of ± 5 to ± 90 mT [49]. The linearity and calibration factor are maintained over a temperature range from -196°C to $+180$°C [50]. The frequency response extends to at least 5 kHz [49].

In addition to its use as a *field sensor*, with a sensitivity of 0.1 μT for dc and 10 pT for ac [49], the device can be adapted as a *current sensor* for busbar currents up to 300 A at up to 5 kHz [50,51]; and for measuring secondary core motor currents of a few amps, at temperatures up to 180°C, and in the presence of stray fields and rotor vibration [50]. Other applications include high-resolution rotary encoding [49], and as a mechanocardiogram, using a small magnet on the body surface to produce field fluctuations [52]. Various arrangements of more groups of cores can be configured as *torque sensors* for static and dynamic torque measurement, free from the large temperature sensitivity that accompanies magnetostrictive torque sensors [50,53].

A device related to the Mohri multivibrator has been described by Kozak et al. [54]. In this the inductance of a coil containing the amorphous wire core forms part of a resonant circuit. The feedback voltage required to maintain stable oscillation varies almost linearly with external field at up to 5 mT, and the noise level is ~ 0.1 μT.

A novel configuration for a field sensor has recently been described by Mohri et al. [55]. Based on what the authors call the *magneto-inductive* (MI) *effect*, it utilises the circumferential field produced by a current in a wire with a circumferential domain structure to produce a circumferential flux change. This, in turn, produces a voltage across the end of the wire. An external axial field reduces the voltage, so the device acts as a field sensor. For use as a field-sensing element (MI-head) a low-magnetostriction FeCoSiB wire is folded into a hairpin shape 5 mm long. It is excited by a current of 30 mA at 10 kHz. A dc field of 0.4 kA/m parallel to the wire axis reduces the induced voltage by 40%.

Two applications of this MI-head are described: a rotary encoder and a cordless data tablet. In a later paper [56] the element is analysed as a field-dependent inductance element. Functionally it behaves very like the Matteucci element in Fig. 3(b), although it does not require any twisting of the wire.

A rather different application of high-permeability amorphous wire cores is as *planar inductance elements*. These consist of a woven combination of copper current-carrying elements and bundles of very fine (5–30 μm) amorphous wires, obtained by etching. Typical performance of an inductor element is $L = 10$ μH, with a Q-factor of > 10 from 0.5–10 MHz [57]. Transformers with coupling coefficients of 0.96 can be made to operate up to 20 MHz.

6.2. Applications based on pulse effects

One of the earliest suggestions for utilising the LBE in amorphous wires was as pulse generator elements. An alternating field applied to a bistable wire produces a sharp voltage pulse in a surrounding pickup coil each time the field goes through the switching field H^*. The sharp flux transition results in a signal spectrum extending to high frequencies, thus enabling objects to be tagged for identification purposes. In as-quenched wires the switching fields are inconveniently low, and a minimum length of 6–7 cm is required for bistable behaviour. Cold drawing FeSiB wires down to 50 μm, followed by annealing under tension, allows the critical length to be reduced to 2 cm and also provides limited control over H^* [58]. Pulse voltages of 0.3 mV per turn were reported. $Co_{39}Fe_{39}Si_9B_{13}$ drawn to 30 or 50 μm, and annealed under tension has been shown to provide accurate control over H^* up to 0.23 mT for pulse generator elements as short as 1 cm. A possible application for several such wires is as *binary coded object markers* for identification purposes [59].

The bistable behaviour of magnetostrictive wires is sensitive to applied stress. The effective small signal ac permeability can thus be modified by the application of stress. Wun-Fogle et al. [29] have suggested the use of this effect as a sensitive strain gage for use in torque sensing. The estimated figure of merit is ~ 2000, compared with the typical value of 2 for resistive strain gages. More detailed characterisation of this device is needed for a proper assessment of its potential.

A data tablet based on the perpendicular Matteucci effect (Fig. 3(c)) has been demonstrated by Kimura et al. [11]. A 40×40 array of 50 μm folded, nonmagnetostrictive FeCoSiB wires, spaced at 5 mm intervals, was powered by a 5 mA dc applied to each wire in turn. The pen was in the form of a cored coil, excited at 140 kHz. The field produced by the pen was perpendicular to the axis of the wires, and the amplitudes of the Matteucci voltages at 280 kHz was decoded to calculate the position to within an estimated 0.1 mm at a data rate of 100 points per second. The Inverse Wiedemann effect has been proposed for use as a magnetic field sensor [60]. A current of 50 mA rms was passed through the twisted FeSiB wire. The frequency was varied from 40 Hz to 5 kHz and the second harmonic signal measured as a function of applied dc field. Linear behaviour was observed at fields up to 20 μT, with a sensitivity of 20 V/mT at 5 kHz. In an area of sensing so well covered by other techniques, this application should perhaps be regarded as an interesting novelty.

6.3. Applications based on magnetomechanical effects

The magnetostrictive response of amorphous wire has been utilised in a recent version of the *Fibre-Optic Magnetometer* [61]. In this system a magnetostrictive element attached to a length of optical fibre produces a phase change in one arm of a Mach–Zehnder interferometer, when the external field is altered. In earlier versions of the system amorphous ribbons were used as the magnetostrictive elements. The use of an annealed, cold-drawn 100 μm FeSiB wire, 5 cm long, improves the performance by virtue of the reduced demagnetizing effect of the wire. The reported sensitivity was 1.7 $nT/\sqrt{Hz}$ at a measuring frequency of 1 Hz.

Magnetostrictive delay lines (MDL) allow the

possibility of position sensing deduced from the time of arrival of a pulse. In this device a small coil excites a magnetostrictive pulse at one point along a wire or ribbon. The pulse propagates along the wire at the speed of sound, and is detected by the voltage induced in another small coil some distance away. The propagation and detection of magnetostrictive waves (sometimes called Magnetoelastic waves, or MEW) along amorphous wires has been studied by Masuda and Kakuno [19], who showed how important scattering can be, and how it can be improved by cold drawing and annealing. An application of a MDL to displacement sensing has been described by Hristoforou and Niarchos [62]. In their arrangement FeSiB and FeCoCrSiB wires were used. The amplitude of the transmitted voltage pulse depends on the bias field at the position of the transmitting and sensing coils, and can therefore be used to measure the position of a bias magnet. A quasi-linear response was obtained over a range of up to 20 mm. Suggestions for one and two dimensional arrays of such sensors are given, but no results. The authors identify nonuniformity of the wire as the major limitation, as indicated in [19]. This application therefore also requires further development before becoming technically attractive.

7. Conclusions

The properties of amorphous wires, both in the as-quenched state, and after a wide range of post-production treatments, are now well characterised. The basic core–shell domain structure can be used as the basis for explaining a wide range of magnetic and magnetomechanical behaviour. It appears that the simplest models of moment distribution in core and shell must be modified to allow significant spread of easy axis directions.

Applications of most of the phenomena observed in amorphous wires have been proposed. Some of these are unique to wires, depending on the core–shell domain structure. Others are developments of applications already demonstrated with amorphous ribbons. There are, as yet, very few applications that can be regarded as fully commercial. Further development of material technology and signal processing may change this conclusion in the next few years.

References

[1] Unitika Ltd., Intermag '90 Symposium on Amorphous Magnetic Wire and Applications (London, April 1990).
[2] F.B. Humphrey, K. Mohri, J. Yamasaki, H. Kamura, R. Malmhäll and I. Ogasawara, in: Magnetic Properties of Amorphous Metals, Eds. A. Hernando et al. (Elsevier, Amsterdam, 1987) p. 110.
[3] Y. Waseda, S. Ueno, M. Hagiwara and K.T. Aust, Progr. Mat. Sci. 34 (1990) 149.
[4] Unitika Ltd., Amorphous Metal Fibres Data Sheet.
[5] Y. Konno and K. Mohri, IEEE Trans. Magn. 25 (1989) 3623.
[6] K. Mohri, F.B. Humphrey, K. Kawashima, K. Kimura and M. Mizutani, IEEE Trans. Magn. 26 (1990) 1789.
[7] M.R.J. Gibbs, I.E. Day, T.A. Lafford and P.T. Squire, J. Magn. Magn. Mater. 104 (1992) 327.
[8] C. Gómez-Polo, M. Vázquez and D.X. Chen, Appl. Phys Let. 62 (1993) 108.
[9] L.V. Panina, H. Katoh, M. Mizutani, K. Mohri and F.B. Humphrey, IEEE Trans. Magn. 28 (1992) 2922.
[10] K. Mohri, F.B. Humphrey, J. Yamasaki and F. Kinoshita, IEEE Trans. Magn. 21 (1985) 2017.
[11] K. Kimura, M. Kanoh, K. Kawashima, K. Mohri, M. Takagi and L.V. Panina, IEEE Trans. Magn. 27 (1991) 4861.
[12] J.L. Costa, Y. Makino and K.V. Rao, IEEE Trans. Magn. 26 (1990) 1792.
[13] J. González, J.M. Blanco, J.M. Barandiarán, M. Vázquez, A. Hernando, G. Rivero and D. Niarchos, IEEE Trans. Magn. 26 (1990) 1798.
[14] A.P. Thomas, Ph.D. Thesis, University of Bath (1991).
[15] S. Atalay, Ph.D. Thesis, University of Bath (1992).
[16] S. Atalay and P.T. Squire, J. Appl. Phys. 70 (1991) 6516.
[17] S. Atalay and P.T. Squire, J. Magn. Magn. Mater. 101 (1991) 47.
[18] S. Atalay and P.T. Squire, J. Appl. Phys. 73 (1993) 871.
[19] S. Masuda and K. Kakuno, IEEE Trans. Magn. 26 (1990) 1800.
[20] C. Gómez-Polo, M. Vázquez, T. Reininger and H. Kronmüller, Proc. 3rd Intnl. Workshop on Non-Crystalline Solids (Seville, 1991).
[21] J.M. Blanco, P.G. Barbon, J. González, C. Gómez-Polo and M. Vázquez, J. Magn. Magn. Mater. 104 (1992) 137.
[22] I. Ogasawara and K. Mohri, IEEE Trans. Magn. 26 (1990) 1795.
[23] D. Atkinson, P.T. Squire, M.R.J. Gibbs, S. Atalay and D.G. Lord, J. Appl. Phys. 73 (1993) 3411.
[24] A. Mitra and M. Vázquez, J. Phys. D: Appl. Phys. 23 (1990) 228.

[25] A. Mitra, K. Mandal and S.K. Ghatak, J. Magn. Magn. Mater. 110 (1992) 135.
[26] S. Atalay, P.T. Squire and M.R.J. Gibbs, IEEE Trans. Magn. 29 (1993) 3472.
[27] C. Gómez-Polo and M. Vázquez, J. Magn. Magn. Mater. 118 (1993) 86.
[28] J. González, P.G. Barbón, J.M. Blanco, M. Vázquez, J.M. Barandián and A. Hernando, IEEE Trans. Magn. 28 (1992) 2769.
[29 M. Wun-Fogle, J.B. Restorff, A.E. Clark and H.T. Savage, J. Appl. Phys. 70 (1991) 6519.
[30] A. Mitra, M. Vázquez, K. Mandal and S.K. Ghatak, J. Appl. Phys. 70 (1991) 4455.
[31] F. Kinoshita, R. Malmhäll, K. Mohri, F.B. Humphrey and J. Yamasaki, IEEE Trans. Magn. 22 (1986) 445.
[32] V. Madurga and A. Hernando, J. Phys. Condensed Matter 2 (1990), 2127.
[33] J. Liu, R. Malmhäll, L. Arnberg and S.J. Savage, J. Appl. Phys. 67 (1990) 4238.
[34] J. Velázquez, M. Vázquez, A. Hernando, H.T. Savage and M. Wun-Fogle, J. Appl. Phys. 70 (1991) 6525.
[35] V. Madurga, J.L. Costa, A. Inoue and K.V. Rao, J. Appl. Phys. 68 (1990) 1164.
[36] A.M. Severino, C. Gómez-Polo, P. Marín and M. Vázquez, J. Magn. Magn. Mater. 103 (1992) 117.
[37] F. Kinoshita, IEEE Trans. Magn. 26 (1990) 1786.
[38] J.D. Livingston, Phys. Stat. Sol. (a) 70 (1982) 591.
[39] P.T. Squire, J. Magn. Magn. Mater. 87 (1990) 299.
[40] M. Letcher, G.A. Jones, D.G. Lord, M. Wun-Fogle and H.T. Savage, J. Appl. Phys. 69 (1991) 5331.
[41] A.O. Olofinjana and H.A. Davies, Script. Metall. Mater. 27 (1992) 1679.
[42] J. Yamasaki, F.B. Humphrey, K. Mohri, H. Kawamura, H. Takamure and R. Malmhäll, J. Appl. Phys. 63 (1988) 3949.
[43] D. Atkinson, P.T. Squire, M.R.J. Gibbs and J. Yamasaki, IEEE Trans. Magn. 29 (1993) 3478.
[44] M. Takajo, J. Yamasaki and F.B. Humphrey, IEEE Trans. Magn. 29 (1993) 3484.
[45] T. Reininger, H. Kronmüller, C. Gómez-Polo and M. Vázquez, J. Appl. Phys. 73 (1993) 5357.
[46] M. Vázquez, C. Gómez-Polo and D.X. Chen, IEEE Trans. Magn. 28 (1992) 3147.
[47 D.X. Chen, M. Vázquez, G. Dejulian and C. Gómez-Polo, J. Magn. Magn. Mater. 115 (1992) 295.
[48] K. Mohri, K. Kasai, T. Kondo and H. Fujimara, IEEE Trans. Magn. 19 (1983) 2142.
[49] K. Mohri, in: Magnetic Properties of Amorphous Metals, Eds. A. Hernando et al. (Elsevier, Amsterdam, 1987) p. 360.
[50] K. Inuzuka and K. Mohri, IEEE Trans. Magn. 28 (1992) 2178.
[51] Y. Kashiwagi, T. Kondo, K. Mitsui and K. Mohri, IEEE Trans. Magn. 26 (1990) 1566.
[52] K. Mohri, T. Jinnouchi and K. Kawano, IEEE Trans. Magn. 23 (1987) 2212.
[53] K. Mohri, Y. Mukai, K. Yasuda and K. Takayama, IEEE Trans. Magn. 23 (1987) 2191.
[54] M.Z. Kozak, E. Misiuk and W. Kwiatkowski, J. Appl. Phys. 69 (1991) 5023.
[55] K. Mohri, T. Kohzawa, K. Kawashima, H. Yoshida and L.V. Panina, IEEE Trans. Magn. 28 (1992) 3150.
[56] K. Mohri, K. Kawashima, T. Kohzawa and H. Yoshida, IEEE Trans. Magn. 29 (1993) 1245.
[57] Y. Kobayashi, S. Ishibashi, K. Shirakawa, J. Toriu, H. Matsuki and K. Murakami, IEEE Trans. Magn. 28 (1992) 3012.
[58] R. Malmhäll et al., IEEE Trans. Magn. 23 (1987) 3242.
[59] I. Ogasawara and K. Mohri, IEEE Trans. Magn. 26 (1990) 1795.
[60] E. Pulido, R.P. del Real, F. Conde, G. Rivero, M. Vázquez, E. Ascasibar and A. Hernando, IEEE Trans. Magn. 27 (1991) 5241.
[61] K.P. Koo, F. Bucholtz, D.M. Dagenais and A. Dandridge, IEEE Photon. Technol. Lett. 1 (1989) 464.
[62] E. Hristoforou and D. Niarchos, J. Magn. Magn. Mater. 116 (1992) 177.

1994 PHYSICS and MATERIALS SCIENCE JOURNALS

Applied Surface Science
Volumes 72-81 in 40 issues. Price: US $ 2114.00 / Dfl. 3910.00

Astroparticle Physics
Volume 2 in 4 issues. Price: US $ 182.00 / Dfl. 336.00

Computational Materials Science
Volume 2 in 4 issues. Price: US $ 211.00 / Dfl. 391.00

Computer Physics Communications
Volumes 79-85 in 21 issues. Price: US $ 2236.00 / Dfl. 4137.00

International Journal of Applied Electromagnetics in Materials
Volume 5 in 4 issues. Price: US $ 203.00 / Dfl. 376.00

Journal of Crystal Growth
Volumes 135-145 in 44 issues. Price: US $ 4822.00 / Dfl. 8921.00

Journal of Geometry and Physics
Volumes 13 and 14 in 8 issues. Price: US $ 358.00 / Dfl. 662.00

Journal of Luminescence
Volumes 59-62 in 24 issues. Price: US $ 1083.00 / Dfl. 2004.00

Journal of Magnetism and Magnetic Materials
Volumes 126-137 in 36 issues. Price: US $ 3347.00 / Dfl. 6192.00

Journal of Non-Crystalline Solids
Volumes 162-176 in 45 issues. Price: US $ 3535.00 / Dfl. 6540.00

Journal of Nuclear Materials
Volumes 206-216 in 33 issues. Price: US $ 3098.00 / Dfl. 5731.00

Materials Letters
Volumes 19-22 in 24 issues. Price: US $ 899.00 / Dfl. 1664.00

Nuclear Instruments and Methods in Physics Research - Section A
Accelerators, Spectrometers, Detectors & Associated Equipment
Volumes 337-351 in 45 issues. Price: US $ 5441.00 / Dfl. 10,065.00

Nuclear Instruments and Methods in Physics Research - Section B
Beam Interactions with Materials and Atoms
Volumes 83-94 in 48 issues. Price: US $ 4352.00 / Dfl. 8052.00
Reduced combined 1994 subscription price to Nuclear Instruments and Methods - A and B: US $ 9063.00 / Dfl. 16,767.00

Nuclear Physics A
Volumes 566-580 in 60 issues. Price: US $ 4792.00 / Dfl. 8865.00

Nuclear Physics B
Volumes 409-432 in 72 issues. Price: US $ 7537.00 / Dfl. 13,944.00

Nuclear Physics B - Proceedings Supplements
Volumes 34-38 in 15 issues. Price: US $ 881.00 / Dfl. 1630.00
Reduced combined 1994 subscription price to Nuclear Physics A + Nuclear Physics B + NPB-Proceedings Supplements: US $ 11,202.00 / Dfl. 20,724.00

Optical Materials
Volume 3 in 4 issues. Price: US $ 206.00 / Dfl. 381.00

Optics Communications
Volumes 103-111 in 54 issues. Price: US $ 2121.00 / Dfl. 3924.00

Physica A - Statistical and Theoretical Physics
Volumes 201-211 in 44 issues. Price: US $ 2503.00 / Dfl. 4631.00*

Physica B - Condensed Matter Physics
Volumes 192-202 in 44 issues. Price: US $ 2503.00 / Dfl. 4631.00*

Physica C - Superconductivity
Volumes 219-236 in 72 issues. Price: US $ 4096.00 / Dfl. 7578.00*

Physica D - Nonlinear Phenomena
Volumes 70-78 in 36 issues. Price: US $ 2048.00 / Dfl. 3789.00*

**Reduced rates are available for combined subscriptions to Physica; please contact the publisher for details.*

Physics Letters A
Volumes 185-197 in 78 issues. Price: US $ 2537.00 / Dfl. 4693.00

Physics Letters B
Volumes 317-340 in 96 issues. Price: US $ 4683.00 / Dfl. 8664.00

Physics Reports
Volumes 240-251 in 72 issues. Price: US $ 2342.00 / Dfl. 4332.00
Reduced combined 1994 subscription price to Physics Letters A, Physics Letters B + Physics Reports: US $ 8502.00 / Dfl. 15,729.00

Solid State Ionics
Volumes 68-76 in 36 issues. Price: US $ 1805.00 / Dfl. 3339.00

Surface Science
(including Surface Science Letters)
Volumes 296-318 in 69 issues. Price: US $ 6104.00 / Dfl. 11,293.00

Surface Science Reports
Volume 18-20 in 24 issues. Price: US $ 618.00 / Dfl. 1143.00
Reduced combined 1994 subscription price to Surface Science (including Surface Science Letters), Applied Surface Science and Surface Science Reports: US $ 8192.00 / Dfl. 15,156.00

Ultramicroscopy
Volumes 52-56 in 20 issues. Price: US $ 1151.00 / Dfl. 2130.00

Dutch Guilder price(s) quoted applies worldwide, except in the Americas (North, Central and South America). US Dollar price(s) quoted applies in the Americas only. Journals are sent by Surface Mail to all countries except to the following where Air Delivery via SAL mail is ensured at no extra cost to the subscriber: Argentina, Australia/New Zealand, Brazil, Hong Kong, India, Israel, Japan, Malaysia, Mexico, Pakistan, P.R. China, Singapore, S. Africa, S. Korea, Taiwan, Thailand, USA & Canada. Customers in the European Community should add the appropriate VAT rate applicable in their country to the price(s).

ELSEVIER SCIENCE B.V.

P.O. Box 103, 1000 AC Amsterdam, The Netherlands

Elsevier Science Inc., Journal Information Center, PO Box 882, Madison Square Station, New York, NY 10159, U.S.A.